UNIVERSITY OF SOUTHAMPTON

Diurnal Warming and Convective CO_2 Exchange in the Tropical Atlantic

by

Christopher D. Jeffery

A thesis submitted in partial fulfillment for the
degree of Doctor of Philosophy

Faculty of Engineering, Science and Mathematics
School of Ocean and Earth Science

June 2008

UNIVERSITY OF SOUTHAMPTON

ABSTRACT

FACULTY OF ENGINEERING, SCIENCE AND MATHEMATICS
SCHOOL OF OCEAN AND EARTH SCIENCE

Doctor of Philosophy

Diurnal Warming and Convective CO_2 Exchange in the Tropical Atlantic

by Christopher D. Jeffery

The distribution of Carbon Dioxide (CO_2) in surface waters is strongly influenced by the kinetics of exchange across the air-sea interface. Simple bulk models characterize the turbulent and molecular processes as strong functions of the wind-speed. At low wind speeds however, other factors such as sea surface temperature become dominant. Since gas solubility is a function of temperature, diurnal variability can significantly alter the amount of gas exchanged. Furthermore, at night, when the outgoing heat fluxes exceed the incoming heat fluxes the surface cools, which can result in unstable conditions. Buoyancy-driven convective overturning enhances mixing and redistributes heat over the water column. This enhanced turbulence will directly affect the transfer of gases across the air-water interface. Equatorial and mid-latitude regions of the worlds oceans such as the Tropical Atlantic are particularly susceptible to conditions such as these. Current estimates of global and regional air-sea CO_2 transfer neglect these important effects.

A one dimensional turbulence closure model is configured to recreate the diurnal temperature structure in the Tropical Atlantic. Surface forcing from a PIRATA mooring is used in conjunction with cloud cover estimates from Meteosat-7 to adequately recreate the near surface temperature record. The model serves as a test-bed for evaluating a modified version of the National Oceanic and Atmospheric Administration Coupled Ocean Atmosphere Response Experiment (NOAA-COARE) air-sea gas transfer parameterization. The modified model includes a new term based on a water-side convective velocity scale, to improve parameterization of convectively driven gas transfer. Twin model experiments, representing idealistic and realistic conditions are used to investigate the upper ocean response to diurnal warming and subsequent convective CO_2 transfer. The global and regional significance is evaluated using the U.K. Met Office FOAM-HadOCC system, a physical model of the ocean coupled to a simple carbon cycle model. Air-sea CO_2 fluxes calculated using the improved COARE model are compared with the existing Met Office implementation, a simple wind-speed dependent model. FOAM-HadOCC simulations incorporating the improved parameterization reveal that convective exchange results in increased ocean degassing of the order 5% globally.

Acknowledgements

I would like to thank David Woolf, Ian Robinson and Craig Donlon, my supervisors, for both their continual support and friendship. Without their guidance this thesis would not have been possible. In addition, I would like to thank Rosa Barciela, David Acreman, and the rest of the NCOF group for their help during my time spent at the U.K. Met Office. I would also like to extend my thanks to the Ocean Observing and Climate research group at the National Oceanography Centre, Southampton, who have been an invaluable source of oceanographic and remote sensing knowledge. In particular Sussane Fanghor, for her valuable comments and criticism. Finally I would like to thank all of my friends that have put up with me from start to finish of this PhD.

Contents

List of Figures

List of Tables

Symbols

Symbol	Property represented	Units
a	Albedo	dimensionless
a_l	Thermal expansion coefficient	K^{-1}
A	Adjustable factor to fit measured transfer velocities	–
A_T	Total alkalinity	mol litre^{-1}
b_c	Saline expansion coefficient	psu^{-1}
b_v	Buoyancy variance	m^2 s^{-5}
B	Adjustable factor for bubble mediated gas transfer	–
B_{fa}	Atmospheric buoyancy flux	W kg^{-1}
B_{fw}	Waterside buoyancy flux	W kg^{-1}
B_r	Buoyancy in the surface layer	N
$B(d)$	Buoyancy at depth (d)	N
c_{dd}, c_{ed}, c_{hd}	Heat and momentum exchange coefficients	dimensionless
c_p	Specific heat capacity of sea water at constant pressure	J g^{-1} K^{-1}
c_{pa}	Specific heat capacity of air at constant pressure	J g^{-1} K^{-1}
c_w	Craig and Banner wave breaking constant	–
c_μ, $c_\mu{}'$	Stability functions	dimensionless
$c_{\epsilon 1}$, $c_{\epsilon 1}$, $c_{\epsilon 1}$	Constants for Rodi (1987)	–
C_1, C_2	Empirical coefficients for Hasse (1963)	–
C_D	Drag coefficient	dimensionless
C_T	Dissolved Inorganic Carbon	μmoles litre^{-1}
C_p, C_z, C_d	Fixed carbon:nitrogen ratios	–
C_r	Redfield ratio	–
d	Depth	m
D	Detritus	μmoles litre^{-1}
D_{cc}	Carbonate dissolution	–
D_v	Molecular diffusivity	m^{-2} s^{-1}

$\mathcal{D}$	Sum of the viscous and turbulent transport terms	$m^{-2}\ s^{-1}$
e	Vapour pressure	Pa
f	Coriolis parameter	s^{-1}
f_w	Whitecap fraction	–
F	Air-sea gas flux	mol $m^{-2}\ yr^{-1}$
g	Acceleration due to gravity	m s^{-2}
G_k	Production of TKE by mean buoyancy	$m^2\ s^{-3}$
G_p, G_d	Loss of phytoplankton and detritus to grazing in nitrogen units	–
$G(\sigma)$	Shape function in the KPP model	–
h_a, h_w	Coefficient of the molecular diffusive sublayer	–
h	Well mixed layer depth	m
h_{bl}	Boundary layer depth	m
h_E	Ekman depth	m
I	Downward irradiance	W m^{-2}
k	Gas transfer velocity	cm hr^{-1}
k_b	Gas transfer enhancement of due to bubbles	cm hr^{-1}
k_e	Turbulent kinetic energy (TKE)	$m^2\ s^{-2}$
k_D	Sum of the turbulent and molecular diffusivities	$m^{-2}\ s^{-1}$
k_T	Thermal conductivity of water	W m^{-1} K
K	Gas exchange coefficient	mol $m^{-2}\ yr^{-1}\ \mu atm^{-1}$
K_d	Turbulent eddy diffusivity	$m^2\ s^{-1}$
$K(z)$	Depth dependent diffusion coefficient	dimensionless
K_0, K_1, K_2	Carbonate system chemical constants	–
l	Dissipative length scale	m
L	Monin-Obukhov length scale	m
L_e	Latent heat of vaporization	J Kg^{-1}
m	Mass per unit area	kg m^{-2}
m_0P	Mortality rate	day^{-1}
M_v	Shear frequency	s^{-1}
n	Fractional cloud cover	–
N	Nutrient	μmoles $litre^{-1}$
N_v	Brunt-Vaisala (buoyancy) frequency	s^{-1}
p	Pressure	Pa
P	Phytoplankton	μmoles $litre^{-1}$
P_k	Production of TKE by mean shear	$m^2\ s^{-3}$
q	Velocity scale	m s^{-1}

q_a	Specific humidity	kg kg^{-1}
q_{rh}	Relative humidity	%
q_s	Specific saturation humidity	kg kg^{-1}
Q	Total cooling at the interface	W m^{-2}
Q_c	Convective transport	W m^{-2}
Q_{cs}	Total radiation reaching surface under clear skies	W m^{-2}
Q_b	Equivalent surface cooling including effects of salinity due to evaporation	W m^{-2}
Q_e	Latent heat flux	W m^{-2}
Q_h	Sensible heat flux	W m^{-2}
Q_l	Net longwave heat flux	W m^{-2}
$Q_l^{\uparrow}$	Longwave back radiation	W m^{-2}
$Q_l^{\downarrow}$	Downwelling longwave radiation	W m^{-2}
Q_{net}	Net surface heat flux	W m^{-2}
Q_{rf}	Sensible heat flux due to rain	W m^{-2}
Q_s	Shortwave heat flux	W m^{-2}
Q_{tot}	Total surface heat flux	W m^{-2}
Q_v	Heat loss due to horizontal advectivion	W m^{-2}
r_a, r_w	Resistances to gas transfer	dimensionless
R	(Jerlov, 1968) water type coefficient	–
R_a	Rayleigh number	dimensionless
R_i	Flux Richardson number	dimensionless
R_p	Specific growth rate for phytoplankton	day^{-1}
S	Salinity	psu
S_a	Average wind speed including gustiness	m s^{-1}
S_c	Schmidt number	dimensionless
S_w	Water-side equivalent of S_a	m s^{-1}
T_0	Temperature at the air-sea interface	°C
T_a	Air temperature	°C
T_i	Rate of change of ecosystem components	–
T_s	Sea surface temperature	°C
T_w	Bulk water temperature	°C
u_{10}	Wind speed at 10 m height	m s^{-1}
u_x	x component of the wind velocity vector	m s^{-1}
u_y	y component of the wind velocity vector	m s^{-1}
u_{*a}	Atmospheric friction velocity	m s^{-1}
u_{*w}	Waterside friction velocity equivalent	m s^{-1}
$\langle u'w' \rangle$	Turbulent fluxes of momentum	m^2 s^{-2}
u, U, v, V	Horizontal velocity components	m s^{-1}
v	kinematic viscosity	m^2 s^{-1}

v_t	Turbulent friction coefficient	–
V_{ix}	Transfer velocity for trace gas (x) in phase (i)	cm hr^{-1}
V_t	Shear due to turbulent velocity	–
$\langle w's' \rangle$	Turbulent fluxes of salinity	m^2 s^{-2}
$\langle w'\theta' \rangle$	Turbulent fluxes of heat	m^2 s^{-2}
w	Wind mixing energy	W m^{-2}
w_{*a}, w_{*w}	Convective velocity scales	m s^{-1}
$w(\sigma)$	Turbulent velocity scale	–
z	Depth of measurement	m
z_i	Planetary boundary layer height	m
z_{ml}	Depth of the convective layer	m
z_r	Depth of molecular diffusion layer	m
Z	Zooplankton	μmoles $litre^{-1}$
α_s	Solubility evaluated using T_s	mol m^{-3} atm^{-1}
α_w	Solubility evaluated using T_w	mol m^{-3} atm^{-1}
β	Convective scaling parameter	–
β_p, β_d	Assimilation efficiencies of phytoplankton and detritus	–
γ	Counter-gradient term in the KPP model	–
γ_c	Carbonate precipitated per unit PP	0.01
$\tilde{\Gamma}_{(U,V,B)}$	Counter-gradient fluxes	m^2 s^{-2}
ΔC	Concentration difference	ppm
ΔE	Energy change	J
ΔT	Temperature change	°C
ΔT_c	Cool skin temperature difference	°C
ΔT_w	Warm layer temperature difference	°C
ϵ	Rate of dissipation	m^2 s^{-3}
η	Respiration rate constant	day^{-1}
$\eta 1$, $\eta 2$	(Jerlov, 1968) water type coefficients	m
θ	Noon solar altitude	°
Θ	Mean potential temperature	°C, K
κ	von Karman constant (0.4)	dimensionless
λ	Generation of TKE tuning parameter	–
λ_n	Latitude dependent cloud cover coefficient	–
λ_s	Saunders parameter	dimensionless
Λ	Empirical coefficient (13.3) defined by Hare et al. (2004)	–
ν_t	Vertical turbulent diffusivity of momentum	m^{-2} s^{-1}

ν_t^B	Vertical turbulent diffusivity of heat	m^{-2} s^{-1}
ξ	Emissivity of the sea surface	dimensionless
ρ_a	Density of air	kg m^{-3}
ρ_w	Density of seawater	kg m^{-3}
σ	Decay of TKE tuning parameter	m
σ_{SB}	Stefan-Boltzman constant (5.67×10^{-8})	W m^{-2} k^{-4}
σ_k, σ_ϵ	Schmidt number for turbulent kinetic energy and dissipation respectively	dimensionless
σ_θ	Density	kg m^{-3}
τ_x^s, τ_y^s	Surface momentum fluxes	N m^{-2}
ϕ	Function to account for buoyancy-driven sublayer processes	–
ψ	Remineralisation rate	day^{-1}
ω	Empirical stability function	–
$\vee(d)$	Vector velocity difference	m s^{-1}

Acronyms

Acronym	Name
AMSR	Advanced Microwave Scanning Radiometer
AOGCM	Atmosphere-Ocean General Circulation Model
ATLAS	Autonomous Temperature Line Acquisition System
AVHRR	Advanced Very High Resolution Radiometer
CFCs	Chlorofluorocarbons
CGMS	Coordination Group for Meteorological Satellites
COARE	Coupled Ocean Atmosphere Response Experiment
CMC	Canadian Meteorological Centre
CTD	Conductivity Temperature Depth
CSIRO	Commonwealth Scientific and Industrial Research Organisation
DIC	Dissolved Inorganic Carbon
DOGEE	Deep Ocean Gas Exchange Experiment
DWBC	Deep Western Boundary Current
EMIC	Earth System Model of Intermediate Complexity
ENSO	El Niño/Southern Oscillation
ESA	European Space Agency
ESRL	Earth System Research Laboratory
FOAM	Forcasting Ocean Assimilation Model
GHRSST-PP	GODAE High Resolution Sea Surface Temperature Pilot Project
GMS	Geostationary Meteorological Satellite
GODAE	Global Ocean Data Assimilation Experiment
GOES	Geostationary Operational Environmental Satellites
GOTM	General Ocean Turbulence Model
GTS	Global Telecommunications System
HadOCC	Hadley Centre Ocean Carbon Cycle Model
IPCC	Intergovernmental Panel on Climate Change
IR	Infrared
ISCCP	International Satellite Cloud Climatology Project
ITCZ	Inter-Tropical Convergence Zone
KPP	K-Profile Parameterization

LT	Local Time
MLD	Mixed Layer Depth
MOC	Meridional Overturning Circulation
MSG	Meteosat Second Generation
MVIRI	Meteosat Visible and Infrared Imager
MW	Microwave
NASA	National Aeronautics and Space Administration
NBC	North Brazil Current
NBUC	North Brazil Undercurrent
NCAR	National Centers for Atmospheric Research
NCEP	National Center for Environmental Prediction
NECC	North Equatorial Counter Current
NOAA	National Oceanic and Atmospheric Administration
OI	Optimum Interpolation
OWS	Ocean Weather Station
PIRATA	Pilot Research Moored Array in the Atlantic
RMS(E)	Root Mean Square (Error)
SCSUI	Standardized Control Suite User Interface
SEC	South Equatorial Current
SOFex	The Southern Ocean Iron Fertilization Experiment
SOIREE	Southern Ocean Iron Enrichment Experiment
SSM/I	Special Sensor Microwave Imager
SST	Sea Surface Temperature
SSTA	Sea Surface Temperature Anomaly
TAO	Tropical Atmosphere Ocean project
TAS	Tropical Atlantic Study
TKE	Turbulent Kinetic Energy
TTO	Transient Tracers in the Ocean
TOGA	Tropical Ocean Global Atmosphere
UKMO	United Kingdom Meteorological Office
UM	Unified Model
UMUI	Unified Model User Interface
UNEP	United Nations Environment Programme
WOCE	World Ocean Circulation Experiment
WMO	World Meteorological Organization
XBT	eXpendable Bathy-Thermograph

Chapter 1

Introduction

1.1 Preface

Heat, momentum and gases are exchanged between the oceans and the atmosphere. The mechanisms that control these exchanges are complex and often coupled. It is important to improve our understanding of the factors that control gas exchange in order to help us quantify more accurately its effect on global climate. Of particular importance is the air-sea exchange of carbon dioxide (CO_2).

Since gas solubility is a function of temperature, during low wind speeds diurnal warming of the upper ocean can significantly alter the amount of gas exchanged. Furthermore, at night, when the outgoing heat fluxes exceed the incoming heat fluxes the surface cools, which can result in unstable conditions. Buoyancy-driven convective overturning enhances mixing and redistributes heat over the water column. This enhanced turbulence will directly affect the transfer of gases across the air-water interface.

The aim of this Ph.D. is to investigate gas transfer occurring during convective conditions, primarily in the tropical Atlantic. In order to do this it will be necessary to characterize the processes which occur near the air-sea interface. Given the similarity between the exchange of heat and gases across the interface it is necessary to understand the subtle interactions between both heat and gas exchange and near surface temperatures.

A one-dimensional model framework is presented as a tool for investigating heat and gas transfer in the tropical Atlantic using data from the PIRATA (Pilot Research Moored Array in the Tropical Atlantic) array. Within this framework, experiments will be

conducted which identify the significance of gas transfer occurring during low wind speeds, where other factors such as temperature play an important role.

Gas exchange will be modelled over the diurnal cycle to assess the net contribution of exchange under convective conditions in the tropical Atlantic. Ultimately the global significance of temperature-related low wind speed exchange will be estimated through a global modelling experiment using a coupled model developed at the U.K. Met Office. This study will identify the implications for integrated fluxes of CO_2, and highlight the discrepancies between existing bulk transfer estimates.

1.2 Thesis structure

This study has been organised in the following manner:

In **Chapter 1**, the research objectives of the thesis are outlined and the rationale behind this work is identified. **Chapter 2** contains a review of the previous research conducted on heat and gas transfer, and also summarizes the oceanographic and meteorological conditions of the study area.

An overview of the models and data used in this study is presented in **Chapter 3**. These data are the basis for the model forcing and initial conditions used in the following chapters. **Chapter 4** contains work based on development and tuning of the 1-d model. In this chapter the model setup is discussed and case studies in the tropical Atlantic are shown.

Chapters 5 to 7 comprise the primary results and discussion sections of the thesis. Two of these sections consist of the content of research articles submitted by the author of this thesis that have either been published by, or accepted by international peer-reviewed journals. In each case the role of the co-authors was advisory, the substantive work being conducted by the lead author.

In **Chapter 5** a modified gas transfer parameterization is detailed and implemented within the modelling framework discussed in the previous chapter. The 1-d model is used to present a case study in the tropical Atlantic and to calculate the effect of convective gas exchange on the kinetics of air-sea CO_2 transfer.

Chapter 6 presents an idealized modelling study, building upon the methods in the previous sections. This study explores the effect of the diurnal warm layer and the convective enhancement with regard to near surface temperature structure and the subsequent change to daily integrated gas transfer in the tropical Atlantic. Model results are compared with previous in situ experiments and modelling studies in the literature. Simple gas exchange calculations are also compared with more complex models, which incorporate near surface temperature variability.

The regional and global significance of low wind speed gas transfer is explored in **Chapter 7**. A state of the art operational model developed by the U.K. Met Office is used to identify the importance of the improved gas transfer parameterization developed and tested in the earlier chapters.

A synthesis of the main conclusions of this study are provided in **Chapter 8**. Broader implications are discussed and suggestions for future work expanding on the findings of this thesis are presented. Finally the **Appendix** contains another published research article which contains further details of the model development discussed in chapter 4. This work was done in collaboration with a researcher at the U.K. Met Office, David Acreman and involves validation and tuning of a number of 1-d mixed layer models. The results described support the use of the model used in this study for investigating heat and gas transfer.

The research undertaken for this thesis highlights the importance of air-sea CO_2 transfer that can occur at low wind speeds, and significantly improves our understanding of gas transfer influenced by temperature-related processes such as diurnal warming and nocturnal buoyancy-driven convection.

1.3 Rationale

In this section the motivation for this thesis is examined in terms of the fundamental science associated with air-sea CO_2 transfer. The research of this thesis is placed into a larger context in order to highlight its potential significance to future global climate studies.

1.3.1 Why is CO_2 important?

Carbon dioxide is one of a number of greenhouse gases. These include, in the order of their relative abundance, water vapour, carbon dioxide, methane, nitrous oxide, and ozone. Solar heating warms the surface of the Earth, and in response the Earth radiates heat at longer infra-red wavelengths. Greenhouse gases in the atmosphere absorb this infra-red radiation more effectively than the shortwave radiation emitted by the Sun. These molecules then reemit infra-red radiation in all directions, some of which is directed back toward the Earth. Naturally occurring greenhouse gases have a mean warming effect of about 33 °C, without which the Earth would be uninhabitable. The greenhouse effect was discovered by Joseph Fourier in 1824 and first investigated quantitatively by Svante Arrhenius in 1896 (Arrhenius, 1896). Arrhenius later became the first person to predict the possibility of man-made global warming.

Photosynthesis appeared on Earth around three billion years ago, and allowed the sun's energy to be harnessed and converted into chemical energy. Such an energy resource

was two to three orders of magnitude larger than that which had been previously available from oxidation-reduction reactions associated with weathering and hydrothermal activity. Marine algae began to utilize solar energy to fix CO_2 by photosynthesis, and gradually transferred CO_2 from the atmosphere to organic carbon stored in ocean sediments. More recently, in terms of geological timescales, trees and plants on land have assisted this process. This has resulted in a large store of fossil carbon within the rocks, thereby lowering the concentration of CO_2 in the atmosphere, and helping to regulate the planet's temperature.

The recent onset of human induced burning of billions of tonnes of fossil carbon has led to an increase in atmospheric concentrations of CO_2. Since the industrial revolution the concentration of CO_2 in the atmosphere has risen from 290 to 365 μatm, and the global average temperature has increased by 0.7 °C during the 100 years ending in 2005 (IPCC, 2007). There is now near complete consensus that anthropogenic emissions of greenhouse gases are the primary factor contributing to global warming. Over 50% of the anthropogenic greenhouse warming is attributed to CO_2, and whilst water vapour is also very important, it has a very short lifetime in the atmosphere, since its concentration is controlled by evaporation and precipitation. Thus, any warming due to CO_2 may be amplified by higher concentrations of water vapour in the atmosphere.

1.3.2 Climate prediction and policy

The Intergovernmental Panel on Climate Change (IPCC) was set up by the World Meteorological Organization (WMO) and by the United Nations Environment Programme (UNEP) to provide the decision-makers and others interested in climate change with an objective source of information. From the IPCC 4th Assessment Summary for Policymakers (IPCC, 2007):

> *Most of the observed increase in global average temperatures since the mid-20th century is very likely due to the observed increase in anthropogenic greenhouse gas concentrations.*

Including uncertainties in future greenhouse gas concentrations and climate modeling, the IPCC anticipates a warming of 1.1–6.4 °C by the end of the 21^{st} century, relative to 1980–1999 (IPCC, 2007). Regional temperature rises may threaten severe disruption to agriculture and ecosystems, an increase in extreme weather events, flooding of low lying coastal area and spread of diseases.

There is considerable confidence that Atmosphere-Ocean General Circulation Models (AOGCMs) can provide quantitative estimates of future climate change, particularly at continental and larger scales. Confidence in these estimates is higher for some properties

(e.g. temperature) than for others (e.g. precipitation). There has been substantial progress in understanding inter-model differences in climate sensitivity. Cloud feedbacks have been confirmed as a primary source of these differences, with low clouds making the largest contribution; corresponding to around a 50% amplification of global mean warming.

Recently, the importance of carbon cycle feedbacks in the climate system has been considered. A few climate AOGCMs and some Earth System Model of Intermediate Complexity (EMICs) have included explicit treatment of the carbon cycle. The projected changes in the marine carbon cycle have a modest effect on atmospheric CO_2 (Joos et al., 1999), which act to compensate the reduction in ocean uptake caused by increasing temperatures. The inclusion of the terrestrial carbon cycle introduces potentially important feedbacks into the climate system on time scales of decades to centuries. These include the response of the terrestrial biosphere to increasing CO_2, climate change and changes in climate variability. The magnitude of the terrestrial sink, however, remains uncertain (Cox et al., 2000; Friedlingstein et al., 2001; Dufresne et al., 2002) because it depends on climate sensitivity as well as on the response of vegetation and soil carbon to increasing CO_2 (Friedlingstein et al., 2003).

Atmospheric composition over the last few hundred years has been derived from the oxygen isotope ratios ($^{18}O/^{16}O$) of gases trapped in bubbles in Antarctic and Greenland ice cores (Fischer et al., 1999). These have shown that CO_2 and temperature were well correlated during the glacial/interglacial cycles, but also that the warming of about 5 °C at the end of each ice age was very rapid. These measurements suggest that positive feedback processes must have amplified any initial warming effect. The anticipated increase in atmospheric CO_2 concentration that results from 'business as usual' scenarios of fossil fuel burning, around 1000 μatm, is much greater than that which existed between glacial and interglacial periods, between 200 to 290 μatm. The result of incorporating the various positive and negative feedback processes is that climate change may occur on abrupt time scales.

In comparison to clean, renewable alternatives and the necessary changes in infrastructure, burning fossil fuels is relatively cheap. As a result, global commitment to a reduction in CO_2 emissions is difficult to achieve. In its absence, policy-makers are required to set targets for levels of CO_2. Such levels should aim to stabilize concentrations of greenhouse gases and prevent dangerous anthropogenic impacts on the climate system. However, to address this, it is necessary to predict not only how CO_2 affects climate change, but also how changes in climate may affect sources and sinks of CO_2.

Annual CO_2 emissions between 2000–2005 were around 7.2 GT C yr^{-1} as a result of fossil fuel burning (IPCC, 2007). Approximately half of the emissions remains in the atmosphere, a third enters the ocean and the remainder is taken up by land. The least well constrained sink is that of the land, and it is important to reduce its uncertainty as

this sink is most directly affected by human activities e.g. farming and deforestation. It is also of great importance to measure the uptake of CO_2 by the ocean more accurately. This will not only better constrain the global budget, but will help to constrain the terrestrial sinks. Complex AOGCMs are necessary to accurately predict future changes to the climate system. However, calibration and testing of such models requires that we can accurately measure the current atmosphere-ocean CO_2 flux, and balance the global carbon budget.

1.3.3 Ocean-atmosphere exchange

The oceans have the potential to absorb much of the natural and anthropogenic addition of CO_2 to the atmosphere. This is because the ocean carbonate system acts as a buffer, and has a large capacity to absorb additional acid. The total amount of inorganic carbon in the ocean is about 40,000 GT C. This is much larger than the total reservoir of CO_2 in the atmosphere, which is about 800 GT C (Siegenthaler and Sarmiento, 1993). The dimensionless solubility for CO_2 is around 1 (Weiss, 1974), much higher than that of other gases such as O_2 and N_2. Approximately one in every ten molecules of CO_2 added to the current ocean remains as dissolved CO_2 and thereby contributes to increasing the water-side partial pressure (pCO_2), the other nine molecules form bicarbonate ions.

The transport of CO_2 from the atmosphere to the bulk ocean is slow, with the primary rate-limiting process being the transfer of CO_2 between the surface mixed layer and the deep ocean, rather than the air-sea exchange itself. Whilst the surface mixed layer gradually equilibrates with atmospheric CO_2, in most regions this does not mix with the bulk ocean water. The upper ocean, in contact with the atmosphere and heated by solar radiation, is typically well mixed to a depth of about 100 m and is less dense than the cold deep-water below. Thus it is physically stable with respect to vertical mixing across the thermocline at the base of the mixed layer.

At high latitudes, surface water cools sufficiently, due to heat loss to the atmosphere and becomes more saline due to ice formation, that it is no longer stable at the surface and sinks to become deep water. Dense water flows between the ocean basins as a result of the meridional overturning circulation and upwells back to the surface hundreds or thousands of years later, mainly in equatorial regions. Since the solubility of CO_2 in seawater at 0 °C is approximately double that at 30 °C, the ocean mixed layer can contain more CO_2 in equilibrium with the atmosphere in the cold polar seas where it is subducted than it can in warm equatorial regions where it had upwelled. The result is that CO_2 is degassed to the atmosphere in equatorial regions, where surface pCO_2 can rise up to 500 μatm. As the surface waters are circulated toward the poles and cool, they begin to absorb CO_2 back from the atmosphere. In the sub-polar North Atlantic, surface water pCO_2 can reach values of 200 μatm. Thus, regional fluxes can be considerably greater than the net global sum, in which the influxes and effluxes mostly

cancel. The coupled physical and chemical process responsible for transporting carbon from the ocean's surface to its interior is known as the 'solubility pump'.

In addition, photosynthesizing organisms are constantly removing CO_2 from the mixed layer and converting it to organic carbon. A large proportion of this is recycled by respiration within the mixed layer, some of this however falls by gravity through the thermocline as particulate organic carbon, the remains of dead phytoplankton, zooplankton and detritus. Whilst most of this sinking material is re-mineralized by bacteria and brought back to the surface in upwelling regions, a small fraction of the particulate organic carbon ($< 1\%$) reaches the bottom and is trapped in sediments and removed from the ocean-atmosphere system. On a geological timescale this is a major biological control on the atmospheric CO_2 (Falkowski et al., 1998). Thus, the biologically mediated transport of carbon from the surface euphotic zone to the deep ocean is known as the 'biological pump'.

Nutrients such as nitrate and phosphate, which are limiting factors for phytoplankton growth are also pumped down through the thermocline in the particulate organic matter, and returned to the surface in upwelling regions. In regions where there is little upwelling or riverine input e.g. tropical gyres, the phytoplankton biomass is very low. Conversely the biological pump is most significant in coastal and polar waters, where nutrient concentrations are higher. In polar seas, light is also a limiting factor, as such phytoplankton blooms occur mainly during the summer. In regions where there are intense blooms, the seasonal cycle of surface water pCO_2 can be almost the inverse of that expected from the physical effect of temperature on the solubility.

1.3.4 Response to changing climate

Increasing emissions of CO_2 must initially increase ΔpCO_2, the thermodynamic driving force for air-sea CO_2 exchange. It will not increase as fast as the emissions because as the pCO_2 in the surface water rises, its chemical buffering capacity goes down. This results in the mixed layer absorbing less CO_2 before reaching equilibrium with the atmosphere. As the surface ocean temperatures increase the solubility of CO_2 will decrease, hence the surface water pCO_2 will rise even if the total CO_2 in upwelled deep water does not change significantly in the short term. Therefore the fraction of anthropogenic emissions which is taken up by the ocean should be expected to decrease if global warming continues.

Schuster and Watson (2007) present a time series of observations from merchant ships in the North Atlantic used to establish the variability of sea surface pCO_2 and air-sea flux from the mid-1990s to early 2000s. The observed decrease in the sink for atmospheric CO_2 is attributed to declining rates of wintertime mixing and ventilation between surface and subsurface water, as a result of increasing stratification linked to variation in the

North Atlantic Oscillation. This decrease is exacerbated by changes in the buffering capacity of the ocean, as the carbon content of surface waters increase.

Because the mixed layer becomes more physically stable with respect to deep water as it warms, it is expected that climate change will weaken the meridional overturning circulation (MOC), which may cease completely if the climate warms beyond a certain threshold (Manabe and Stouffer, 1994). This could have important consequences for the transfer of heat between the ocean and atmosphere. It would also greatly reduce the 'solubility pump' transferring CO_2 to the deep water, and thus accelerate the increase of atmospheric CO_2 concentration.

Less apparent is the resultant impact on the 'biological pump'. Should climate change reduce the sinking of cold saline water in polar regions, the upwelling of deep water elsewhere would decrease. This would reduce the flux of nutrients to the surface and thus decrease the growth of phytoplankton and the downward flux of organic carbon. However it would also lead to a decrease in the flux of remineralised CO_2 returned to the surface in upwelling deep water. As a result phytoplankton may take up less atmospheric CO_2 in a warmer more stratified ocean, which would be a positive biogeochemical feedback.

1.3.5 Why measure air-sea CO_2 exchange?

Calibration of the complex carbon cycle models required to predict future climate change requires that we have accurate measurements of the CO_2 fluxes between the atmosphere and ocean. However, if the main rate-determining process for CO_2 exchange between ocean and the atmosphere is the transfer of carbon between the surface mixed layer and the deep ocean, why is it important to measure the transfer across the air-sea interface?

The net global air-sea CO_2 flux is not particularly sensitive to the rate of air-sea CO_2 exchange. Global average transfer velocities predicted by two well known parameterizations, such as Liss and Merlivat (1986) and Wanninkhof (1992), differ by about 60%. In comparison, the net global CO_2 flux predicted by models which compare these parameterizations differs by only 10%. This is because pCO_2 in the mixed layer will approach equilibrium with the atmosphere more rapidly when the gas exchange rate is faster, and thus ΔpCO_2 (the thermodynamic driving force) will be correspondingly reduced. Comparing the 'potential pump', assuming instant equilibration of the mixed layer with the atmosphere, with the combination of the 'solubility' and 'biological' pumps, there are large differences in regional air-sea CO_2 fluxes, but not such large difference in the integrated global flux.

Although it is the transfer to the deep ocean that is the major rate-limiting step, it is much easier to measure the transfer of CO_2 across the air-sea interface, than it is to measure the organic particle fluxes and physical mixing. Measurements of the thermocline require time-consuming depth profiles from research vessels. Measuring the mixing

of water by eddies moving in 3 dimensions is difficult, recent experiments have involved deliberately adding tracers such as SF_6 to patches of water, but these can only be conducted infrequently and in a few locations. As such, it is not possible to monitor the entire ocean on sufficient temporal nor spatial scales.

There are a number of techniques for estimating the export production of organic carbon across the thermocline. However, there are large errors associated with such methods, and these are still too large compared to the accuracy required to improve estimates of the net global air-sea CO_2 flux. Because of the large regional CO_2 positive and negative fluxes which cancel with each other, the accuracy needs to be high. In addition, relatively small changes in TCO_2 predicted by models of biological carbon uptake create much larger changes in pCO_2 due to the response of the carbonate system.

The direct calculation of CO_2 transfer across the air-water interface tells us how much CO_2 is actually leaving the atmosphere. This is a more immediate concern to policy-makers than the amount which is exported to the deep ocean. It should be noted however, that these two quantities are not exactly the same, as the mixed layer itself is a substantial pool of carbon which must 'catch up' with the atmospheric increase. In addition, because the sea-surface is more accessible far greater temporal and spatial coverage is possible, either by in situ measurements from ships, or moored or drifting buoys. Moreover, the key parameters which control the kinetics of gas transfer; wind and temperature can be monitored by earth observing satellites, enabling a synoptic view that is not possible with ship-based measurements.

Thus accurately estimating the uptake of CO_2 by the world's oceans is one of the most critical issues for monitoring the global carbon cycle and studying climate change. Present global estimates ignore the fine details of the impact of surface processes, such as those reviewed in chapter 2. This thesis focuses on but a fraction of such research, which should eventually lead to improved estimates of air-sea CO_2 transfer. Ultimately this work is just a small piece of a much larger puzzle.

1.4 Objectives

Given the context of this research, the primary scientific objectives of this thesis are as follows:

1. To determine the effect of convective air-sea CO_2 exchange in the tropical Atlantic. Does neglecting the gas exchange which takes place due to free convection at night have an appreciable effect on net estimates of air-sea CO_2 transfer?

2. To estimate the impact of diurnal temperature variability on net daily estimates of CO_2 exchange. Many current estimates ignore diurnal changes in seawater temperature when estimating the air-sea flux of CO_2, either by using temperatures at some depth below the surface or by using daily averaged data. Thus, this thesis seeks to answer the following question: What is the integrated effect of accounting for diurnal temperature variability on the flux of CO_2?

3. To quantify the regional and global significance of low wind-speed, temperature related CO_2 transfer. Does the combined effect of such processes significantly alter calculations of air-sea gas fluxes, or are such processes unimportant as they are confined to small regions of the ocean, and infrequent conditions?

4. Since estimates of the air-sea CO_2 flux let us know how much CO_2 the ocean is absorbing from the atmosphere or vice versa, this thesis aims to identify whether accounting for these low-wind speed processes affects regional and global estimates of the carbon uptake.

Chapter 2

Background

This chapter contains a review of the important processes which determine the rate of air-sea carbon dioxide exchange under low wind conditions. As a result this chapter contains a diverse, yet relevant, range of sections providing background on both heat and gas transfer, as well as the typical meteorological and oceanographic conditions of the tropical Atlantic.

2.1 Processes of heat and gas exchange

Convective air-sea carbon dioxide transfer is largely dependent on wind speed and the daily cycle of upper ocean temperatures, which itself is controlled by the surface heat budget. This section aims to cover the necessary science required to understand the factors influencing low wind speed gas exchange.

2.1.1 Surface ocean heat budget

Changes in heat stored in the upper layers of the ocean result from a local imbalance between input and output of heat through the sea surface. The flux of heat to deeper layers is usually much smaller than the flux through the surface. Heat is also carried out of the area by currents, although, this tends to be small in many locations. Globally, the sum of all the heat fluxes into and out of the ocean must be near zero, otherwise the oceans as a whole would heat up rapidly or cool down. As a result of increasing anthropogenic greenhouse gas emissions (see chapter 1) ocean temperature is increasing, albeit more slowly due to the ocean's large thermal inertia.

The sum of the heat fluxes into or out of a volume of water is the heat budget. The major terms in the budget at the sea surface are:

1. Insolation Q_s, the flux of sunlight into the sea;
2. Net Infrared Radiation Q_l, net flux of infrared radiation from the sea;
3. Sensible Heat Flux Q_h, the flux of heat out of the sea due to conduction;
4. Latent Heat Flux Q_e, the flux of heat carried by evaporated water; and
5. Advection Q_v, heat carried away by currents.

Conservation of heat requires:

$$Q_{net} = Q_s + Q_l + Q_h + Q_e + Q_v \tag{2.1}$$

where Q_{net} is the resultant heat gain or loss. Units for heat fluxes are W m^{-2} and the flux from air to sea is positive. Thus Q_l, Q_h and Q_e are typically negative quantities. The product of flux times surface area multiplied by time is energy in Joules. Thus, the change in temperature, ΔT, of the water is related to change in energy, ΔE, through:

$$\Delta E = C_p m \Delta T \tag{2.2}$$

where m is the mass of water being warmed or cooled, and C_p is the specific heat of sea water at constant pressure.

2.1.2 Gas exchange

The exchange of gases across the air-water interface is determined by: the concentration gradient of the gas across the interface; the gas exchange velocity (transfer velocity); the chemical reactivity; and solubility of the gas in the aqueous phase.

The transfer velocity varies with the rate at which exchanging molecules are transported into or away from the interface via a combination of molecular and turbulent processes. Turbulent diffusivity, determined by the spatial and temporal scale of turbulent motions, is the dominant process, whereas molecular characteristics operate on much smaller scales (Jähne and Haußecker, 1998; Donelan and Wanninkhof, 2002). The flux of CO_2 or other gas, F, across the air-sea interface is often determined from the bulk formula:

$$F = k\Delta C \tag{2.3}$$

Where k is the transfer velocity and ΔC is the effective concentration difference driving the net flux. k is the primary rate constant. In the case of CO_2, C is normally approximated by $[CO_{2a}] = \alpha pCO_{2a}$ and $[CO_{2w}] = \alpha pCO_{2w}$. Thus

$$F = k\alpha[(pCO_{2w}) - (pCO_{2a})] \tag{2.4}$$

where α is solubility as a function of temperature and salinity and $p\mathrm{CO}_{2w}$ and $p\mathrm{CO}_{2a}$ are the partial pressures of CO_2 in water and air respectively (Wanninkhof and McGillis, 1999). The flux from sea to air (efflux) is defined as positive.

Gas transfer is regulated by turbulence at the air-sea interface, boundary layer stability, wave type, breaking waves, surfactants and bubbles (Broecker et al., 1978; Broecker and Siems, 1984; Monahan and Spillane, 1984; Memery and Merlivat, 1985; Phillips, 1991; Woolf, 1997). Small-scale surface waves are important at low to intermediate wind speeds (Bock and McCready, 1988), and small gravity and capillary waves appear to play a dominant role (Szeri, 1997).

Whilst surface wind speeds are relatively easy to measure, only limited data on other parameters influencing turbulence are available for the oceans. Thus the most common estimates of CO_2 flux are based solely on the relationships between wind speed and gas exchange, such as those conducted in wind-wave tanks and lakes/estuaries (Liss, 1983; Wanninkhof et al., 1985; Clark et al., 1994). Global estimates of the air-sea CO_2 flux may be calculated using remotely sensed parameters such as wind speed and sea surface temperature when combined with climatologies of the difference between partial pressures of CO_2 in the air and ocean respectively.

Such simple parameterizations are approximations. In reality, gas exchange does not scale with wind speed alone. More accurate is the dependence on sea surface roughness i.e. the slope of short surface waves and breaking waves (Bock et al., 1999). A strong relationship exists between the mean square slope of these waves and the gas transfer velocity. Although it is the overlying wind field that drives the waves on the surface ocean there is not a 1:1 relationship between wind speed and wave height; the two fields vary both spatially and temporally (Frew et al., 2004, 2007). During low wind conditions, other factors may contribute to the near surface turbulence and hence increase the rate of gas transfer.

The difference between $p\mathrm{CO}_2$ in the surface ocean and that of the overlying air represents the thermodynamic driving potential for CO_2 transfer across the air-sea interface (see equation 6.1)(Takahashi et al., 2002). However there are relatively few measurements of $p\mathrm{CO}_2$ due to the difficulty of sampling at sea. Moreover, certain areas contain fewer measurements than others; areas such as the Southern Ocean are particularly difficult to sample in situ because of harsh conditions and a lack of ships of opportunity passing through the region. Inadequate data coverage for $p\mathrm{CO}_2$ and uncertainty in the

Source	Global CO_2 flux (GT C yr^{-1})
Sigenthaler (1983)	2-2.5
Liss and Merlivat (1986)	1.17
Etcheto et al. (1991)	0.89
Nightingale et al. (2000a)	1.7
Boutin et al. (2002)	1.2-2.7
Takahashi et al. (2002)	2.2

TABLE 2.1: Global estimates of air-sea CO_2 exchange, as reported by different sources.

transfer velocity ultimately limits confidence in global estimates of carbon dioxide flux. Although we cannot improve the estimates of pCO_2, it is at least possible to reduce the uncertainty in global flux estimates caused by inadequate parameterizations of the gas transfer velocity.

Takahashi et al. (2002) present the most comprehensive estimate of global air-sea CO_2 exchange to date (see table 2.1). It is based upon 940,000 measurements of surface water pCO_2 (see figure 2.1). The authors use the (Wanninkhof, 1992) parameterization for the gas transfer velocity (see section 2.1.6) and compute the monthly annual net air-sea CO_2 flux using NCEP/NCAR 41-year mean monthly wind speeds. They arrive at an annual net uptake flux of 2.2 GT C yr^{-1} and produce maps of global CO_2 flux showing a zone between 40°–60° latitude in both northern and southern hemispheres corresponding to a major sink for atmospheric CO_2 (see figure 2.2). They conclude that these areas, also sources for deep and intermediate water, are direct pathways for CO_2. Global estimates such as these show us that the ocean contains both areas that are strong sources and areas that are strong sinks for CO_2. The global surface pCO_2 dataset has recently been updated and now contains measurements performed during 1968-2006 (Takahashi et al., 2008).

There have been a number of efforts to remotely obtain the oceanic CO_2 concentration. These have been based primarily on observed correlations to the SST and related quantities. Relationships between SST and oceanic pCO_2 have been found to exist in the subtropical (Stephens et al., 1995) and equatorial (Boutin et al., 1999) Pacific and the Caribbean Sea (Olsen et al., 2004). Additional relationships between the oceanic fugacity of CO_2 (the partial pressure corrected for the non-ideality of the gas) and SST and chlorophyll content have been observed in the southern ocean (Rangama et al., 2005). However, there are significant spatial and temporal variations in these expressions, and no clear approach has been found to systematically relate variations in pCO_2 to remotely sensed parameters on a global scale. Conversely, atmospheric CO_2 concentrations have been obtained solely from direct measurements but because variability of the atmospheric pCO_2 is much smaller, both spatially and temporally, it is not a major factor limiting the accuracy of the flux estimates.

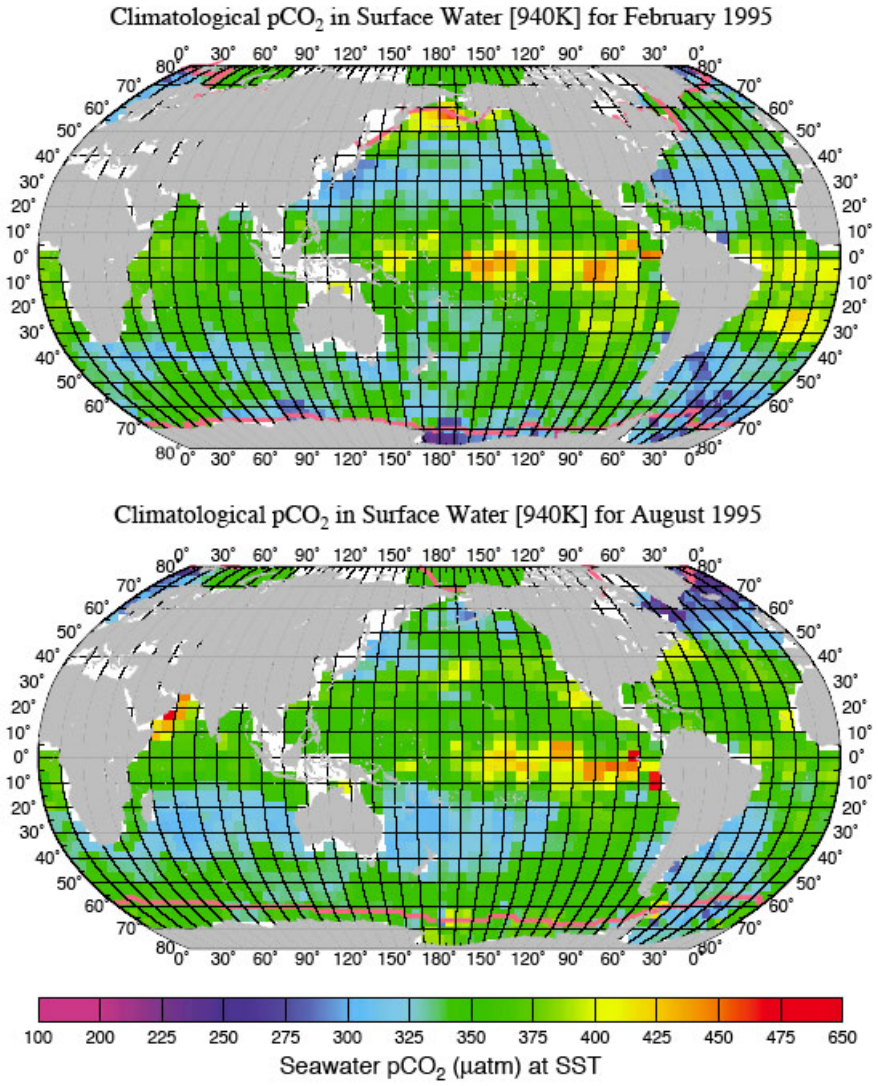

FIGURE 2.1: Climatological mean distribution of surface-water pCO_2 (μatm) in February (top) and August (bottom) 1995 (Takahashi et al., 2002).

2.1.3 The air-sea interface

It is important to understand the structure of the water column in which heat and gas transfer takes place. Deeper water is well mixed, but close to the boundary, in the top 10-50 μm, motions become constricted. Exchange of gases across the air-sea interface occurs via molecular and turbulent diffusion. Although turbulence is dominant, close to the interface it is suppressed and exchange is dependant on molecular diffusivity (Donelan and Wanninkhof, 2002). There is a significant difference between the temperature at depth, and the near surface temperatures, such as those derived via remote sensing methods. It is therefore necessary to understand surface renewal processes.

Under conditions of surface cooling there is a layer below the interface, around a millimetre thick, where temperature decreases rapidly toward the surface. Cool water on the

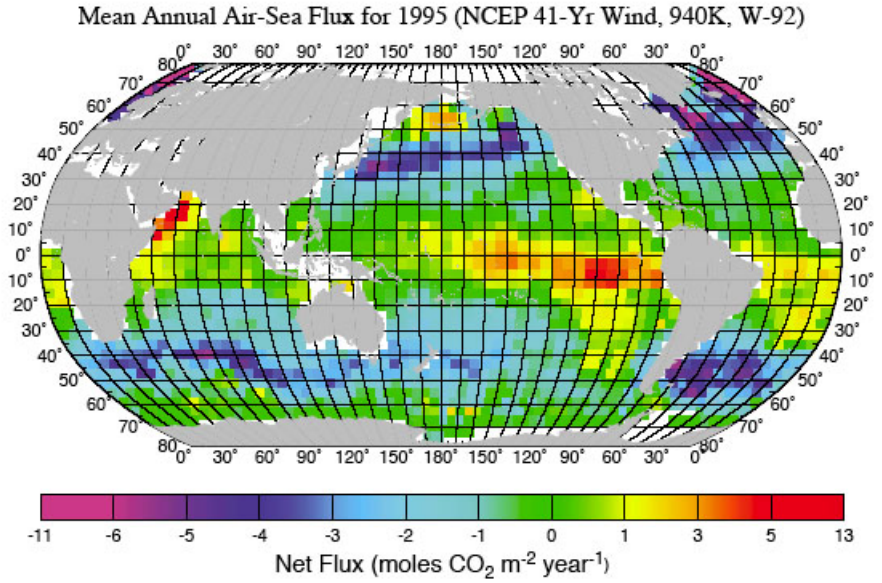

FIGURE 2.2: Mean annual air-sea flux of CO_2 (mol CO_2 m^2 yr^{-1}) for 1995 (Takahashi et al., 2002). Transfer velocity, k, calculated according to Wanninkhof (1992), and NCEP 41-yr wind data. Positive values indicate outgassing regions, negative values indicate CO_2 drawdown.

surface collects together, producing thickened regions of the boundary layer. When these regions become unstable they collapse causing cooler water to plunge down in vertical sheets, reducing the surface layer thickness. Thus, the temperature of the boundary layer varies with both horizontal position and time. Further from the surface the variation becomes organised into periodic cold deviations from an almost constant temperature. As the magnitude of these cold deviations decreases the distance between them increases (Katsaros et al., 1977). The temperature profile in the boundary layer is highly non-linear, and the air-sea interface is sometimes subject to strong temperature gradients (around -300 K m^{-1} Khundzhua et al. (1977)). As a result, the boundary layer can range in thickness from a few centimetres to fractions of millimetres (Ward, 2007).

There are at least three causes for these deviations in temperature near the surface: radiation; evaporation; and conduction. Incoming solar radiation is able to penetrate to a depth of several tens of metres in clear seawater. The energy supplied is distributed throughout the mixed surface layer. The shortwave radiation serves to warm both the surface and subsurface layers. Evaporative and sensible heat transfer to the atmosphere may add to cooling depending on the temperature and humidity of the air. Conduction, evaporation and losses through the re-emission of infrared radiation return energy to the atmosphere. As a consequence, when solar radiation is zero the surface layer cools. But note that the surface tends to lose heat to the atmosphere even for quite strong solar radiation.

The temperature at the interface of a body of water losing heat to the atmosphere above is typically colder than the lower turbulent layers by a few tenths of a degree, although

in extreme cases values of 1 °C have been reported (Ward and Donelan, 2006). This is known as the cool/thermal skin effect:

$$\Delta T = T_0 - T_w \tag{2.5}$$

Where ΔT is the thermal skin anomaly (and is negative for the cool skin), T_0 is the temperature of the water at the interface, and T_w is the bulk water temperature (usually measured between 0.2–2 m). Hasse (1963) gives empirical formulae for the night-time and day-time temperature deviations such that:

$$\begin{aligned} \Delta T_{Night} &= C_1 \left(\frac{Q_{tot}}{u} \right) \\ \Delta T_{Day} &= C_1 \left(\frac{Q_{tot}}{u} \right) + C_2 \left(\frac{Q_s}{u} \right) \end{aligned} \tag{2.6}$$

Where Q_{tot} is the sum of effective back radiation and latent and sensible heat transfer to the atmosphere, u is the wind speed, Q_s is the solar radiation and C_1 and C_2 are coefficients which depend on the depth at which measured temperatures are taken.

Sensible and latent heat fluxes are approximately proportional to wind speed, but infrared heat loss is not. The surface temperature deviation will only be weakly affected by wind speed but will decrease with wind speed when the infrared heat flux is large. Other turbulence producing processes also limit ΔT (Katsaros et al., 1977). Hence, we should expect the largest negative values of ΔT during low wind speed and low current speeds. In most natural bodies of water when wind speed drops below 2 m s^{-1}, if no mean current is present a state of free convection exists, i.e. they have a high Rayleigh number, R_a, around 10^5.

Saunders (1967) describes the basic physics of the cool skin. The layer itself is a result of the combined cooling effects of the net longwave radiation Q_l, the sensible heat flux Q_h and the latent heat flux Q_e. Because the cooling occurs at the interface (i.e. the longwave penetration depth is about 10 μm) the temperature gradient is controlled by molecular thermal conductive processes. Away from the interface this gradient is destroyed by turbulent mixing (Schlüssel et al., 1990; Soloviev and Schlüssel, 1994; Fairall et al., 1996b).

The skin temperature of the ocean, SST_{skin} (see table 2.2), is the temperature measured by a radiometer at depth within a thin layer at the water side of the air-sea interface (Donlon et al., 2002). The skin temperature deviation has been observed both in the laboratory (Ward and Donelan, 2006) and in situ, using ship-mounted infrared radiometers (Donlon and Robinson, 1997; Donlon et al., 1999; Minnett, 2003; Ward, 2006).

The implication of the cool skin for gas fluxes and CO_2 is that since the temperature at the surface is lower than the water below, the solubility, α, will be slightly higher, i.e. $\alpha_s = \alpha_w(1 + \delta)$. Although water temperature will vary across the surface layer, the boundary layer limiting air-sea CO_2 transfer should be thinner than the thermal skin, since heat diffuses more readily through the surface microlayer than dissolved gases (Doney, 1994). Therefore, it is reasonable to assume a uniform cool skin temperature across the gas exchange boundary layer. Thus our CO_2 flux from (2.4) now becomes:

$$F = k\alpha_w[(pCO_{2w}) - (pCO_{2a})] + [\delta\alpha_w kpCO_{2a}] \tag{2.7}$$

2.1.4 Diurnal warming

The diurnal cycle, directly associated with solar forcing, can lead to significant temperature variations, and has implications for both biological and physical processes in the mixed layer. It is important for the carbon budget as the dissolution of gases is dependent on the surface temperature. Diurnal heat fluxes generate daytime surface ocean stratification and subsequent large nighttime buoyancy fluxes. Low winds and large heat fluxes lead to significant diurnal temperature variations that have an important effect on gas fluxes.

The existence of this diurnal warm layer was first recognized by Sverdrup et al. (1942) and subsequently by Stommel (1969) and has since been studied extensively (Woods and Barkman, 1986; Schlüssel et al., 1990; Fairall et al., 1996b; Donlon et al., 2002; Ward, 2006). In the absence of wind, or during periods of low wind speeds, strong solar heating leads to warming within a thin surface layer. Under summer heating conditions, with no wind, this heating extends to a depth of approximately 1 m (Price et al., 1986). More commonly, when light winds are present the depth extends to around 10 m below the surface due to increased vertical mixing and may persist for hours (Yokoyama et al., 1995; Minnett, 2003). The depth to which the warming penetrates is dependent on a balance between positive buoyancy flux, related to the incoming solar radiation, and the wind driven turbulent energy available to mix the upper layer (Stuart-Menteth et al., 2003).

The difference between the skin and temperature at depth, ΔT_w, is controlled by turbulence and the surface fluxes of heat and momentum. The omission of diurnal temperature variability in SST's can lead to significant errors in determining surface fluxes for numerical weather prediction (NWP) and climate models (Woods et al., 1984; Webster et al., 1996). Cornillon and Stramma (1985) estimate the effect of diurnal warming on the net heat flux and found that when diurnal effects were considered the monthly mean SST was higher by 0.2 °C (corresponding to an increase in heat flux of 5 W m^{-2}). Furthermore, Donlon and Robinson (1997) and Ward (2006) report that the error in the

total surface heat budget can exceed 100 W m^{-2} when comparing flux estimates made using SST_{skin} rather than SST_{bulk}. At low wind speeds (< 8 m s^{-1}), ΔT_w exhibits a wind speed dependency, decreasing as the wind speed increases. At wind speeds > 10 m s^{-1} the break up of the surface micro-layer reduces ΔT_w to a mean value of $\sim$0.1 K, and there is no further evidence of wind speed dependency.

Price et al. (1986) report 3 main stages of the thermal cycle that repeatedly occur in the data:

1. Warming throughout: From sunrise until noon, the water column undergoes warming. Heat is trapped in the upper few metres.

2. Cooling and Warming: Within a few hours of noon wind mixes heat downward, the heat flux profile develops a knee which corresponding to the deepening surface mixed layer, continued wind mixing pushes the knee down during late afternoon.

   (a) Wind mixing above the knee caused rapid cooling during the early afternoon

   (b) Below the knee vertical mixing leads to warming.

   Surface cooling results in large convective motions, these store kinetic energy that continues to be available for further mixing after several hours. This results in residual mixing below the surface layer (McNeil and Farmer, 1995).

3. Cooling throughout: By midnight the downward movement of the heat flux knee has reached about 30 m. The heat flux profile is dominated by loss to the atmosphere and is monotonic. This loss continues until the following sunrise. Convection breaks down the diurnal thermocline.

Large regions of the world's ocean are susceptible, primarily the tropics and sub-tropics where weak winds are concentrated (see figure 2.5) and where the majority of the ocean-atmosphere heat flux occurs (Stuart-Menteth et al., 2003). In fact, wind speeds of less than 5 m s^{-1} account for nearly 40% of global hourly averaged winds (Shankaranarayanan and Donelan, 2001). Near surface warming in favorable conditions can reach temperature differences of 3.5 °C (Stramma et al., 1986) and can exceed 6 °C in extreme cases (Flament et al., 1994). Kawai and Wada (2007) also point out that diurnal temperature variation can become large even at high latitudes, as evidenced by seasonal mean day-night differences from satellite based microwave radiometers.

Due to changes in solubility, the thermodynamic driving force, ΔpCO_2 is also dependent on temperature; the change in pCO_2 for a given concentration as a function of temperature ranges between 3.8–4.23% $°C^{-1}$ (Millero, 2007). Thus in the equatorial/tropical source regions diurnal warming will lead to increased sea to air fluxes of CO_2, although the net integrated effect remains uncertain.

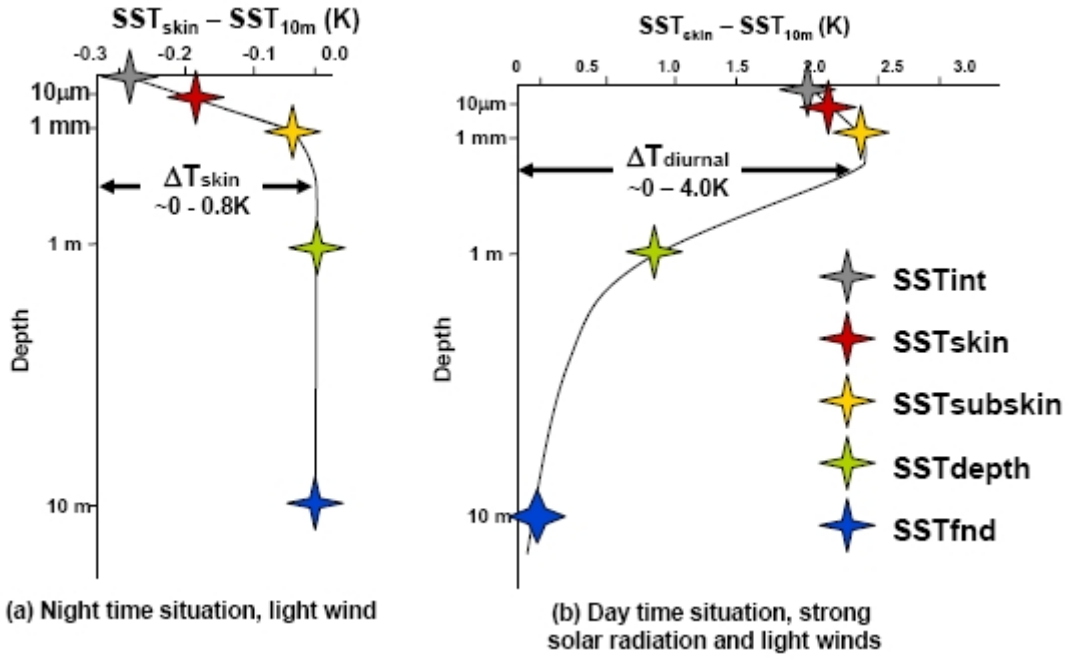

FIGURE 2.3: Schematic showing a) idealized nighttime vertical temperature deviations from the foundation SST and b) idealized daytime vertical temperature deviations from the foundation SST in the upper ocean. Based on GHRSST-PP near surface temperature definitions (see table 2.2) (Donlon et al., 2007).

Name	Abbreviation	Temperature represented	Instrument to measure it
Interface SST	SST_{int}	Theoretical temperature at the precise air-sea interface.	None
Skin SST	SST_{skin}	Temperature within the conductive diffusion-dominated sub-layer ≈ 10–20 μm depth.	Infrared radiometer with a 3.7–12 micrometer spectral waveband.
Subskin SST	$SST_{subskin}$	Temperature at the base of the conductive laminar sub-layer.	Microwave radiometer with a frequency range 6–11 GHz, high-performance autonomous profiler e.g SkinDeEP (Ward et al., 2004).
Temperature at depth	SST_{depth}	In situ temperature measured below the conductive laminar sub-layer typically referred to as 'bulk' SST.	Traditional in situ sensor e.g. thermistor, CTD, XBT etc. To be useful, measurement depth should be noted.
Foundation SST	SST_{fnd}	Temperature of the water column free of diurnal temperature variability or equal to $SST_{subskin}$ in the absence of any diurnal signal.	same as SST_{depth}.

TABLE 2.2: Definitions of sea surface temperature proposed by GHRSST-PP (Donlon, 2007), based on table 1 in Kawai and Wada (2007).

The Global Ocean Data Assimilation Experiment (GODAE) recognized the benefits of global cooperation in the provision of SST data, and launched the GODAE High Resolution SST Pilot Project (GHRSST-PP). One of the key developments of the GHRSST-PP has been the supply of satellite SST in a common format in near real time, through a global network of data providers (Donlon et al., 2007). A critical driver behind improving satellite SST measurements are to enable their use in creating climatically important products and investigating their global and regional variability with respect to changing climate.

The GHRSST-PP science team has defined five kinds of SST: interface SST (SST_{int}), skin SST (SST_{skin}), subskin SST ($SST_{subskin}$), sea temperature at depth (SST_{depth}) and foundation SST (SST_{fnd}). Figure 2.3 shows a schematic of the vertical temperature profile taking into account processes such as the warm layer and cool skin. These temperatures are defined in table 2.2 and are used in this thesis wherever possible.

Ward et al. (2004) examines the biases in the air-sea flux of CO_2 which result from the near surface temperature gradients described above. The warm layer will affect the air-sea flux of CO_2 whenever present. The absolute effect on the air-sea flux will be small however because the warm layer is only important at low wind speeds when rates of exchange are low. The cool skin however, is persistent on a global basis and varies with the warm layer, thus SST_{skin} is the most critical temperature for accurate representation of the air-sea flux of CO_2.

2.1.5 Convective exchange

From section 2.1.4 we know that diurnal heat fluxes generate daytime surface ocean stratification and subsequent large nighttime buoyancy fluxes. Low winds and large heat fluxes lead to significant diurnal temperature variations that have an important effect on gas fluxes. Convection is likely to be the dominant mechanism controlling gas fluxes at low wind speeds, however the contribution due to convection in the water is still poorly understood. According to MacIntyre et al. (2002) energy budget analyses indicate that current parameterizations will likely underestimate gas fluxes in tropical regions by a factor of two. Additionally, the presence of a cool skin (see section 2.1.3) leads to an increase in solubility and hence additional flux of gas.

Eugster et al. (2003) report measurements of two lakes in which air-water fluxes of CO_2, water vapour and energy were taken during periods of convective mixing. They observed strong and significant differences between CO_2 fluxes during non-convective and convective conditions within the lakes. CO_2 fluxes increased by 4.7% during periods with penetrative convection over stably stratified periods. The authors state that gas fluxes are not only enhanced by low winds, but also by the entrainment of water with increased gas flux concentrations (although this is not applicable in the open ocean as the surface

layer is not close to the bottom sediments). Thus convection is most important when coupled to vertical stratification of CO_2 in the water.

Results from GasEx-2001, a 15-day air-sea carbon dioxide exchange study in the equatorial Pacific were presented by McGillis et al. (2004). The study took place in February 2001, in a region of high CO_2 exchange (average ΔpCO_2 of 80–150 μatm), the largest sustained source of CO_2 to the atmosphere from the ocean. Wind speed was low and relatively constant, approximately 6 m s^{-1}. The ΔpCO_2, solar incidence, barometric pressure and bulk temperature showed obvious diurnal cycles. The sea surface temperature variations were established over periods of hours due to the large heat fluxes and low winds. Under these conditions radiation absorbed over the top several metres of the water column is released at night, cooling the surface.

Cooling at night resulted in a decrease of both air temperature and water temperature. The mean diurnal ocean temperature was greater than the air temperature, with a small increase in the difference at night. This led to a nighttime decrease in pCO_2. While the bulk CO_2 concentration showed no discernible diurnal variation, the surface/skin CO_2 concentration increased at night. This was due to an increase in gas solubility as a result of cooler surface water. Although the effect on diurnal solubility and ΔpCO_2 is additive, the combined contribution to increasing nighttime fluxes was small, around -2.7%. However, measurements showed a 40% increase in CO_2 flux at night over daytime values. Because the gas transfer velocity was calculated using diurnal concentration of CO_2, the thermal effects on solubility and diffusivity were taken into account. McGillis et al. (2004) attribute the residual increase in transfer velocity to physical processes; enhanced mixing at night and surface turbulence throughout the diurnal cycle.

The Pacific GasEx-2001 results are important as they indicate that the diurnal heating and subsequent cooling of the ocean surface can lead to significant gas flux variability. The data suggested an elevated gas transfer velocity at wind speeds less than 6 m s^{-1}, and a very weak dependence on wind speed. Chemical enhancement (Wanninkhof and Knox, 1996) may also have played a role in increasing the measured transfer velocities, whilst other environmental factors also affect low wind gas exchange, such as surfactants (Frew et al., 1990). However, the GasEx-2001 site was very remote, with no direct anthropogenic influence or significant biological activity, resulting in a region with low CDOM levels and little in the way of background surface films.

2.1.6 Gas transfer velocity

The gas transfer velocity, k, serves to represent physical processes at the air-sea interface. However, it is often represented by a simple wind-speed dependent parameterization. These simple models of the gas transfer velocity tend to underestimate the air-sea CO_2 flux in equatorial and tropical regions. One reason is that at low wind speeds these

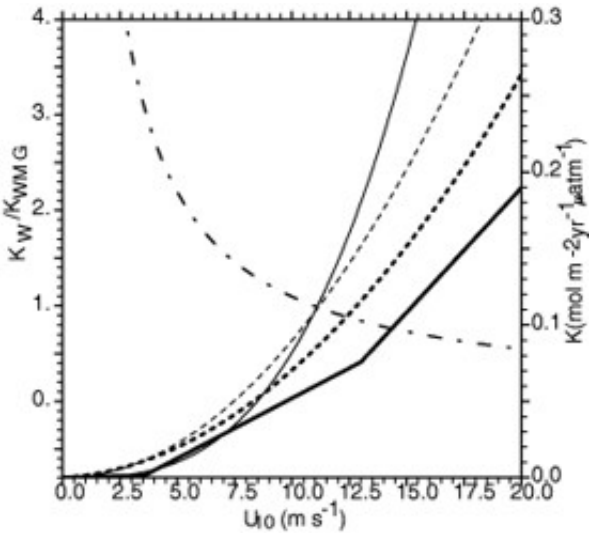

FIGURE 2.4: Comparison of various models for the gas transfer velocity, k, at 20 °C. From Liss and Merlivat (1986) thick line; Nightingale et al. (2000a) thick dashed line; Wanninkhof (1992) thin dashed line; Wanninkhof and McGillis (1999) thin line. The dashed dotted line shows K_W/K_{WMG} versus u_{10}. Source: Boutin et al. (2002).

parameterizations tend toward zero, the implication being that gas flux becomes zero at low winds. However, this does not account for flux driven by factors other than wind induced turbulence, such as convective enhancement.

Experimental models range from linear (Liss and Merlivat, 1986) to quadratic (Wanninkhof, 1992) and cubic (Wanninkhof and McGillis, 1999) expressions for the wind-speed dependence of k. These simple expressions have been applied subsequently to numerous estimates of the CO_2 transfer velocity from satellite-derived wind speed retrievals (e.g. Etcheto et al. (1991); Olsen et al. (2005)). Alternative estimates of the transfer velocity from satellites utilized simplified empirical models based on the mean square slope of the sea surface (Bock et al., 1999; Frew et al., 2007). However, these simplified approaches fail to capture all the processes influencing gas transfer. For example, at low wind speeds, surfactants, rain, microscale wave breaking, and biological processes may significantly affect gas transfer. Low wind speeds predominate in the tropical regions, where biological productivity is relatively high due to the upwelling of nutrients and large flux of solar energy. In addition, recent analysis of CO_2 and DMS flux measurements demonstrated that a simple wind speed-Schmidt number parameterization cannot fit all gases (Blomquist et al., 2006).

Boutin et al. (2002) examine the consequence of using 4 popular exchange coefficient vs. wind speed parameterizations (see figure 2.4). Here the exchange coefficient K is the product of the transfer velocity and solubility, and wind speed u_{10} is normalized to 10 m above the sea surface. The Schmidt number (S_c) is a dimensionless number defined as the ratio of the kinematic viscosity (v) and the molecular diffusivity (D_v). The S_c for CO_2 at 20 °C is 600 in freshwater and 660 in seawater. Different parameterizations have consequences for both the global net flux and out-gassed and absorbed fluxes. They

determined that the wind speed range of 4–17 ms^{-1} is the most critical on global scales. Boutin et al. (2002); Woolf (2005) note that k vs. u_{10} parameterization is particularly difficult at higher wind speeds with a diverse range of values occupied dependent on the particular parameterization used. These four common parameterizations for the transfer velocity are listed below.

- The Liss and Merlivat (1986) model — which is based on results of wind tunnel and lake experiments and split into 3 wind regimes:

$$\begin{aligned} k &= 0.17 u_{10} \left(\frac{600}{S_c}\right)^{2/3} && 0 \leq u_{10} \leq 3.6\,\mathrm{ms}^{-1} \\ k &= 2.85 u_{10} - 9.65 \left(\frac{600}{S_c}\right)^{1/2} && 3.6 \leq u_{10} \leq 13\,\mathrm{ms}^{-1} \\ k &= 5.9 u_{10} - 49.3 \left(\frac{600}{S_c}\right)^{1/2} && u_{10} \geq 13\,\mathrm{ms}^{-1} \end{aligned} \tag{2.8}$$

- The Wanninkhof (1992) quadratic curve — which is fitted such that it is in agreement with the global mean transfer velocity determined from the uptake of bomb-derived radiocarbon. The coefficient a for steady winds and long term winds is 0.31 and 0.39 respectively:

$$k = a\, u_{10}^2 \left(\frac{S_c}{660}\right)^{-1/2} \tag{2.9}$$

- The Wanninkhof and McGillis (1999) curve — based on a cubic relationship using eddy correlation data obtained during GasEx-98. The relationship fits within global bomb $^{14}\mathrm{C}$ oceanic constraints, although enhancement is greater for higher wind speeds:

$$k = 0.0283 u_{10}^3 \left(\frac{S_c}{660}\right)^{-1/2} \tag{2.10}$$

- The Nightingale et al. (2000a) relationship — which shows an intermediate dependence when compared to equation 2.8 and equation 2.9. The model was based on a combination of data from a conservative tracer experiment (spores of bacterium *Bacillus globigii var. Niger*) and a dual volatile tracer technique ($^3\mathrm{He}/\mathrm{SF}_6$):

$$k = 0.222 u_{10}^2 + 0.333 u_{10} \left(\frac{S_c}{660}\right)^{-1/2} \tag{2.11}$$

As a side note, SF_6 which is used in air-sea gas exchange experiments, is also a transient tracer in the ocean. Its atmospheric mixing ratio over the past few decades has been

increasing rapidly. Additionally, chlorofluorocarbons (CFCs) have lost some of their effectiveness as tracers for the most recently ventilated waters because of their declining atmospheric mixing ratios. The increase in SF_6 mixing ratio has the potential to restore a unique time marker for recent decades. Thus the availability of an alternative tracer for ocean tracer release experiments would eliminate the interference for these two uses of SF_6. Recent experiments have demonstrated that SF_5CF_3 is a viable replacement tracer for ocean tracer release experiments (Ho et al., 2008).

The small-scale field experiments such as those conducted by Liss and Merlivat (1986); Nightingale et al. (2000b) yield mean global transfer velocities (10–15.4 cm hr^{-1}) far smaller than estimates using global inventories of either natural or bomb-produced radiocarbon (21.3–21.9 cm hr^{-1}, Tans et al. (1990); Wanninkhof (1992)). Such field experiments have added significantly to our understanding of processes that control gas transfer over short timescales and specific regions. The disagreement between methods results from differences in factors such as fetch, surfactants, wind speed and mixed layer turbulence.

There is still ongoing debate as to how much of the radiocarbon, released into the atmosphere by nuclear weapons testing, the ocean has taken up. Hesshaimer et al. (1994) argued that the value of 305×10^{26} atoms in the global budget of Broecker et al. (1985, 1995), which is based on an observed correlation between natural radiocarbon and dissolved silicate in waters assumed to be free of bomb-derived tracers, was an overestimate. This is important as equation 2.9, the Wanninkhof (1992) parameterization is scaled to give an average exchange rate matching that given by the bomb-radiocarbon budget. Peacock (2004) presented a global estimate of the bomb-radiocarbon inventory in Broecker et al's estimates.

More recently, Sweeney et al. (2007) have compiled a new database of $DI^{14}C$ measurements. Their study finds a 25% decrease in the ocean inventory of bomb radiocarbon compared to previous estimates (Broecker et al., 1985, 1995), and a 33% lower globally average transfer velocity using the NCEP/NCAR Reanalysis 1 1954–2000 where global mean winds are 6.9 m s^{-1}. Following Wanninkhof (1992), the authors use the implied relationship between wind speed and gas transfer velocity $k_s = 0.27u_{10}^2(Sc/660)^{-0.5}$ and arrive at a new estimate of global ocean CO_2 flux (1.8 ± 0.5 GT C yr^{-1}), which includes the carbon transfered from rivers into the deep ocean. Their estimate agrees more closely with the small scale dual tracer studies.

An additional factor that must be considered when calculating the air-sea flux of CO_2 is the effect of averaging wind speed measurements. During a long time period (monthly or seasonally), the use of the mean wind speed can significantly underestimate the transfer velocity (Memery and Merlivat, 1985). This is because the mean wind speeds do not describe the temporally varying global wind field (Van Scoy et al., 1995). Use of a

Rayleigh distribution function provides an approximation of the global wind speed frequency distribution of the mean monthly winds (Wentz et al., 1984; Wanninkhof, 1992). Recently Fangohr et al. (2008) have highlighted the impact of the temporal variability of satellite based wind speed on CO_2 exchange, and presented a simple methodology to correct monthly mean data.

There are objections to the use of Rayleigh distributed winds as this implies that transfer velocities should be scaled with a factor of 1.25 when long-term rather than short-term winds are employed. Wanninkhof et al. (2002) showed that although this is roughly true on a global basis, there is non-Rayleigh behaviour in many regions so that the correct scaling factor is frequently only 1.1–1.2. This overestimation of the scaling factor leads to an overestimation of the magnitude of the transfer velocity (Olsen et al., 2005). More recently, Blomquist et al. (2006) state that traditional k vs. u_{10} models based on a quadratic fit to tracer or radiocarbon data overestimate flux at high wind speeds and underestimate the flux as wind speed approaches zero for DMS.

The equations, 2.8–2.11, highlight the dependence of gas exchange estimates on wind speed to the exclusion of other factors. In order to improve estimates of gas transfer we must first improve our parameterizations of the transfer velocity. Thus, in situ observation must be available for both low and high wind speeds, at sufficient spatial and temporal resolution and with various surface conditions present e.g. surface films and bubbles.

Since we are primarily concerned with gas transfer during low wind conditions, it is likely that the use of such simple k vs. u_{10} parameterizations described above will underestimate the flux of CO_2. More appropriate will be to utilize physically-based models derived from surface renewal and turbulent-molecular diffusion theory near the air-sea interface (Soloviev and Schlüssel, 1994; Fairall et al., 2000).

The COARE bulk flux algorithm was developed as a physically-based model to estimate air-sea fluxes of momentum, heat, and moisture (Fairall et al., 1996a). It has been tested against thousands of ship-based direct flux measurements and updated to include surface wave effects (Fairall et al., 2003). The algorithm contains internal models to account for the oceanic warm layer and cool skin effects on relating the bulk ocean water temperature to the SST (Fairall et al., 1996b). The physics contained in the cool skin model have been adapted to describe the air-sea exchange of trace gases in terms of turbulent and molecular diffusive processes in both the air and the water. Fairall et al. (2000) define a transfer velocity on each side of the air-sea interface such that:

$$V_{ix}^{-1} = \int_0^{z_r} [K_{di}(z) + D_{vix}]^{-1} dz \tag{2.12}$$

where K_d is the turbulent eddy diffusivity, D_v the molecular diffusivity, and subscripts i and x refer to the phase (air or water) and trace gas respectively. The total transfer velocity is given by:

$$k_x = [V_{wx}^{-1} + \alpha V_{ax}^{-1}]^{-1} \tag{2.13}$$

From surface-layer similarity theory $K_d(z) \equiv \kappa z u_*$, where κ is the von Karman constant ($\kappa = 0.4$) and u_* the friction velocity in the fluid (air or water). Small-scale turbulence is suppressed by dissipation, there is a region near the interface ($z_r < \delta_u$) where transport is dominated by molecular diffusion (Blomquist et al., 2006). The integral can be approximated as:

$$V_{ix}^{-1} = \frac{1}{u_{*i}} \left[\frac{ln(z_{ri}/\delta_{ui})}{\kappa} + h_i S_{ci}^{1/2} \right] \tag{2.14}$$

where S_c is the Schmidt number for the gas in the fluid, and h is a coefficient of the molecular diffusion sub-layer. The NOAA-COARE gas transfer model (Hare et al., 2004) uses this method in the form:

$$u_{*a} V_{ax}^{-1} = \left[h_a S_{ca}^{1/2} + C_D^{-1/2} - 5 + ln(S_{ca})/(2\kappa) \right] \tag{2.15}$$

$$u_{*a} V_{wx}^{-1} = \sqrt{\rho_w/\rho_a} \left[h_w S_{cw}^{1/2} + ln(z_{wr}/\delta_{uw})/\kappa \right] \tag{2.16}$$

where C_D is the atmospheric velocity drag coefficient. The factor of the ratio of density of water to air in (2.16) assumes that the momentum flux is the same on both sides of the interface. Hare et al. (2004) define:

$$h_w = \frac{\Lambda}{A\varphi} \tag{2.17}$$

where $\Lambda = 13.3$, ϕ is an empirical function to account for buoyancy-driven transfer at low wind speeds, and A is a factor that is adjusted to fit measured gas transfer velocities. Soloviev and Schlüssel (1994) suggest a value of $A = 1.85$ for CO_2.

The model accounts for bubble mediated gas transfer, using the Woolf (1997) parameterization:

$$k_x = \left[(V_{wx} + k_b)^{-1} + \alpha_x V_{ax}^{-1} \right]^{-1} \tag{2.18}$$

where k_b describes the enhancement of transfer caused by plumes of whitecap-generated bubbles.

$$k_b = BV_0 f \alpha_x^{-1} [1 + (e\alpha_x S_{cw}^{1/2})^{-1/n}]^{-n} \tag{2.19}$$

where f is the whitecap fraction, a strong function of wind speed at 10 m, u_{10}.

$$f = 3.84 \times 10^{-6} u_{10}^{3.41} \tag{2.20}$$

Woolf (1997) gives the values $V_0 = 6.8 \times 10^{-3}$ m s^{-1} = 2450 cm hr^{-1}, $e = 14$, $n = 1.2$ for CO_2. The factor B is adjusted to fit measured transfer velocities.

The COARE gas transfer parameterization, above, incorporates more of the physics of air-sea gas transfer than any previously published model to date. The model describes the turbulent and molecular processes on both sides of the two-fluid interface; it incorporates the surface renewal concepts of Soloviev and Schlüssel (1994) and the empirical bubble enhancement model of Woolf (1997). Furthermore, this parameterization describes the flux on the scale (sub-hour) of the physical processes which drive the gas transfer.

The model has recently been extended to include gases such as ozone that are destroyed by chemical reactions after deposition to the ocean surface. Despite these advances, Hare et al. (2004) demonstrated that deviations still exist in the observations that cannot be explained by the current parameterization. Possible explanations for these discrepancies include inadequate representation of the surface mixed layer or biological influences. Thus, the implementation and further refinement of the COARE model will enable potential accuracy improvements especially where diurnal warming and convective exchange is prevalent.

2.2 Study area

The region of study for this project is the tropical Atlantic, situated geographically between 30°N and 30°S and from 70°W to the African Coast, linking the European, African and American continents (refer to figure 3.2 for a location map). The tropical oceans themselves are characterized by a relatively shallow thermocline, which separates warm, light water from cooler denser water below. Maintained by permanent easterly trade winds, the annual mean thermocline tends to be deeper on the western side of the ocean basins. Additionally the effect of the diurnal cycle is prevalent across much of the tropics, and during times of low wind and strong solar insolation can lead to the presence of a warm surface layer.

2.2.1 Atmospheric circulation and wind

The Inter-Tropical Convergence Zone (ITCZ) is a region of light winds, often referred to as the 'doldrums'. The convergence of southeast and northeast trade winds creates a zone of cumulus clouds and increased precipitation. The surface wind field in the tropical Atlantic is dominated by the northeast trade winds to the north of the ITCZ and the southeast trade winds to the south (Foltz et al., 2003). The width of the ITCZ can vary from 20 miles to 300 miles and has an undulating pattern (see figure 2.5). The ITCZ migrates north and south with the seasons, northward movement occurs during the high-sun seasons of the northern hemisphere and vice versa. However, this movement is not symmetrical due to the influence of the land masses.

The easterly trade winds intensify during the northern summer and autumn (Philander and Chao, 1991). To the east a monsoonal circulation develops in boreal summer, causing the northeast trades to reverse direction. Zonal currents are induced in response to these changing winds and to the resulting Ekman divergence. Since the width of the equatorial Atlantic is significantly less than that of the Pacific Ocean, the response to variations in wind forcing is less than the seasonal timescale. This results in an equilibrium response to seasonal forcing, corresponding to a succession of steady states (Philander and Chao, 1991).

There are differences between the seasonal variability of the northeast trade winds compared to the southeast trades (Hellerman and Rosenstein, 1983). The mean seasonal cycle of wind stress shows that the northeast trade winds are stronger in February (in an area near 10°N, 45°W). A second smaller peak in magnitude occurs slightly farther northwest in June. These northeast trades are weak from August to November with a minimum between October and November. The magnitude of the southeast trade winds is greatest in June-July and limited to an area around 10°S, 20°W.

In the western part of the tropical Atlantic, the wind is mainly zonal and has a strong annual amplitude. In the Gulf of Guinea (5°N–5°S, 5°W–10°E), the wind is orientated meridionally with an eastward component at its easternmost part due to the presence of a low pressure system over the African continent (du Penhoat and Treguier, 1985). The winds are at their weakest during July and August, and reach a maximum in November.

Nobre and Shukla (1996) investigated SST and wind stress anomalies in the tropical Atlantic, they found that values for both SST and wind stress were twice as high in the northern hemisphere compared to the southern hemisphere and that there was a tendency for the anomalies to be out of phase, with wind stress amplitudes largest over the western equatorial Atlantic.

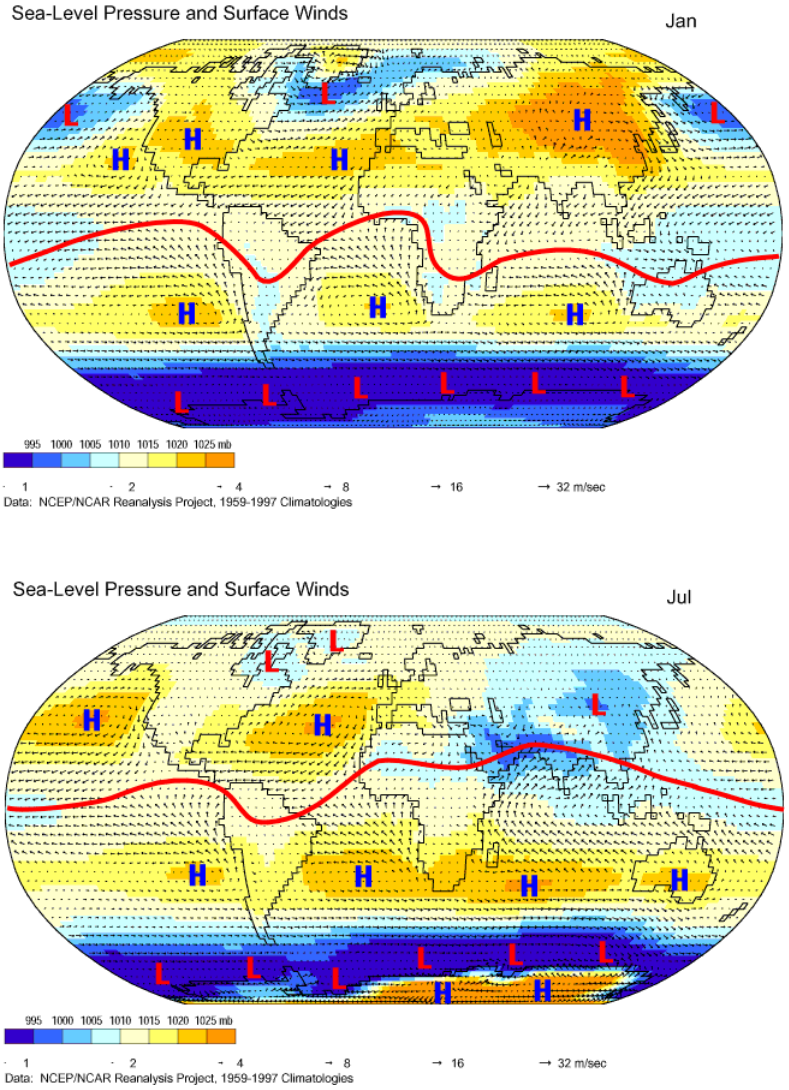

FIGURE 2.5: Mean January and July NCEP/NCAR Reanalysis 1969-1997 climatologies of sea-level pressure and surface winds. The red line represents the intertropical convergence zone (ITCZ). Centers of high (H) and low (L) pressure have also been labeled. Modified from Climate Lab section of the Environmental Change Research Group (2000).

2.2.2 Rainfall

The diurnal cycle of rainfall in the tropical Atlantic can influence surface mixing, and thus affect both the upper ocean heat and salt budgets. Cumulonimbus clouds, which are a characteristic of the ITCZ, are also associated with heavy rainfall. As such, the density of surface waters in the equatorial zone can be significantly affected by changes in precipitation. Colling (2001) note that salinity has a greater control of the density distribution in the equatorial zone than in most other regions.

Studies from satellites based on indirect precipitation indicate that tropical open ocean cloudiness has a pre-dawn maximum (Reed and Jaffe, 1981; Janowick et al., 1994; Nesbitt and Zisper, 2003), however there is also evidence for an afternoon maximum occurring in some regions of the tropical Atlantic (Reed and Jaffe, 1981; Janowick et al., 1994). Similarly, (Yang and Slingo, 2001) also find that while there is a general trend for open ocean cloudiness to occur in early morning, the phase of maximum cloudiness can be highly variable near coastlines and even in the open ocean.

Serra and McPhaden (2004) present observations of the diurnal cycle of rainfall. The authors use measurements from self-siphoning rain gauges on moored buoys (TAO and PIRATA) within the tropical Pacific and Atlantic. They find that the diurnal harmonic in particular dominates hourly rain accumulation, with a maximum from 0400 to 0700 local time (LT), and a minimum around 1800 LT. Afternoon maxima were also observed and correspond with peaks in rainfall intensity, and are consistent with previous satellite and in situ analysis.

2.2.3 Oceanic circulation

Circulation in the tropical Atlantic plays an important role in the interhemispheric transport of mass, heat and salt. The Deep Western Boundary Current (DWBC) transports cold North Atlantic Deep Water toward the Southern hemisphere. The North Brazil current (NBC) transports warm surface waters northward to close the overturning cell. the magnitude of this cross equatorial exchange has been estimated at about 13 Sv (Schmitz and Richardson, 1991).

The tropical and equatorial Atlantic Ocean is marked by variability occurring over a wide range of temporal and spatial scales. Satellite altimeter retrievals have enabled global, synoptic views of the upper ocean, Arnault and Kestenare (2004) use 10 years of TOPEX/Poseidon data to describe the seasonal variability of the tropical Atlantic geostrophic circulation.

As a result of the movement of the ITCZ, the equatorial current system in the Atlantic is not symmetrical either side of the equator. The position of ITCZ itself does not run simply east-west as it is distorted by the continental masses, particularly that of

Africa. Since there is a much larger proportion of land in the Northern hemisphere than the Southern hemisphere the ITCZ is shifted north of the equator. Furthermore, the northward and southward migration of the ITCZ causes changes in the upper ocean circulation on seasonal timescales (Stramma et al., 2005).

Since the ITCZ is characterized by light winds, there is no significant Ekman transport in the region between the north and south trade winds. Water moving across the Equator in response to the Southeast trade winds converges with water in the region (at about 4°N). There is also a divergence at about 10°N as a result of water moving away from the ITCZ in response to northeast trade winds. The westward flow in surface waters is also a direct result of the trade winds. These blow at 45° to the equator and surface flow in the South and North equatorial currents is 45° to this (to the west in both cases).

Westward moving water is eventually blocked by land-masses along the western boundaries of the basin. As a result the sea surface slopes up toward the west causing an eastward horizontal pressure gradient force. Because winds are light along the ITCZ, water is able to flow down the horizontal pressure gradient in a counter current to the prevailing wind direction between about 4°N–10°N (Colling, 2001). In addition, there is some deflection to the right by the coriolis force contributing to the convergence at 4°N. The sea surface therefore slopes up from about 10°N to 4°N giving rise to a northward horizontal pressure gradient force, driving a geostrophic current towards the east. In the Atlantic, the North Equatorial Counter Current (NECC) is present throughout the year only in the eastern part of the basin, where it is known as the 'Guinea Current' (see figure 2.6). There is also a weak south equatorial counter current which can be distinguished in the western and central ocean between 5°S and 10°S.

In the western equatorial Atlantic the seasonal change in winds and in the slope of the thermocline also drive an undercurrent which, at a fixed depth (approximately 100 m) is intense when the wind is strong and weak when winds are reduced (Philander and Chao, 1991). The effect of the wind is transmitted down to deeper layers via turbulence and is mainly confined to the mixed surface layer above the thermocline (Colling, 2001). The equatorial undercurrent is generally aligned along the Equator, but displacement of the current can occur due to northerly or southerly winds. Because the current is flowing to the east, when it strays from the equator it is always deflected back by Coriolis force.

The South Equatorial Current (SEC) is the major southern pathway by which water is imported into the tropical Atlantic. Off Brazil, the water continues northward as a component of the North Brazil Undercurrent (NBUC) in the region of 11°S–5°S. Just north of the north-eastern tip of Brazil, the SEC merges with the NBUC and crosses the equator as the North Brazil Current (NBC) (Stramma et al., 2005). Strongest in boreal summer, the SEC can reach speeds of 55 cm s^{-1} in the central basin (Richardson and Reverdin, 1987). Close to the latitude of the ITCZ (5°N–10°N) the eastward NECC is strong during boreal summer and autumn with speeds of 35 cm s^{-1}. Between

FIGURE 2.6: Schematic showing surface currents of the Atlantic Ocean. Adapted from Bartholomew (1973).

these two major current systems, and on the northern edge of the cold tongue, lie the strong meridional fluctuations of tropical instability waves, which may be important in transporting heat into the cold tongue in the eastern and central basins (Weingartner and Weisberg, 1991). According to model investigations the NECC is barotropically unstable, radiating Rossby waves of the first baroclinic mode (Stramma et al., 2005). These waves reflect at the South American coast and create 6–7 anticyclones per year, these anticyclones intensify and eventually become NBC rings.

2.2.4 Heat

The sensible heat flux (Q_h) in the tropical Atlantic is small (≤ -10 W m^{-2}) due to small air-sea temperature differences, while net emission of longwave radiation (Q_l) is relatively constant at about -50 W m^{-2} (Foltz et al., 2003). Due to the axial tilt of the Earth (23.5°) the Sun is almost directly overhead at noon, during summer, in the tropics; this results in the maximum solar insolation (Q_s) occurring near the equator.

Seasonal variations in latent heat (Q_e) and solar insolation (Q_s) are significant, both are influenced by the latitudinal movement of the ITCZ. Shortwave radiation is additionally influenced by changes in the solar zenith angle. In the northern tropics, latent heat loss is lowest during boreal summer and autumn, when winds are weak and relative humidity is high (less than 85%). Latent heat loss rises during boreal winter and spring when the ITCZ is close to the equator, low-level humidity is lower, and the northeast trade winds are stronger. In the eastern equatorial zone, latent heat loss has only weak seasonal variations, as low-level relative humidity and wind speed are fairly constant throughout the year (Foltz et al., 2003).

In contrast to the shortwave radiation at the top of the atmosphere, surface shortwave radiation has a significant annual harmonic at most locations. North of 5°N, surface solar radiation reaches a maximum in boreal spring, when the ITCZ is near its southernmost position and the solar zenith angle is high. Between the equator and 5°N, there is a strong semiannual component, with maxima in boreal spring and autumn, while on the equator the annual harmonic is again significant, with increasing amplitude toward the west and a maximum insolation in boreal autumn. The reduced amplitude in the east is due to the appearance of reflective stratus clouds in boreal autumn over the cool waters of the eastern basin (Philander et al., 1996).

Along the equator, absorbed shortwave radiation and zonal advection have significant seasonal variations. The seasonal cycle of absorbed shortwave radiation is enhanced by the fact that mixed layer depth and surface solar radiation vary in phase (the mixed layer is deepest in autumn when skies are clear). Seasonal variations of absorbed shortwave radiation are larger in the west leading to larger variations of both mixed layer depth and surface shortwave radiation. Horizontal heat advection has strong seasonal variations along the equator (except at 10°W) because of the seasonal variations in currents and there are strong horizontal temperature gradients.

Foltz et al. (2003) summarize the heat budget of the tropical Atlantic based on data from the PIRATA array of moorings:

- In the western (along 38°W) and eastern (along 10°W) tropical Atlantic, changes in mixed layer heat content are balanced primarily by changes in net surface heat flux (latent heat loss and solar heat gain). As the equator is approached, contributions from horizontal heat advection become increasingly important.
- Along the equator in the western basin (35°W) the seasonal cycles of zonal heat advection (resulting from the seasonally varying flow of the South Equatorial Current), eddy heat advection (associated with tropical instability waves), entrainment (caused by zonal mass divergence), and net surface heat flux all contribute significantly to seasonal SST variability.

- The mixed layer heat balance in the central equatorial Atlantic (23°W) is similar to that in the west (35°W), with the exception that seasonal variations of latent heat loss and entrainment are significantly smaller and zonal advection is stronger at 23°W.
- In the eastern equatorial Atlantic (10°W), cooling from meridional advection and warming from eddy advection tend to balance, so seasonal changes in SST tend to reflect seasonal variations in absorbed shortwave radiation. Entrainment and unresolved vertical diffusion may explain anomalous cooling.

In the equatorial Atlantic, Hastenrath (1977) and Merle (1980) used climatologies of surface heat flux and heat storage to deduce that horizontal and vertical temperature advection are necessary to balance the annual mean net surface heat flux. Molinari et al. (1985) looked at atmospheric and oceanic measurements and evaluated explicitly the effects of surface energy fluxes and zonal temperature advection on the seasonal cycle of mixed layer temperature. Results revealed important contributions from zonal advection between 3°N and 9°N. The authors calculated the sum of vertical and meridional advection/diffusion as a residual and found this term to be important within 3° of the equator. Unfortunately, none of the above studies were able to calculate explicitly the effects of meridional advection or vertical entrainment/diffusion on the mixed layer heat balance (Foltz et al., 2003).

Modelling studies have also stressed the importance of ocean dynamics in the equatorial Atlantic heat budget. Carton and Zhou (1997) concluded that zonal mass divergence causes cooling in the equatorial region east of 20°W, while meridional Ekman divergence plays an important role in the west. Their results indicate that solar heating is most important south of 5°S and north of 10°N, while latent heat loss is dominant in the western basin between 8°N and 12°N. Advection also plays a crucial role in the equatorial region, while the importance of latent heat loss increases toward the subtropics (Foltz et al., 2003).

2.2.5 Sea surface temperature

Surface temperatures in the tropical Atlantic vary under an annual cycle influenced by local heat transfer process and advective factors, with maximum mean annual temperature of 27.5 to 27.7 °C observed in regions located south of the inter-trade counter current (Ivanov and Polonskiy, 1992). Surface fluxes as well as horizontal and vertical temperature advection play a major role in shaping the seasonal cycle of SST in the equatorial Atlantic. However, the limited duration and spatial coverage of previous in situ observational programs has hindered efforts to quantify these contributions.

A westward shift of warm (less than 27 °C) SST in the latitude band 5°N–15°N occurs in boreal summer, along with the development of a tongue of cool (around 23 °C) SST

along and just south of the equator east of 30°W. This shift occurs concurrently with the annual growth and eastward expansion of the Atlantic warm pool west of 50°W (Wang and Enfield, 2001). In the west, seasonal changes in SST are weak in the equatorial zone, while north of 8°N a strong annual signal appears with a maximum in boreal autumn. South of the equator, SST reaches its maximum in boreal spring with an annual signal that increases in amplitude eastward to up to 3 °C near the African coast (Reynolds and Smith, 1994).

Sea surface temperature in the tropical Atlantic is asymmetric relative to the equator, the primary forcing for thermal changes is due to variation in strength of the trade winds (Nobre and Shukla, 1996). Weak trade winds are associated with warmer SST and stronger trade winds with cooler SST. SST anomalies exhibit a dipole pattern between the northern and southern hemispheres. In addition, SSTs in the tropical Atlantic show strong annual variation resulting from coastal upwelling induced by annual variations in alongshore winds (Carton and Zhou, 1997).

Weingartner and Weisberg (1991) examined the seasonal heat budget based on 1 year of observations from an equatorial mooring at 28 °W. They concluded that upwelling creates the cold SST tongue in boreal spring, while SST increases in boreal summer as the result of tropical instability waves. In late summer and autumn, advection terms are small and compensating, and diffusion at the base of the mixed layer balances net surface heat gain. In boreal winter, SST increases in response to a net surface heat flux concentrated by the shallower mixed layer Foltz et al. (2003).

In addition to the annual cycle; the diurnal cycle, directly associated with solar forcing, can lead to significant diurnal warming. Stuart-Menteth et al. (2003) state that the equatorial and tropical regions, primarily the Mediterranean and mid-Atlantic are particularly susceptible. Given that such regions are sources for CO_2, this has important implications for net estimates of the air-sea flux of CO_2 (see section 2.1.4).

2.2.6 Upwelling, productivity and enrichment

Mid-ocean equatorial upwelling, like coastal upwelling, is subject to seasonal variations. The primary upwelling period in the Atlantic is during July-September. The maximum is partly due to increased divergence of surface water in response to a seasonal increase in the strength of the south-east trade winds (Colling, 2001). The increased wind speeds result in increased south equatorial current flow, so that the north-south slope of the thermocline becomes so steep that it intersects the surface, allowing deeper nutrient rich waters to come to the surface. In low latitudes the thermocline slopes downwards towards the western coastal boundary. Because the mixed layer is thinner in the eastern ocean it is more affected by wind, thus deep water may be brought to the surface.

In addition, in certain locations of the eastern tropical Atlantic, the isotherms bow up into a dome-like shape (e.g. the 'Guinea Dome' and 'Angola Dome'). Their existence is linked to strong subsurface cyclonic flow patterns, and the degree of 'doming' varies seasonally. During the northern summer, when the ITCZ is at its northernmost position, the Guinea Dome protrudes into the thermocline, but the Angola Dome is weak. In the southern Summer the situation is reversed (Colling, 2001).

Houghton (1989) suggests that upwelling in the Gulf of Guinea is neither associated with local winds, nor the local ocean circulation. Instead the author states that remote wind forcing in the western equatorial region generates Kelvin wave pulses which travel eastwards. Weisberg and Tang (1987) conclude that the Gulf of Guinea is forced remotely, however it is local wind stress variability that determines the local maximum of upwelling. Furthermore Weisberg and Tang (1990) state that inter-annual variations in wind stress are crucial to the response of the equatorial ocean.

The highest atmospheric concentrations of dust over marine areas are found over the tropical north Atlantic, the northern Indian Ocean including the Arabian Sea, and the western north Pacific (Duce et al., 1991). Dust deposition is important as it contains iron, which can play a significant role in biological activity (Tovar-Sanchez et al., 2006). Measurements of dust over the tropical Atlantic Ocean by (Chiapello et al., 1995) indicate a pronounced seasonal pattern with maximum concentrations occurring during winter. Large quantities of dust are carried out of north western Africa and from the Sahel region at low latitudes in the trade wind layer. The authors suggest that this pathway may dominate the annual budget to the region. Furthermore, laboratory experiments have shown that the gas transfer velocity, k, can vary with biological activity (Goldman et al., 1988), thus regions of high marine productivity might be expected to reduce k via the presence of natural surfactant films (Frew et al., 1990; Frew, 1997). The recent SOLAS DOGEE II (Deep Ocean Gas Exchange Experiment) cruise in 2007 conducted two $SF_6/^3He$ tracer release experiments in the North Atlantic. One patch was labeled with a surfactant (a surrogate for natural sea surface surfactants) and one without in order to compare gas exchange data for two patches.

According to the iron hypothesis of Martin (1990), addition of iron to nutrient rich surface waters will increase phytoplankton biomass, resulting in increased uptake of CO_2 by the phytoplankton living in the surface ocean. In situ experiments, such as IronEx 1 and 2 have been conducted to test the hypothesis. Gas transfer was measured following artificially induced bloom events in the equatorial Pacific (Nightingale et al., 2000a). Similarly, in the Southern Ocean there have been three open-ocean iron enrichment experiments: SOIREE (Southern Ocean Iron Enrichment Experiment), EisenEx-1, and SOFeX (The Southern Ocean Iron Fertilization Experiment). All three produced notable increases in biomass and associated decreases in dissolved inorganic carbon and macronutrients (Buesseler and Boyd, 2003).

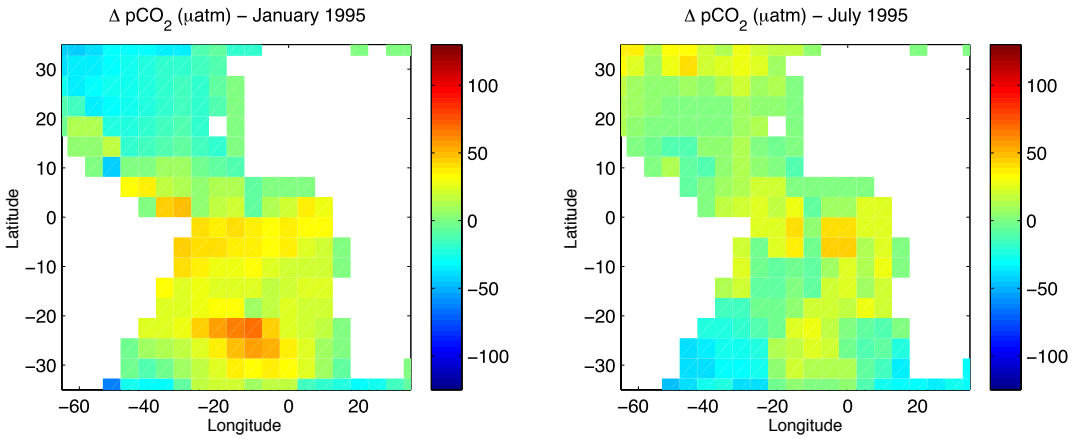

FIGURE 2.7: Tropical Atlantic ΔpCO_2 (μatm) climatology during January (left) and July (right) for reference year 1995 (Takahashi et al., 2002). Positive values indicate a source regions ($pCO_{2w} > pCO_{2a}$).

2.2.7 CO_2

The tropical Atlantic Ocean is generally a source of CO_2 to the atmosphere, due to pCO_2 in the surface being slightly supersaturated, with equatorial and coastal upwelling supplying CO_2 to the surface layer. Thus, the region plays a significant role in the global carbon cycle. Climatological ΔpCO_2, the difference between the oceanic and atmospheric partial pressure of CO_2 can be seen in figure 2.7, where positive values indicate a source region (Takahashi et al., 2002). The annual contribution of CO_2 to the atmosphere from the oceanic equatorial belt is approximately 0.6–1.5 GT C yr^{-1}. However, the source from the central and eastern equatorial Pacific is significantly larger than that of the tropical/equatorial Atlantic (Feely et al., 2004).

Smethie et al. (1985) mapped the CO_2 flux in the tropical Atlantic, calculated from ^{222}Rn and pCO_2 measurements as part of the TTO/TAS (Transient Tracers in the Ocean/Tropical Atlantic Study) program. Differences between surface water and atmospheric pCO_2 values were low in the northwest tropical Atlantic, with values less than -30 μatm at 15°N, and increases southward to a maximum of $+60$ μatm at 5°S. High pCO_2 in the southwest equatorial Atlantic can be explained by lateral advection of surface water from the east and biological consumption of total CO_2 and alkalinity within. The authors found that the net flux of CO_2 in the tropical Atlantic is into the ocean north of 10°N, and out of the ocean south of 10°N, accounting for a flux of roughly 0.15 GT C yr^{-1} to the atmosphere.

Lapshin et al. (1998, 1999) investigated seasonal and interannual variations in pCO_2, inferred from temperature salinity, pH, and alkalinity measured from survey ships between 1926–1992. During winter the highest areas of pCO_2 are located near the northwestern coast of South America and western coast of Africa, with the lowest areas occupying the interior of the ocean. In summer the local maximums and minimums move anticlockwise by roughly 1000–1500 km. In the western part of the tropical Atlantic pCO_2 is

higher in winter rather than summer, while between 20°W–35°W the ratio is reversed. The authors suggest that horizontal advection and water temperature variations do not play a dominant role in the spatial distribution of pCO_2, rather it is forced by upwelling-downwelling. Lefevre et al. (1998) observe that biological activity near the coastal upwelling zones causes strong drawdown in April associated with a decrease in SST, which suggests a supply of subsurface waters rich in nutrients.

The equatorial Atlantic is a source of CO_2 to the atmosphere because of the equatorial upwelling of CO_2-rich deep waters (see section 2.1.2). Sink regions may appear due to river runoff and precipitation, affecting the partial pressure of CO_2 in the surface ocean. These sinks may be enhanced by primary production driven by nutrients supplied from rivers. Kortzinger (2003) investigated the effect of the Amazon River plume on CO_2 concentrations in the tropical Atlantic. The Amazon discharges CO_2 supersaturated, nutrient rich water. Due to outgassing and primary production the plume becomes undersaturated with respect to CO_2. The result is a sink of approximately 0.014 ± 0.005 GT C yr^{-1} in contrast to the typical supersaturated source waters of the tropical Atlantic. Similarly Da Cunha et al. (2005) attempt to study the effect of the riverine nutrient fluxes on the tropical Atlantic productivity and air-sea CO_2 flux. Their results indicate that the fertilizing effect of rivers decreases the CO_2 to the atmosphere, somewhere between 21–53%.

Chapter 3

Models and forcing data

This chapter describes the one-dimensional model used as the basis for the majority of this study. Some background on 1-d modelling, and an overview of the data used for initial conditions and model forcing is also presented. In addition, the global model used in this thesis is also described. Since the various model configurations are slightly different for each of the experiments, that detailed information is not included here, instead a description of the model setup can be found in the relevant chapters.

3.1 Overview of 1-d models

A one-dimensional model provides an ideal environment for investigating processes in the diurnally mixed layer, and at the air-sea interface. Given that full ocean and climate models are both time consuming and computationally expensive to run, 1-d models provide the ability to perform multiple simulations in a relatively short amount of time. As such, these models are particularly useful for implementing and testing new parameterisations.

The near surface vertical resolution in a 1-d model can be much finer than in large scale models where computing power is a limiting factor. Thus, single column models are particularly suitable for modelling the diurnal cycle of SST, where fine resolution is necessary for capturing the diurnal thermocline. In comparison, horizontal gradients present in three dimensional models are less important. Niiler and Kraus (1975) state that vertical exchange processes across the air-sea interface, as well as vertical mixing within the water column are likely to affect the local conditions much more rapidly than horizontal advection and horizontal mixing.

One-dimensional models for the ocean mixed layer can be broadly categorized into two approaches:

1. Bulk models, which integrate the equations of heat and momentum over the entire mixed layer and make adjustments based on the effects of momentum and buoyancy fluxes e.g. Kraus and Turner (1967) and Price et al. (1986).

2. Diffusion models, which directly parameterize turbulent mixing and diffusion in the mixed layer e.g. Mellor and Yamada (1982); Large et al. (1994); Kantha and Clayson (1994).

The earliest modelling study of the diurnal cycle was by Price et al. (1986) who used surface fluxes and vertical profiles of temperature, salinity and velocity. Within the mixed layer the model mixes surface fluxes down until there is convective stability and the bulk and gradient Richardson numbers are stable. Shinoda and Hendon (1988) and Shinoda (2005) also used this model to investigate diurnal variability in the western equatorial Pacific. Another model developed by Large et al. (1994) uses a K-profile mixing parameterization (KPP) to determine vertical mixing. Such models have been extensively tested and compared to in situ measurements under light to moderate wind conditions (Anderson et al., 1996; Fairall et al., 1996b; Webster et al., 1996; Weller and Anderson, 1996; Cronin and McPhaden, 1997).

In a study by Horrocks et al. (2003), the bulk model of Kraus and Turner (1967) was compared to the diffusion model of Kantha and Clayson (1994). The authors found that the Kraus-Turner model could predict when the diurnal thermocline would form, but not its magnitude. The primary limiting factor was the reliance on mechanical and buoyancy driven mixing, which under strong solar heating and low wind speed is reduced leading to surface heat build up, with no mechanism to draw heat downwards. In comparison, the diffusion model of Kantha-Clayson, which was more effective at producing downward mixing, was better at predicting diurnal amplitudes.

In addition, Stips et al. (2002) compared measured and model simulated temperature and dissipation rate profiles from a two equation $k_e - \epsilon$ turbulence closure model and found that the basic features of convectively driven turbulence were well described by the model, with the temporal dynamics of the temperature field correctly simulated. More recently Acreman and Jeffery (2007) have compared a number of one-dimensional upper ocean models including the Kraus-Turner, a two-equation $k_e - \epsilon$ turbulence closure and the K-profile mixing parameterization (KPP), with in situ measurements from OWS Papa and Argo float data.

Based on model experiments using TAO data from the western Pacific warm pool, an upper layer resolution of the order 1 m is required to capture 90% of the diurnal variability (Horrocks et al., 2003). Furthermore, the way in which the incident solar energy is

transmitted through the water column is critical for modelling the warm layer. Despite its simplistic structure a single spectral band parameterization (Paulson and Simpson, 1977) is still widely used e.g. Bernie et al. (2005) and Shinoda (2005). However, Horrocks et al. (2003) implemented a 9 band parameterization (Paulson and Simpson, 1981), and Ohlmann and Sigel (2000) use an empirical solar transmission model that is dependent on upper ocean chlorophyll concentrations.

A number of studies have been conducted using mooring data from the TOGA-COARE sites as high frequency meteorological data is available (every 15 minutes) e.g. Webster et al. (1996); Shinoda (2005); Bernie et al. (2005). Bernie et al. (2005) performed experiments using different temporal resolutions of the forcing fluxes and concluded that to capture 90% of the diurnal variability of SST, 3 hourly flux forcing was required. However, the study by Horrocks et al. (2003) used six hourly surface fluxes from U.K. Met Office NWP analyses.

3.2 General Ocean Turbulence Model (GOTM)

For this study a diffusion type model called the General Ocean Turbulence Model (GOTM) was chosen. This model is freely available for download together with documentation at `http://www.gotm.net/`. GOTM is a one-dimensional water column model for the hydrodynamic and thermodynamic processes related to vertical mixing (Burchard et al., 1999), and has been widely used as a platform for studying turbulence (Burchard and Bolding, 2001; Umlauf and Burchard, 2003, 2005). Originally published in 1999, it has been regularly extended since then (Umlauf et al., 2006).

The model computes solutions for one-dimensional versions of the transport equations of momentum, heat and salt. The key component in solving these equations is the model for the turbulent fluxes of these quantities. GOTM includes a number of turbulence closure models which include simple prescribed expressions for the turbulent diffusivities up to complex stress models with several different transport equations to solve.

GOTM consists of a number of modules which carry out the required calculations. A main program provides a framework for the interaction of the lower level modules, in addition it is responsible for the model time-stepping and calling subroutines for air-sea interaction and model output. The primary GOTM modules we are concerned with include: **Meanflow**; **Turbulence**; and **Airsea**. Individual user specifications for each of the modules and subroutines are defined in simple text 'namelist files'. Once read, each of the above modules are initialized.

3.2.1 The mean flow model

This module contains the definitions of the important mean flow variables used in geophysical models, the mean horizontal velocity components (U and V), the mean potential temperature (Θ) and the mean salinity (S).

Due to the one-dimensional nature of GOTM, these state-variables are assumed to be horizontally homogeneous, depending only on the vertical z-coordinate. Consequently, all horizontal gradients have to be taken from observations, or they have to be estimated, parameterised or neglected. Alternatively, another option in GOTM for parameterising the advection of Θ and S is to relax the model results to observations.

The vertical grid is also defined in the meanflow module. Choices for the numerical grid include σ-coordinates with layer heights having a fixed portion of the water depth throughout the simulation. In addition, equidistant and non-equidistant grids are possible e.g. exponentially spaced grids.

3.2.2 The turbulence model

Parameterisations of the turbulent fluxes of momentum, $\langle u'w' \rangle$, heat $\langle w'\theta' \rangle$, and salinity $\langle w's' \rangle$ are required to calculate the differential equations for momentum, heat, and salt.

GOTM contains different types and level of turbulence closure model to compute the vertical turbulent fluxes (Umlauf and Burchard, 2005). These range from simple models which rely on the idea that theses fluxes can be computed as the product of a positive turbulent diffusivity and a profile gradient. Contributions to the fluxes that are not 'down-gradient', are summarized in so-called counter-gradient terms. Using these assumptions, the fluxes of momentum and buoyancy can be expressed as:

$$\langle u'w' \rangle = -\nu_t \frac{\partial u}{\partial z} + \tilde{\Gamma}_U \ , \quad \langle v'w' \rangle = -\nu_t \frac{\partial v}{\partial z} + \tilde{\Gamma}_V \ , \quad \langle w'b' \rangle = -\nu_t^B \frac{\partial B}{\partial z} + \tilde{\Gamma}_B \ , \tag{3.1}$$

where $\tilde{\Gamma}_{(U,V,B)}$ refer to the counter-gradient fluxes. They can be important under very strong stratification and during convection. The current version of GOTM identifies the diffusivities of heat and salt with ν_t^B

Using an analogy to the kinetic theory of gases, the vertical turbulent diffusivities, ν_t and ν_t^B, are often assumed to be the product of a typical velocity scale of turbulence, q, times a typical length scale, l. The velocity scale q can be identified with the average value of the turbulent fluctuations expressed by the turbulent kinetic energy, $k_e = q^2/2$. Then, the diffusivities of momentum and heat can be written as:

$$\nu_t = c_\mu k^{\frac{1}{2}} l \ , \quad \nu_t^B = c_\mu' k^{\frac{1}{2}} l \ , \tag{3.2}$$

where the dimensionless quantities c_μ and $c_\mu{}'$ are usually referred to as the 'stability functions'. Depending on the level of turbulent closure, these stability functions can be either constants, empirical functions, or functions of some non-dimensional flow parameters resulting from a higher-order turbulence model. The same applies to the counter-gradient fluxes $\tilde{\Gamma}_{(U,V,B)}$ used in (3.1).

Similarly, there are a number of different options in GOTM to compute the scales q (or k_e) and l appearing in (3.2). According to their level of complexity, they are ordered in GOTM as follows:

1. Both, k_e and l are computed from algebraic relations. The algebraic equation for k_e is based on a simplified form of the transport equation of the turbulent kinetic energy. The equation for the length-scale may result from different approaches. The most simple models assume an empirically motivated, prescribed vertical distribution of the length-scale. Algebraic models are an over-simplification in many situations.

2. At the next level, k_e is computed from the differential transport equation for the turbulent kinetic energy. As before, the length-scale is computed from an empirically or theoretically based relationship.

3. In the two-equation models, both, k_e and l are computed from differential transport equations. As before, k_e follows from the transport equation of the turbulent kinetic energy. Now, however, the length-scale also is determined from a differential transport equation. This equation is usually not directly formulated for the length-scale, but for a related, length-scale determining variable. Presently, there are different possibilities for the length-scale determining variables implemented in GOTM, such as the rate of dissipation, ϵ, or the product $k_e l$.

The main advantage of the two-equation models is their greater generality. For example, there are a number of fundamental flows which cannot be reproduced with an algebraically prescribed length-scale. These include the temporal decay of homogeneous turbulence, the behaviour of turbulence in stratified homogeneous shear flows, and the spatial decay of shear-free turbulence from a planar source (Umlauf et al., 2006).

In addition to the various turbulence models used to calculate turbulent kinetic energy and the length scale, GOTM also includes different schemes for solving transport equations, which range from simple to complex:

1. At the lowest level of this scheme $c_\mu = c_\mu^0$ and $c'_\mu = c_\mu'^0$ are constant. Because these models implicitly assume an isotropic tensor relation between the velocity gradient and the tensor of the Reynolds-stresses, they usually fail in situations of strong anisotropy, most notably in stably stratified, curved or shallow flows. In unstratified flows with balanced aspect ratios (which rarely occur in nature), however, they may compute reasonable results. Models of this type are referred to as the 'standard' models.

2. Some problems associated with 'standard' models can be minimised by making c_μ and c'_μ empirical functions of one or several significant non-dimensional flow parameters. At this level, the simplest approach would be to formulate empirical relationships based on observations in the field or in the laboratory.

3. A more consistent approach results from the solution of simplified forms of the transport equations for the Reynolds-stresses and the turbulent heat fluxes, in addition to the transport equations for k_e and the length-scale determining variable. Under some assumptions, the turbulent fluxes computed by these models can be expressed by (3.2). The important difference is that the existence of vertical eddy diffusivities is a result of the model. The stability functions c_μ and c'_μ can be shown to become functions of some non-dimensional numbers like:

$$\alpha_M = \frac{k^2}{\epsilon^2} M_v^2 \ , \quad \alpha_N = \frac{k_e^2}{\epsilon^2} N_v^2 \ , \quad \alpha_b = \frac{k_e b_v}{\epsilon^2} \ , \tag{3.3}$$

   with the shear-frequency, M_v, and the buoyancy frequency, N_v, respectively. k_e and b_v are the turbulent kinetic energy and the buoyancy variance respectively, and ϵ represents the dissipation rate.

   The most well-known models of this type have been implemented into GOTM. Further information can be found in Canuto et al. (2001), and their evaluation for the oceanic mixed layer has been extensively discussed by Burchard and Bolding (2001)

4. Even more complete models include further differential equations for the buoyancy variance and for some or all of the turbulent fluxes. These models cannot be reduced to the form (3.2).

3.2.3 Air-sea interaction

This module provides the surface forcing for GOTM. Boundary conditions are necessary for all of the dynamic equations. For the momentum equations, these are the surface momentum fluxes τ_x^s and τ_y^s in N m^{-2}. For the temperature equation, it is the total surface heat flux (W m^{-2}) that has to be determined:

$$Q_{tot} = Q_h + Q_e + Q_l^{\uparrow} \tag{3.4}$$

The total surface heat flux Q_{tot} is calculated as the sum of the latent heat flux Q_e, the sensible heat flux Q_h, and the long wave back radiation $Q_l^{\uparrow}$. In contrast to the total surface heat flux Q_{tot}, the net short wave radiation at the surface, Q_s, is the basis of a 'volume source term' (Paulson and Simpson, 1977). For the salinity equation, the fresh water fluxes at the surface are given by the difference of the evaporation and the precipitation in m s^{-1}.

There are two ways of calculating the surface heat and momentum fluxes implemented into GOTM. They can either be prescribed (as constant values or to be read in from files) or calculated on the basis of meteorological data which is read in from files. For the latter, the necessary parameters are: the sea surface temperature (SST in °C); air temperature (in °C); air humidity (either as relative humidity in %, as wet bulb temperature or as dew point temperature in °C); air pressure (in hectopascal), each at 2 m height above the sea surface; and the wind velocity vector at 10 m height in m s^{-1}. Instead of the observed SST, the model SST may be used for the calculation of the surface fluxes. These may be calculated with the bulk formulae of Kondo (1975) or Fairall et al. (1996b).

3.3 In situ data

It was decided that the method of calculating the surface heat and momentum fluxes from bulk formulae would be used to drive the 1-d model. This allowed for future, additional expressions for the surface fluxes to be implemented, such as the NOAA-COARE bulk flux algorithm.

The choice was also based on the types of in situ data available for the tropical Atlantic. Unlike the Tropical Atmosphere Ocean project (TAO/TRITON) array in the Pacific, the moored buoys in the tropical Atlantic do not contain all of the necessary sensors to estimate the surface heat budget, thus additional data from satellite and model reanalyses were necessary to force the model.

Since the completion of this work, there have been a number of additional moorings added to the array, and upgrades to some of the existing buoys. Two such buoys at 0°23°W and 10°S10°W, are equipped with longwave radiation and barometric pressure sensors; data available for 2006–onward. As part of the OceanSITES program additional PIRATA mooring sites in 2007 have been instrumented with long wave radiation and barometric pressures sensors, current meters at 10 m depth, and enhanced temperature and salinity measurements in the upper 60 m. The additional sensors will allow for

Measurement	Sensor Type	Resolution	Range	Accuracy
Wind speed	Propeller	0.2 m s^{-1}	1–20 m s^{-1}	±0.3 m s^{-1} or 3%
Air temperature	pt-100 RTD	0.01 °C std	14-31 °C	±0.2 °C
Relative humidity	Capacitance	0.4% (real time) 0.02% (delay mode)	55–95%	±2.7%
Downwelling shortwave radiation	Pyranometer	0.4 W m^{-1}	200–1000 W m^{-2}	±1%
Sea surface and subsurface temperature	Thermistor	0.001 °C	1–31 °C	±0.003 °C
Salinity	Internal field conductivity cell	0.0001 S m^{-1}	3–6 S m^{-1}	±0.02 psu

TABLE 3.1: Sensor details for Next Generation ATLAS moorings. Source: TAO Project Office (2008).

estimation of all components of the surface heat flux and improve the estimation of mixed layer depth.

3.3.1 PIRATA mooring data

The field phase of the PIRATA program began in late 1997 and was scheduled to last three years, however the program has continued to be in operation. The PIRATA program is a multinational effort involving Brazil, France and the United States. The moorings used in the array are primarily ATLAS (Autonomous Temperature Line Acquisition System) moorings like those used in the equatorial Pacific as part of the TAO/TRITON array. Many of the moorings have been upgraded and the next generation of ATLAS moorings (see figure 3.1) provide improved accuracy, temporal resolution, flexiblity and an increased number of measured variables.

The PIRATA moored array consists of 20 ATLAS Moorings, as of early 2008, spanning 15°N–10°S, 38°W–0°. The 12 PIRATA moorings considered during this study can be seen in figure 3.2, and the availability of their data is shown in figure 3.3.

The variables measured by the array inlcude surface winds, SST, sea surface conductivity (salinity), air temperature, relative humidity, incoming shortwave radiation, rainfall, subsurface temperature (10 depths in the upper 500 m), subsurface conductivity (three depths in the upper 500 m) and subsurface pressure (at 300 m and 500 m). Table 3.1 shows information on the types of sensors used on the PIRATA moorings and lists their accuracies. Most of the instrumental accuracies are based on laboratory calibrations, both pre- and post-recovery, and are based on root mean square drift of a group of sensors.

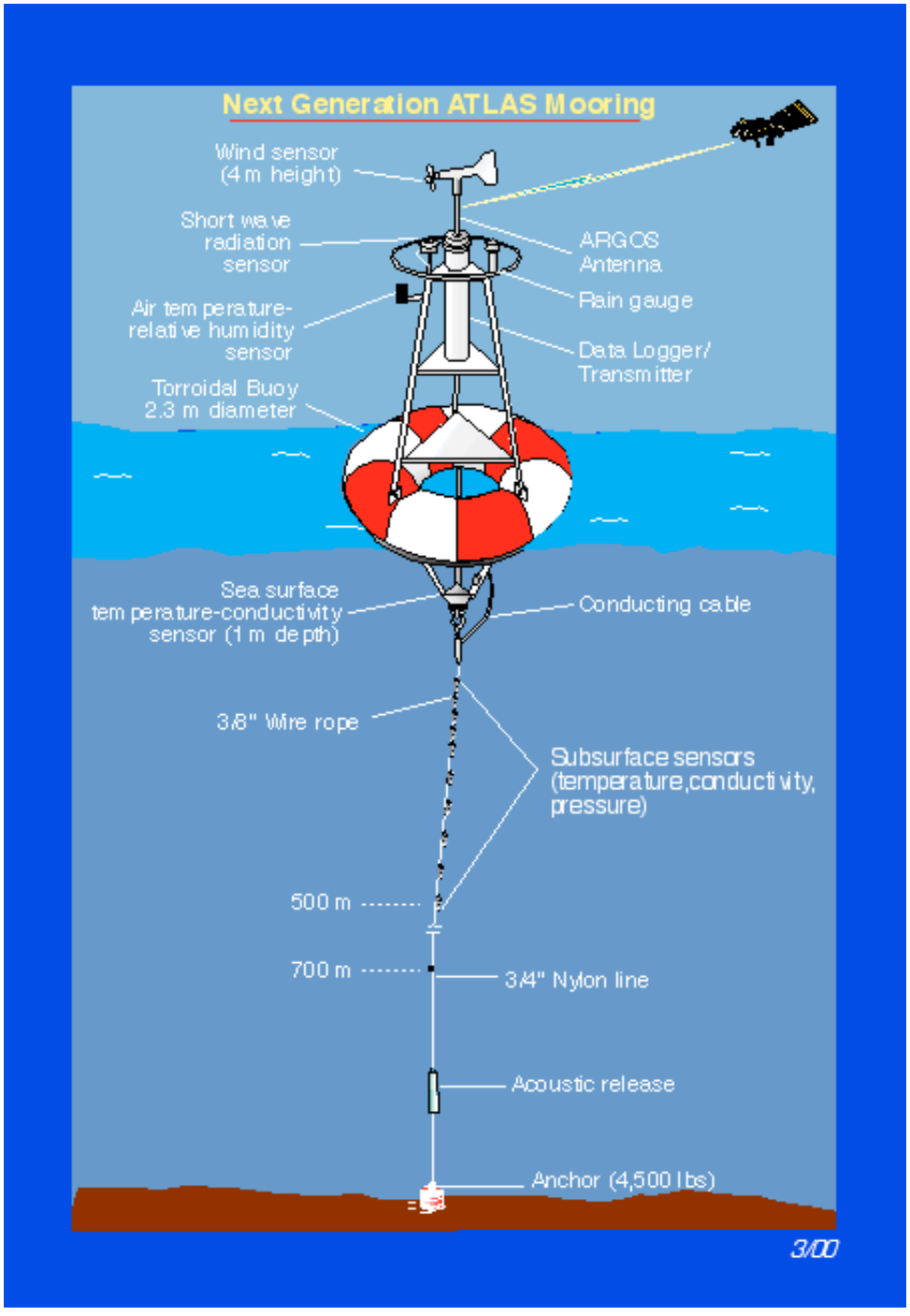

FIGURE 3.1: The Next Generation ATLAS mooring. Source: TAO Project Office (2008).

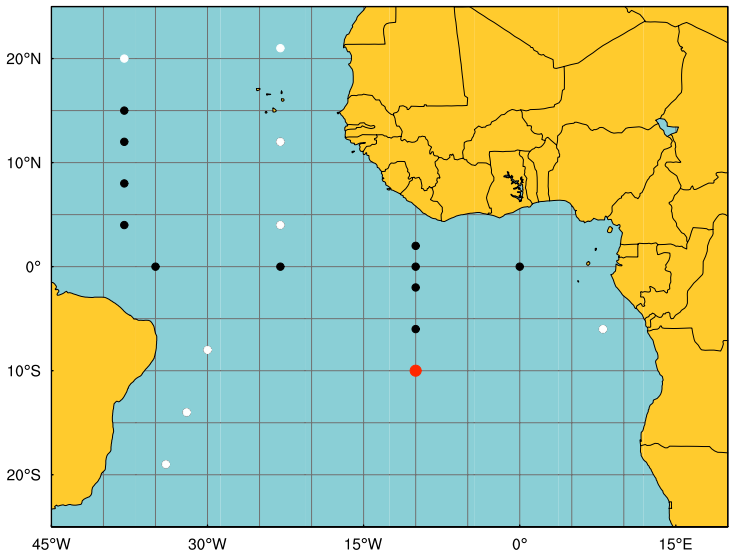

FIGURE 3.2: Location of PIRATA moorings in the Tropical Atlantic. Red circle indicates location of mooring at 10°S10°W, white circles indicate the location of moorings added after work was completed. Source: TAO Project Office (2008).

Once a year, the buoys are recovered and replaced with new instrument sensors. The instruments that have been recovered are then delivered to PMEL (Pacific Marine Environmental Laboratory) in Seattle, USA, for post-calibration and retrieval of the high frequency data, which are stored in the instruments data loggers. ATLAS moorings transmit daily mean values from the previous day and the most recent hourly surface meteorological observations via Service Argos utilizing the NOAA polar orbiting satellites, with 10 minute or 2 minute resolution data available in delayed mode following their recovery. The design lifetime of the moorings is 1 year.

3.4 Additional datasets

In order to force GOTM we require measurements of: air temperature; wind speed; air pressure; relative humidity; and cloud fraction. As the PIRATA array of moorings does not provide measurements of all the variables necessary to drive the model (we are missing estimates of cloud fraction and air pressure), additional data from model climatology and satellite products is used to supplement the in situ data.

3.4.1 Meteosat-7 cloud analysis

Launched in 1997, Meteosat-7 is a geostationary satellite, in orbit at 0° longitude at an altitude of 36,000 km. It is one of a network of five satellites placed in geostationary

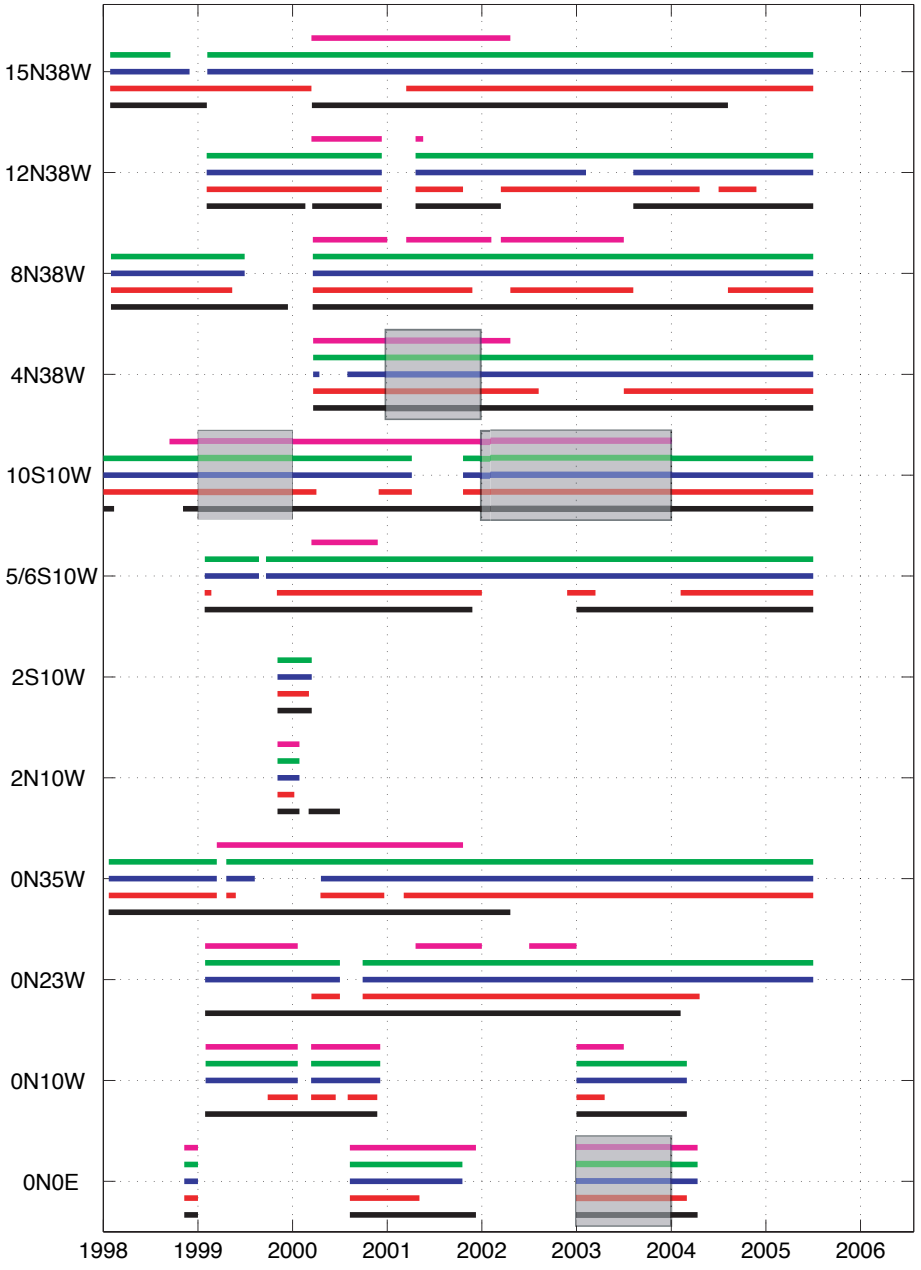

FIGURE 3.3: Availability of high resolution PIRATA data, SST (black), wind (red), air temp. (blue), rel. hum. (green) and salinity (magenta). Grey boxes indicate continuous data throughout the year. Source: TAO Project Office (2008).

Spectral Bands	0.5-0.9 μm Visible	5.7-71 μm IR water Vapour	10.5-12.5 μm Terrestrial IR
Number of detectors	2 (+2)	1 (+1)	1 (+1)
Detector type	Si	HgCdTe	HgCdTe
Field of view	0.065 mrad	0.14 mrad	0.14 mrad
Resolution at nadir	2.5 km	5 km and	5 km
Radiometer performance	S/N > 200 for 25% albedo	Net < 1.0 K at 260 K	Net < 0.4 K at 290 K

TABLE 3.2: Characteristics of METEOSAT radiometer MVIRI. Source: Mohr (1999).

orbit to observe cloud cover, wind speed, sea and cloud surface temperatures and water vapour distribution in the upper troposphere.

The Meteosat Visible and Infrared Imager (MVIRI) sensor acquires images every 30 minutes in 3 bands: visible; a water absorption band; and thermal infrared. The sensor characteristics can be seen in table 3.2. The satellite scans the full earth disc within a 30 minute period. Scanning in the east-west direction is achieved through the rotation of the entire satellite, sweeping out a line of data during each spin. Scanning from south to north is achieved by stepping the direction of the telescope the equivalent of one line further north after each revolution of the satellite (Mohr, 1999).

In addition to the provision of images of the Earth and its atmosphere, a range of operational processed meteorological products is produced. The cloud analysis (CLA) is an automatically generated product describing the total cloud amount and the cloud top temperatures. It is derived from an internal intermediate CLA which provides extensive information about cloud properties. The resulting CLA is at a reduced resolution 232×232 lines (formed by 16×16 pixels) and contains data derived only from cloud pixels. Each segment contains information on total cloud cover, and for each low-, mid- and high-level cloud band (cloud type, amount, phase cloud top temperature and height). The cloud analysis produced by Eumetsat is a coded representation of the cloud in a single image, and is based directly on the cloud clusters extracted during segment processing (EUMETSAT, 1998).

3.4.2 ISCCP cloud data

The International Satellite Cloud Climatology Project (ISCCP) was established in 1982 to collect weather satellite radiance measurements and to analyze them to infer the global distribution of clouds, their properties and their diurnal, seasonal and inter-annual variations.

Data are collected from a suite of weather satellites operated by several nations and processed by several groups. For each operational satellite a processing centre collects

the raw satellite data and sends it to the global processing centre where it normalizes the calibration of the geostationary satellites with respect to a polar orbiter satellite standard. Cloud data processed by ISCCP is from a selection of satellites including GMS-5, GOES-10, GOES-8, METEOSAT-5, METEOSAT-7, NOAA-16 and NOAA-17.

Cloud cover fraction, as defined by the ISCCP, represents the fractional area covered by clouds as observed from above by satellites. It is estimated by counting the number of cloudy pixels in the satellite's field-of-view (approximately 5 km across) and dividing by the total number of pixels in a region about 280 km across. It depends heavily on the geostationary satellite's measurement of cloud cover using the visible channels. Problems can arise in regions where there are gaps between geostationary coverage e.g. the Indian Ocean (Shiffer and Rossow, 1983).

3.4.3 NCEP air pressure data

The NCEP/NCAR Reanalysis project is a joint project between the National Centers for Environmental Prediction (NCEP) and the National Center for Atmospheric Research (NCAR).

The NCEP/NCAR reanalysis 1 project uses a state-of-the-art analysis/forecast system to perform data assimilation using past data from 1948 to the present. The NCEP Reanalysis surface level data set is based on a 2.5 degree latitude $\times$ 2.5 degree longitude global grid with 4 individual observations per day.

3.5 Data availability

The limited availability of the the high resolution PIRATA mooring data between 1998-2006 is shown in figure 3.3. The grey boxes highlight those locations where each of the necessary parameters (SST, wind speed, air temperature, relative humidity and salinity) are available for a year or more. There are many large gaps in the data where either one or more of the sensors failed to record the desired parameters.

The 1-d model requires temperature and salinity profiles for its initial starting conditions, the other in situ parameters are required, continuously, as model forcing. The availability of the additional datasets for the region corresponding to the PIRATA mooring located at 10°S10°W is shown in figure 3.4.

Whilst both the newer MSG-1 and Meteosat-7 satellites provide continuous cloud cover records for 2004-onward, there are no PIRATA mooring locations that contain all of the required input/forcing parameters. Instead, the best available option for the additional data coverage appears to be 2002, where Meteosat-7 has almost a complete year of coverage, and the ISCCP D2 dataset can be used to fill the gaps if necessary.

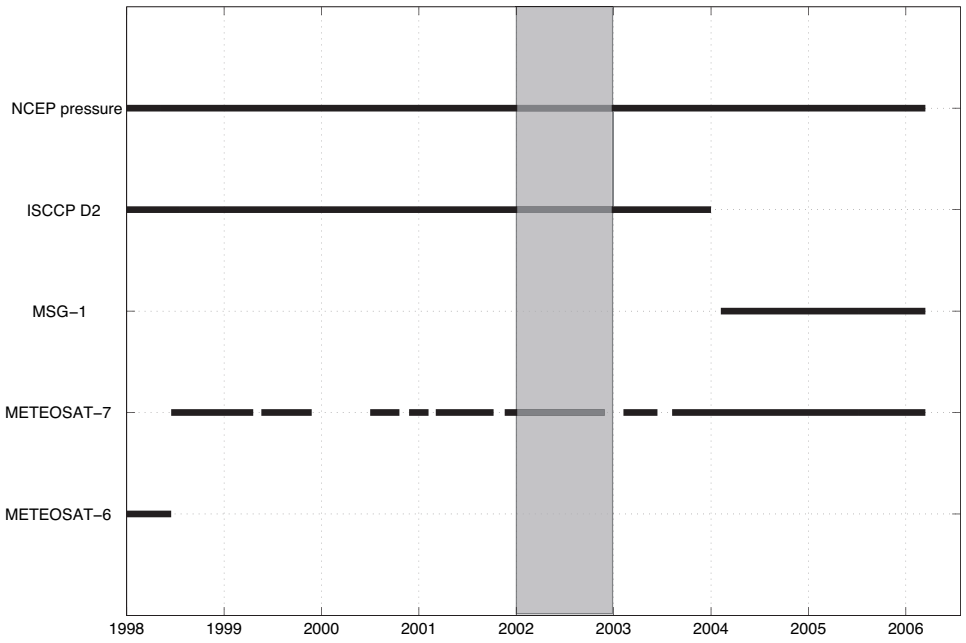

FIGURE 3.4: Availability of additional datasets. Meteosat-6,-7, MSG-1 (cloud fractions); ISCCP (cloud cover climatology), NCEP (surface pressure data). Grey highlight during 2002 indicates a near complete data record when data from PIRATA buoy 10°S10°W is included.

	Annual Mean, W m^{-2}	Annual Amplitude, W m^{-2}	Annual Phase, months	Semiannual Amplitude, W m^{-2}	Semiannual Phase, months
Latent	−140	30	1	10	4
Surface Shortwave	210	40	2	10	3
Absorbed Shortwave[a]	200	30	2	0	3
Entrainment	−10	10	0	0	3
Zonal advection	−10	10	2	0	5
Meridional advection	20	0	7	0	6
Eddy advection	−10	20	9	10	1
Heat storage	−10	70	1	10	5
Mixed layer depth[b]	50	20	9	0	1

[a]Explains the largest amount of variance at this location.
[b]Annual mean, annual amplitude, and semiannual amplitude values for mixed layer depth are given in metres.

TABLE 3.3: Amplitude and phase of annual and semiannual cosine harmonics (with respect to 1 January) and annual mean of terms in the mixed layer heat balance at 10°S10°W. Based on table 1 from (Foltz et al., 2003).

Based on this availability and the Foltz et al. (2003) study, the PIRATA mooring located at 10°S10°W was selected. The advection terms (see table 3.3) at this location are relatively low compared to other PIRATA mooring sites, but -20 W m^{-2} is significant compared to the sensible and net longwave fluxes at this location. This is important as the advective contribution to the heat budget is neglected in our modelling studies.

3.6 The Unified Model

The following section describes the Unified Model and the submodels that were utilized in this study. It is important to remember that the U.K. Met Office models are operational in nature, thus they must perform consistently. New advancements and code changes are rarely implemented without rigorous testing.

Originally introduced into operational service in 1992 the Unified Model (UM) consists of a number of atmosphere and ocean models. The UM can be run on a variety of global and regional domains and over various spatial and temporal scales. It is used for both numerical weather prediction and climate modelling in addition to related research activities.

The system can be run in several coupled or individual modes such as atmosphere-only and ocean-only mode. Each model run may include a period of data assimilation followed by the run itself. When used for forecasting the prediction phase is of the order of days, however when the model is used for climate runs, the prediction phase may be up to hundreds or thousands of years. The horizontal and vertical resolution of the model can be defined by the user, but in practice a standard suite of resolutions is used.

A large number of user configurable options exist for the Unified Model in order to specify and control a particular model configuration. A configuration tool known as the Unified Model User Interface (UMUI), an X-windows based control panel, is used to define the model setup. Parameters such as model resolution, the date and time of the initial data, length of the the model run and the choice of output diagnostics is specified using the UMUI. A similar tool, the Standardized Control Suite User Interface (SCSUI) is also used for controlling parameters related to batch runs of the UM and its output.

Whilst the UM is an operational system, a number of parallel, development versions of the model suite are used to test code changes and conduct research. Thus the UM incorporates a code configuration management system in order to coordinate changes made to the individual model components. A proprietary source code revision system is used to merge new code with the development stream. These new source code developments are often known as modification sets.

The Unified Model is made up of a number of numerical submodels:

- The Atmosphere Sub-Model — covers all or part of the Earth's surface area with multiple atmospheric layers.
- The Ocean Sub-Model — covers all or part of the Earth's water areas with multiple depth layers.
- The Slab Ocean Sub-Model — is a reduced model of the oceans with only one depth layer (or a slab), suitable for maintaining sea-surface coupling with the atmosphere sub-model.
- The Wave Sub-Model — is a separate model for calculating surface waves on the oceans and seas using wind data from an atmospheric model.
- The Sea-Ice Sub-Model — is for modelling the properties and behaviour of sea-ice and this must be used in conjunction with an ocean model.

The Unified Model can be split up in a number of different ways, with various submodel components switched on or off for a specific modelling application. The exchange of physical variables, or coupling between the submodels can be either one- or two-way. For example, wind properties from the atmospheric submodel will influence wave height in the wave submodel. This coupling could work both ways however, as wave height determines the friction experienced by atmospheric motions and could therefore be coupled back into the atmospheric submodel.

Dividing the UM into manageable submodels enables easier development and integration of modification sets (or modsets). The UM was originally written in Fortran 77, however recent work has enabled the use of Fortran 90 standards.

3.6.1 Forecasting Ocean Assimilation Model

The ocean submodel component of the U.K. Met Office Unified Model is based on the Cox (1984) formulation of discretised primitive equations (Bryan, 1969). The model is used in coupled ocean-atmosphere climate simulations, for seasonal forecasting and for short-term ocean forecasting application.

The Forecasting Ocean Assimilation Model (FOAM) is an operational system to forecast the state of the global ocean a few days ahead and is built around the ocean and sea-ice components of the UM. FOAM consists of a $1^\circ \times 1^\circ$ resolution numerical ocean model driven by 6-hourly surface fluxes from the UKMO numerical weather prediction (NWP) suite, and assimilates temperature and salinity profiles from in situ instruments, and remotely sensed data such as surface temperature, sea-ice concentration and sea surface height data (Bell et al., 2000). Observations from the previous 10 days are assimilated with variable weighting.

A coarse resolution global configuration of FOAM with 20 vertical levels was implemented in the Met Offices operational suite in 1997. Nested models with finer grid spacings ranging from 30 km to 6 km are used to provide detailed forecasts for selected regions. The FOAM system is fully relocatable, allowing high-resolution configurations to be set up for any deep ocean region. Because FOAM is intended for short-range integrations, the oceanic initial state is very important. The success of FOAM is therefore very dependent on the quality of the Unified Model's data assimilation scheme.

The model bathymetry is derived from the DBDB5 dataset (U.S. Naval Oceanographic Office and the U.S. Naval Ocean Research and Development Activity, 1983) by interpolating onto the 1° global grid and smoothing to remove large bathymetric gradients. In addition some channels have been widened or deepened (Johns et al., 1997). The model includes a rigid-lid approximation and the velocity is represented by a baroclinic component and a barotropic streamfunction. Tracer advection is calculated using a centered difference leapfrog scheme. Fourier filtering is applied to the tracer and velocity fields north of 75°N (Bell et al., 2000).

Horizontal and vertical mixing on the sub-grid scale are parameterized in the model. The Richardson number dependent vertical diffusion scheme of Pacanowski and Philander (1981) is applied to mix temperature, salinity and horizontal momentum (using the recommended coefficients). An additional mixed layer scheme based on Kraus and Turner (1967) and Davis et al. (1981) is used to mix the tracers; 70% of the wind mixing energy is assumed to be available for turbulent mixing and this is taken to decay exponentially with a depth scale of 100 m; and 15% of convectively generated turbulent kinetic energy is taken to be available for entrainment at the base of the mixed layer (Bell et al., 2000).

A simple version of the Large et al. (1994) scheme also mixes horizontal momentum in the vertical, using a quadratic mixing profile, appropriate in neutral stability conditions. The base of the mixing layer is set at a depth where the Richardson number first exceeds the critical value of 0.3, but is limited to be no deeper than 140 m. The diffusion coefficient is chosen to match the Pacanowski and Philander (1981) value at this depth. Both the Kraus and Turner (1967) and Large et al. (1994) models were compared in Acreman and Jeffery (2007) (see Appendix A) in terms of their skill at representing the ocean mixed layer. Figure 3.5 shows the seasonal average mixed layer depth as calculated by FOAM for a model run over 2003.

Lateral mixing of tracers along isopycnal surfaces follows the method of Redi (1982) as amended by Gerdes et al. (1991) with values of 2000 m^2 s^{-2} at the surface decreasing to 500 m^2 s^{-2} over a depth scale of 500 m and reduced where isopycnal slopes are greater than 1 in 1000. There is also a small amount of purely horizontal mixing (100 m^2 s^{-1}), which is necessary to control grid scale noise. The horizontal viscosity is set to 6000 m^2 s^{-2}.

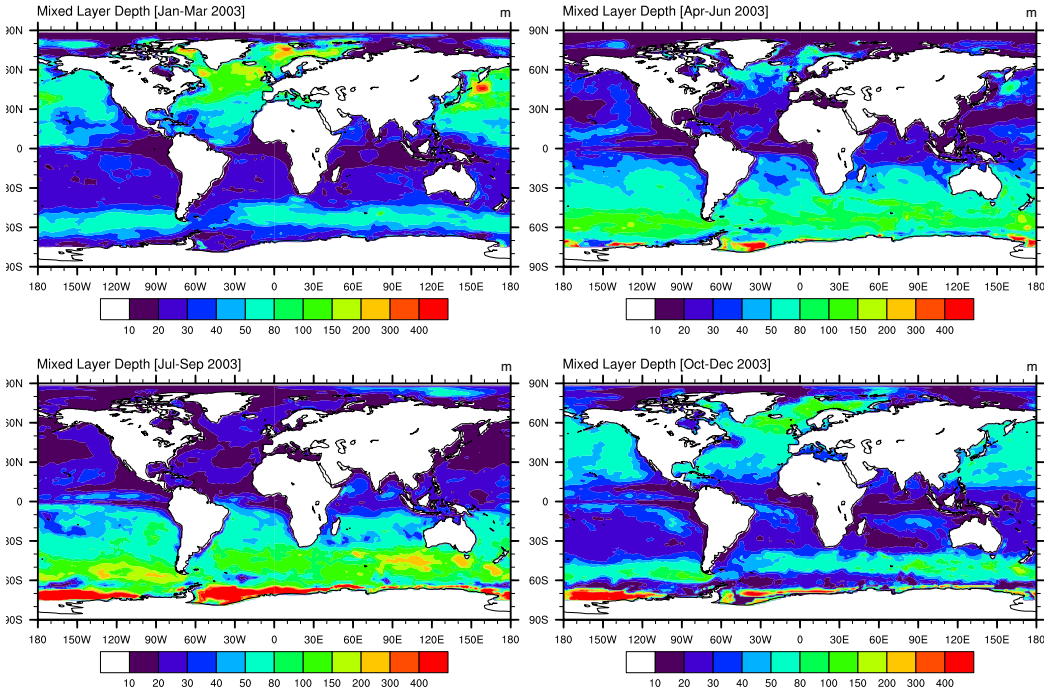

FIGURE 3.5: Seasonal average mixed layer depth (m) from FOAM-HadOCC for 2003.

The temperature of the top layer of the ocean model (10 m depth) is relaxed towards a temperature climatology (as suggested by Haney (1971)) with a relaxation coefficient of 35 W m^{-2} K^{-2}. The surface salinity is also relaxed to climatology. The Levitus (1994) climatology is used for both temperature and salinity and sea ice thickness is relaxed to a climatology derived from the second coupled version of the Unified Model (Johns et al., 2006). Both climatological and Numerical Weather Prediction (NWP) derived estimates of surface forcing fluxes are available to drive the ocean model. Surface forcing fields derived from global NWP model analysis are produced four times daily at the UKMO.

Both thermodynamic and sea-ice processes are modelled in FOAM. The thermodynamic scheme is based upon the models of Semtner (1976) and for lead processes, Hibler (1979). The dynamic component is a simple advection scheme based on Bryan (1975), in which the ice thickness is advected with the top model level ocean currents.

The data assimilation scheme used in FOAM was originally developed to assimilate thermal profile and SST observations, it has been subsequently enhanced to assimilate salinity observations and measurements from satellite radar altimeters. SST and sub-surface thermal profile observations are received in near real-time over the Global Telecommunications System (GTS) (Bell et al., 2000). The majority of the thermal profiles used are measured by expendable bathythermographs (XBTs) from the Volunteer Observing Ship (VOS) program, data from Argo profiling floats, and the thermistor chains from the TOGA-TAO and PIRATA moored buoy arrays in the tropical Pacific

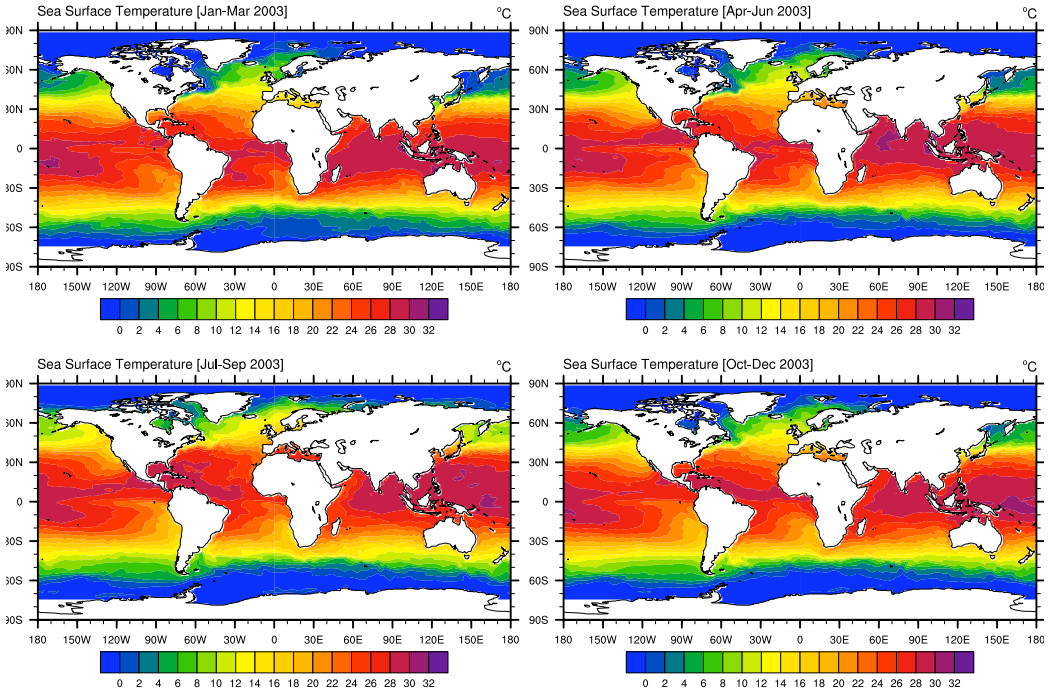

FIGURE 3.6: Seasonal average sea surface temperature (°C) from FOAM-HadOCC for 2003.

and Atlantic respectively. Thermal observations are generally confined to the top 800 m and are concentrated along shipping lanes and mooring lines in the tropics.

In comparison, the surface ocean temperature is relatively well observed from both in situ and satellite observing platforms. The SST data used by FOAM includes observations from ships, moored and drifting buoys and coarse resolution (2.5°) data from the AVHRR radiometers on board the polar orbiting NOAA satellites. In addition, sea-ice concentration fields supplied by the Canadian Met. Centre (CMC) on a daily basis are also assimilated. These fields are based on SSM/I (special sensor microwave imager) data. Figure 3.6 shows seasonal average SST for a model run conducted over 2003.

The observations assimilated are subject to automated quality control processes and is based on comparison with a 'background field', which may be either climatology or an earlier analysis. The data assimilation component of FOAM is based on the iterative analysis correction method of Lorenc et al. (1991). The technique is essentially a modified successive correction scheme which approximates Optimum Interpolation (OI). Both the quality control and implementation of the assimilation scheme are described in detail by Bell et al. (2000).

3.6.2 Hadley Centre Ocean Carbon Cycle Model

Representing the global carbon cycle in a computer model is a complex task. The chemical reactions of carbon dioxide in the surface waters need to be represented to provide a good estimate of the air-sea flux of CO_2. There are also several mechanisms for the CO_2 entering at the surface to reach deep ocean waters. The physics of the ocean needs to be well represented in the model to capture the solubility pump. Ocean biology needs to be included in the model to capture the biological pump, including the carbonate pump.

The Hadley Centre Ocean Carbon Cycle (HadOCC) model has been developed for use in global ocean carbon cycle modelling. It is implemented as part of the Unified Model ocean submodel. HadOCC simulates the essential aspects of carbonate chemistry and biological production and export. These are dissolved inorganic carbon (DIC), total alkalinity (A_T), a nitrogenous nutrient, phytoplankton, zooplankton and sinking detritus. Radioactive ^{14}C is also included in the model. Its implementation is dependent on the air-sea gas exchange of CO_2.

The HadOCC model can be divided conceptually into separate inorganic and biological parts. The inorganic chemistry and partial pressure physics are well understood and can be reproduced with fair accuracy even in simple carbon cycle models where assumptions are made about the concentrations of minor ionic species. The surface temperatures and salinities that control the CO_2 solubility can be prescribed or modelled. Given the surface concentration of DIC, the model is then limited by the accuracy and detail of the ocean circulation.

The export of biologically generated organic matter and carbonate to the deep ocean, collectively known as the biological pump, is much more difficult to model accurately. The HadOCC ecosystem model and its primary production, the total uptake of carbon by phytoplankton during growth, are described in Palmer and Totterdell (2001). The modelled primary production is shown to be largely consistent with that observed, however it is not total primary production that is the key biological driving field for an ocean carbon cycle model. Nutrients can be cycled through the food web many times before being lost to the deep ocean, and it is the final export of carbon and nutrients to deeper water, largely as a sinking particle flux, that determines the cycling of carbon and nutrients on timescales of decades to centuries.

Oceanic fugacity of CO_2

The fugacity of CO_2 in the surface waters is a requirement in the air-sea flux calculation. As mentioned previously, fugacity is dependent on the concentration of dissolved $CO_{2(aq)}$. In order to determine its concentration in the model, a number of equations representing chemical reactions of the seawater acid-base system must be solved.

Carbon dioxide dissolved in water $CO_{2(aq)}$ quickly produces carbonic acid, H_2CO_3. Since it is difficult to distinguish between $CO_{2(aq)}$ and H_2CO_3 the two species are considered together as CO^*_{2aq}. The reactions which take place when carbon dioxide dissolves in water can then be written as:

$$CO^*_{2(aq)} \rightleftharpoons H^+ + HCO_3^-$$
$$HCO_3^- \rightleftharpoons H^+ + CO_3^{2-}$$

Carbonic acid loses protons H^+ to produce the hydrogen carbonate HCO_3^- and then the carbonate CO_3^{2-} ion. The three species together are referred to as dissolved inorganic carbon (DIC), which we also write as C_T:

$$C_T = CO_2^* + HCO_3^- + CO_3^{2-}$$

The thermodynamic balance between these three species is governed by the reaction rates, which are dependent on temperature, composition of water, and on the concentrations of the species involved. Because the timescales for the reactions are a few minutes or less, the system can be written in terms of chemical equilibria with constants K_0, K_1 and K_2:

$$K_0 = [CO_2^*]/fCO_2$$
$$K_1 = [H^+][HCO_3^-]/[CO_2^*]$$
$$K_2 = [H^+][CO_3^{2-}]/[HCO_3^-]$$

fCO_2 is the fugacity of carbon dioxide in the gas phase and the brackets represent total stoichiometric concentrations of the chemical species enclosed. The equilibrium constants are functions of temperature, composition (particularly salinity) and pressure of the seawater. Expressions for these constants can be found in DOE (1994). Many air-sea gas transfer expressions require the partial pressure of the gas, which is defined as the mole fraction multiplied by the total pressure of the gas phase. Fugacity is a 'corrected' partial pressure which accounts for the non-ideal nature of the gas phase. The ratio of the fugacity to partial pressure of CO_2 under typical oceanic conditions is approximately 0.995–0.997 μatm.

To solve for $[CO_2^*]$, and hence the fugacity of CO_2, we need to solve the entire seawater acid-base system to determine $[H^+]$. This can be done if the concentration of all significant weak acid-base pairs and their equilibrium constants are known, as well as the total alkalinity A_T. This is defined as the number of moles of hydrogen ions equivalent to the excess of bases formed from weak acids under certain constraints (Dixon, 1981). In a simple carbon cycle model the alkalinity is prescribed as a constant or as a linear function of salinity. In the HadOCC model the plankton uptake of NO_3^- raises the alkalinity through release of OH^-, whereas uptake of CO_3^2- for shell building lowers the alkalinity.

The state variables of the carbonate system in the HadOCC model are total inorganic carbon and total alkalinity. They are stored as oceanic tracers in units of μmoles/litre and μeqs/litre (eqs=equivalents). The units are 'per litre' and not 'per kg' because the ocean model conserves volume but not mass.

Air-sea gas exchange

As we know from previous chapters the air-sea exchange of CO_2 is usually expressed as a gas transfer coefficient $k\alpha$. In the HadOCC model the flux is expressed simply as the gas transfer coefficient multiplied by the air-sea partial pressure difference:

$$F = k\alpha(pCO_{2w} - pCO_{2a}) \tag{3.5}$$

The HadOCC model uses the value of $\alpha = K_0$ described in the previous section for the solubility. The expression used does not account for the small difference between fugacity and partial pressure as it is assumed that the errors introduced will be small ($\leq 1\%$).

The gas transfer velocity k in HadOCC is represented by two simple wind-speed dependent parameterizations. The Liss and Merlivat (1986) and both the instantaneous and long-term averaged versions of the Wanninkhof (1992) parameterizations are available. However, when the ocean sub-model is run by itself wind speed u_{10} is not available, and HadOCC must calculate it from the wind mixing energy w using the following expression:

$$u_{10} = \frac{\rho_w^{1/6} w^{1/3}}{C_D^{1/2} \rho_a^{1/3}} \tag{3.6}$$

where $\rho_w = 1026.0$ kg m^{-3} is a typical density of sea water, $\rho_a = 1.2$ kg m^{-3} is a typical density for air, and $C_D = 0.003$ is a typical drag coefficient. An example of the seasonal average wind mixing energy for 2003 can be seen in figure 3.7.

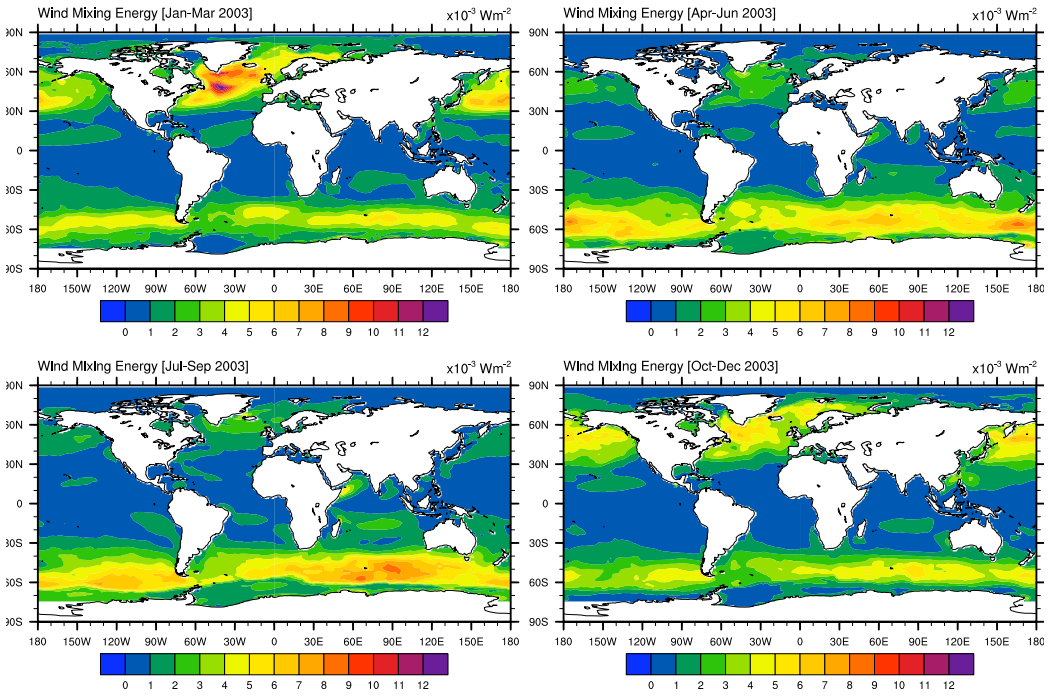

FIGURE 3.7: Seasonal average wind mixing energy (W m^{-2}) from FOAM-HadOCC for 2003.

Ecosystem model

To represent the ocean biology in the model, the biological system is greatly simplified and is represented by a single class of phytoplankton, a single class of zooplankton, detritus (the particulate waste products from the biology) and (nitrogenous) nutrient. Phytoplankton require sunlight and nutrients to grow. Zooplankton prey on phytoplankton and in turn are prey themselves, which is represented by a mortality loss for the zooplankton. Waste products and dead material form detritus, which breaks down back to nutrient (Palmer and Totterdell, 2001).

The HadOCC ecosystem model calculates the flow of nitrogen between four model compartments; nutrient, phytoplankton, zooplankton and detritus (N, P, Z, D). The flows of carbon within the system are coupled to the flows of nitrogen by fixed carbon:nitrogen ratios C_p, C_z and C_d, but these have no effect on the ecosystem because growth is not carbon limited. An average 'Redfield' carbon:nitrogen ratio, C_r, is used in the calculation of biomass equivalent for zooplankton grazing. A schematic showing the links between the four model compartments is shown in figure 3.8.

The Eulerian equation for the rate of change of any of the ecosystem components T_i can be written as

$$\frac{dT_i}{dt} = \text{advection} + \text{diffusion} + \text{mixing} + \text{sinking} + \text{biology} \tag{3.7}$$

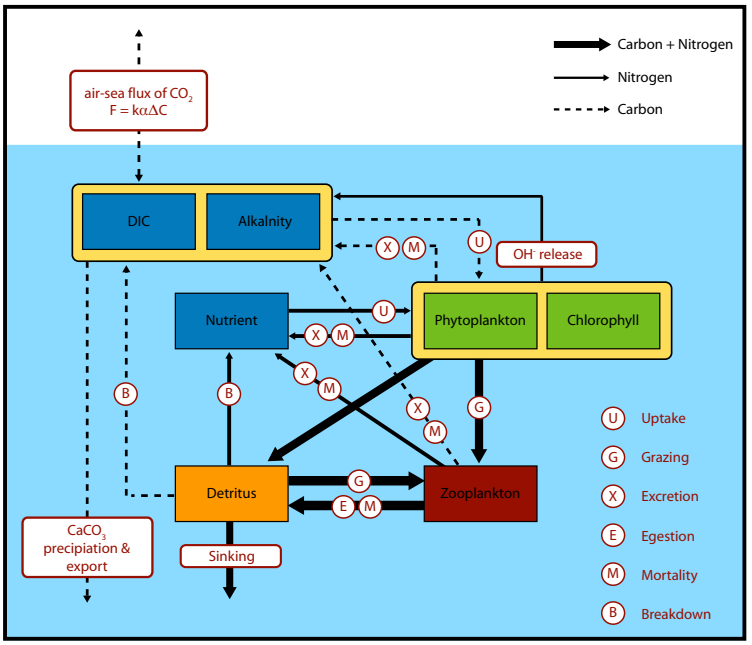

FIGURE 3.8: Schematic showing the Hadley Ocean Carbon Cycle model; a NPZD model embedded within FOAM.

The advection, diffusion and mixing terms include all physical transport processes of a tracer in the ocean sub-model. The sinking term is zero except for detritus which sink at a speed of 10 m day^{-1}.

The biological terms for each of the four ecosystem compartments (N, P, Z, D) are described as follows;

$$\left.\frac{\partial P}{\partial t}\right|_{biology} = RP - G_p - m_0 P^2 - \eta P \tag{3.8}$$

$$\left.\frac{\partial Z}{\partial t}\right|_{biology} = \beta_p G_p + \beta_z G_z - \mu_1 Z - \mu_2 Z^2 \tag{3.9}$$

$$\left.\frac{\partial D}{\partial t}\right|_{biology} = \frac{C_p}{C_d} m_o P + \frac{1}{3}\mu_1 Z + \frac{1}{3}\mu_2 Z^2 + (1-\beta_p)G_p + (1-\beta_z)G_z - \psi D - G_z \tag{3.10}$$

$$\left.\frac{\partial N}{\partial t}\right|_{biology} = -RP + \psi D + \frac{2}{3}\mu_1 Z + \frac{2}{3}\mu_2 Z^2 + \left\{\frac{C_d - C_p}{C_d}\right\} m_0 P + \eta P \tag{3.11}$$

where R is the specific growth rate of phytoplankton, P (see equation 3.8), and is controlled by light and nutrient limitation (Palmer and Totterdell, 2001). Loss mechanisms for the phytoplankton population include respiration with a constant specific rate, η, grazing by zooplankton, G_p and mortality with a rate $m_0 P^2$ that is quadratic in P to represent stress by overpopulation. Mortality is reduced to zero if the phytoplankton

population falls below a concentration of 0.01 μmoles/litre. The mortality flow of nitrogen to detritus is limited by the higher carbon content of the detritus. Mortality nitrogen that is left over goes into dissolved nutrient.

Zooplankton, Z (see equation 3.9), graze on phytoplankton and detritus. The rate of grazing of zooplankton on phytoplankton is based not on nitrogen content of P and D but on the biomass equivalents. The loss of phytoplankton and detritus due to grazing in nitrogen units is G_p and G_d respectively. The assimilation efficiencies of phytoplankton and detritus β_p and β_d account for messy feeding. As much of the unassimilated material as possible is egested as detritus, any surplus carbon immediately becomes dissolved inorganic carbon. Zooplankton mortality represents grazing by higher order predators as well as death by natural causes. It is modelled as the sum of density independent and dependent terms, with coefficients μ_1 and μ_2. The density dependent term is justified by the observed behavior of high grazers, which tend to aggregate where food is plentiful, and acts to increase winter survival rates at high latitudes. Two thirds of the zooplankton mortality flux is immediately re-mineralized to nutrient and dissolved organic carbon, representing material travelling up the food chain and being excreted at each stage. The remainder is egested as detritus.

The detritus, D (see equation 3.10), compartment comprises a combination of dead phytoplankton and zooplankton and egested fecal pellets. It is recycled through zooplankton grazing and remineralisation, which is largely mediated by bacteria. Remineralisation is specified by a constant rate, ψ. At depths down to 240 m a remineralisation rate of 0.05 day^{-1} is used. Below the euphotic zone where grazing rates are small, the constant sinking rate of 10 m day^{-1} and constant remineralisation rate of 0.02 day^{-1} imply a detritus density which falls away exponentially with a depth scale of 500 m. Ocean circulation subsequently brings this exported nutrient back to the photic zone. Note that the nutrient, N, equation 3.11 includes sources and sinks deriving from the N, P and Z equations.

In addition to the N, P, Z, D biological components, there are two components representing carbon in the ocean. These are dissolved inorganic carbon (DIC) and alkalinity (A_T). The dissolved inorganic carbon is taken up by phytoplankton growth and returned with biological breakdown. The amount of carbon in the forms of dissolved inorganic carbon and in the four biological components is kept track of in the model. Alkalinity is required to calculate the proportion of dissolved inorganic carbon that is in the form of CO_2 in the surface waters, in order to calculate the air-sea flux of CO_2. Alkalinity is treated in a similar fashion to dissolved inorganic carbon with its concentration changed by biological processes. DIC and A_T are represented in the system by the following equations:

$$\left.\frac{\partial(DIC)}{\partial t}\right|_{biology} = (mC_p - m_D C_d)P^2 + (C_z - \frac{C_d}{3})(\mu_1 Z + \mu_2 Z^2) + (C_p G_p + C_d G_d - C_z G_z - C_d E_D) + \eta C_p P + \psi C_d D - RC_p P - \gamma_c RC_p P + D_{cc} \tag{3.12}$$

and

$$\left.\frac{\partial A_T}{\partial t}\right|_{biology} = -\left.\frac{\partial N}{\partial t}\right|_{biology} - 2\gamma_c RC_p P + 2D_{cc} \tag{3.13}$$

where total alkalinity is defined as :

$$A_T = [HCO_3^-] + 2[CO_3^{2-}] + [B(OH)_4^-] + [OH^-] - [H^+]$$

Carbon is not limiting in phytoplankton growth and has no influence on the nitrogen cycling of the ecosystem model. Carbon is carried with nitrogen in the various ecosystem processes according to the C:N ratios of the constituents. Most of the terms in the DIC equation are equivalent to terms in the nutrient equation. There are two additional terms which account for the formation of carbonate shells by plankton in surface waters and their subsequent remineralisation at depth. The first is the rate of formation of carbonate, which is assumed to be a fraction γ_c of the total plankton growth. Carbonate is assumed to re-dissolve evenly throughout the water column below 1500 m depth. The modelled sinking flux and remineralisation is instantaneous, unlike the sinking flux of detritus which is modelled explicitly. Carbonate dissolution is represented by the following term D_{cc}:

$$D_{cc} = \begin{cases} 0 & \text{for layer-depth} \leq 1500\,\text{m}, \\ \frac{\gamma_c C_p}{D_{ocean} - 1500} I(RP) & \text{otherwise} \end{cases} \tag{3.14}$$

The depth integral of phytoplankton growth is I(RP). The rate of dissolution depends on the depth of the water column D_{ocean}. Where the ocean is shallower than 1500 m the carbonate pump is inactive. The precipitation of one mole of carbonate removes two moles of alkalinity from the water because CO_3^{2-} is a divalent base. This alkalinity is released at depth with the associated carbon. Alkalinity is also modified by the uptake of nutrient, as OH^- is observed to be released during nitrate uptake. Thus the alkalinity equation includes the full nutrient time derivative.

Chapter 4

1-d model development

The results from early model testing and development are presented in this chapter. GOTM is setup in order to recreate near surface temperature structure and evolution over the course of a day in the tropical Atlantic. Model output is compared with in situ observations from the PIRATA mooring located at 10°S10°W, and previous studies. This initial testing forms the basis for the subsequently published research articles contained in the later chapters.

4.1 Model setup

An exponential vertical grid containing 601 levels over 260 m was used in order to achieve high resolution (sub-millimetre) near the air-sea interface, and to reduce the possibility of numerical instabilities caused by grid size. The time step of the model was set to 30 seconds, with the model output being written to a 'Netcdf' file every hour. The model was run over the course of a whole year, with a model start date of 1/1/2002 00:00:00, finishing on 12/31/2002 23:00:00. In addition, selected 24 hour model runs were also conducted, which start at 03:00 in order to investigate the diurnal cycle of SST.

Version 3.2 of GOTM was used, although, the default model setup was substantially altered over the course of this study. However in this early testing stage many of the default settings and parameterizations are used. The 'airsea' module was modified to output the individual fluxes of longwave, latent, and sensible heat, so that the heat budget could be investigated.

The model is run with no assimilation (relaxation) of independent observations, it is merely forced with initial conditions of temperature and salinity profiles from the buoy

at 10°S10°W. The particular location was chosen based on availability of in situ data (see figure 3.3) and additional data needed for calculation of heat fluxes (see figure 3.4).

The turbulence method used is that of a two-equation model, calculating turbulent kinetic energy (TKE) and length scale. The TKE method is that of the dynamic equation (k_e-epsilon style), the length scale is that of the dynamic dissipation rate equation, and uses constant stability functions.

4.1.1 Calculation of surface fluxes

Surface fluxes in the air-sea module of GOTM are calculated by means of bulk formulae, with solar radiation being calculated from time, latitude and cloud coverage. Data sources are described in sections 3.3 and 3.4. We use the following convention: heat fluxes into the ocean are positive.

The latent and sensible heat flux, the longwave back radiation and surface momentum flux are calculated based on the exchange coefficients c_{dd}, c_{ed} and c_{hd}, which are derived from the model sea surface temperature, the wind vector at 10 m height, the air pressure at 2 m, the air temperature and the air pressure at 2 m , and the relative humidity according to Kondo (1975):

$$\begin{aligned} \tau_x^s &= c_{dd}\rho_a u_x u_{10} \\ \tau_y^s &= c_{dd}\rho_a u_y u_{10} \\ Q_e &= c_{ed}L\rho_a u_{10}(q_s - q_a) \\ Q_h &= c_{hd}C_{pa}\rho_a u_{10}(T_w - T_a) \end{aligned} \tag{4.1}$$

with the air density ρ_a, the wind speed at 10 m, u_{10}, the x and y component of the wind velocity vector, u_x and u_y respectively, the specific evaporation heat of sea water, L, the specific saturation humidity, q_s, the actual specific humidity, q_a, the sea surface temperature, T_w and the dry air temperature, T_a.

For the longwave back radiation, the formulae of Clark et al. (1974) is used:

$$Q_l^{\uparrow} = \xi\sigma_{SB}T_w^4(0.39 - 0.05e^{1/2})(1 - \lambda_n n^2) + 4\xi\sigma_{SB}T_w^3(T_w - T_a) \tag{4.2}$$

where e is the vapor pressure, n is the fractional cloud cover, ξ is the emissivity of the sea surface, taken to be 0.98, σ_{SB} is the Stefan-Boltzman constant (5.67×10^{-8} W m^{-2} K^{-4}), and λ_n is a latitude dependent cloud cover coefficient. The assumption is made that the fractional cloud cover n derived from satellite is comparable to that of a marine observer.

The net shortwave radiation is calculated based on latitude, longitude, time, fractional cloud cover and albedo. The monthly values of albedo are taken from Payne (1972). The basic formula for the short wave radiation at the surface, Q_s, has been taken from Rosati and Miyakoda (1988); Simpson and Paulson (1999):

$$Q_s = Q_{cs}(1 - 0.62n + 0.0019\theta)(1 - a) \tag{4.3}$$

with the total radiation reaching the surface under clear skies, Q_{cs}, the solar noon altitude, θ, fractional cloud cover n, and the albedo, a.

4.1.2 The turbulence model

The particular choice of turbulence model employed is a two-equation $k_e - \epsilon$ type model based on Rodi (1987);

The transport equation for turbulent kinetic energy, k_e can be written as:

$$\frac{\partial k_e}{\partial t} - \frac{\partial}{\partial z}\left(\frac{v_t}{\sigma_k}\frac{\partial k_e}{\partial z}\right) = P_k + G_k - \epsilon \tag{4.4}$$

where P_k and G_k are the production of k_e by mean shear and buoyancy, respectively, and ϵ the rate of dissipation of TKE.

$$P_k = v_t\left[\left(\frac{\partial u}{\partial z}\right)^2 + \left(\frac{\partial v}{\partial z}\right)^2\right], \quad G_k = -\frac{v_t}{\sigma_t}N_v^2 \tag{4.5}$$

where v_t is the turbulent friction coefficient, u and v components of velocity and N_v the Brunt-Vaisala frequency.

For horizontally homogenous flows, the sum of the viscous and turbulent transport terms $\mathcal{D}$ can be expressed by a simple gradient formulation:

$$\mathcal{D} = \frac{\partial}{\partial z}\left(\frac{v_t}{\sigma_\epsilon}\frac{\partial \epsilon}{\partial z}\right) \tag{4.6}$$

where σ_ϵ is the constant Schmidt-number for ϵ.

The rate of dissipation is balanced to:

$$\frac{\partial \epsilon}{\partial t} = \mathcal{D}_\epsilon + \frac{\epsilon}{k_e}(c_{\epsilon 1}P + c_{\epsilon 3}G - c_{\epsilon 2}\epsilon) \tag{4.7}$$

The rate of dissipation ϵ, can be obtained either directly from its parameterized transport equation or from any other model yielding an appropriate dissipative length scale, l. Then, ϵ becomes

$$\epsilon = \left(c_\mu^0\right)^3 \frac{k_e^{\frac{3}{2}}}{l} \tag{4.8}$$

The model constants are summarized in table 4.1.

	c_μ^0	σ_k	σ_ϵ	$c_{\epsilon 1}$	$c_{\epsilon 2}$	$c_{\epsilon 3}$
Rodi (1987)	0.5577	1.0	1.3	1.44	1.92	0.0

TABLE 4.1: Constants appearing in equations 4.7 and 4.8

4.1.3 The temperature equation

The model calculates temperature such that

$$\frac{\partial \Theta}{\partial z} = \mathcal{D}_\Theta - \frac{1}{\tau_R^\Theta}(\Theta - \Theta_{obs}) + \frac{1}{C_p \rho_0}\frac{\partial I}{\partial z} \tag{4.9}$$

where Θ is the mean potential temperature, and $\mathcal{D}_\Theta$ is the sum of the turbulent and viscous transport terms modelled according to:

$$\mathcal{D}_\Theta = \frac{\partial}{\partial z}\left((v_t^\Theta + v^\Theta)\frac{\partial \Theta}{\partial z} - \tilde{\Gamma}_\Theta\right) \tag{4.10}$$

In this equation, v_t^Θ and v^Θ are the turbulent and molecular diffusivities of heat, respectively, and $\tilde{\Gamma}_\Theta$ denotes the non-local flux of heat. Relaxation with the timescale τ_R^Θ towards a prescribed profile Θ_{obs}, changing in time, is possible.

The sum of latent, sensible, and longwave radiation is treated as a boundary condition. Solar radiation is treated as an inner source, $I(z)$. It is computed according to the exponential law (Paulson and Simpson, 1977):

$$I(z) = I_0\left(Re^{-\eta 1 z} + (1-R)e^{-\eta 2 z}\right) \tag{4.11}$$

The absorption coefficients $\eta 1$ and $\eta 2$ depend on the water type and are prescribed either by specifying a Jerlov (1968) class or by reading in an extinction file. In this case the Jerlov (1968) class has been set to type 1 (see table 4.2). There are six types I, 1, IA, IB, II and III ranging from clear to increasingly opaque water.

		R	$\eta 1$ (m)	$\eta 2$ (m)
Jerlov (1968)	-Type I	0.58	0.35	23
	-Type 1 (upper 50m)	0.68	1.2	28
	-Type IA	0.62	0.60	20
	-Type IB	0.67	1.0	17
	-Type II	0.77	1.5	14
	-Type III	0.78	1.4	7.9

TABLE 4.2: Jerlov (1968) defined water types, coefficients for equation 4.11.

4.2 Investigating the heat budget

As described in section 2.1.1, the net heat flux, Q_{net} (see equation 2.1) can be expressed as the sum of the individual heat budget terms, e.g. the latent heat, sensible heat, net longwave radiation and shortwave solar radtiation. Whilst these terms are calculated within GOTM, they were not part of the model's default output, thus the relevant source-code was modified to include these fluxes.

Using the calculated surface fluxes (see section 4.1.1) from GOTM, a heat budget was derived for the PIRATA mooring location 10°S10°W during 2002. One of the reasons this particular site is chosen is that advection is less important (see section 2.1.1) compared to other PIRATA sites, such as those on the western side of the basin (Foltz et al., 2003).

Accurately modelling the surface heat budget is important for recreating the near surface temperatures in the model. This work is ultimately concerned with accurately describing the diurnal temperature variation, e.g. the skin-bulk temperature difference, ΔT. These temperature variations are important for gas exchange mainly through its dependence on solubility, α, but also, in part, because of the change in mass via the carbonate reaction (Fairall et al., 2003), and subsequently due to the effects of buoyancy on turbulence and the gas transfer velocity.

In addition to the model simulations over the diurnal cycle, a model run is also conducted over the whole of 2002, without assimilation or relaxation to observed data. Model output is compared with the PIRATA observations for that year and the previous study by (Foltz et al., 2003).

In order to investigate the effect of the diurnal cycle, case studies are compared. These are based on the following two situations:

1. A 'convective' case, where wind speed is < 7 m s^{-1} and the cloud fraction is < 0.7.

2. A 'non-convective' case, where wind speed is > 7 m s^{-1} and the cloud fraction is > 0.7.

It is important to understand the flow of heat in the upper mixed layer over the diurnal cycle. Energy is supplied to the system by both the incoming solar radiation and via wind driven mixing. By looking at the convective transport and flux of solar radiation we can infer the distribution of heating throughout the upper water column.

The flux of solar radiation is defined by equation 4.11 (see Paulson and Simpson (1977)), and is positive as it serves to warm the water column.

The convective transport, Q_c, is defined as:

$$Q_c = k_D \frac{\partial T}{\partial z} \rho_w C_p \tag{4.12}$$

where k_D is the sum of the turbulent and molecular diffusivities, T is the temperature, ρ_w is the density of the seawater and C_p is the specific heat capacity. Q_c can be positive or negative depending on the circumstances e.g. positive during nighttime heating at depth after diurnal warming.

The net effect of the penetrative solar radiation term and the convective transport term can be evaluated by looking at the rate of energy flux, $\frac{\partial R}{\partial z}$, such that:

$$\frac{\partial R}{\partial z} = \left(-\frac{\partial Q_c}{\partial z}\right) + \left(-\frac{\partial I}{\partial z}\right) \tag{4.13}$$

and is related to the temperature, T, via the expression:

$$-\frac{\partial R}{\partial z} = \rho_w C_p \frac{\partial T}{\partial t} \tag{4.14}$$

For both categories defined above, profiles of total diffusivity ($m^2\ s^{-1}$), penetrative solar radiation ($W\ m^{-2}$), convective transport ($W\ m^{-2}$), rate of total energy flux ($W\ m^{-3}$), and temperature (°C) are compared. In addition, sea surface temperature (°C) at 1 m, wind speed ($m\ s^{-1}$), cloud fraction and mixed layer depth (m) are examined over the diurnal cycle.

4.3 Uncertainty and error

In order to ascertain the significance of the modelled results, it is assumed that the in situ observations are true to reality, or rather that they are close enough to meet the objectives. That is, they can provide validation of the model SST over a diurnal cycle. A number of statistical quantities are used in order to estimate the significance of the modelled results. In these, the observed variable is defined as the model output, and the expected value as that of the in situ PIRATA data.

4.3.1 Root mean square error

The mean square error of an observed variable is defined as the average squared distance of an observed variable, d_{obs} from the true value, d_{exp}:

$$MSE = \frac{1}{N}\Sigma_{i=1}^{N}\left(d_{obs}^{i} - d_{exp}^{i}\right)^{2} \tag{4.15}$$

where N is the number of observations, and $d_{obs}^{i} - d_{exp}^{i}$ is the difference between the *ith* observed and expected results.

The square root of the mean square error, MSE, is called the 'root mean square error' or $RMSE$. It has the same units as the observed variable.

4.3.2 Correlation coefficient

The correlation coefficient measures how strong a linear relationship exists between two variables. To define the correlation coefficient, first consider the sum of squared values s_{xx}, s_{yy}, and s_{xy} and a set of n data points (x_i, y_i) about their respective means:

$$S_{xx} = \Sigma(x_i - \bar{x})^2 \tag{4.16}$$

$$S_{yy} = \Sigma(y_i - \bar{y})^2 \tag{4.17}$$

$$S_{xy} = \Sigma(x_i - \bar{x})(y_i - \bar{y}) \tag{4.18}$$

The correlation coefficient, R^2 is defined by:

$$R^2 = \left(\frac{ss_{xy}}{ss_{xx}ss_{yy}}\right)^2 \tag{4.19}$$

R^2 is the fraction of the total squared error that is explained by the model. The correlation coefficient gives us a measure of the reliability of the linear relationship between the model and the observations. Values close to 1 indicate excellent linear reliability, although this does not account for any offset/calibration factors. In which case, RMSE may be more reliable.

4.3.3 Residuals

The residual of a particular model parameter is defined as the difference between the observed value and the expected value (or the model value and the validation data). If the model values were to perfectly fit the validation data then the residual at each time-step of the model would be equal to zero. By looking at the residuals over time, under similar conditions, i.e. during convective and non-convective days, it is possible to identify if the residuals are distributed randomly or if there is any systematic deviation in the model output compared to the validation data.

4.4 Results and discussion

The majority of the results presented in this chapter illustrate modelling of near surface temperature and heat fluxes. Before gas exchange can be estimated it is necessary to have accurate profiles of temperature near the surface. Comparison is made between the modelled output and that of the available data from the PIRATA array, in order to gauge the skill of the model. Thus, we make the assumption that the PIRATA data are themselves unbiased.

The temperature profiles are created using the surface heat fluxes calculated within GOTM's 'airsea' subroutine. The surface fluxes themselves are forced by the in situ and additional data described in section 3.3 and 3.4. The accuracy and precision of the forcing data is ultimately important for considering errors on our calculated air-sea flux of CO_2.

4.4.1 Case studies

Given the objectives in section 1.4, accurately modelling near surface temperature over the diurnal cycle during both convective and non-convective conditions is crucial. A number of convective and non-convective cases were selected based on examination of the PIRATA wind speed and Meteosat cloud fraction. The statistics of the model output errors for the convective days can be seen in table 4.3 and for the non-convective days in table 4.4.

Looking at table 4.3, it is immediately apparent that the model simulated SST's are all very highly correlated with the observed SST data from the PIRATA array, with R^2 values above 0.9, and RMSE of less than 0.17 °C.

Similarly, table 4.4 shows the statistics for a selection of non-convective cases. As with the convective cases, the RMS errors are very low. The greatest RMSE occurs on the 8-Sep-2002 and is 0.126 °C. In comparison, SST's for the non-convective days are not

Dates	RMSE	R^2
27^{th}-Jan-2002	0.0866	0.9860
25^{th}-Feb-2002	0.1617	0.9871
17^{th}-Apr-2002	0.1093	0.9754
21^{st}-Sep-2002	0.1315	0.7851
28^{th}-Feb-2002	0.0526	0.9589
15^{th}-Jul-2002	0.0673	0.8433

TABLE 4.3: SST statistics for selected days (3am–3am) deemed to be convective (windspeed < 7 ms^{-1} and cloud cover < 0.7).

Dates	RMSE	R^2
10^{th}-Jan-2002	0.0628	0.7141
2^{nd}-Feb-2002	0.0800	0.3351
8^{th}-Apr-2002	0.0924	0.6585
22^{nd}-Apr-2002	0.1117	0.8813
28^{th}-Jul-2002	0.0492	0.4784
8^{th}-Sep-2002	0.1264	0.4803

TABLE 4.4: SST statistics for selected days (3am–3am) deemed to be non convective (windspeed > 7 m s^{-1} and cloud cover > 0.7).

as well correlated with results as the convective days. This is likely due to the fact that during the non-convective conditions, turbulent energy transfer (i.e. wind driven mixing) causes increased error in GOTM's turbulence module. It is also the case that since temperature variations are small, measurement errors are more significant. Based on this information one convective and one non-convective case were selected for more detailed investigation of the near surface profiles of temperature, heat fluxes and the flow of heat. The comparison of the model SST_{1m} with the PIRATA data can be seen in figure 4.1.

The purpose of modeling the near surface temperature structure, through the calculation of surface fluxes, is to estimate the skin-bulk temperature difference, ΔT. Figure 4.1 also shows the ΔT for both the selected convective and non-convective case studies. It is clear that during the non-convective case ΔT is small, due to the increased turbulence preventing the formation of warm layers. During the convective case ΔT peaks around 15:00 at 0.6 °C. The implication of the diurnal warm layer on estimating the flux of CO_2 is through the dependance of solubility on temperature. For CO_2 source regions, such as the tropical Atlantic, it is expected that during convective conditions, the formation of warm layers will tend to increase the flux of CO_2.

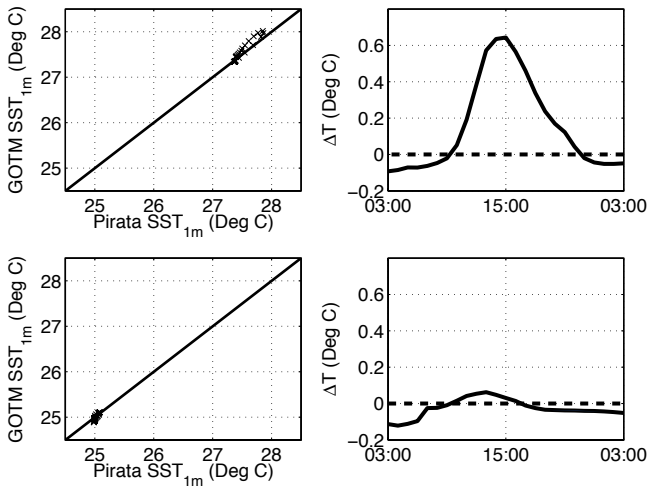

FIGURE 4.1: Left side: Model SST (°C) versus observations for PIRATA mooring location 10°S10°W. Right side: PIRATA ΔT (°C). Top: Convective case. Bottom: Non-convective case. Dashed line represents 0 °C.

4.4.2 Convective case — 17^{th}-Apr-2002

Profiles of molecular and turbulent diffusivity are plotted every 2 hours from 3 am to 1 am the following day (see figure 4.2). The profiles show the top 10 m of the water column. Below the mixed layer turbulent diffusion is suppressed, and the molecular diffusion which remains is very small in comparison. Since this is a convective case, the particular day was selected based on low wind speed, the turbulent energy transfered into the water column is appropriately small. During the period between 10:00 and 19:00 the diffusivity is virtually zero.

Convective transport (figure 4.3), as defined in section 4.2, acts in the opposite direction to the penetrative solar radiative flux (figure 4.4) which serves to warm the water column. Due to its dependance on molecular and turbulent diffusivity there is little effect during the day time, which increases from 19:00 to 03:00. The diurnal cycle of penetrative solar radiation is shown in figure 4.4. Naturally, between 03:00 and dawn the incident solar radiation is zero. During the daylight hours there is a flux of energy into the water column which follows an exponential curve, with a large proportion of the energy being absorbed in the top 1m.

The combination of the penetrative solar heating and the conductive heating can be seen in figure 4.5. This figure shows the rate of the total heat transport, expressed in W m^{-3}. Most important is the time period between 07:00 and 01:00 the following morning, we can see that initially, before the sun comes up, the near surface is cooling, as represented by negative values. Looking at 09:00 we can see that the profile is almost reversed with some warming below 2 m. Between 11:00 and 17:00 the surface steadily warms, after 19:00 when the sun goes down, cooling begins to occur again at the surface, however

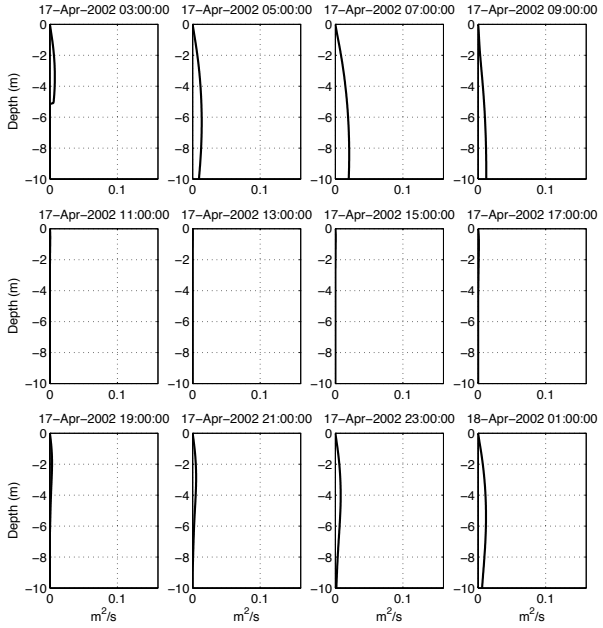

FIGURE 4.2: Diurnal cycle of molecular and turbulent diffusivity ($m^2\ s^{-1}$) versus depth (m) during a convective case (wind speed < 7 m s^{-1} and cloud fraction < 0.7) for PIRATA mooring location 10°S10°W.

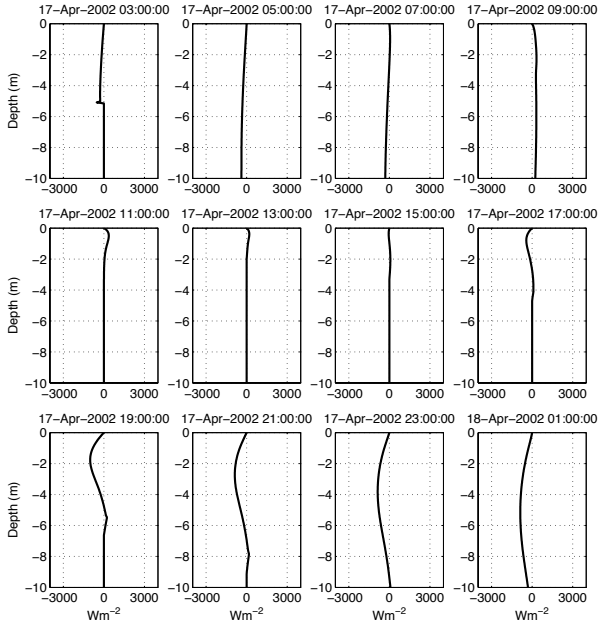

FIGURE 4.3: Diurnal cycle of convective transport (W m^{-2}) versus depth (m) during a convective case (wind speed < 7 m s^{-1} and cloud fraction < 0.7) for PIRATA mooring location 10°S10°W.

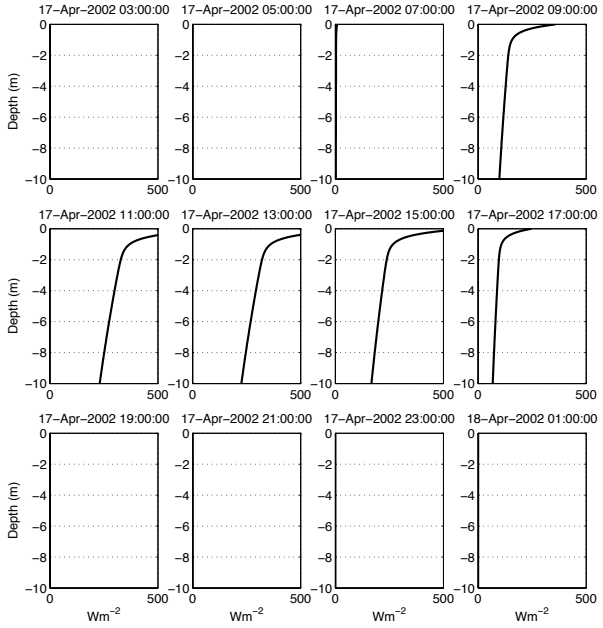

FIGURE 4.4: Diurnal cycle of penetrative solar heating (W m^{-2}) versus depth (m) during a convective case (wind speed < 7 m s^{-1} and cloud fraction < 0.7) for PIRATA mooring location 10°S10°W.

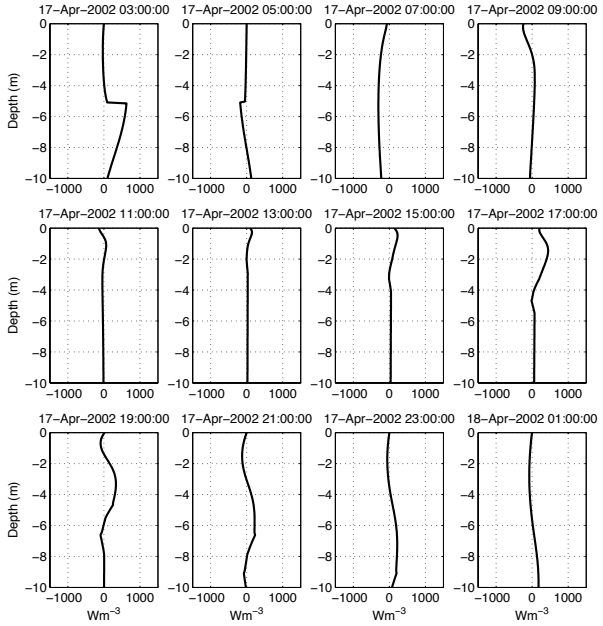

FIGURE 4.5: Diurnal cycle of total heating rate (W m^{-3}) versus depth (m) during a convective case (wind speed < 7 m s^{-1} and cloud fraction < 0.7) for PIRATA mooring location 10°S10°W.

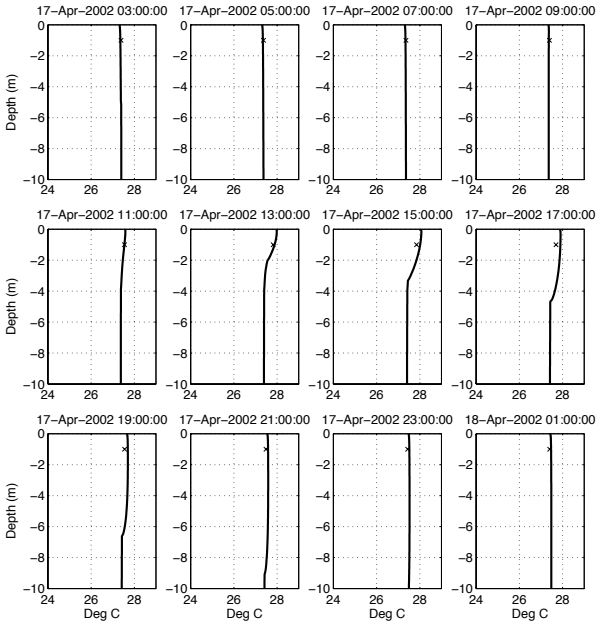

FIGURE 4.6: Temperature (°C) profiles versus depth (m) over a diurnal cycle during a convective case (wind speed < 7 m s^{-1} and cloud fraction < 0.7) for PIRATA mooring location 10°S10°W. Line shows the model results, crosses show PIRATA observations of temperature.

heating continues at depth. Between 19:00 and 01:00 it would appear that convective overturning is taking place and the surface is losing heat. The heat energy is being moved down the water column, as shown by the peak of around 200 W m^{-3} deepening throughout the night.

The subtle changes in heating throughout the water column are not always expressed by the temperature profiles (see figure 4.6). Looking at the temperature in the early morning, the near surface appears nearly constant. It is only between the hours of 11:00 and 17:00 that we clearly observed the formation of diurnal warm layers. Similarly, after 19:00 the warm layers begin to break down due to the lack of solar input and the onset of convection. In comparison, the temperature profiles reveal only a return to the near uniform profile. Figure 4.6 also shows the temperature recorded by the PIRATA mooring at the same time, the modelled temperature profiles are in good agreement.

In addition to the profiles discussed above, the SST, wind speed, cloud fraction and mixed layer depth are shown in figure 4.7. The modelled SST_{1m} is in good agreement with the buoy observations. However, it would appear that the timing and magnitude of the peak of diurnal warming is slightly overestimated by the model, with an increase in observed values of approximately 0.2 °C and the peak itself occurring 1 or 2 hours later than the observations. For the majority of the model run the cloud cover and wind speed were low, critically during the morning to late afternoon when the majority of the solar heating and diurnal warming are taking place. Slightly higher winds occur in early morning and during the following night.

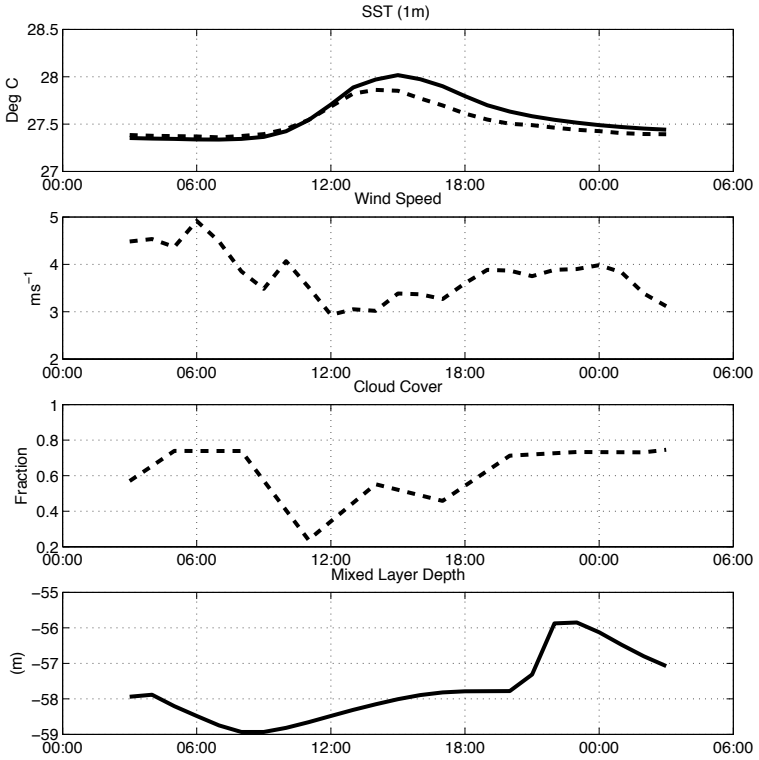

FIGURE 4.7: SST (°C), wind speed (m s^{-1}), cloud fraction (tenths) and mixed layer depth (m) over a diurnal cycle during a convective case (wind speed < 7 ms^{-1} and cloud fraction < 0.7) for PIRATA mooring location 10°S10°W. Model results (unbroken line), observations (dashed line).

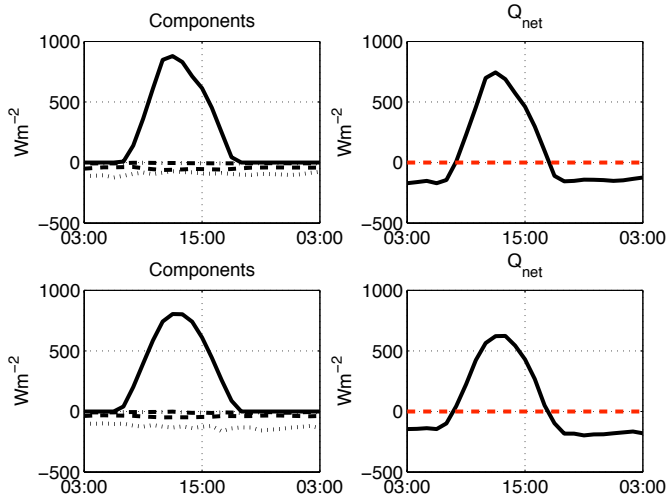

FIGURE 4.8: Heat budget over the diurnal cycle (3am–3am) for PIRATA mooring location 10°S10°W. Left side: Components of the heat budget (W m^{-2}) — Solid line: Q_s, dashed line: Q_e, dotted line: Q_l dot-dashed line: Q_h. Right side: Net heat flux (W m^{-2}). Top: convective case. Bottom: non-convective case). Heat fluxes into the ocean are positive

The modelled heat budget for the convective case study can be seen in the top row of figure 4.8. The latent heat, sensible heat, and longwave back radiation remain reasonably constant, it is only the shortwave radiative flux which varies on the diurnal timescale. Looking at Q_{net}, the maximum transfer of heat into the water column occurs at 12:00, however heating continues into early afternoon as seen in the temperature profiles and in the observed and modeled SST in figure 4.7.

Variable	RMSE	R^2
SST (°C)	0.11	0.98
Temperature — 20 m (°C)	0.01	0.21
SWR (W m^{-2})	93.25	0.93
SSS (psu)	0.02	0.27

TABLE 4.5: 17th April 2002 — selected convective case (based on statistics from table 4.3).

Comparing the modelled results to the PIRATA observations at 10°S10°W, we get an idea of the skill of the model. Looking at table 4.5 we can see that the model is highly correlated near the surface, with RMS error for SST only 0.11 °C and only 0.01 °C for temperature at 20 m depth. The SST shows a high correlation coefficient of 0.975, although, the variation in temperature is small in magnitude. At depth the RMSE increases and the level of correlation decreases, as indicated by both the low R^2 values.

4.4.3 Non-convective case — 10^{th}-Jan-2002

The same profiles and statistics are generated from model data for the selected non-convective case. During this day, the sky is predominately overcast and wind speeds remain high, ensuring increased turbulent energy transfer. Figure 4.9 illustrates the difference between the non-convective case the convective case well. Throughout the model run there is a reasonable amount of turbulent and molecular diffusivity occurring in the upper water column within the mixed layer.

In figure 4.10 increased convective transport is evident compared to the convective day. Throughout most of the day greater fluxes of heat occur, especially between 19:00 and 01:00 the following morning. As expected there is not much difference in the shape of the profiles for penetrative solar heating (figure 4.11, although the total amount of energy input into the water column is reduced by around 100-200 W m^{-2}, as can be seen in figure 4.8).

This observed reduction in penetrative solar heating, in combination with increased conductive heating in the opposite direction, clearly influences the profiles of the rate of total heat transport (figure 4.12). It is clear that the magnitude of the heat transport terms is greater, and that during the period between 11:00 and 17:00 the incoming radiative flux is counteracted by the conductive heating flux.

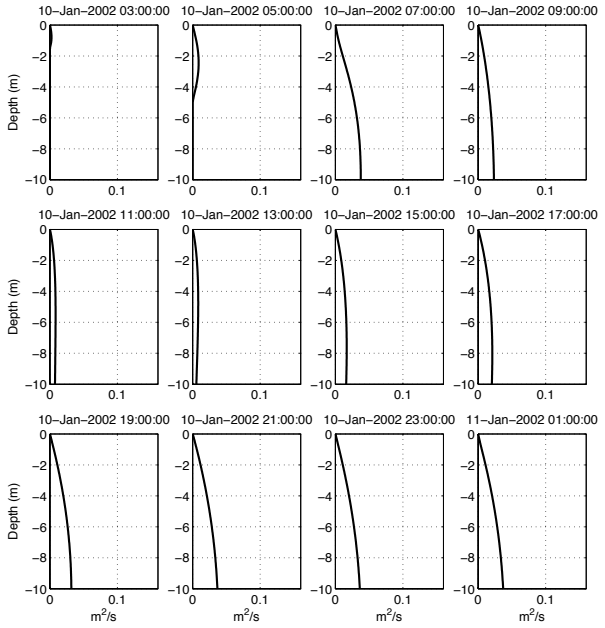

FIGURE 4.9: Diurnal cycle of molecular and turbulent diffusivity ($m^2\ s^{-1}$) verus depth (m) during a non-convective case (wind speed > 7 m s^{-1} and cloud fraction > 0.7) for PIRATA mooring location 10°S10°W.

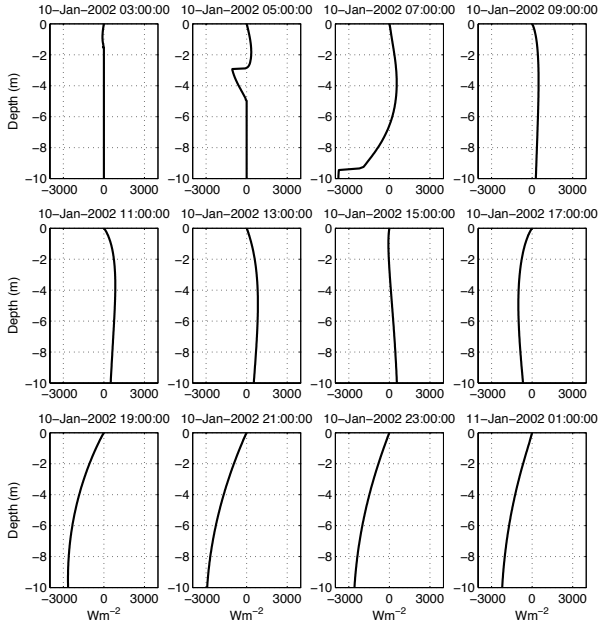

FIGURE 4.10: Diurnal cycle of convective transport (W m^{-2}) versus depth (m) during a non-convective case (wind speed > 7 m s^{-1} and cloud fraction > 0.7) for PIRATA mooring location 10°S10°W.

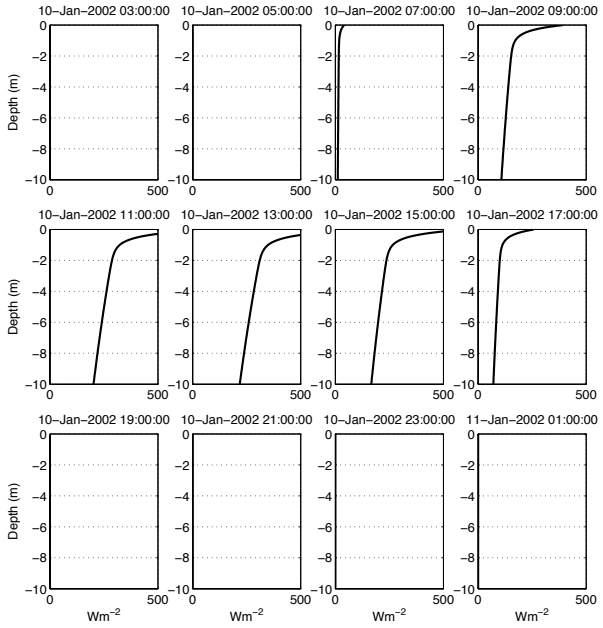

FIGURE 4.11: Diurnal cycle of penetrative solar heating (W m^{-2}) versus depth (m) during a non-convective case (wind speed $>$ 7 m s^{-1} and cloud fraction $>$ 0.7) for PIRATA mooring location 10°S10°W.

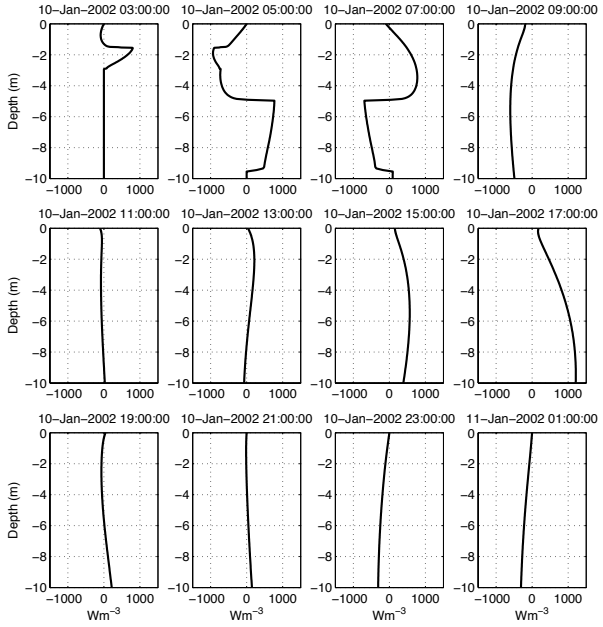

FIGURE 4.12: Diurnal cycle of total heating rate (W m^{-3}) versus depth (m) during a non-convective case (wind speed $>$ 7 m s^{-1} and cloud fraction $>$ 0.7) for PIRATA mooring location 10°S10°W.

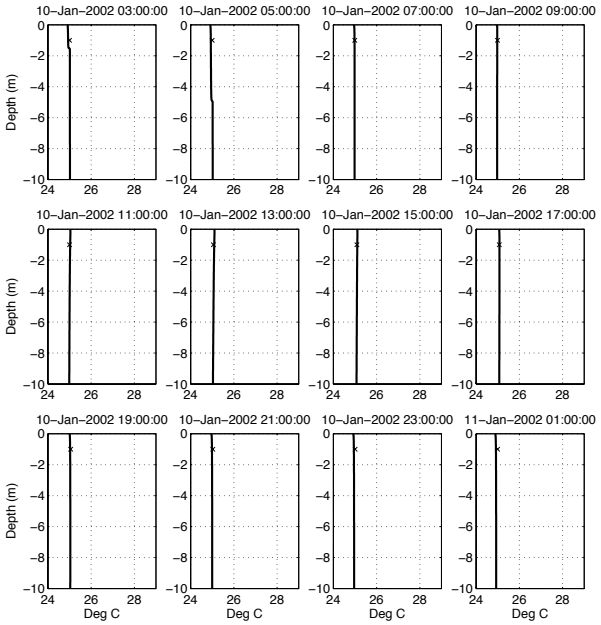

FIGURE 4.13: Temperature (°C) profiles versus depth (m) over a diurnal cycle during a non-convective case (wind speed > 7 m s^{-1} and cloud fraction > 0.7) for PIRATA mooring location 10°S10°W. Crosses show PIRATA observations of temperature.

Similarly, the changes in heat failed to be represented by the temperature profiles in figure 4.13. In this case, the formation of diurnal warm layers does not occur during the afternoon as the input of wind driving mixing energy serves to disrupt their formation. In fact the profiles of temperature throughout the course of the day remain virtually constant, not a clear representation of the interplay occurring in terms of the transport of heat itself. As with the convective case, the observed temperatures from the PIRATA moorings seem to closely resemble the modeled temperatures from GOTM.

Figure 4.14 shows the SST, wind speed, cloud cover and mixed layer depth for the entire model period. Both wind speed and cloud cover are high, and the SST of the model appears to fit reasonably with the observations (also see table 4.6). The correlation coefficients are lower than their convective counterparts. The RMS errors are lower for the non-convective case compared with the convective case. For SST the rmse is only 0.063 °C. Although the subtle variations in temperature near the surface do not appear to be represented as well during the non-convective case, the deviation from the observed values is lower.

Variable	RMSE	R^2
SST (°C)	0.06	0.71
Temperature — 20 m (°C)	0.08	0.08
SWR (W m^{-2})	110.60	0.92
SSS (PSU)	0.01	0.03

TABLE 4.6: Model vs. observations for 10th January 2002 — selected non-convective case (based on statisitcs from table 4.4).

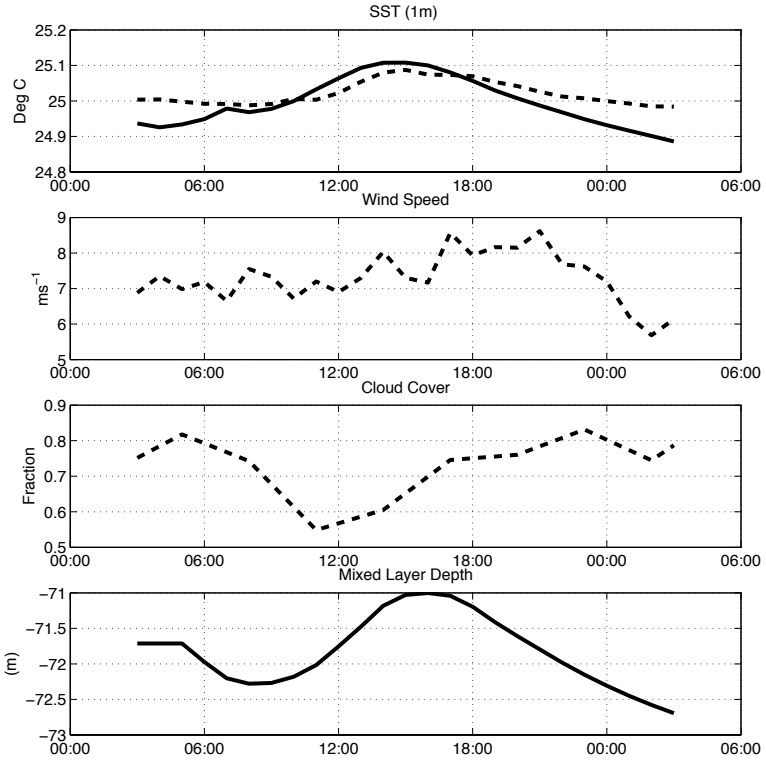

FIGURE 4.14: SST (°C), wind speed (m s^{-1}), cloud fraction (tenths) and mixed layer depth (m) over a diurnal cycle during a non-convective case (wind speed > 7 m s^{-1} and cloud fraction > 0.7) for PIRATA mooring location 10°S10°W. Model results (unbroken line), observations (dashed line).

4.4.4 Bias over the diurnal cycle

The differences between the model variables and the PIRATA data highlight the type of uncertainty present in the model. By looking at the residuals it is possible to identify the presence of systematic error. For each of the convective and non-convective days listed in tables 4.3 and 4.4 the residuals over the course of the diurnal cycle were examined. Figure 4.15 shows the residuals of SST, temperature at 20 m depth, SSS (Sea Surface Salinity) and SWR (shortwave radiation) for the convective days. If the modeled data were to fit perfectly with the observations then the residuals would be zero.

During most of the day the residual SST is generally small and centered around 0 °C, during early afternoon, around 15:00, there is a definite tendency for the model to overestimate, i.e. warming too much, compared with the observations. This warming trend is not apparent in the residuals for temperature at 20 m, which seem to be closely distributed around 0 °C, with little spread. The residual deviation for salinity tends to be less than ±0.05 psu. For shortwave radiation, the residuals range between ±300 W m^{-2} during daylight hours, and can likely be attributed to the choice of equation used in its calculation.

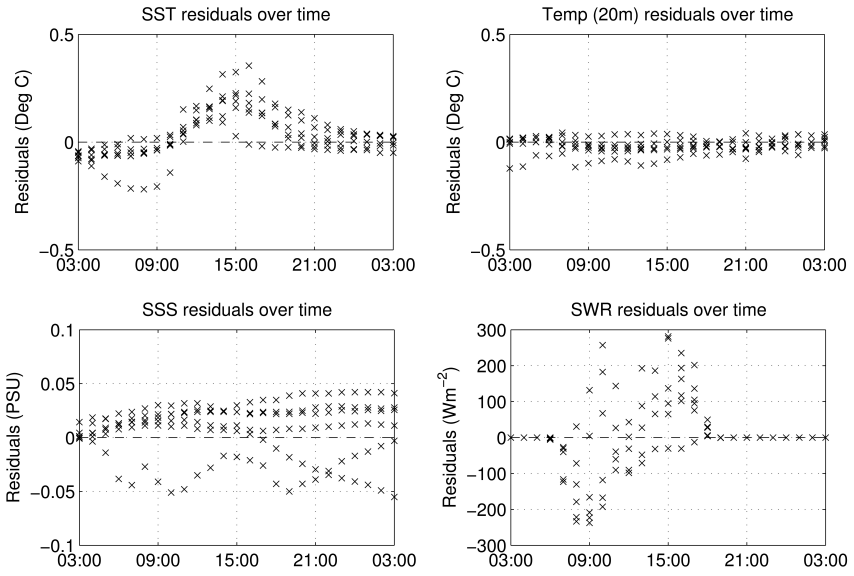

FIGURE 4.15: Residuals (GOTM minus observations) versus time for a diurnal cycle (3am-3am) for SST, temp (20 m) (°C), SSS (PSU) and SWR (W m^{-2}) for selected convective days (see table 4.3).

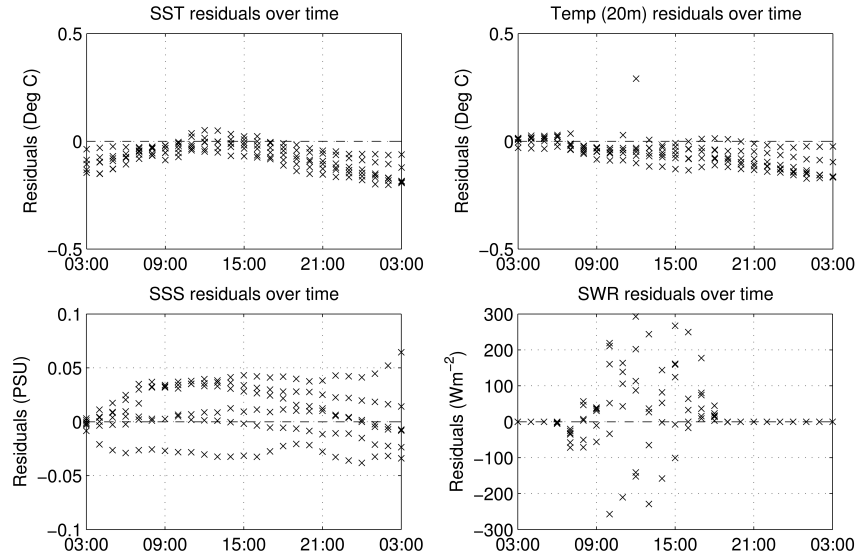

FIGURE 4.16: Residuals (GOTM minus observations) versus time for a diurnal cycle (3am-3am) for SST, temp (20 m) (°C), SSS (PSU) and SWR (W m^{-2}) for selected non-convective days (see table 4.4).

In the case of the non-convective residuals in figure 4.16, there is not such strong tendency to overestimate the warming during mid-afternoon in the SST signal. Instead, SST residuals indicate that the model is slightly too cool, by about 0.2 °C, which is also visible in the residuals for temperatures at 20 m. There does not appear to be a systematic bias only random variation in the SSS and SWR residuals.

The GOTM near surface temperature appears to follow the PIRATA observations closely to within 0.2 °C, however during convective cases the model tends to slightly overestimate the amount of warming. Since the parameter of most concern is the near surface temperature, or rather more precisely the skin-bulk temperature difference, ΔT (see figure 4.1), these results show that GOTM is sufficiently accurate in its prediction of the diurnal cycle of near surface temperature in order to warrant its use in the calculation of air-sea CO_2 exchange. Further calibration of the model setup is required to reduce the amount of systematic error in SST visible during the convective cases (figure 4.15). One possibility may be to raise the level of turbulence so that the warm layers are deeper but less intense.

4.4.5 Annual heat budget

In addition to running simulations over a 24 hour period, the model was also allowed to run for the whole of 2002. Figure 4.17 shows the component terms of the net heat flux, Q_{net}, at 10°S10°W for 2002. Each of the components; shortwave radiation, Q_s, latent heat, Q_e, sensible heat, Q_h, and net longwave radiation, Q_l, are calculated by GOTM's 'airsea' module as described in section 4.1.1. Importantly, we do not consider the influence of advection. The figure shows both the annual trend (a low pass filter has been applied to the data), and the higher resolution (unfiltered) data. Figure 4.18 shows the filtered components together and net heat flux Q_{net}.

The sensible heat flux at the beginning of 2002 is around -10 W m^{-2}, increasing to -20 W m^{-2} between June and August, then reducing again between October-December. Longwave radiation is relatively constant over the annual cycle, around -50 W m^{-2}. Seasonal variations in latent heat flux and shortwave radiation are more significant and are in agreement with Foltz et al. (2003), who calculate the seasonal heat budget based on average measurements from 1997–2002, see table 3.3 in section 3.5.

Over the annual cycle, the seasonal variation in shortwave radiation and latent heat controls the sign of the net heat flux, Q_{net}. From figure 4.18, (note the convention — positive into the ocean), between January-April and September-December Q_{net} is positive indicating warming, during May-August the surface is cooling, as the shortwave radiation reaches is lowest value of around 200 W m^{-2} and the latent heat reaches its

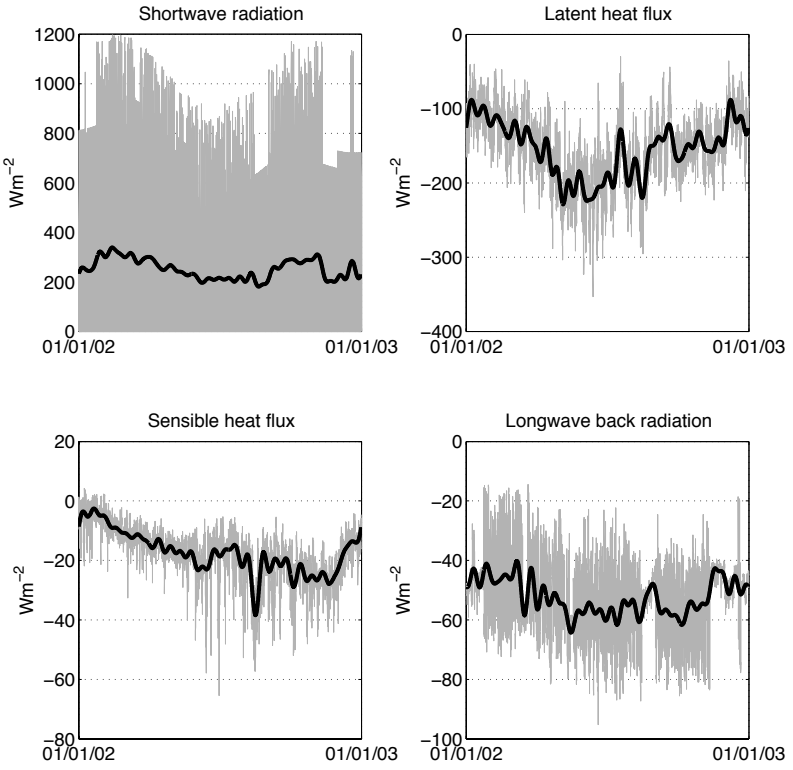

FIGURE 4.17: GOTM derived surface heat fluxes for PIRATA mooring location 10°S10°W: shortwave radiation; latent heat flux; sensible heat flux; and longwave back radiation. Solid black line (low pass filtered), grey line (hourly unfiltered data) for 2002 in W m^{-2}. Fluxes are positive into ocean.

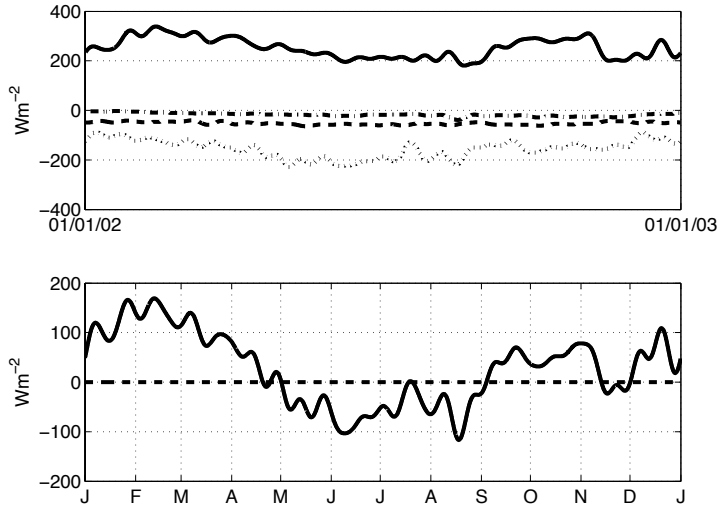

FIGURE 4.18: GOTM derived radiation budget for PIRATA mooring location 10°S10°W. Top: shortwave radiation (solid line); latent heat (dotted line); sensible heat (dotted dashed line); and longwave back radiation (dashed line) for 2002 in W m^{-2}. Bottom: Net heat flux (Q_{net}) for 2002 in W m^{-2}. Fluxes are positive into ocean.

peak of around the same. Calculating mean amplitude we arrive at a value of approximately 250 Wm^{-2} for shortwave and -155 W m^{-2} for latent, slightly larger than those of Foltz et al. (2003).

Discrepancies in the heat budget may be due to the lack of a cool skin, which would serve to reduce the latent heat flux, and secondly that the shortwave radiation in the model has been calculated according to equation 4.3 which relies on our estimate of cloud fraction and albedo. We also make an important assumption, in that, cloud cover estimates from satellite are equivalent to those taken by a marine observer looking up.

In comparison to the latent and shortwave mean for 10°S10°W, Foltz et al. (2003) state that the contributions from zonal advection, meridional advection and eddy advection are -10, 20 and -10 W m^{-2} respectively. Additionally, the annual amplitudes are 10, 0 and 20 W m^{-2}. A caveat of our 1-d treatment of the heat budget is that we do not consider the advective terms in our calculations. However, they are significantly less important when compared to both the latent and shortwave fluxes, and should be less important over the diurnal cycle.

Currently, the shortwave radiation flux, Q_s, is calculated using equation 4.3 (see Simpson and Paulson (1999)). This value is based simply on cloud fraction, albedo, latitude, longitude and noon solar altitude. Improved results may be achieved by using the in situ shortwave radiation data measured by the PIRATA array. This may be important for the timing of warming and cooling events in the upper water column, as the penetrative shortwave radiation (defined in equation 4.11) is a boundary condition for the model temperature. Altering the magnitude and onset of this input energy flux will alter the heat transport, which is balanced by the convective transport (which incorporates the molecular and turbulent effects). The annual mean of the shortwave radiation as measured by the PIRATA mooring is $\sim$224 W m^{-2}, which is closer to the Foltz et al. (2003) values.

Furthermore, the current equations governing the longwave, latent and sensible terms are outdated. A sensitivity study into the effect of improved heat flux parameterizations may prove beneficial for accurately predicting SST over the diurnal cycle. For example, replacing the current formulation for longwave back radiation, Q_l, equation 4.2 (see Clark et al. (1974)), with the longwave formula from Josey et al. (2003) may prove beneficial. The Clark formula tends to be an overestimate of order 10 W m^{-2}, i.e. too little heat loss. The Josey et al. (2003) formula tends to agree with in situ measurements to within 2 W m^{-2} at latitudes greater than 35°. However closer to the equator the formula is less accurate, underestimating by 8.5 W m^{-2}, though this is still an improvement over the Clark formulation.

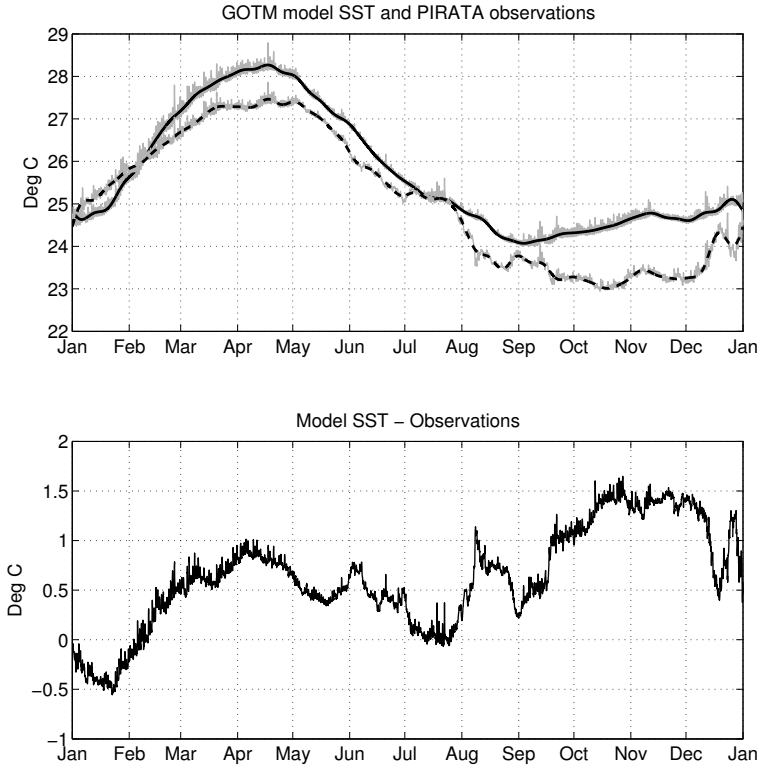

FIGURE 4.19: Top: Comparison of GOTM (solid black line) modelled SST (°C) (at 1 m) and PIRATA (dashed black line) SST observations (at 1 m) at 10°S10°W over 2002. Grey lines show high frequency unfiltered data. Bottom: Residual over the same period. Model results from a continuous run.

4.4.6 Model yearly run vs. observations

Comparisons between the model run over the whole of 2002 were made with available data from the PIRATA buoy at 10°S10°W. The variables that are compared include SST (at 1 m depth), temperature at 20 m, SSS (at 1 m depth) and shortwave radiation. Other than temperature and salinity profiles used as initial conditions, the above variables are not used to force the model and so are considered 'independent'. The following question is posed: How well does the model represent the annual cycle, and can a single yearly model simulation be used to provide realistic ΔT values for calculating the CO_2 flux?

Figure 4.19 shows the annual cycle of SST_{1m} from both the model and from the PIRATA observations in the upper panel and the residual in the lower panel. It is clear that for the majority of the year the model values are of the order 0.5–1.5 °C wamer than the observations, the exception being in January 2002, where the model is on average less than 0.5 °C cooler than the observations. This is in contrast to the model runs conducted over 24 hour periods (in those cases the residuals were low, with a tendency to warm too much in early afternoon). Looking at table 4.7 we can see that the RMSE between the model and observations for SST is 0.50 °C, around 3–4 times larger than those over the diurnal period.

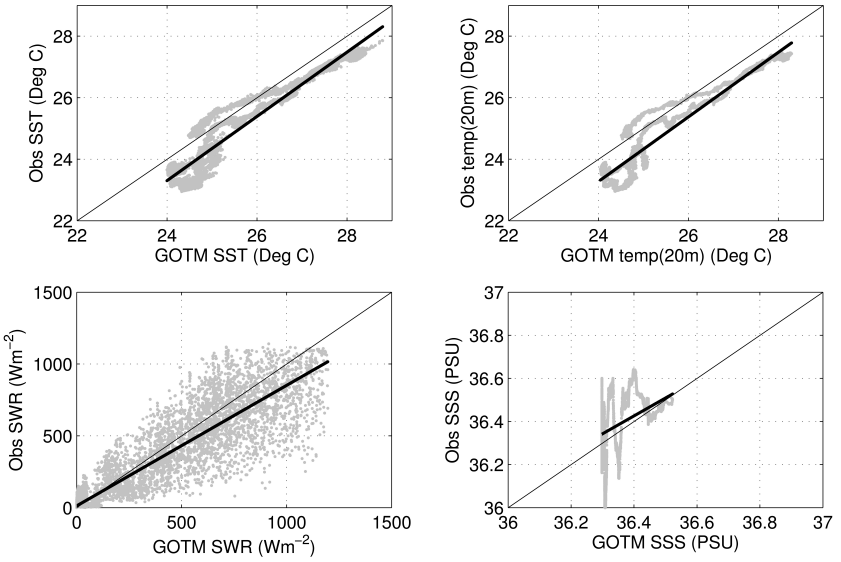

FIGURE 4.20: Scatter-plots showing model versus observations for SST, temperature at 20 m (°C), SSS (PSU) and shortwave radiation (W m^{-2}). Data is in grey, thin black line represents y=x and thick black line represents the 1st order regression equation.

During the course of the the yearly simulation, the modelled values for SST deviate significantly compared to the shorter timescale simulations. However, given this deviation from observations, the R^2 correlation coefficient for SST remains highly significant at 0.89. It may be that the slow seasonal drift observed in the annual cycle can be accounted for by the influence of advection (see Section 2.1.1), which is not so important on diurnal timescales.

Variable	RMSE	R^2
SST (°C)	0.50	0.90
Temperature — 20 m (°C)	0.51	0.89
SWR (W m^{-2})	118.87	0.85
SSS (PSU)	0.11	0.18

TABLE 4.7: Model versus observations for a selection of variables, RMSE and R-squared correlation coefficients during 2002 (see figure 4.20).

SST and temperature at 20 m depth have RMSEs of around 0.5 °C and are reasonably correlated. Figure 4.20 compares scatter-plots of observations vs. model values. As indicated by the R^2 correlation coefficients in table 4.7, the SST, temperature at 20 m and the shortwave radiation fall closest to a linear relationship. The temperature at greater depths and the surface salinity do not follow the $y = x$ relationship, although the deviation in RMSE for SSS is low, at around 0.11 (PSU).

In the model's current configuration, the annual cycle is not sufficiently represented to enable the use of yearly simulations. The residual difference between the model

and observation is considerably larger than the typical magnitude of ΔT. It is more appropriate to reinitialize the model for every diurnal simulation, as this provides a more accurate fit to the observed near surface temperatures.

4.4.7 Air-sea CO_2 exchange

At this stage in the model development GOTM does not contain any routines for calculating air-sea gas transfer. This section presents preliminary results using the GOTM temperature output as variables in a CO_2 flux calculation. The aim is to highlight the use of GOTM near surface temperatures for improving such calculations. Further model development will implement gas exchange sub-routines into GOTM.

The flux of CO_2 can be expressed in terms of the bulk and interfacial (skin) solubilities:

$$F = k_s(\alpha_w fCO_{2w} - \alpha_s fCO_{2a}) \tag{4.20}$$

The subscript 's' indicates that the transfer velocity, k, and solubility, α are computed using the skin temperature and salinity, whereas the subscript 'w' refers to bulk measurements. The interfacial characteristics strongly affect the gas flux. For example, cool skin temperature depression could range from 0.1–0.4 degrees, and warm layer elevation under light winds could be as large as 2–3 degrees in the tropics (Fairall et al., 1996b). This thermal structure from the bulk water up to the surface will certainly alter the flux (Ward et al., 2004):

$$fCO_{2s} = fCO_{2w}(1 + 0.0423\Delta T) \tag{4.21}$$

This 4.2% change per degree C was determined at a reference temperature of 20 °C, and it also includes the effect of solubility, whose temperature dependence is empirically formulated from Weiss (1974) or Wanninkhof (1992).

Additional influences of temperature structure on the flux include the effects of the warm layer (and/or cool skin) on the fugacity of CO_2 dissolved in seawater (Takahashi et al., 1993) via the carbonate reaction. This requires a deviation from the mass conservation assumption, so that the surface fugacity is expressed in terms of the bulk fugacity through an empirical relationship. Fairall et al. (2003) express the flux with a small temperature correction associated with the carbonate reaction as:

$$F = k_s\alpha_s \left[fCO_{2w}\frac{\alpha_w}{\alpha_s}(1 + 0.015\Delta T) - fCO_{2a} \right] \tag{4.22}$$

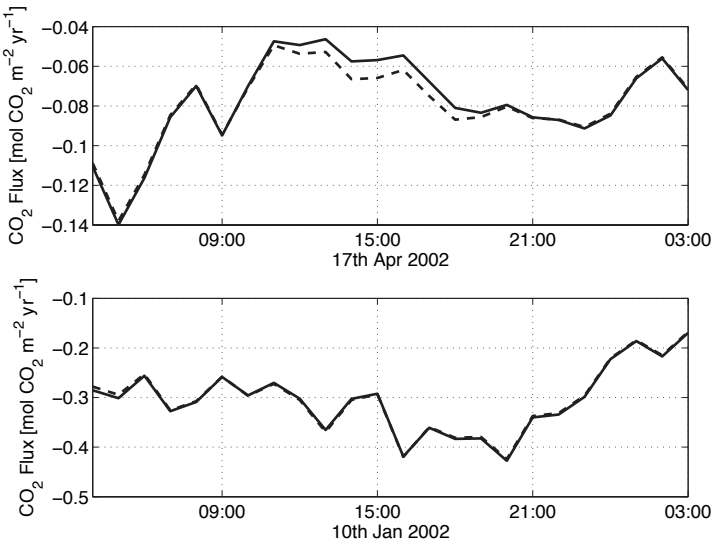

FIGURE 4.21: Preliminary calculation of air-sea CO_2 flux (mol CO_2 m^{-2} yr^{-1}). Solid line: CO_2 flux calculated using Fairall et al. (2003) (see equation 4.22). Dashed line: CO_2 flux calculated using equation 2.4. Top: convective case, Bottom: non-convective case. In both cases the flux is negative as $pCO_{2w} < pCO_{2a}$ i.e. an oceanic sink.

This expression is more accurate and provides a statement of the flux in terms of the measured fugacities, bulk water temperature, and skin temperature. The fugacity coefficient (i.e. the ratio between fugacity and partial pressure of CO_2), is on the order 0.996 to 0.997 under typical conditions ($p = 1$ atm, $T = 270$–300 K, $pCO_2 = 350$ μatm). Thus, it is proposed to use the climatological values of pCO_2 from Takahashi et al. (2002) in order to determine the CO_2 flux. Ultimately, integrating the net CO_2 flux over the course of a diurnal cycle is the aim.

Given the temperature dependencies of the gas exchange calculation, the GOTM temperature output is used to supply T_s and T_w in equation 4.22 to demonstrate its validity. The result is compared with CO_2 flux calculated for the same period, using only 'bulk', T_w measurements and equation 2.4.

Figure 4.21 shows the flux of CO_2 during both the selected convective and non-convective days in a weak sink region. It is apparent that during the time when the warm surface layer is present, the flux of CO_2 has decreased. Integrating the flux of CO_2 over the diurnal cycle we observe roughly a 2.5% difference when the ΔT is taken into account during convective conditions. Since the formation of warm layers does not occur during the non-convective case, ΔT is virtually zero and hence there is little difference in integrated flux. It is important to note that for a source region (i.e. $pCO_{2w} > pCO_{2a}$), ΔT would serve to increase the flux.

One caveat of this method is that the (Wanninkhof, 1992) parameterization for the gas transfer velocity was used. This is significant as simple k vs. u_{10} models tend to underestimate flux as wind speed approaches zero (Blomquist et al., 2006). The transfer

velocity is dependent on the turbulence in the water and the diffusivity of the gas. Since diffusivity varies with both temperature and salinity there is a further influence on the flux of CO_2 related to buoyancy effects on k which must be accounted for.

In addition, buoyancy effects which arise due to spatial variations in density can affect turbulence. Forcing can occur in the case of unstable stratification, which may be present at night due to surface cooling. Unstable stratification in the ocean can also result from evaporation, which increases surface salinity and hence surface density. In each of these cases, unstable stratification results in convective turbulence, which can be extremely vigorous. Convective turbulence usually restores the fluid to a stable state soon after the destabilizing flux ceases (e.g. when the sun rises).

Further model development will implement the NOAA-COARE gas transfer velocity parameterization (as described in section 2.1.6), as this takes into account processes such as surface renewal and turbulent-molecular diffusion near the air-sea interface (Fairall et al., 2000). These preliminary results serve as a proof of concept, that the gas flux is improved when GOTM temperature output is included.

4.5 Conclusions

The results from the model testing and development stage identified a gap in the current understanding of gas exchange under low wind conditions. Current estimates for gas transfer based on k versus u_{10} have a tendency to underestimate gas exchange under low winds. If buoyancy effects become a dominant control at low wind speeds and during clear skies, there is a missing contribution to net estimates of gas transfer that must be addressed.

Evaluating the data available in the tropical Atlantic, the in situ PIRATA data was found to be highly variable in terms of its availability and consistency. When combined with additional data from satellite and climatologies, there is enough information to calculate surface fluxes and temperature profiles. The model results from GOTM are similar to those found in the literature, and the discrepancies can be attributed to the uncertainty in the model input data and its one-dimensional nature.

Given the nature of the physical processes involved and the timescales on which they operate, a modeling approach is well suited. The one-dimensional model framework of GOTM provides the ability to implement and test new parameterizations over a range of timescales using forcing data from the PIRATA moorings in the tropical Atlantic.

Preliminary results investigating heat transport and near surface temperature structure are the first step in using the model to estimate CO_2 exchange. These suggest that GOTM is an appropriate framework for modeling near surface temperature over the diurnal cycle under both convective and non-convective conditions, when reinitialized

over short periods (days). Producing estimates of the skin and bulk temperature over the course of a day enables us to look at the change in ΔT over a diurnal cycle. This ΔT is important for gas exchange due its effect on solubility and the carbonate reaction. A 2.5% reduction in net daily CO_2 flux was estimated during a convective day (for a weak sink region), compared with a parameterization which did not account for ΔT (see equation 2.4). It is expected that even larger deviations will be present once the buoyancy effects on k are considered.

Work reported in subsequent chapters, building upon the preliminary results, aims to estimate gas exchange in the tropical Atlantic via an embedded gas flux model within the GOTM framework. Ultimately the importance of gas transfer under low wind speeds and convective conditions will be considered, and its significance on the net air-sea CO_2 flux will be addressed.

Chapter 5

1-d modelling in the Tropical Atlantic

This chapter is a research article (Jeffery et al., 2007) that has been published in Ocean Modelling, Volume 19, Issues 3–4, Pages 161–182, doi:10.1016/j.ocemod.2007.07.003. The manuscript was submitted on the 13^{th} April 2007, accepted 24^{th} July 2007 and was available online on the 2^{nd} August 2007. The role of the co-authors was supervisory in nature, with the substantive work carried out by the lead author.

5.1 Introduction

Accurate estimates of the air-sea exchange of climatically important gases such as CO_2 are vital for addressing the problem of global warming. Understanding the mechanisms controlling exchange allows for improved parameterization, and ultimately benefits climate model predictions. A lack of data due to the difficulty of in situ measurement leads to large uncertainties in parameterizing the air-sea flux of gases; modelling studies provide a means of investigating exchange processes, which operate on short ($\leq$ 1 hour) timescales, thus improving our understanding.

Approaching the air-sea interface, dominant turbulent processes are suppressed and molecular processes become the dominant control. This leads to strong gradients of properties such as temperature and gas concentrations close to the surface compared with weak gradients away from the interface (Danckwerts, 1951; Deacon, 1977; Jähne and Haußecker, 1998; Donelan and Wanninkhof, 2002; Soloviev and Schlüssel, 2002). Conceptual models of the air-sea interface divide the boundary layers either side into

turbulent outer layers and diffusive inner sub-layers. Since the diffusivity of CO_2 in the atmosphere is much greater than that in the water, the flow across the interface is limited by the resistance in the diffusive aqueous boundary layer. In addition solubility, which is a function of temperature and salinity, plays an important role (Weiss, 1974). CO_2 is poorly soluble in water resulting in the liquid phase controlling the exchange of mass.

The flux of a gas across the air-sea interface is determined by the product of the gas transfer velocity, which characterizes the resistance to gas exchange across the boundary layers, and the air-sea concentration difference, which is the driving potential. Conventional estimates of air-sea exchange rely on simple, empirical, wind-speed dependent parameterizations of the gas transfer velocity (Wanninkhof, 1992; Liss and Merlivat, 1986; Wanninkhof and McGillis, 1999). However, a number of physical processes contribute to gas transfer across the interface. These include penetrative convection due to heat loss (Jähne and Haußecker, 1998; Csanady, 1997), shear due to wind forcing, microwave breaking at moderate wind speeds (Zappa et al., 2001) and bubbles at high wind speeds (Woolf, 1993, 1997).

In regions with low or intermediate winds and strong insolation, changes in the heat budget and ocean circulation may have significant feedbacks on air-sea gas exchange and conventional estimates are likely to underestimate the amount of exchange taking place (McGillis et al., 2004). Questions arise such as: Is the net effect of underestimated convective gas exchange important when integrated over longer timescales e.g. monthly averages?

Diurnal warming can occur in the upper ocean wherever solar heating at midday is greater than the heat lost from the ocean surface, but is more significant where winds are fairly light. Large regions of the world ocean are susceptible and temperature differences can exceed 6 °C in extreme cases (Stuart-Menteth et al., 2003). The resultant nighttime cooling may drive enhanced gas transfer (McGillis et al., 2004).

Fluxes of CO_2 will be appreciably higher when the surface is cooling, as heat loss will contribute to the turbulent mixing via buoyancy forcing within the aqueous boundary layer. Gas transfer will also be modified where the mixed layer deepens, entraining dissolved gases from below (MacIntyre et al., 2002). Thus the daily cycle in oceanic surface mixed layers becomes important. Lombardo and Gregg (1989); Brainerd and Gregg (1993a,b) investigated cycles of nocturnal convection and diurnal re-stratification in the Pacific Ocean during PATCHEX; daily observations showed that the ocean lost heat and buoyancy starting several hours before sunset and continuing a few hours after sunrise. Anis and Moum (1992, 1994) also conducted hydrodynamic and turbulence measurements in the Pacific Ocean as part of the Tropic Heat Experiment. In these cases turbulent kinetic energy predicted by wind stress was insufficient to account for

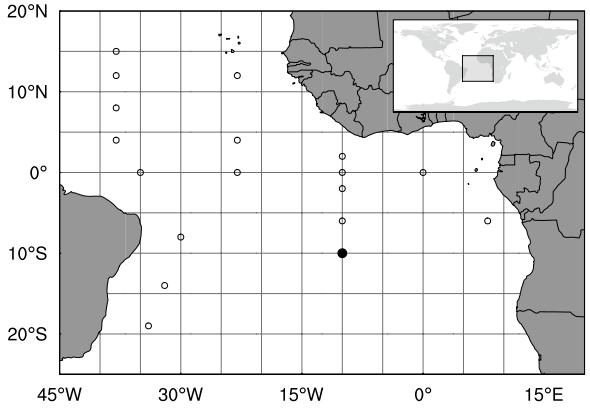

FIGURE 5.1: Study area and location of the PIRATA array of ATLAS moorings in the Tropical Atlantic. The filled black circle represents the PIRATA mooring located at 10°S10°W. Source: TAO Project Office (2008).

the observed dissipation; i.e. production due to convective motions may also be an important term (Stips et al., 2002).

This study explores these issues with the intention of quantifying the contribution of convective processes overlooked by conventional air-sea exchange parameterizations. It focuses on the Tropical Atlantic, using meteorological data from the PIRATA array in 2002 (see figure 5.1), cloud cover estimates from Meteosat-7, and NCEP pressure fields to force a modified version of the General Ocean Turbulence Model (GOTM) at 10°S10°W. We modify the existing NOAA-COARE gas transfer parameterization to include additional effects from low wind-speed buoyancy driven exchange and mixed layer deepening, in order to better estimate the air-sea exchange of CO_2.

5.2 Background

5.2.1 Heat budget

Changes in heat stored in the upper layers of the ocean result from a local imbalance between input and output of heat through the sea surface. The surface heat flux can be described as;

$$Q_{net} = (1 - a)Q_s - [Q_l + Q_h + Q_e + Q_v + Q_{rf}] \tag{5.1}$$

where α is the albedo, Q_s is the incident short wave solar radiation, Q_l is the net longwave radiation, Q_h is the sensible heat loss, Q_e is the latent heat loss, Q_v is the heat loss due to horizontal advective processes and Q_{rf} is the sensible heat flux due to rain. Units for heat fluxes are W m^{-2} and the flux from air to sea is positive. When the flux

is integrated over time this represents an energy change ΔE per unit surface area. This is related to the temperature change ΔT through $\Delta E = C_p m \Delta T$, where m is the mass per unit area of water being warmed or cooled, and C_p is the specific heat of sea water at constant pressure. The horizontal advection term is not considered in the 1-d vertical modelling framework. The heat budget is important as the processes controlling heat and gas transfer are similar and gas solubility is sensitive to temperature.

5.2.2 Air-sea CO_2 transfer

The flux of CO_2 or other gas, F, across the air-sea interface is often estimated from the bulk formula:

$$F = k\Delta C \tag{5.2}$$

where k is the primary rate constant, often known as the gas transfer velocity and ΔC is the effective concentration difference driving the net flux. The flux from sea to air is positive. In the case of CO_2, ΔC is normally approximated as the difference between $\alpha p\mathrm{CO}_{2w}$ and $\alpha p\mathrm{CO}_{2a}$. Thus:

$$F = k\alpha[(pCO_{2w}) - (pCO_{2a})] \tag{5.3}$$

where α is the solubility as a function of temperature and salinity and $p\mathrm{CO}_{2w}$ and $p\mathrm{CO}_{2a}$ are the partial pressures of CO_2 in water and air respectively (Wanninkhof and McGillis, 1999).

Boutin et al. (2002); Olsen et al. (2005); Woolf (2005) compare several traditional wind-speed dependent transfer velocity models. The authors find that flux estimates are highly sensitive to the selection of the gas transfer relationship. Although turbulence is usually driven by the wind, there is not a unique relationship between gas transfer and wind speed due to a number of effects, with diverse results evident especially at higher wind speeds.

The tropical Atlantic Ocean is generally a source of CO_2 to the atmosphere, due to $p\mathrm{CO}_2$ in the surface being slightly supersaturated, with equatorial and coastal upwelling supplying carbon-rich water to the surface layer (Takahashi et al., 2002). Thus, the region plays a significant role in the global carbon cycle. The annual contribution of CO_2 to the atmosphere from the oceanic equatorial belt is approximately 0.6–1.5 GT C yr^{-1}. However, the source from the central and eastern equatorial Pacific is significantly larger than that of the tropical/equatorial Atlantic (Feely et al., 2004).

5.2.3 Cool skin and diurnal warm layer effects

The skin temperature at the air-sea interface differs measurably from the water temperature a few mm below the surface because the primary mechanism of heat transport in this skin layer is molecular conduction. This requires a strong gradient to supply heat to match the sum of the sensible and latent fluxes and net longwave radiation acting at the surface. Since the sum of surface fluxes is almost always from ocean to atmosphere, the skin is kept cooler than the subskin temperature (defined at the bottom of the molecular conduction layer) by an amount ΔT_c called the skin temperature deviation. This is only weakly affected by wind speed but will decrease with increasing wind speed when the infrared heat flux is large. Other turbulence-producing processes also limit ΔT_c (Katsaros et al., 1977). Donlon and Robinson (1997) report that ΔT_c is approximately 0.17 °C, but increases (the skin becomes cooler) during periods of low wind speed.

The implication of ΔT_c for CO_2 exchange is that the lower temperature at the surface means that α will be slightly increased. Since heat diffuses faster through the surface microlayer than dissolved gases (Doney, 1994) it is the solubility at the surface skin, α_s, rather than its average across the skin layer that limits air-sea CO_2 transfer. Thus the CO_2 flux now becomes:

$$F = k\alpha_s[(pCO_{2w}\frac{\alpha_w}{\alpha_s}(1 + 0.015\Delta T) - pCO_{2a}] \tag{5.4}$$

In the case of the above equation, $\Delta T = T_w - T_s$, and α_w and α_s are evaluated at temperatures T_w and T_s respectively (Hare et al., 2004). It includes the addition of the small temperature correction to the mass of the carbonate reaction.

In addition to the cool skin, the diurnal cycle of solar forcing can lead to significant rapid temperature variations in the upper ocean. Diurnal warming occurs when solar short wave radiation exceeds the instantaneous flux of heat lost from the oceans surface. The depth to which warming penetrates depends on a balance between the positive buoyancy flux, derived from incoming solar radiation, and the wind-driven turbulent energy available to mix the upper layer. Strong wind mixing distributes the heat through the upper mixed layer and the diurnal temperature rise is negligibly small. The temperature rise is larger and concentrated close to the surface when the wind stress is low and unable to mix the heat far down the water column. Large regions of the worlds oceans are susceptible to the formation of a diurnal thermocline within the upper few metres, where afternoon temperature increases of order 1 °C occur (Stuart-Menteth et al., 2003). The equatorial/tropical regions, primarily the Mediterranean and mid-Atlantic, are particularly susceptible to diurnal warming. In extreme cases the layer may be less than 1 m thick and can exceed 6 °C (Flament et al., 1994).

The formation of a diurnal thermocline will have a much greater impact on the surface water CO_2 solubility than the cool skin effect and must therefore be taken into account when calculating CO_2 fluxes. However, after sunset the warm surface layer rapidly loses heat through the surface and gravitational instability occurs, destroying the diurnal thermocline and possibly promoting deeper mixing than would be expected in low wind conditions. The successive absorption of heat modifies the stratification locally and even may reverse the skin effect (Hasse, 1971; Fairall et al., 1996a,b; Schlüssel et al., 1997). The surface ocean stratification generated by diurnal heat fluxes can be followed by subsequent large nighttime buoyancy fluxes (Price et al., 1986), this is the phenomenon on which the rest of the paper will focus.

5.3 Buoyancy driven gas transfer

5.3.1 NOAA-COARE gas transfer parameterization

The object of this study is to explore the contribution of convective processes to gas transfer during low wind conditions. As such, it is inappropriate to use a simple k vs. u_{10} parameterization e.g. Wanninkhof (1992), which is likely to underestimate the flux of CO_2. Instead the choice is made of a physically-based model, derived from surface renewal or turbulent-molecular diffusion theory near the air-sea interface (Soloviev and Schlüssel, 1994; Fairall et al., 1996a, 2000). The gas transfer parameterization presented by Fairall et al. (2000) considers resistance to transfer in air and water, which are expressed in terms of both their molecular and turbulent components such that:

$$k = \frac{u_{*a}}{((\frac{\rho w}{\rho a})^{1/2} r_w) + r_a \alpha} \tag{5.5}$$

The above expression can be applied to any gas, the transfer velocity being divided into 2 components either side of the air-sea interface. Here, u_{*a} is the atmospheric friction velocity, ρ_w and ρ_a are the densities of water and air respectively. The dimensionless resistances r_w and r_a are defined as;

$$r_a = \left[h_a S_{ca}^{1/2} + C_{Da}^{-1/2} - 5 + ln(S_{ca})/(2\kappa) \right] \tag{5.6}$$

$$r_w = \left[h_w S_{cw}^{1/2} + ln(z_{wr}/\delta_w)/\kappa \right] \tag{5.7}$$

where S_c is the Schmidt number for the gas in the fluid, z is the depth of the measurement, δ is the estimated turbulent surface layer thickness, κ is the von Karman

constant, h is a coefficient of the molecular diffusive sublayer, and C_{Da} is the atmospheric drag coefficient. In equation 5.5 the resistances are non-dimensionalized by the effective wind-forcing, u_{*a}, but as described in sections 5.3.2–5.3.3, u_{*a} can incorporate buoyancy effects in addition to regular wind-driven forcing. It is the water-side of the equation that primarily controls the magnitude of the transfer velocity as $r_w \gg r_a$ (for CO_2 and other poorly soluble gasses ($\alpha \leq 1$)).

The model accounts for bubble mediated gas transfer, using the Woolf (1997) parameterization:

$$k_w = k_b + \frac{u_{*w}}{r_w} \tag{5.8}$$

where k_b describes the enhancement of water-side transfer caused by plumes of whitecap-generated bubbles.

$$k_b = BV_0 f_w \alpha^{-1}[1 + (e\alpha S_{cw}^{1/2})^{-1/n}]^{-n} \tag{5.9}$$

where f_w is the whitecap fraction, a strong function of wind speed at 10 m, u_{10}.

$$f_w = 3.84 \times 10^{-6} u_{10}^{3.41} \tag{5.10}$$

Woolf (1997) gives the values $V_0 = 6.8 \times 10^{-3}$ m s^{-1} = 2450 cm h^{-1}, $e = 14$, $n = 1.2$ for CO_2. The additional factor B is adjusted to fit measured transfer velocities. Note that Woolf (2005) has suggested that f_w may be sea-state dependent rather than solely a function of wind speed.

During low wind speed conditions diurnal radiative forcing leads to heating of the upper ocean during the day until late afternoon, followed by nighttime cooling and subsequent buoyancy driven overturning. The effects of buoyancy driven convection on gas transfer can be incorporated into the parameterization of k. The modified NOAA-COARE model used here improves upon previous simple parameterizations by separating the atmospheric and water-side and by including a term (in our version) for convective enhancement on the water-side of the gas transfer expression.

5.3.2 Sublayer effects of buoyancy

Buoyancy driven convection enhances gas transfer during low wind speeds in both the thermal molecular sub-layer and the turbulent diffusion layer. The h_w term in equation 5.7 contains the sublayer effects on the water-side, which are neglected on the atmospheric side. From Fairall et al. (2000) this is:

$$h_w = \frac{13.3}{A\phi} \tag{5.11}$$

Literature values vary for empirical coefficients in equations 5.9 and 5.11 where appropriate, based on in situ and laboratory experiments [A=1.85 B=1 Soloviev and Schlüssel (1994), A=0.63 B=1.2 GasEx 98 - Hare et al. (2004), A=1.3 B=0.82 GasEx 2001 - McGillis et al. (2004)]. It should be noted that the empirical constant A is chosen to fit measured transfer velocities and that it is important to correctly determine this, as it has a large effect on the calculated value of k and hence the net CO_2 flux. The empirical function ϕ accounts for buoyancy-driven transfer, and is simply $6/\lambda_s$ (Saunders, 1967), where;

$$\lambda_s = 6\left[1 + \left(\frac{Q_b 2^4 g\alpha\rho_w C_p v^3}{u_{*a}^4(\rho_a/\rho_w)^2 k_T^2}\right)^{3/4}\right]^{-1/3} \tag{5.12}$$

The term inside the 3/4 power contains a number of constants and the expression for the surface buoyancy flux, where g is the acceleration due to gravity, v is the kinematic viscosity and k_T is the thermal conductivity of water. Finally, Q_b is the equivalent surface cooling that includes the effects of salinity due to evaporation on the buoyancy flux:

$$Q_b = Q + \left(\frac{Sb_c C_p}{\alpha L_e}\right) Q_{lat} \tag{5.13}$$

Where S is the salinity, b_c is the saline expansion coefficient, L_e is the latent heat of vaporization and Q is the total cooling at the interface, including the effects of solar flux, as set out by Fairall et al. (1996b).

5.3.3 Convective scaling theory

Fairall et al. (2000) use the low wind speed limit, or 'gustiness' parameter, which prevents the transfer velocity approaching zero at low winds to account for convective buoyancy effects in the atmospheric turbulent layer of the NOAA-COARE gas flux parameterization. The calculation of the atmospheric friction velocity (u_{*a}) includes a modified wind vector, such that;

$$u_{*a} = (C_{Da} S_a^2)^{1/2} \tag{5.14}$$

where S_a is the average value of the wind speed, which according to Stull (1994) and Godfrey and Beljaars (1991) can be expressed as;

$$S_a^2 = u_{10}^2 + w_g^2 \tag{5.15}$$

where u_{10} is the wind speed at 10 m and w_g is known as the convective buoyancy/velocity scale and is defined as;

$$w_g = \beta w_{*a} \tag{5.16}$$

here β is an empirical, tuneable constant of the order 1 and w_{*a} is;

$$w_{*a} = (B_{fa} z_i)^{1/3} \tag{5.17}$$

B_{fa} is the buoyancy flux and z_i is the depth of the actively mixing layer. Fairall et al. (2000) defines z_i as the planetary boundary layer (PBL) depth or approximately 600 m and B_{fa} is calculated according to;

$$B_{fa} = \frac{g}{T_a}\left[\frac{Q_h}{\rho_a C_{pa}} + 0.61 T_a \frac{Q_e}{\rho_a L_e}\right] \tag{5.18}$$

Where g is the acceleration due to gravity, T_a is the air temperature and where Q_h and Q_e are the sensible and latent heat fluxes respectively. As the mean wind vector approaches zero, S_a will approach βw_{*a}. There have been a number of papers that describe the above equations for the atmospheric side e.g. Stull (1994); Godfrey and Beljaars (1991).

This approach deals effectively with convective effects in the atmospheric turbulent layer but neglects analogous processes in the oceanic turbulent layer (Shay and Gregg, 1984, 1986). Since the latter processes should be more significant to the transfer of poorly soluble gases, this is an important omission.

5.3.4 Water-side convection

Convection in the oceanic mixed layer arises from evaporative cooling of the surface, where gravitational instability of the near surface fluid generates convection extending to the bottom of the mixed layer, at which depth stability suppresses turbulence (Csanady, 1997). The contribution due to convection is likely to be the dominant mechanism of gas exchange taking place during low wind speeds. MacIntyre et al. (2002) suggest that typical k vs. u_{10} parameterizations will underestimate gas fluxes by a factor of two in tropical regions, where evaporation is a major component of the surface energy budget. In addition, McNeil and Merlivat (1996) reveal that upper ocean processes, such as the

warm layer, can produce a significant net asymmetry in CO_2 transfer between evasion and invasion over daily timescales.

Convective mixing not only increases the vertical transport of dissolved CO_2 in the mixed layer, but also leads to enhanced turbulence at the air-water interface, thereby increasing gas transfer between the water and atmosphere (Eugster et al., 2003). In this regard we add a velocity scale to the water side of the NOAA-COARE gas flux equation, that is analogous to the atmospheric convective scaling described above. We define w_{*w} as;

$$w_{*w} = (B_{fw} z_{ml})^{1/3} \tag{5.19}$$

z_{ml} is the depth of the convective layer (upper mixed layer depth), and is the part of the mixed layer through which temperatures are uniform within 0.02 °C (MacIntyre et al., 2002). The corresponding timescale of vertical mixing due to convection alone is z_{ml}/w_{*w}, less if mechanical turbulence is also taken into account. In this way, heat gains and losses in the upper water column affect the end result. We therefore explicitly define the water-side buoyancy flux as;

$$B_{fw} = \left[\frac{g a_l Q_{net}}{C_{pw} \rho_w} + \frac{g b_c Q_e}{L_e \rho_w} \right] \tag{5.20}$$

Where a_l is the thermal expansion coefficient, Q_{net} is the surface heat flux, and ρ_w is the density of water.

We redefine u_{*w} in a similar fashion to u_{*a}, by analogy with equation 5.14, to take into account the convective buoyancy flux. This term is introduced into the NOAA-COARE gas flux equation by rewriting it in terms of both the water side and atmospheric friction velocities since $u_{*a} = u_{*w}(\rho_w/\rho_a)^{0.5}$ for the simple wind-driven case. This approach is an improvement over the existing parameterization as it represents diurnal changes of the solar heating cycle and mixed layer deepening, compared to simply scaling the atmospheric-side 'gustiness' parameter based on fluid density differences. Thus (5.5); is rewritten as:

$$k = \left[\frac{r_w}{u_{*w}} + \frac{r_a \alpha}{u_{*a}} \right]^{-1} \tag{5.21}$$

In order to apply this new contributing term, we need first to define w_{*w} in terms of a 'water-side drag coefficient', C_{Dw}.

$$u_{*w} = \sqrt{C_{Dw} S_w^2} \tag{5.22}$$

where the water-side drag coefficient is

$$C_{Dw} = \frac{u_{*w}^2}{u_{ref}^2} \tag{5.23}$$

and u_{ref} is analogous to a wind speed at some reference depth, which we can define from:

$$u_{ref} = \frac{u_{*w}}{\kappa} ln(z_{ref}/z_0). \tag{5.24}$$

Following the atmospheric analogue in (5.15) our new S_w^2 term is calculated as;

$$S_w^2 = u_{ref}^2 + w_{gw}^2 \tag{5.25}$$

where the water-side convective velocity scale, w_{gw} is scaled from w_{*w}, as defined in equation 5.19:

$$w_{gw} = \beta w_{*w} \tag{5.26}$$

During the daytime, when the buoyancy flux is positive, w_{gw} is set to zero as the flux serves to stabilize the exchange by adding buoyancy to the surface. During convective conditions, where the water-side buoyancy flux is negative, w_{gw} is calculated by the method outlined above. In this way, we recalculate the water-side friction velocity (u_{*w}) so that it includes a contribution driven by w_{*w}. Note that from this point forward β is set to 1 as we are not attempting to scale the enhancement to agree with any experimental data.

Liu and Businger (1975) and Zülicke (2005) consider the two aymptotic conditions; simple wind driven surface renewal (forced convection) and solely buoyancy driven renewal (free convection). Instead, our approach ignores the free convection case and considers a simple way to describing how buoyancy forcing can modify pure wind-driven forcing. In the ocean true free convection is rare (i.e. zero wind speed is rare) but there will be many more occasions where buoyancy forcing is significant and the NOAA-COARE approach, used here, offers a practical way of including these.

In order to assess the potential impact of this new parameterization for buoyancy effects it is helpful to compare the changes in k resulting separately from the atmospheric buoyancy flux and the water-side buoyancy flux. This is achieved by using a set of theoretical values for input variables in the NOAA-COARE gas flux parameterization, and calculating the transfer velocity for a reasonable range of wind speeds (0–10 m s^{-1}) and velocity scales (w_{*a} = 0–0.8 and w_{*w} = 0–0.03).

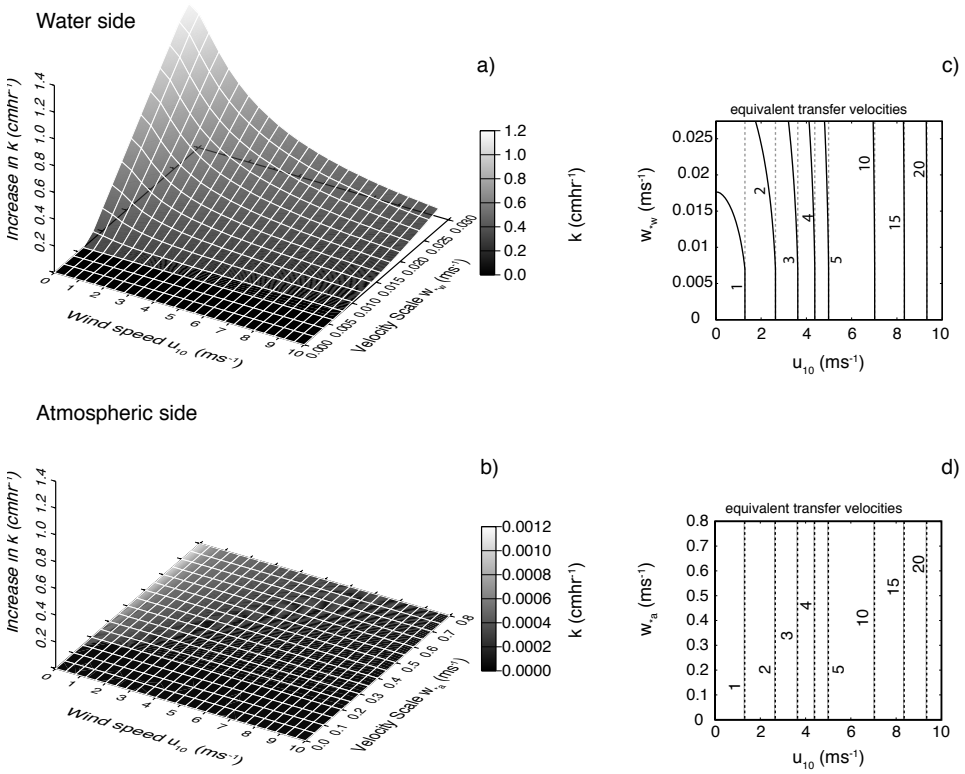

FIGURE 5.2: Comparison of varying wind speed (m s^{-1}) and convective velocity scales (m s^{-1}) on both the water side (a) and atmospheric side (b) of the air-sea interface, on the increase in transfer velocity due to buoyancy effects. (c) and (d) show equivalent transfer velocites (cm hr^{-1}) without buoyancy (dotted line) and with buoyancy (solid line). Transfer velocity, k, was calculated using the NOAA-COARE gas flux parameterization. The following conditions were used; Air temperature = 30 °C; Water temperature = 30 °C; Air specific humidity = 0.0298 g kg^{-1}; Downward IR flux = 18.5 W m^{-2}; Sensible heat flux = 5 W m^{-2}; Latent heat flux = 100 W m^{-2}; $\beta = 1.0$; $A = 0.63$; and $B = 1.2$.

The results are shown in figure 5.2, where the iso-surfaces represent the difference between the gas transfer velocity calculated with and without the convective velocity scales applied. It is clear that the effect of w_{*w} on the water side of the equation is far greater than that of w_{*a} on the atmospheric side. The relative increase in k due to w_{*a} is only of the order 10^{-3} cm hr^{-1}, compared to 10^{-1}–10^{0} cm hr^{-1} on the water-side from w_{*w}. As expected, the largest differences occur during low wind speeds and larger velocity scales. The relative differences appear to be significant up to 5–6 m s^{-1}.

This suggests that the contribution to gas exchange from convective processes in the oceanic turbulent layer may be a significant missing term in previous estimates of CO_2 transfer. This enhancement will certainly be important regionally, especially in those areas where diurnal warming is prevalent and low wind speed conditions occur. Applying the above and integrating the net CO_2 transfer over a diurnal cycle we now expect to see enhanced gas flux during low winds related to buoyancy driven convective overturning at night.

Admittedly, given that traditional wind-speed only based parameterizations such as Wanninkhof (1992); Liss and Merlivat (1986); Wanninkhof and McGillis (1999) show a transfer velocity of over 20 cm hr^{-1} for a 10 m s^{-1} wind, a convective enhancement of the order 1 cm hr^{-1} may make little difference to the globally integrated transfer of CO_2. It is important however, to remember that it primarily enhances exchange in regions with a net sea to air flux of CO_2 (namely the tropics), so it is possible that this could significantly reduce the globally integrated air to sea flux.

5.4 Data

A combination of in situ observations, satellite data, and model climatology were used to calculate radiative and turbulent fluxes at the surface of the Tropical Atlantic. These fluxes were used to drive a 1-d turbulence closure model.

The radiative fluxes were calculated using data from the PIRATA mooring located at 10°S10°W (see figure 5.1). The next generation ATLAS (Autonomous Temperature Line Acquisition System) supplied the following fields: surface winds; sea surface temperature at 1 m; sea surface conductivity at 1 m (salinity); air temperature; relative humidity; incoming shortwave radiation; rainfall; subsurface temperature (10 depths in the upper 500 m); subsurface conductivity (three depths in the upper 500 m) and subsurface pressure (at 300 m and 500 m). Location 10°S10°W was chosen as Foltz et al. (2003) state that the contribution to the heat budget from advection was minimal in this region.

The temperature data from the PIRATA mooring were used to extract information about the extent of diurnal warming over the course of 2002 (apparent in day-night SST; see figure 5.3). An experimental period between the 1-8th of February 2002 was selected for conducting the model runs since it contained a significant number of days where diurnal warming was greater than 0.4 °C. In addition, this period maximized the availability of the PIRATA data and ancillary fields necessary to drive the model.

In order to force the model we require measurements of: air temperature; wind speed; air pressure; relative humidity; and cloud fraction. As the PIRATA array of moorings does not provide measurements of all the variables necessary to drive the model (estimates

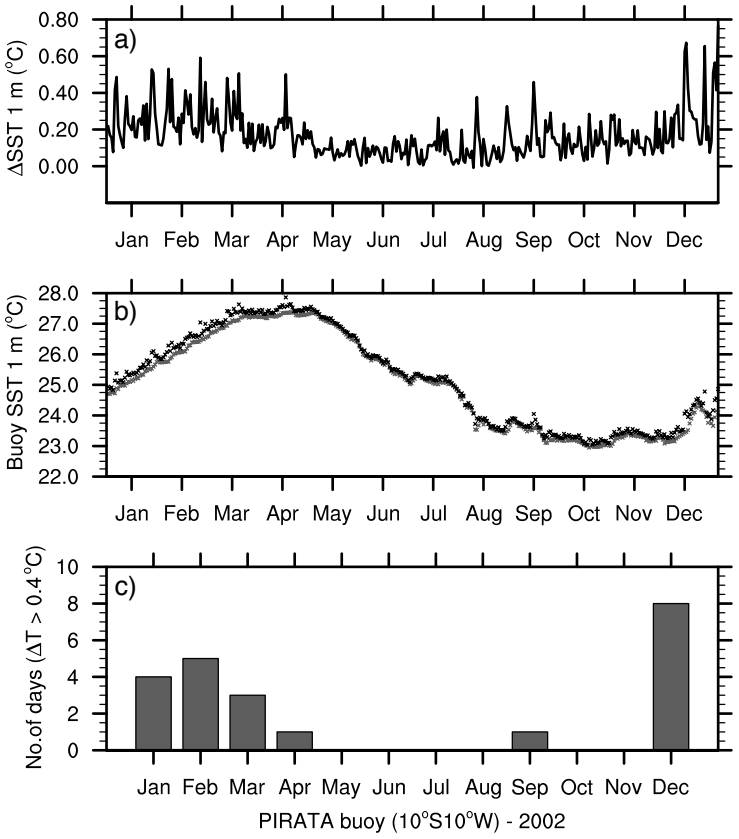

FIGURE 5.3: Sea surface temperature data from the PIRATA mooring located at 10°S10°W over the course of 2002. (a) ΔT, difference between day and night SST 1 m. (b) Maximum daytime SST (Black) and Minimum nighttime SST (Grey). (c) Number of Days with $\Delta T > 0.4$ °C for each month.

of cloud fraction and air pressure are missing), additional data from model climatology and satellite products were used to supplement the in situ observations.

The EUMETSAT operational cloud analysis (CLA) is an automatically generated product describing the total amount of cloud and the cloud top temperatures. The cloud analysis is a coded representation of the amount of cloud in a single image, and is based directly on the cloud clusters extracted during segment processing (EUMETSAT, 1998). We used the CLA from Meteosat-7, a geostationary satellite in orbit at 0° longitude, to estimate the cloud cover necessary for the calculation of the longwave radiation term.

Finally, surface pressure data from the NCEP Reanalysis surface level data set, based on a 2.5 degree latitude $\times$ 2.5 degree longitude global grid with 4 individual observations per day, was interpolated onto an hourly grid for ingestion into the model.

5.5 Model setup

A modified version of the one dimensional General Ocean Turbulence Model (GOTM) was used to generate realistic hydrodynamic and thermodynamic quantities (Burchard et al., 1999). The model computes solutions for the one-dimensional versions of the transport equations of momentum, heat and salt. Initial conditions consist of temperature and salinity profiles with input data on an hourly grid, containing the following parameters: x and y components of wind stress, pressure, air temperature, relative humidity, cloud cover, shortwave radiation, and rain-rate. The model was allowed to run free for the entire experimental period. Model output consists of a 200 level exponential grid with increased resolution near the surface to a depth of 200 m (see figure B.1). The time-step is 120 seconds, with no relaxation to observed profiles. Heat budget and surface fluxes were calculated using COARE 3.0 bulk formulae with the longwave radiation formula of Josey et al. (2003). We define the convention for heat fluxes into the water as positive.

We choose a two equation k_e-ϵ turbulence closure scheme with dynamic dissipation rate equations for the length scales, as it is a good compromise between complexity and simplification (Mellor and Yamada, 1974; Rodi, 1987; Canuto et al., 2001). Furthermore, Stips et al. (2002) compared measured and simulated temperature and dissipation rate profiles from a two equation $k_e - \epsilon$ model and found that the basic features of convectively driven turbulence were well described by the model, with the temporal dynamics of the temperature field correctly simulated. In addition the model includes; Stability method: Kantha and Clayson (1994); Wave breaking parameterization: Burchard (2001); and a parameterization for internal waves: Large et al. (1994).

The model has been modified to include routines for calculating gas transfer. Calculating the air-sea flux of CO_2 requires knowledge of the concentration difference across the interface. This ΔC is approximated as $\alpha \Delta pCO_2$ (see equation 6.3), where ΔpCO_2 is the difference between the partial pressures of CO_2 either side of the air-sea interface. Climatological monthly values are used for pCO_{2a} and pCO_{2w} (Takahashi et al., 2002), and only deviate due to changes in solubility and barometric pressure. As described in equation 5.4, temperature changes affect dissolved ΔC through solubility and the change in mass via the carbonate reaction. In addition, barometric pressure changes are also accounted for by modifying the value of atmospheric pCO_2 as described by Kettle and Merchant (2005). We define the convention for CO_2 effluxes as positive.

The effects of biological or surfactant processes e.g. surface films were not included, although their effects are potentially significant (Goldman et al., 1988; Frew et al., 1990). The NOAA-COARE model contains no provision for the effects of biological processes, and biological feedback was not included within GOTM. Instead we focus solely on the physical aspects of the air-sea exchange.

A separate model for the skin temperature (Fairall et al., 1996b), within GOTM, is present to further improve calculation of gas fluxes by incorporating T_s and α_s. To correctly evaluate the gas transfer taking place during low wind convective conditions the NOAA-COARE gas transfer parameterization with the additional contributions from the water side convective velocity scale as set out in equations (5.19) to (5.26) was used. The temperature and buoyancy effects were explicitly included as gas transfer was calculated at every time-step. While 1-d model simulations will not perfectly agree with observations, especially where 3-d processes are important, the model does allow the contributions from various physical exchange processes to be examined within a realistic framework.

5.6 Results and discussion

5.6.1 Heat budget, meteorology and upper ocean at 10°S10°W

The heat budget for the 7 day experimental period, 1–8th of February 2002, as calculated by the 1-d model is shown in figure 5.4. In situ observations of incoming solar shortwave radiation (as seen in the top panel), along with the calculated fluxes from the COARE version 3.0 algorithm produce the resultant net surface heat flux, as described in equation 5.1. The diurnal cycle is evident during the day as the incoming solar radiation heats the surface ocean followed by infrared radiation, evaporation and sensible heat fluxes cooling the surface at night. Q_s was in the range of 0–1200 W m^{-2} with large fluxes of Q_l and Q_e -40 to -100 W m^{-2} and -40 to -160 W m^{-2} respectively. The sensible heat loss and the contribution due to rain were small in comparison to the other fluxes, not exceeding -25 W m^{-2}.

The modeled 1 m temperatures generally agree well with the observations from the buoy, although the amplitude of the modelled diel variations are generally larger than those observed. Assuming that the observed values are accurate, the model surface 1 m temperatures have a rmse of 0.017 °C (see figure 5.5). Each 24 hour period showed distinct warming during mid-late afternoon with a maximum model ΔT of at least 0.4 °C, which was as great as 0.7 °C on 6th February. Where ΔT is the diurnal variability and is defined as the difference between the maximum SST after 9 am and the minimum SST before 9 am on the following day.

The calculated fluxes, and the meteorological forcing drive the thermodynamic and hydrodynamic equations which produce the temperature, salinity and density profiles shown in figure 5.6. The response of the ocean to the diurnal forcing produced obvious diurnal temperature stratification in the upper ocean, along with corresponding changes in salinity (S) and density (σ_θ). Warm layers occurred daily throughout the experimental period down to a depth of approximately 20 m and were repeatedly broken up by

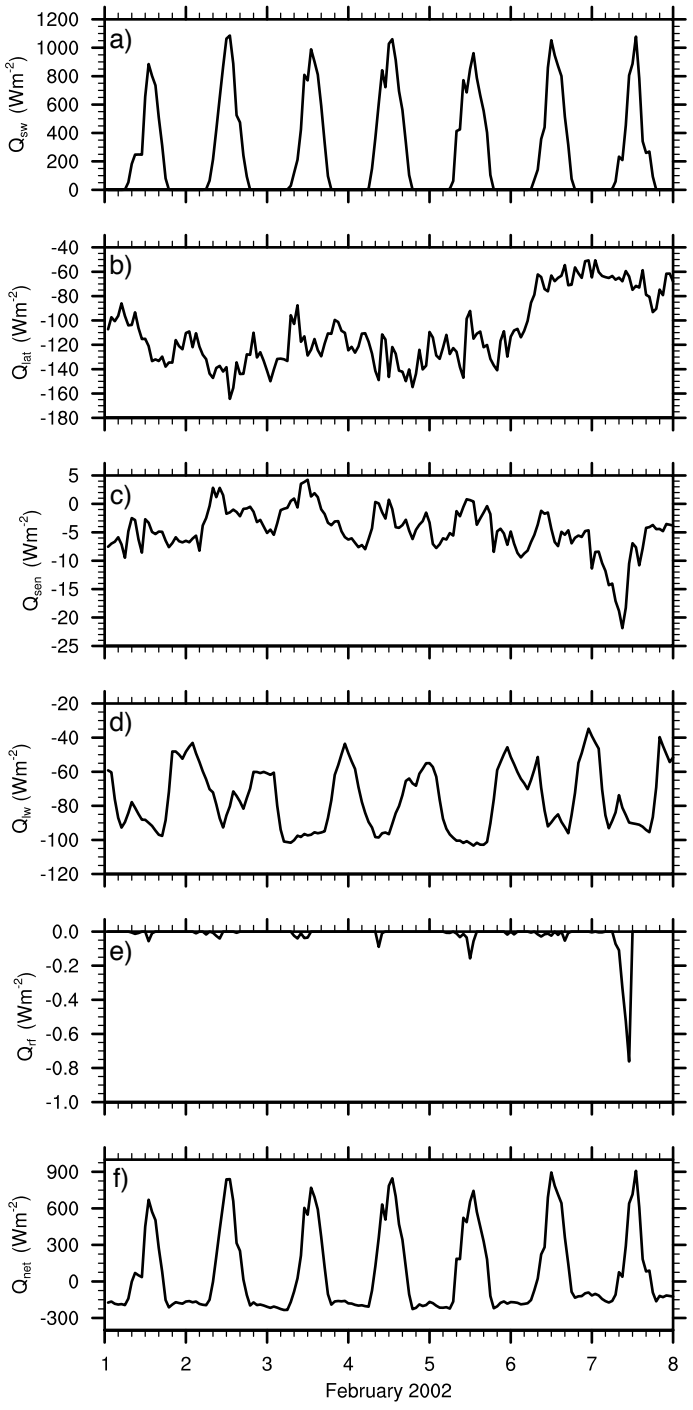

FIGURE 5.4: GOTM derived heat budget calculated using NOAA-COARE v3.0 with observations from the PIRATA buoy located at 10°S10°W between 1–8th February 2002. (a) Observed Incoming solar shortwave radiation, (b) Latent heat flux, (c) Sensible heat flux, (d) Net longwave heat flux, (e) Sensible heat flux due to rain and (e) Net heat flux. All units are W m^{-2}, positive sign indicates flux into the ocean.

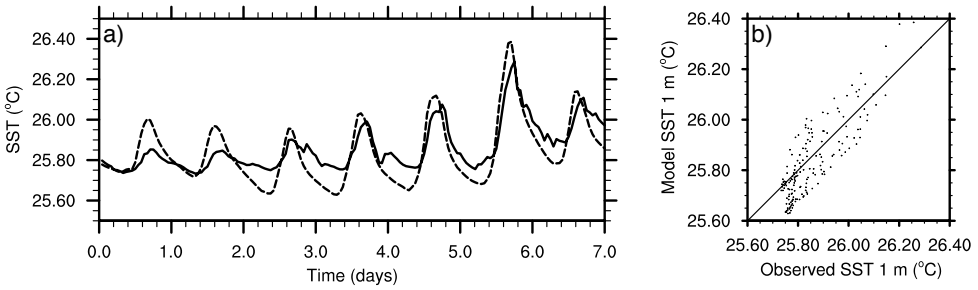

FIGURE 5.5: (a) Comparison between modelled (dashed line) and observed (solid line) 1 m SST plotted against time. (b) Scatter plot showing GOTM 1 m SST against PIRATA 1 m SST. Units are °C.

nighttime cooling and mixing. Modelled cool-skin temperatures at the interface were between 0.10–0.35 °C cooler than that of the turbulent water below (see figure 5.7).

Wind speeds over the experimental period were in the range 3.8–10.0 m s^{-1} and did not show significant diurnal variations (see figure 5.8). The mean wind speed was 7.2±1.3 m s^{-1}. Thus diurnal processes, namely the heating and cooling of the ocean's surface, are likely to be responsible for the majority of the variability in the heat budget. Accounting for this variability is important for accurately evaluating CO_2 exchange.

Figure 5.7 also shows ϕ, the buoyancy scaling parameter responsible for the processes occurring in the thermal molecular sub-layer (see equations 5.11 and 5.12). Its effect is to increase the transfer velocity and for the majority of the model period is low, not reaching a value greater than 1.02. On three occasions, 3rd, 5th and 6th of February, however, there are significant 'spikes' corresponding to low wind speed events (see figure 5.8), as the Saunders (1967) parameter is dependent on u_* to the fourth power.

The surface buoyancy flux (B_{fw}) calculated according to Dorrestein (1979) can be seen in figure 5.8. The Q_s term is included within the formulation for the net surface heat flux, and as such B_{fw} follows the diurnal heating cycle and is negative during convective conditions. The Monin-Obukhov length scale, $L \equiv -u_*^3/\kappa B_{fw}$ (figure 5.7), gives the relative strength of the wind stress and surface buoyancy flux. $|L|$ is the depth scale at which wind stress and B_{fw} are equally as effective in producing turbulence within the mixed layer. Thus, convection should be the dominant mechanism for $|z_{ml}/L| > 1$, if $|L|$ is less than the mixed layer depth, z_{ml} (Shay and Gregg, 1984).

The lower 2 panels in figure 5.8 show the atmospheric and water-side velocity scales. These scales serve to represent the effects of convective processes on gas transfer. Although w_{*a} is of the same order of magnitude as u_{*a}, we know from figure 5.2 that its effect is negligible. More important is the w_{*w} term, which is a function of B_{fw} and z_{ml}. It is greatest wherever evaporative cooling causes gravitational instability and convective mixing (Csanady, 1997) and whenever z_{ml} is large. It is the same order of magnitude

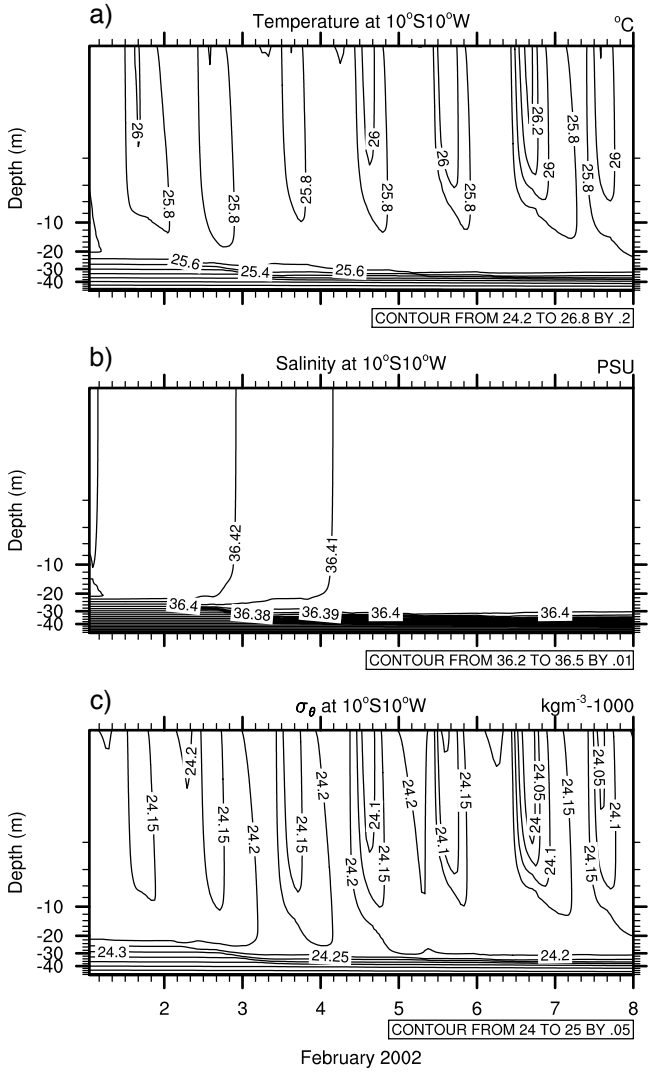

FIGURE 5.6: Upper ocean time-series as modelled by GOTM at PIRATA location 10°S10°W, (a) Subsurface temperature (°C), (b) Salinity (PSU) and (c) Density (kg $m^{-3} - 1000$) plotted against depth in metres (logarithmic), between 1–8th February 2002.

as u_{*w} and is set to zero during times when the B_{fw} is positive. During convective conditions, when $B_{fw} < 0$, it serves to enhance the transfer velocity and hence CO_2 flux.

The above modelled conditions serve as the basis for the following model experiments. Realistic conditions are provided by the 1-d model, driven by in situ PIRATA observations, remotely sensed data and model reanalysis fields. It appears from the results that the 1-d model adequately relates temperature changes and sensible estimates of the turbulent structure. It was chosen as the basis for simulating the CO_2 flux and its dependance on convective processes when the wind is low.

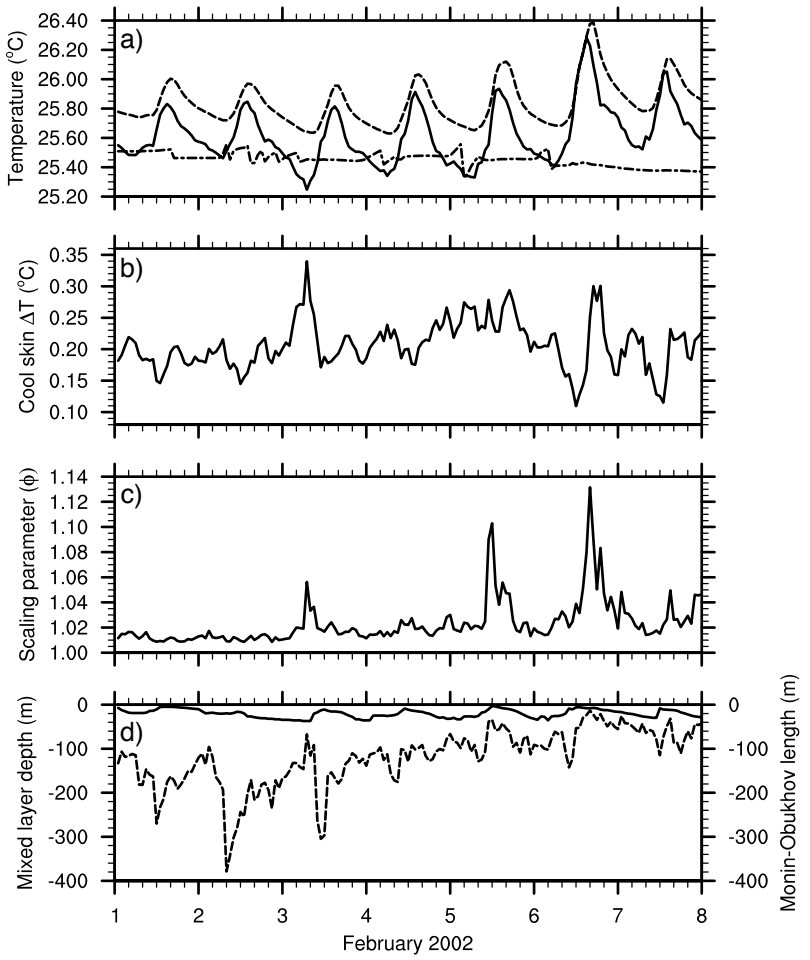

FIGURE 5.7: Modelled (a) Skin temperature (^oC) - solid line; SST_{1m} (^oC) - dashed line; and temperature along the 24.5 kg m^{-3} isosurface (°C) - dotted dashed line, (b) Cool skin ΔT (°C), (c) Buoyancy scaling paramter ($\phi = 6/\lambda_s$) and (d) Mixed layer depth (solid line) and Monin-Obukhov length (dashed line) (m), between 1–8th February 2002 at PIRATA buoy location 10^{o}S10^{o}W.

5.6.2 Constant wind profiles

Large scale estimates of CO_2 fluxes are typically calculated over periods of months, using time averaged data, which is often at an inadequate resolution. Averaging the wind speed data over periods that are too long results in the loss of extreme values, and hence underestimate of the amount of CO_2 exchanged. Wanninkhof et al. (2002) avoid this problem by proposing an alternative formulation for their k vs. u_{10} based parameterization, one for instantaneous wind fields and another for long-term wind data. They propose not to use time averaged winds but rather compute the time-averages of higher moments needed for non-linear relationships from reanalysis or satellite winds. In our case this is resolved by using hourly in situ observations, which include wind speed. The flux of CO_2 is evaluated at every time-step, thus the net flux of CO_2 over

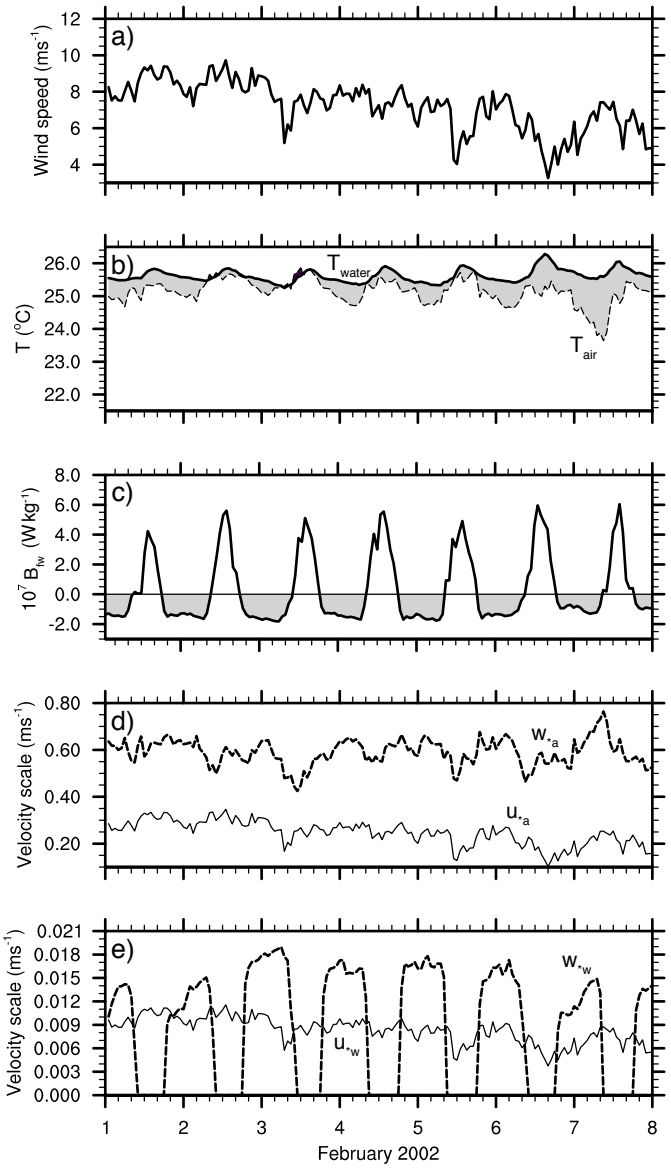

FIGURE 5.8: Observed and calculated surface meteorological variables between 1–8th February 2002 at 10°S10°W. (a) Observed wind speed (m s^{-1}), (b) Observed air temperature and water temperature at 1 m (°C), (c) Calculated water-side surface buoyancy flux (W kg^{-1}) (d) Calculated friction velocity (u_{*a}) and convective scaling velocity (w_{*a}) on the atmosphere side (m s^{-1}) (e) Calculated friction velocity (u_{*w}) and convective scaling velocity (w_{*w}) on the water side (m s^{-1}).

the experimental period is simply integrated over time. In this way changes in diurnal radiative forcing and the subsequent effects on the upper ocean are better taken into account.

Replacing the observed wind speed data with constant wind forcing for the duration of the model run (1–8th February), causes the variability in k and hence CO_2 flux to become a result of the heat budget and barometric pressure variation over the diurnal cycle. A range of constant wind levels between 0–10 m s^{-1} were used to evaluate the effect of the convective processes. The relative differences in k and CO_2 flux generated with and without the convective effects were compared. The mean k and net CO_2 flux for each wind level are presented in table 5.1, calculated using the Soloviev and Schlüssel (1994) A and B coefficients (see equations 5.9 and 5.11).

Figure 5.9a shows the mean increase in k over the experimental period versus wind speed (cm hr^{-1}), and figure 5.9b shows equivalent percentage change. The following values for A are used: 1.85 (Soloviev and Schlüssel, 1994); 1.3 (McGillis et al., 2004); and 0.63 (Hare et al., 2004). The model run included near zero values during the day, which increased at night, during convective conditions. Looking at the percentage change in k we can see that, for each A, the greatest increase occurs at low winds ($\leq$ 4 m s^{-1}), with substantial increases in transfer velocity up to 6 m s^{-1} (corresponding to about 10%).

Comparing the convectively enhanced k with traditional estimates (figure 5.9c) we can see that the transfer velocities predicted by Wanninkhof (1992), Liss and Merlivat (1986) and Wanninkhof and McGillis (1999) are near zero, and remain low until about 5-6 m s^{-1}. Conversely, the modified NOAA-COARE parameterization ($A = 1.85, B = 1$) includes substantially higher values for k in the low wind speed range. The simple wind speed based relationships underestimate k, and hence the flux of CO_2 during low wind conditions. However at wind speeds greater than 6 m s^{-1}, where the largest CO_2 fluxes occur, the increase due to convective processes is marginal (see table 5.1). The variability in figure 5.9 is estimated as 1σ, calculated for each wind level and A over the experimental period.

In this region of the tropical Atlantic, CO_2 flux is positive, (from the sea to the air), as dictated by the partial pressure difference of the gases either side of the interface. The addition of the convective processes serves to increase the flux (i.e. it becomes more positive). Comparing average k and net CO_2 flux for each of the constant wind levels in table 5.1, it is clearly evident that the relative importance of the buoyancy driven contribution is greatly reduced at higher wind speeds.

Nonetheless, the response of k and CO_2 flux to increasing buoyancy driven convection is generally smaller than the response to choosing different empirical coefficients for A. Conversely, B, which is a strong function of wind speed, is less important as its effect is minimal when the contribution from convective processes are strongest. These adjustment factors are designed to fit the model to measured transfer velocities, they produce

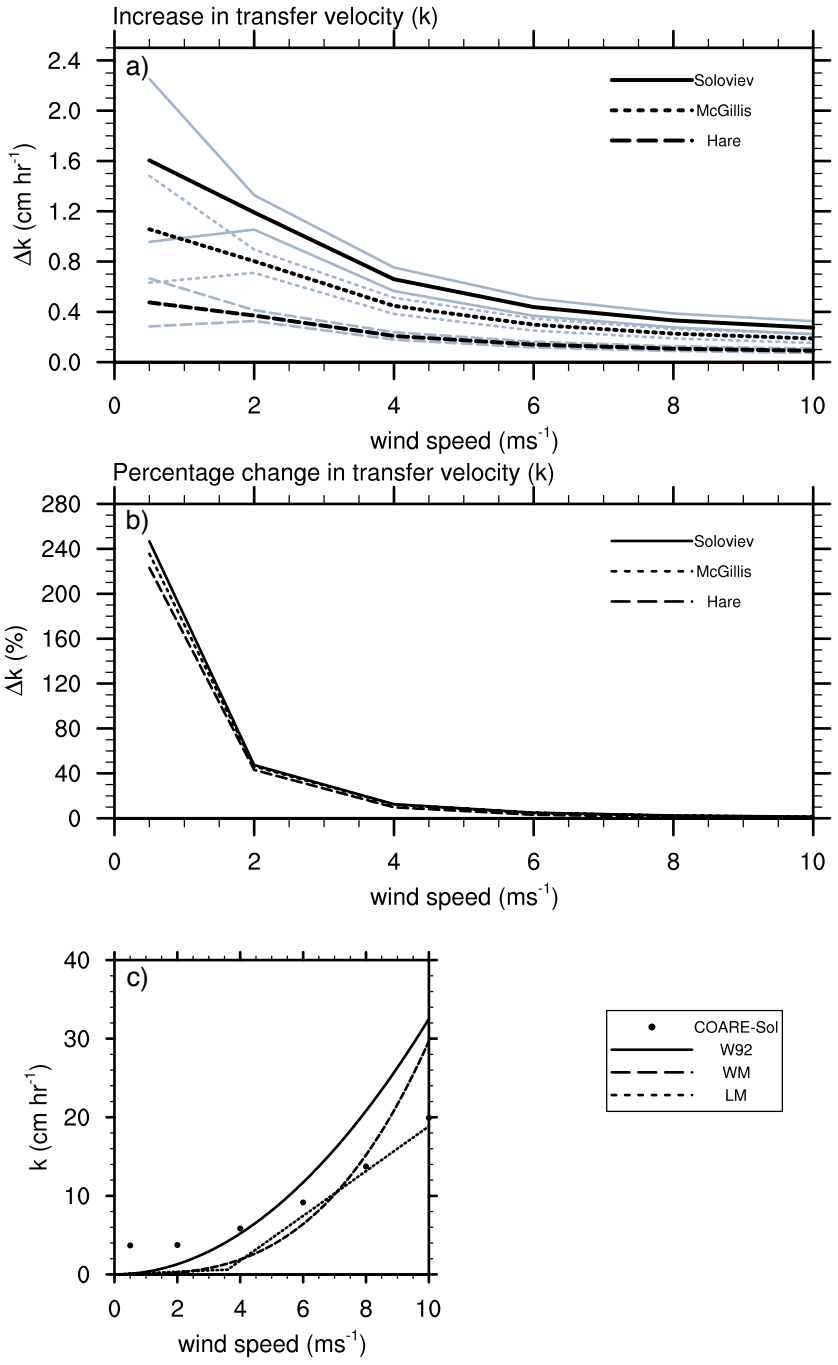

FIGURE 5.9: a) Mean convective enhancement to transfer velocity, k (cm hr^{-1}) for a range of constant wind speeds, with variability of 1σ plotted as thin grey lines and b) Percentage change in k with wind speed for three applications of empirical coefficients: $A = 1.85, B = 1$ (Soloviev and Schlüssel, 1994) (Solid line), $A = 1.3, B = 0.82$ (McGillis et al., 2004) (dotted line) and $A = 0.63, B = 1.2$ (Hare et al., 2004)(dashed line). c) Comparison of the following transfer velocity parameterizations against wind speed: k COARE ($A = 1.85, B = 1$), W92 (Wanninkhof, 1992), WM (Wanninkhof and McGillis, 1999) and LM (Liss and Merlivat, 1986) based on $T = 20°$C.

$\overline{u_{10}}$ (m s^{-1})	$\overline{k}$ (cm hr^{-1})	$\uparrow \overline{k}$	$Net\ F_{CO2}$ (mol m^{-2} yr^{-1})	$Net \uparrow F_{CO2}$	$\uparrow \overline{k}$ (%)
0.5	2.25 ± 0.648	1.60	2.01 ± 0.045	1.41	246.76 ± 96.72
2	3.70 ± 0.137	1.19	2.76 ± 0.034	0.85	47.42 ± 5.44
4	5.92 ± 0.094	0.65	9.47 ± 0.068	1.03	12.51 ± 1.78
6	9.24 ± 0.070	0.44	18.36 ± 0.004	0.86	4.97 ± 0.78
8	13.81 ± 0.055	0.33	30.65 ± 0.004	0.73	2.50 ± 0.41
10	19.98 ± 0.052	0.27	47.71 ± 0.004	0.65	1.39 ± 0.26

TABLE 5.1: Effect of increasing constant wind speeds on transfer velocity and CO_2 flux. Results are averaged values over experimental the period 1–8th February 2002 at 10°S10°W, k was calculated for $A = 1.85, B = 1$; Soloviev and Schlüssel (1994). Fluxes employing other empirical coefficients as described in section 5.3.2 were calculated but are not shown. Stated errors are 1σ.

curves with differing magnitudes but of nearly constant ratio. Hence an appropriate value must be chosen for the NOAA-COARE parameterization before the convective processes are considered.

5.6.3 CO_2 exchange at 10°S10°W

Incorporating the data available, the 1-d model was used to estimate the transfer velocity and net CO_2 flux at the PIRATA site defined in section 5.4, taking into account the diurnal convective contributions. Strong diurnal cycles in near surface temperatures, solar incidence, bulk temperatures and surface buoyancy flux were observed (figures 5.7 and 5.8). Under these conditions radiation absorbed over the top several metres of the water column is released at night, cooling the surface.

In figure 5.10, k (upper panel) and CO_2 flux (middle panel) showed increased effects from w_{*a}, w_{*w} and ϕ during periods of lowest wind speed consistent with the earlier idealized experiments. The difference between model runs with and without the convective terms are shown as a percentage change (lower panel). This residual represents the enhancement to k from buoyancy-driven convective processes. The largest enhancement to k, occurred on the 6th of February, and was almost 20%. At higher wind speeds, however, the residual enhancement was small (around 2–3%).

In addition to enhancing k, the presence of a diurnal mixed layer and varying temperature and salinity gradients (see figures 5.6 and 5.7) also influenced the thermodynamic driving force, the product of the solubility and ΔpCO_2. Incorporating these upper ocean processes modifies the exchange during the course of the day, which is important when considering the time-integrated CO_2 flux.

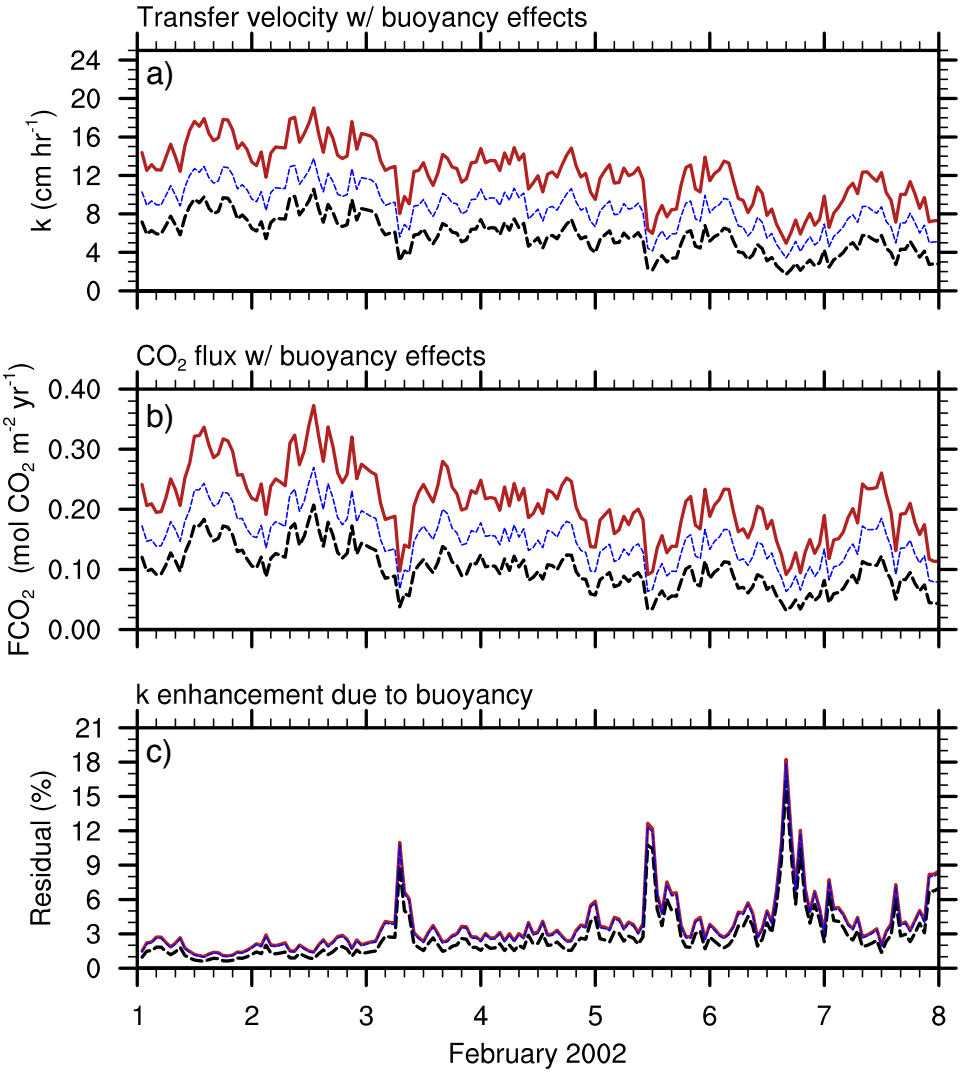

FIGURE 5.10: Modelled (a) Transfer velocities (cm hr^{-1}) and CO_2 (mol CO_2 m^{-2} per unit time) fluxes; (b) Integrated daily CO_2 flux difference; (c) Residual (%) enhancement due to buoyancy, between 1-8th February 2002 at 10°S10°W. Different lines represent the following A and B coefficients for the NOAA-COARE gas transfer model: Solid red lines - (Soloviev and Schlüssel, 1994); thin blue dashed lines - (McGillis et al., 2004); thick black dashed lines - (Hare et al., 2004).

As in figure 5.9, the three curves in figure 5.10 represent different applications of the A and B coefficients within the modified NOAA-COARE model (as described in equations 5.9 and 5.11). The coefficients are adjustment factors based on measured transfer velocities, and their values chosen from previous studies: A=1.85 B=1 — Soloviev and Schlüssel (1994); A=0.63 B=1.2 GasEx 98 — Hare et al. (2004); A=1.3 B=0.82 GasEx 2001 — McGillis et al. (2004). The result is three curves which differ mainly in magnitude, and have nearly a constant difference. Since the wind speed remains < 10 m s^{-1} for the duration of the experimental period, the low wind speed empirical coefficient, A, is primarily responsible for these differences. Whereas the factor B, relating to the contribution from whitecap generated bubbles, has little effect as it is a strong function of wind-speed.

COARE coefficients	$\overline{k}$ (cm hr^{-1})	$\uparrow \overline{k}$	$Net\ F_{CO2}$ (mol m^{-2} yr^{-1})	$Net \uparrow F_{CO2}$	Flux enhancement (%)
A =1.85, B = 1.0	12.2 ± 3.1	0.40	35.5 ± 0.06	1.10	3.1
A = 0.63, B = 1.2	5.8 ± 1.9	0.12	16.8 ± 0.04	0.35	2.1
A = 1.30, B = 0.82	8.7 ± 2.3	0.26	25.2 ± 0.04	0.75	3.0

TABLE 5.2: Average transfer velocities (cm hr^{-1}), integrated CO_2 fluxes (mol m^{-2} yr^{-1}) and actual and percentage effects over the experimental period 1–8th February 2002 at 10°S10°W as calculated by the GOTM model. Stated errors are 1σ. Results are based on a number of values for the NOAA-COARE empirical coefficients A and B based the on the literature.

The Soloviev and Schlüssel (1994) version of the model produces the largest transfer velocities, which on average are almost twice that of the Hare et al. (2004) version. This corresponds to integrated fluxes of CO_2 around three times as large. The enhancement to the net CO_2 flux when integrated over the week was approximately 3% (see table 5.2). As described earlier in section 5.6.2, the result of using the different factors for A and B when calculating the CO_2 flux is substantially greater than that resulting from convective enhancement. Additionally, the residual produced by the convective effects is generally quite small and of a similar fraction for the chosen adjustment factors of A. It is therefore important that these should be carefully selected before attempting to 'fine-tune' the model.

Similar results were observed by McGillis et al. (2004) during the GasEx-2001 study in the equatorial Pacific during February 2001. The authors report prevalent low wind speeds (< 6 ms^{-1}) in a region of high CO_2. Their data suggested an elevated k at wind speeds less than 6 ms^{-1}, and a very weak dependence on wind speed. Nighttime cooling resulted in a decrease of both air temperature and water temperature, similarly observed in our modelled fields. They attributed the observed 40% increase in CO_2 flux at night over daytime values to enhanced convective overturning at night and surface turbulence throughout the diurnal cycle. The similarity of our results (10°S10°W) to the behavior

observed in the Pacific suggests that the contribution to gas exchange from convective processes is an important missing term within the calculation of the net gas transfer, with common environmental conditions producing significant flux enhancement, up to 20% instantaneously and around 3% when integrated over a week.

We have chosen to focus on the physical aspects of the air-sea exchange, namely the convective contributions to the transfer velocity. For completeness, we have included temperature and salinity information as calculated by the 1-d model to improve estimation of the CO_2 flux. We express the CO_2 flux in terms of commonly used, partial pressures of CO_2 in air and surface seawater respectively. Note that the fugacity of a gas is the partial pressure corrected for non-ideality of the gas with respect to molecular interactions between CO_2 and air. The values for fugacity of CO_2 and corresponding pCO_2 are very similar with $fCO_2 = (0.9956\ pCO_2)$ at 0 °C, and $fCO_2 = (0.9970\ pCO_2)$ at 30 °C (Weiss, 1974).

According to a recent study by McGillis and Wanninkhof (2006), it is the concentration gradient in the aqueous boundary layer that determines the magnitude and direction of the flux. Their study suggests that it is more appropriate to express the flux in terms of $[CO_{2aqw}]$ and $[CO_{2aq0}]$, the aqueous CO_2 concentrations at the bottom and the top of the aqueous boundary layer. This approach is fully interchangeable with using fugacities (or partial pressures), and the result yields numerically the same flux as when using fCO_2, although the mechanism is different. Given an increase in temperature at the diffusive boundary layer, when using the concentration gradient, $[CO_{2aq0}]$ decreases and $[CO_{2aqw}]$ increases. While for fCO_2, the conceptual picture is the only the bulk water values appreciably change. The authors also suggest that since the CO_2 concentration gradient in the molecular boundary layer will only extend over a small part of the temperature gradient, the cool-skin effect is overestimated. While this would serve to reduce the overall magnitude of the CO_2 flux, the contribution from convective enhancement should remain important.

Using the method from McGillis and Wanninkhof (2006) requires that $[CO_{2aq0}]$ and $[CO_{2aqw}]$ be determined using the temperature at the surface and at the bottom of the boundary layer. The conversion of fCO_2 at the depth of measurement has to be done with empirical estimates of the relationship between fCO_2 and temperature. The values used for fCO_{2w} in our study were modified from the climatology of Takahashi et al. (2002) according to $dfCO_2/dT = 0.0423\ °C^{-1}$ (Takahashi et al., 1993). This temperature dependance is actually a function of temperature, salinity and the T_{CO_2}/T_{Alk} ratio. The relationship $dfCO_2/dT$ can range from 0.053 to 0.037 $°C^{-1}$ for surface water with significant differences between parameterizations. In order to better improve the estimates of CO_2 flux the uncertainty in the temperature dependance of pCO_2 at different T_{CO_2} and T_{Alk} concentrations as well as the CO_2 solubility of environmental temperature and salinity ranges needs to be resolved. Given that our estimates of the CO_2 flux are not intended to represent the true flux, since we are using the climatological

values of Takahashi et al. (2002). They are more than suitable to provide context for the impact of the convective enhancement of the transfer velocity on the flux of CO_2.

Another important process, not explicitly included within our study, is the role of chemical enhancement at low winds (Johnson, 1982; Wanninkhof and Knox, 1996). Under conditions of low turbulence and high pH, chemically reactive gases can bypass the rate-limiting molecular diffusion step by undergoing hydration reactions the boundary layer with hydroxide ions and water molecules. The reaction rates are a function of temperature, pH and ionic strength (and therefore salinity). In the study by Wanninkhof and Knox (1996) the authors show that chemical enhancement has a minor effect on air-sea gas exchange under average oceanic turbulent conditions. However, for the equatorial CO_2 source regions, with high temperatures and low winds, the calculated CO_2 enhancement amounts to 4–8% of the total exchange. While this is not important globally, it is important in the same regions as the enhancement from convective processes. Thus we would expect to see even larger discrepancies in regional CO_2 flux estimates where both processes occur.

In addition, it is likely that the diel wind history will play an important role in determining the CO_2 flux. Periods of sufficiently low winds and strong insolation are required to produce diurnal stratification necessary for convective enhancement. The timing of these low wind periods is crucial for determining the upper ocean temperature structure and hence the magnitude of the enhancement to the integrated CO_2 flux. This follows from McNeil and Merlivat (1996), where the authors introduce the concept of regional asymmetry in net CO_2 flux brought about by processes such as the warm surface layer. For example, equatorial and mid-latitude regions, which are strong sources of CO_2 would see enhanced CO_2 evasion from the ocean. Conversely, high latitude regions, CO_2 sinks, would not be expected to develop a warm layer. In these regions, the effects should be minimal. Future work should serve to validate the convective terms and investigate the role of wind history on integrated fluxes.

5.7 Conclusions

This study serves to highlight the importance of convective processes for estimates of gas transfer, in particular air-sea CO_2 fluxes. 1-d modelling using in situ observations from the PIRATA array, cloud cover estimates from Meteosat-7 and model reanalysis pressures from NCEP have allowed the calculation of transfer velocities and CO_2 fluxes on timescales required to identify the effect of buoyancy driven convection on the air-sea flux of CO_2.

The model results reveal that exchange under convective conditions is important on daily time scales, with traditional wind speed dependent parameterizations overlooking

significant increases brought about by convective processes. Transfer velocity enhancement of up to 20% was observed in the tropical Atlantic, under conditions of strong insolation and low wind speeds. Tropical regions, susceptible to the greatest effect, tend to have a net sea to air flux of CO_2, thus it is possible that this could significantly reduce the globally integrated air to sea flux, but this is yet to be demonstrated.

Certainly however, where wind speeds are typically low, neglecting this additional contribution will cause errors that are significant when evaluating local/regional space-time variability of CO_2 fluxes. The phenomena required to produce noticeably significant modifications to the CO_2 flux are quite variable on both temporal and spatial scales. Future work requires validation of the model, and the integration of a number of different datasets containing additional information such as skin temperature measurements from IR radiometers and in situ pCO_2 data.

In order to improve estimates of the net CO_2 flux, parameterization of these convective effects is necessary. An understanding of factors controlling the likelihood of convective enhancement is required e.g. strong solar insolation, large buoyancy fluxes and low winds. It has become obvious that the highest possible resolution data, or at least data on the timescales of the significant transfer processes, are necessary; coupled with the use of physically-based micrometeorological models for the gas transfer velocity where appropriate. As new remote sensing products become available, such as diurnal warming estimates and heat flux products, the ability to improve regional and global gas flux estimates should be possible.

Chapter 6

Phase dependent forcing and diurnal warming

This chapter is a research article (Jeffery et al., 2008) that has been published in Ocean Modelling, Volume 23, Pages 33-48 (doi:10.1016/j.ocemod.2008.03.003). The manuscript was submitted on the 16^{th} November 2007, accepted 7^{th} March 2008 and was available online on the 29^{th} March 2008. The role of the co-authors was supervisory in nature, with the substantive work carried out by the lead author.

6.1 Introduction

Upper ocean temperatures are directly affected by the daily cycle of solar insolation. The characteristics of the temperature structure ultimately depend on the surface heat flux and on the wind stress which provides the mechanical energy available to mix heat down. Diurnal variations caused by the daily cycle of solar radiation are important for air-sea interaction processes. CO_2 exchange is highly sensitive to variations in temperature at low wind speeds through its dependence on solubility (Jeffery et al., 2007).

The purpose of this study is to model the diurnal variation of temperature and gas transfer, in order to estimate how the CO_2 flux responds to varying wind speed and cloud fraction, during generally low wind conditions. In particular it explores whether the phasing of time-dependent wind stress and cloud fraction with respect to the solar heating cycle can lead to enhanced diurnal sea surface temperature (SST) amplitudes, and whether this has climatically important consequences for air-sea CO_2 exchange.

6.1.1 Upper-ocean temperature

Almost half the incoming shortwave radiation penetrating through the ocean's surface is absorbed within the top metre of the water column (Ivanov, 1977). During clear-sky, low-wind conditions, solar irradiance creates a highly stratified, buoyant warm layer in the top few metres (Price et al., 1986). For progressively lower wind, the diurnal warm layer becomes shallower and hotter, with a surface temperature rise during the day as large as 6 °C in calm conditions (Stuart-Menteth et al., 2005b). At night, surface heat loss cools the surface, promoting convective overturning which destroys the diurnal thermocline.

In considering how diurnal temperature variability affects the air-sea flux of CO_2, it is important to distinguish between the skin temperature (SST_{skin}), the sub-skin temperature ($SST_{subskin}$) and the foundation temperature (SST_{fnd}), using the terminology adopted by the GODAE High-Resolution SST Pilot Project (GHRSST-PP) (Donlon, 2007).

The skin temperature (SST_{skin}) refers to the topmost 10–20 μm layer of the sea, directly in contact with the atmosphere. It is measured by an infrared radiometer operating at wavelengths between 3.7–12 μm. Heat transport very close to the air-sea interface is constrained by molecular conduction, down to a depth of a few mm where turbulent processes dominate (Jähne and Haußecker, 1998; Donelan and Wanninkhof, 2002; Soloviev and Schlüssel, 2002; Ward and Donelan, 2006). A steep temperature gradient is required to drive heat conductively across this layer in order to supply the heat flux at the air-sea interface, which is the sum of the sensible, latent and longwave fluxes and nearly always flows from the sea to the air. $SST_{subskin}$ is the temperature at the bottom of this thermal skin layer. It is approximately the temperature measured by satellite microwave radiometers, and corresponds to the temperature measured by thermometers in the ocean surface mixed layer in strong wind conditions. The conventional 'bulk SST' refers to the in situ temperature measured below the conductive laminar sub-layer, and corresponds to SST_{depth} as described by the GHRSST science team. The terminology used throughout this paper is well described by Kawai and Wada (2007), in particular table 1.

Observations show the cool-skin deviation, SST_{skin} - $SST_{subskin}$, to be approximately -0.17 °C (Donlon and Robinson, 1997; Donlon et al., 1999) and estimates of air-sea CO_2 flux must take this into account. However, the cool-skin deviation is only weakly affected by wind speed and is thought to contain little diurnal variability because both SST_{skin} and $SST_{subskin}$ vary together over the diurnal cycle. Diurnal variability of SST is caused by temperature gradients in the upper few metres of the water column and can be characterised as $\Delta T = SST_{subskin}$ - SST_{fnd}. The foundation temperature, SST_{fnd}, is by definition the temperature at the base of the diurnal thermocline. It is the temperature of the upper mixed layer in the morning before any diurnal warming has commenced,

identical to $SST_{subskin}$ at dawn. For simplicity we define the the diurnal variability, ΔT as the difference between the peak daytime value and the preceding nighttime SST minimum, near daybreak (Webster et al., 1996; Clayson and Weitlich, 2006).

This study supercedes the experiments conducted by Dickey and Simpson (1983), in which they modelled the impact of time-varying wind speed on the magnitude of the diurnal cycle. By forcing a diurnal signal in the wind field at different phase lags with respect to the solar radiation, they found that maximum ΔT occurred on days when winds were low during the daytime, particularly around local noon. From field observations, Price et al. (1987); Flament et al. (1994); Yokoyama et al. (1995) report that ΔT_{max} occurs at a mean local time of 14:30 but with considerable scatter ranging between 11:00 and 18:00. Stuart-Menteth et al. (2005b) used field data from buoys deployed in the Arabian Sea and the Western Equatorial Pacific to investigate more than 250 individual diurnal SST cycles. They classified the shapes of the diurnal cycles into four separate categories based on different daily wind and insolation variations, providing examples against which to compare the model results in this paper.

In addition, near surface profiles and skin temperature measurements were obtained in the Gulf of California as part of the Marine Optical Characterization Experiment (MOCE-5), using the Skin Depth Experimental Profiler (SkinDeEP) and Marine Atmosphere Emitted Radiance Interferometer (M-AERI) (Ward, 2006).The results identified strong diurnal warming within the upper few meters, and a strong dependency of the SST on air-sea heat flux, with warm-layer errors of almost 60 W m^{-2}. These errors, associated with intense stratification, highlight the importance of the inclusion of the skin temperature for accurate calculation of latent, sensible, and net longwave heat fluxes (Ward, 2006; Kawai and Wada, 2007)

6.1.2 Air-sea gas exchange

The diurnal variation in the upper-ocean is also important for understanding air-sea interaction processes (Webster et al., 1996), including carbon dioxide exchange (Ward et al., 2006). The flux of CO_2 or other gas, F, across the air-sea interface can be described by the bulk formula:

$$F = k\Delta C \tag{6.1}$$

where k is the gas transfer velocity, which characterizes the resistance to gas exchange across the boundary layers, and ΔC is the effective concentration difference driving the net flux.

Conventional estimates of air-sea exchange rely on simple, empirical, wind-speed dependent models of k (Liss and Merlivat, 1986; Wanninkhof, 1992; Wanninkhof and McGillis,

1999). However, it is difficult to parameterize all the physical processes contributing to the flux. These include, but are not limited to penetrative convection due to heat loss (Jähne and Haußecker, 1998; Csanady, 1997), shear due to wind forcing, wave breaking at moderate wind speeds (Zappa et al., 2001) and bubbles at high wind speeds (Woolf, 1993, 1997). Comparisons of several k parameterizations have been undertaken by Boutin et al. (2002); Olsen et al. (2005); Woolf (2005), and reveal that flux estimates are highly sensitive to the selection of the gas transfer relationship. Although turbulence is usually driven by the wind, there is not a unique relationship between gas transfer and wind speed due to a number of effects, with diverse results evident at higher wind speeds. Variability in the turbulent exchange is also evident at low wind speeds as the presence of biological surfactants can reduce the transfer (Frew et al., 1990).

Gases such as CO_2, which are only slightly soluble in water, are rate-limited by the aqueous boundary layer (Liss, 1983). McGillis and Wanninkhof (2006) define the flux across the aqueous mass boundary layer for CO_2 as:

$$F = k([CO_{2aqw}] - [CO_{2aq0}]) \tag{6.2}$$

where $[CO_{2aqw}]$ and $[CO_{2aq0}]$ are the aqueous CO_2 concentrations at the bottom and top of the aqueous mass boundary layer. The $[CO_{2aq0}]$ is controlled by the convection of CO_2 in the atmosphere and the temperature at the top of the boundary layer, and to a lesser extent the salinity, whereas $[CO_{2aqw}]$ is a function of the temperature, salinity, alkalinity and total inorganic carbon content of the seawater.

However, the CO_2 flux is often presented in terms of the fugacity or partial pressure difference, rather than as a concentration difference across the interface, such that:

$$F = k\alpha[(fCO_{2w}) - (fCO_{2a})] = k\alpha\Delta fCO_2 \tag{6.3}$$

where α is the solubility as a function of temperature and salinity and $f\mathrm{CO}_{2w}$ and $f\mathrm{CO}_{2a}$ are the fugacity of CO_2 in water and air respectively (Wanninkhof and McGillis, 1999; Ward et al., 2004). The fugacity of a gas is its partial pressure corrected for non-ideality of the gas with respect to molecular interactions between CO_2 and air. The values for fugacity of CO_2 and corresponding $p\mathrm{CO}_2$ are very similar with $f\mathrm{CO}_2 = (0.9956\ p\mathrm{CO}_2)$ at 0 °C, and $f\mathrm{CO}_2 = (0.9970\ p\mathrm{CO}_2)$ at 30 °C (Weiss, 1974). The product of α and $\Delta p\mathrm{CO}_2$ is often referred to as the thermodynamic driving potential.

Since α is a function of temperature, it will vary across the aqueous boundary layer. Given equation 6.3 heat diffuses faster through the surface microlayer than dissolved gases. Hence it is the solubility at the air-sea interface rather than its average across the skin layer that limits air-sea CO_2 transfer (Doney, 1994; Ward et al., 2004). The correct expression of the flux in terms of $f\mathrm{CO}_2$ is:

$$F = k(\alpha_w fCO_{2w} - \alpha_s fCO_{2a}) \tag{6.4}$$

The solubility (α) is now expressed either as α_w at depth w, or α_s at the air-sea interface s. The warm layer and/or cool skin will also effect the fugacity of CO_2 dissolved in seawater via the carbonate reaction. This requires a deviation from the mass conservation assumption. The surface fugacity can be expressed in terms of the bulk water fugacity through an empirical relationship, $dfCO_2/dT = 0.0423$ °C^{-1} (Takahashi et al., 1993), however McGillis and Wanninkhof (2006) note that the exact relationship remains uncertain ranging from 0.053 to 0.037 °C^{-1}. Hare et al. (2004) calculate that the effect on temperature alone on solubility accounts for approximately 2.7% of the total change in fugacity at a reference temperature of 20 °C. Therefore the remaining 1.5% change in fugacity of carbon dioxide due to a temperature difference between the bulk water and interface comes from the change in mass due to the carbonate reaction. Hence:

$$fCO_{2s} = fCO_{2w}\frac{\alpha_w}{\alpha_s}(1 + 0.015\Delta T) \tag{6.5}$$

where the subscripts s and w denote the interface and measurement depth respectively, and $\Delta T = SST_{subskin} - SST_{skin}$. Thus the expression for the flux in terms of data in its most commonly available units becomes:

$$F = k[pCO_{2w}\alpha_w(1 + 0.015\Delta T) - pCO_{2a}\alpha_s] \tag{6.6}$$

In the case of the above equation α_w is calculated using the temperature at depth of the $p\mathrm{CO}_{2w}$ measurement and α_s is evaluated at SST_{skin}. This expression is more accurate than equation 6.3 and provides a statement of the flux in terms of the partial pressures available and the bulk water temperature, along with an estimate of the skin temperature. Whilst equation 6.2 is conceptually correct, in practice expressing the difference across the aqueous boundary in terms of $[\mathrm{CO}_{2aq}]$ yields numerically the same flux as when using $p\mathrm{CO}_2$, although the mechanism is different (McGillis and Wanninkhof, 2006).

At low wind speeds the flux of gases across the air-sea interface is very sensitive to SST_{skin} and the temperature at the depth of the $p\mathrm{CO}_2$ measurement (which is usually between 1 and 10 m). Since CO_2 is more soluble in cold water than in warmer water, variations in temperature over the diurnal cycle alter the integrated flux of CO_2. A larger diurnal cycle results in increased heat loss to the atmosphere (Cornillon and Stramma, 1985) and reduced transfer of CO_2 into the oceans (McNeil and Merlivat, 1996). Following conditions of low wind and strong diurnal warming, further enhancement of CO_2 exchange is possible due to gravitational instability. Resultant nighttime

cooling and restratification of the unstable layers drives enhanced gas transfer and destroys the diurnal warm layer. The heat loss contributes to buoyancy-driven turbulent mixing (Stips et al., 2002; McGillis et al., 2004; Jeffery et al., 2007), and gas transfer will also be modified where the mixed layer deepens, entraining dissolved gases from below (Lombardo and Gregg, 1989; Brainerd and Gregg, 1993a,b; MacIntyre et al., 2002).

It is common for climatologies of daily, weekly and monthly estimates of the gas transfer velocity and air-sea CO_2 flux to use mean nighttime values to remove the diurnal effect of sea surface temperature. In this modelling study we pay close attention to estimating the daily integrated CO_2 flux. Existing bulk techniques for calculating the air-sea transfer of gases rely on parameterization of the gas transfer velocity and already incorporate adjustments for the cool-skin and warm layer temperature deviations. However, if SST and wind speed data of insufficient temporal resolution is used; we are likely to introduce errors into the flux of CO_2 exchanged due to the non-linear nature of the k-parameterization versus wind-speed relationship (Bates and Merlivat, 2001).

The results presented here build upon the idealized modelling approach presented by Dickey and Simpson (1983), the observations of diurnal variability reported by Stuart-Menteth et al. (2005a), and the methods outlined in Jeffery et al. (2007). We incorporate estimates of the gas transfer velocity and air-sea CO_2 exchange to determine their sensitivity to the diurnal cycle and subsequently the phase relationship between the wind stress, cloud fraction and the surface heating. This work is ultimately important as accurate measurement of CO_2 fluxes will help to constrain the oceanic carbon budget, and improve future prediction of climate change.

6.2 Model setup

In order to investigate the senstivity of upper ocean temperature and CO_2 fluxes to phase-dependent wind stress and cloud fraction we conduct a series of experiments within a 1-d model framework. We use a modified version of the General Ocean Turbulence Model (GOTM) (Burchard et al., 1999). For a full description of the model setup and parameterizations used refer to Jeffery et al. (2007). The primary focus is on 'warm layers' and resulting changes in flux.

Input data are supplied on an hourly grid, containing the following parameters: x and y components of wind stress, pressure, air temperature, relative humidity, cloud cover, shortwave radiation, and rain-rate. The model is configured with 200 vertical levels for the upper 250 m of the water column and a time step of 1 h. The duration of the model run is 168 h. The vertical grid spacing uses zooming near the surface, resulting in very fine resolution near the air-sea interface and is ideal for updating the vertical divergence of downward solar irradiance. Initial conditions consist of temperature and salinity profiles for the first timestep, and we allow the model to spin-up for 48 hours.

We choose a two equation k_e-ϵ turbulence closure scheme with dynamic dissipation rate equations for the length scales, as it provides adequate complexity without computational expense (Mellor and Yamada, 1974; Rodi, 1987; Canuto et al., 2001). Furthermore, Stips et al. (2002) compared measured and simulated temperature and dissipation rate profiles from a two equation $k_e - \epsilon$ model and found that the basic features of convectively driven turbulence were well described by the model, with the temporal dynamics of the temperature field correctly simulated. Table 6.1 outlines the chosen parameters in our implementation of GOTM.

Model setup	
Turbulence closure	k_e-ϵ: Rodi (1987)
Heat fluxes	NOAA-COARE v3.0
Cool-skin layer	Fairall et al. (1996b)
Stability method	Kantha and Clayson (1994)
Wave breaking	Burchard (2001)
Internal waves	Large et al. (1994)
Optical water type	Jerlov type III (Jerlov, 1968)
Gas transfer velocity (k)	Jeffery et al. (2007)
Empirical coefficients for k	Soloviev and Schlüssel (1994)

TABLE 6.1: Model implementation parameters for the modified GOTM used in this study.

The 1-d Model uses the NOAA-COARE v3.0 air-sea bulk flux algorithm to compute the latent and sensible heat fluxes, with the longwave radiation term calculated according to Josey et al. (2003). The total heat flux is defined as

$$Q_{net} = (1 - a)Q_s + Q_l + Q_e + Q_h \tag{6.7}$$

where Q_{net} is the total heat flux into the ocean, Q_s is the incident solar flux, a is the albedo of the sea surface, Q_l is the net longwave flux, Q_e is the latent heat flux and Q_h is the sensible heat flux. Heat gained by the ocean is considered positive. The shortwave flux term penetrates the sea surface and dominates the heat budget of the upper ocean. The net longwave term is frequently as large as the latent heat flux. Generally the sensible heat flux is small compared to the latent heat flux over the ocean. The location of the model experiments is 10°S10°W, and the model run is based on the period of 7 days starting on the 1st February 2002, but manipulated as explained in the following paragraphs.

The model is forced using a time series of clear-sky shortwave radiation values based on a simple half-sine model repeated over each 24-hour 'model day', with a maximum amplitude of 1000 W m^{-2}. The albedo of the sea surface is a function of the solar altitude and the atmospheric transmittance (Payne, 1972), hourly values are calculated within GOTM. Diurnal variations in the albedo of the sea surface contribute little to

the thermal boundary condition as the albedo is large only for low solar altitudes when the incident shortwave radiation (Q_s) is near zero.

We restrict the number of time-varying free parameters by fixing a number of the model forcing conditions. For this study, we vary only the wind speed and cloud fraction. Table 6.2 contains the forcing information used to drive the model. Each of the constant parameters listed was computed from the average of the in situ measurements, recorded by the PIRATA Atlas mooring at 10°S10°W between 1–8^{th} February 2002. The data from this location was selected as the heat budget study of Foltz et al. (2003) states that the influence from advection is lower at this site than the other PIRATA moorings across the Tropical Alantic.

Forcing	Value	Unit	Remarks
Air pressure (p_a)	101600	hecto-pascals	NCEP climatology
Air temperature (T_a)	25.16	°C	Atlas mooring average
Relative humidity (q_{rh})	80.1	%	Atlas mooring average
Rain rate	0	mm hr^{-1}	Fixed
Solar radiation (Q_s)	0–1000	W m^{-2}	Diurnal half-sine model
Wind speed (u_{10})	2–12	m s^{-1}	Time varying diurnal profiles
Cloud fraction (n)	0–90	%	Time varying diurnal profiles

TABLE 6.2: Details of 1-d model forcing used in the study.

To assess the influence of cloud fraction on the diurnal response, cloud feedback on the clear sky solar forcing is calculated according to Reed (1977);

$$Q_s/Q_0 = 1 - 0.62n + 0.0019\theta \tag{6.8}$$

Q_0 is the insolation under clear skies, n is the cloud fraction and θ is the noon solar altitude. The feedback effect of cloud on the longwave flux is also included as cloud fraction is present in the Josey et al. (2003) formulation. We do not consider the influence of rain on this study nor do we account for differences in optical water type.

The turbulence closure part of the 1-d model is driven by a wind stress obtained from the quadratic drag law;

$$\tau = \rho_a C_D u_{10}^2 \tag{6.9}$$

where ρ_a is the density of air, C_D is the drag coefficient, and u_{10} is the mean wind speed at 10 m above the ocean surface.

The model has been modified to include routines for calculating gas transfer. Calculating the air-sea flux of CO_2 requires knowledge of the concentration difference across the interface. This ΔC is approximated as $\alpha \Delta pCO_2$ (see equation 6.3), where ΔpCO_2 is

the difference between the partial pressures of CO_2 either side of the air-sea interface. A positive value for the CO_2 flux represents a sea to air flux (i.e. ocean degassing). Climatological monthly values are used for pCO_{2a} and pCO_{2w} (Takahashi et al., 2002), and only deviate due to changes in solubility and barometric pressure. For the duration of the model run, the region is a source for CO_2 with pCO_{2w} being slightly greater than pCO_{2a}. As described in equation 6.6, temperature changes affect dissolved ΔC through solubility and the change in mass via the carbonate reaction. In addition, a barometric pressure correction is applied by modifying the value of atmospheric pCO_2 using the method described in Kettle and Merchant (2005).

The effects of biological or surfactant processes e.g. surface films were not included, although their effects are potentially significant (Goldman et al., 1988; Frew et al., 1990). The NOAA-COARE model contains no provision for the effects of biological processes, and biological feedback was not included within GOTM. Instead we focus solely on the physical aspects of the air-sea exchange.

A separate model for the skin temperature (Fairall et al., 1996b), within GOTM, is used to further improve calculation of gas fluxes by incorporating SST_{skin} and α_s. To correctly evaluate the gas transfer taking place during low wind convective conditions the NOAA-COARE gas transfer velocity (k) parameterization was used with the additional contributions from the water-side convective velocity scale as set out in Jeffery et al. (2007). The temperature and buoyancy effects were explicitly included by calculating gas transfer at every time-step.

While 1-d model simulations will not perfectly agree with observations, especially where 3-d processes are important, the model does allow the relative contributions from various physical exchange processes to be examined within a realistic framework. The time-varying temperature field obtained from the 1-d model, given atmospheric forcing at each time-step, is used to improve the accuracy of the gas transfer velocity and ultimately the air-sea flux of CO_2.

6.3 Results

6.3.1 Diurnal warming at uniform wind speed and cloud cover

We first consider the simple case of diurnal response for steady winds and cloud-free conditions. Sea surface temperature as a function of time for uniform wind speeds of 2, 4, 6, 9 and 12 m s^{-1} are shown in figure 6.1. The range of wind speeds was selected based on that observed by the PIRATA mooring at 10°S10°W during 2002. A clear warming trend over the model period is observed for low to moderate wind speeds (2–6 m s^{-1}). For wind speeds larger than 9 m s^{-1} the sea surface temperature decreases as

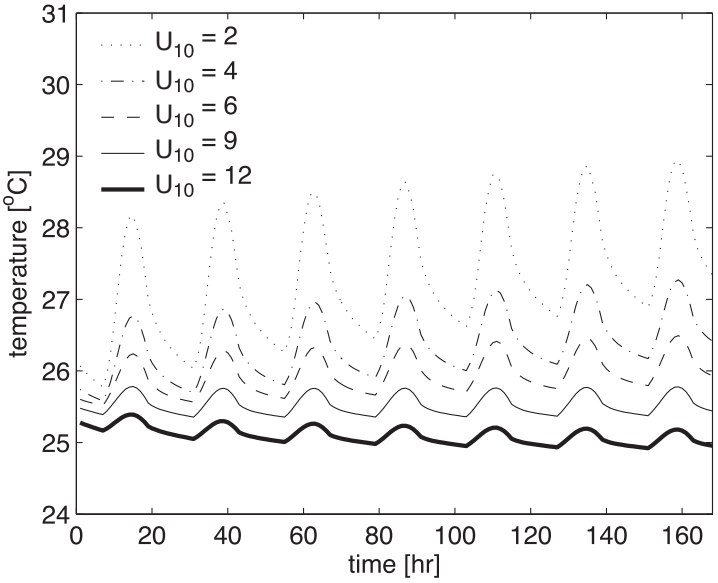

FIGURE 6.1: Time series of sea surface temperature for uniform wind speeds of 2, 4, 6, 9 and 12 m s^{-1}.

a function of time as the wind is sufficiently strong to produce a sustained deepening of the well-mixed layer.

In figure 6.2 we can see that increasing the wind speed (u_{10}) not only reduces the mean sea surface temperature, but also reduces the amount of diurnal warming which takes place during the course of the modelled day. The increase in wind speed serves to mix heat down, and hence the diurnal mixed layer (figure 6.2c) deepens.

Isotherms as a functions of time and depth for u_{10} = 2, 4, 6, 9 m s^{-1} are shown in figure 6.3. For u_{10} = 2 m s^{-1} the diurnal response is confined to the upper 5 m, whereas for u_{10} = 4, 6, 9 m s^{-1} the depth of penetration is larger than 20 m. The incoming

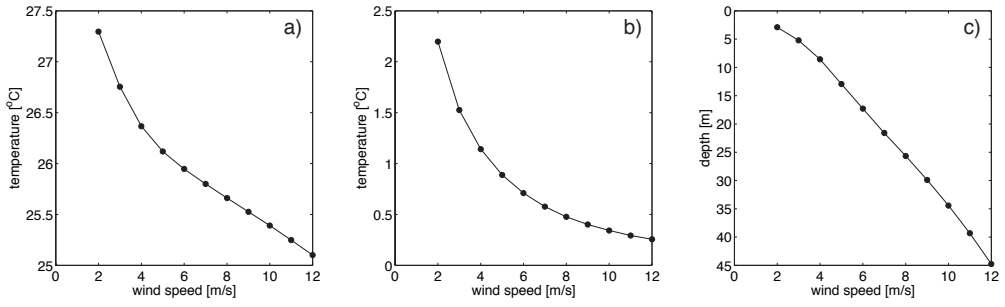

FIGURE 6.2: Modelled mean values over experimental period for a) skin temperature (°C) b) diurnal temperature increase, ΔT_{1m} (°C) and c) diurnal layer depth (m) versus constant wind speed (m s^{-1}).

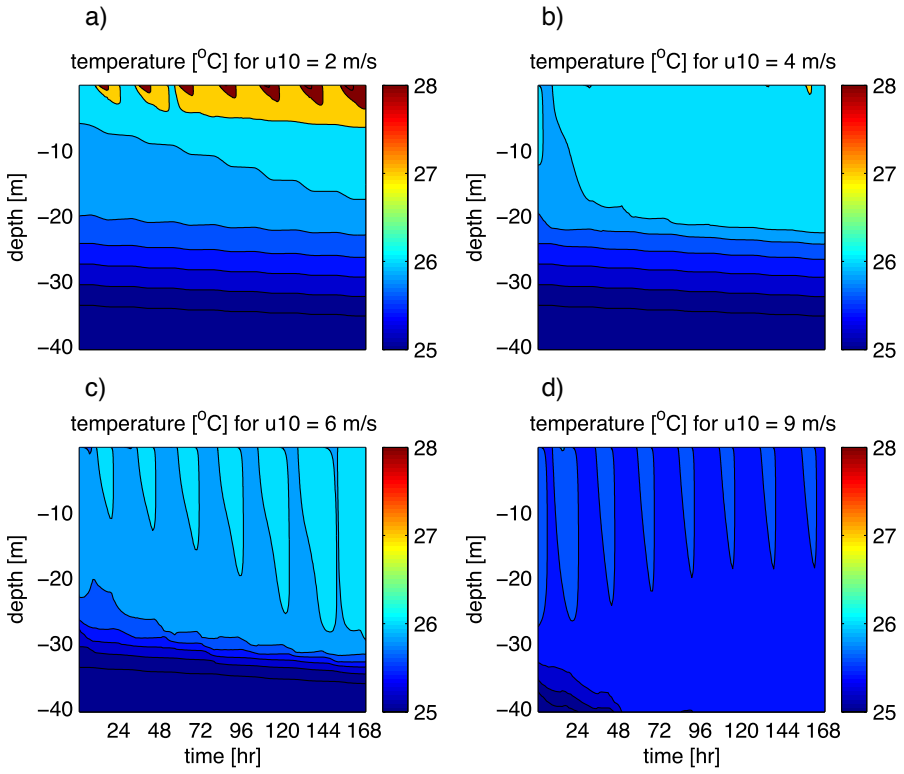

FIGURE 6.3: Modelled temperature (°C) as a function of depth (m) and time (hr) for constant wind speeds, where u_{10} = 2, 4, 6, and 9 m s^{-1}.

solar energy has been distributed over a greater depth, hence the temperature gradient associated with larger wind speeds is weaker.

Further complexity arises when we consider the impact of cloud cover on the diurnal response of the upper ocean. When the 1-d model was forced using various combinations of constant wind speeds and constant cloud fractions the results are as shown in figure 6.4. The maximum sea surface temperatures and diurnal temperature differences

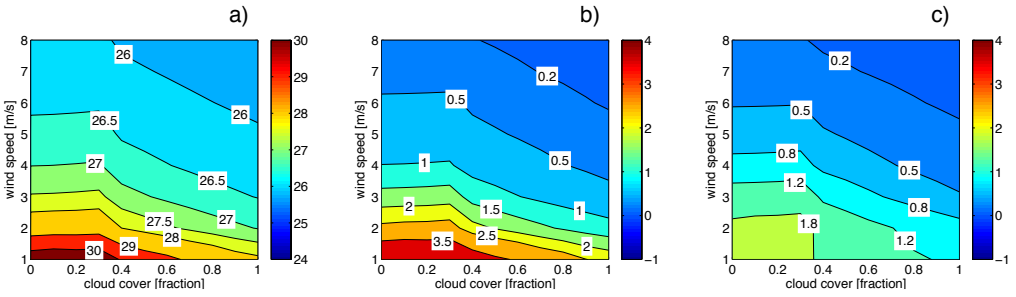

FIGURE 6.4: Contour plots showing modelled a) Maximum sea surface temperature at 1 m (°C), b) Maximum $\Delta T_{subskin}$ (°C) and c) Maximum ΔT_{1m} (°C) for constant wind speeds (m s^{-1}) and cloud cover (fraction).

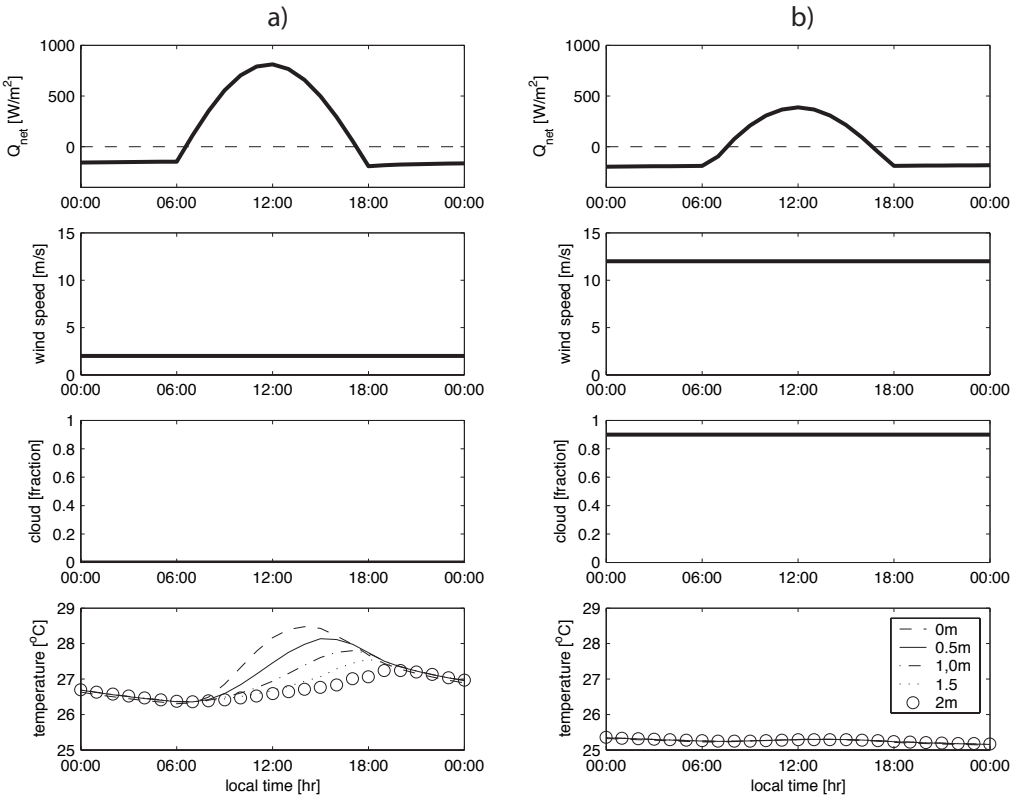

FIGURE 6.5: Two examples (a and b) of the sensitivity of the diurnal mixed layer to wind and cloud. Top panel shows the net heat flux, the middle panels show wind speed and cloud fraction respectively and the bottom panel shows temperatures at 0.5 m intervals ranging from sub-skin to 2 m.

illustrate that increasing wind stress is clearly the dominant factor responsible for the reduction in both surface temperature and the magnitude of the diurnal signal. However, increasing cloud fraction can also reduce the response by modifying the surface heat budget. The relative importance of this effect increases when wind speed is low.

In reality the magnitude of the diurnal temperature cycle will be highly dependent on factors such as the time of year and latitude, as these will determine the amount of solar energy available to heat the water column. These idealized model cases assume that the meteorological forcing is constant throughout the day, which itself is highly unlikely. Nonetheless the trend of increasing diurnal warming with decreasing wind speed is consistent with observations and assures us that the model is performing sensibly given the appropriate forcing.

Two detailed examples of the sensitivity of the diurnal mixed layer to wind and cloud are shown in figure 6.5. In example 6.5a, we have a constant wind speed of 2 m s^{-1} and no cloud cover. The net heat flux, Q_{net} is large and positive during the day, and this leads to strong upper-ocean stratification. The upper few metres of the water column rapidly stratify, and the strong temperature gradient is explained by the exponential absorption of the radiative forcing with depth through the water column. The peak of

	low	pm burst	pm low	am low	am burst	moderate	high
	I	II	III	IV	V	VI	VII
u_{am} (m s^{-1})	2	2	5	2	12	5	12
u_{pm} (m s^{-1})	2	12	2	5	2	5	12
u_{nght} (m s^{-1})	2	2	2	5	2	5	12

TABLE 6.3: Morning (am), afternoon (pm) and nighttime (nght) wind speeds for 7 distinct diurnal profiles used to force the 1-d model.

	clear	cloudy	am burst	am cloudy	pm burst	am cloudy
	I	II	III	IV	V	VI
Cld_{am} (fraction)	0	0.9	0.9	0.9	0	0
Cld_{pm} (fraction)	0	0.9	0	0	0.9	0.9
Cld_{nght} (fraction)	0	0.9	0	0	0	0.9

TABLE 6.4: Morning (am), afternoon (pm) and nighttime (nght) cloud fractions for 6 distinct diurnal profiles used to force the 1-d model.

the temperature is reduced, and occurs later as depth increases. Conversely, in example 6.5b, during high winds (in this case 12 m s^{-1}) and cloudy conditions, no obvious upper ocean response is visible. The near surface remains well mixed throughout the day, with little or no diurnal variation in upper ocean temperatures.

6.3.2 Diurnal shape classification

We now move on from steady conditions, to consider the effect of diel variations in wind and cloud. In order to investigate the sensitivity of the diurnal warm layer to cloud and wind fluctuation during the day, we use 7 distinct diurnal wind speed profiles I–VII (table 6.3) and 6 cloud cover profiles I–VI (table 6.4) to force the 1-d model. These are shown schematically in figure 6.6 and encompass the archetypes described in Stuart-Menteth et al. (2005a,b). In their study, the authors analyze over 250 cases of diurnal cycles of SST and their associated meteorological fields from IMET buoys in the Arabian Sea and the Western Pacific warm pool. They divide the diurnal SST signal into four categories, defined and related to wind and insolation fluctuations. The classifications are described in detail in Stuart-Menteth et al. (2005a) and are summarized in table 6.5. We have added an extra shape classification to the original set; type 5, which describes persistent high wind and cloud cover, this control case was selected as it leads to a minimal diurnal response.

Class	Cloud	Wind	Description
1a	I	VI	clear, moderate winds throughout
1b	II	I	cloudy, low winds throughout
2	I	I	clear, low winds throughout
3a	V	VI	pm cloudy, moderate winds throughout
3b	I	II	clear, pm wind burst
4a	IV	VI	am cloudy, moderate winds throughout
4b	I	V	clear, am wind burst
5*	II	VII	cloudy, high winds throughout

TABLE 6.5: Diurnal shape classification from Stuart-Menteth et al. (2005a) with corresponding cloud cover and wind speed profiles (as shown figure 6.6) required to reproduce in situ IMET buoy observations. *Note class 5 is not described in the original reference and is a control case showing little or no diurnal response.

Running the 1-d model with the archetype wind and cloud parameters in figure 6.6 adequately recreates diurnal temperatures observed in the buoy data by Stuart-Menteth et al. (2005a,b). Using the idealized wind and cloud forcing we reproduce the diurnal shape classifications; these modelled examples are shown in figure 6.7. The close agreement with Stuart-Menteth et al. (2005a) serves to validate the ability of the 1-d model to describe the diurnal cycle of the upper ocean temperature structure given the appropriate meteorological forcing.

As previously demonstrated in section 6.3.1, increased wind speeds produce a greater reduction in ΔT than that of the increased cloud fraction, which affects primarily the net heat flux. The combination of low wind speeds and large heat fluxes generate the strongest diurnal warming. Where there is an asymmetry in the wind forcing between the morning and afternoon, it is the timing as well as the magnitude that determines the amplitude and duration of ΔT and the shape of the diurnal signal.

It is important to notice that information about the wind and to a lesser extent the cloud fraction is a pre-requisite for determining the extent of the diurnal response. This is particularly noteworthy for those interested in compensating for the effects of the diurnal cycle on sea surface temperature measurements e.g. GHRSST-PP. Without high frequency measurements of the wind and the heat budget it is very difficult to accurately correct for its effect on skin and sub-skin temperatures.

6.3.3 Wind phasing

To determine the role of wind stress in the diurnal variability of near surface temperature, and subsequent alteration of the air-sea flux of CO_2, we examine a number of model simulations where the diurnal profile of the wind forcing is phase-dependent when compared to the solar heating cycle. This theoretical experiment allows us to compare the effects of a single wind event should it occur at different points throughout the day. We

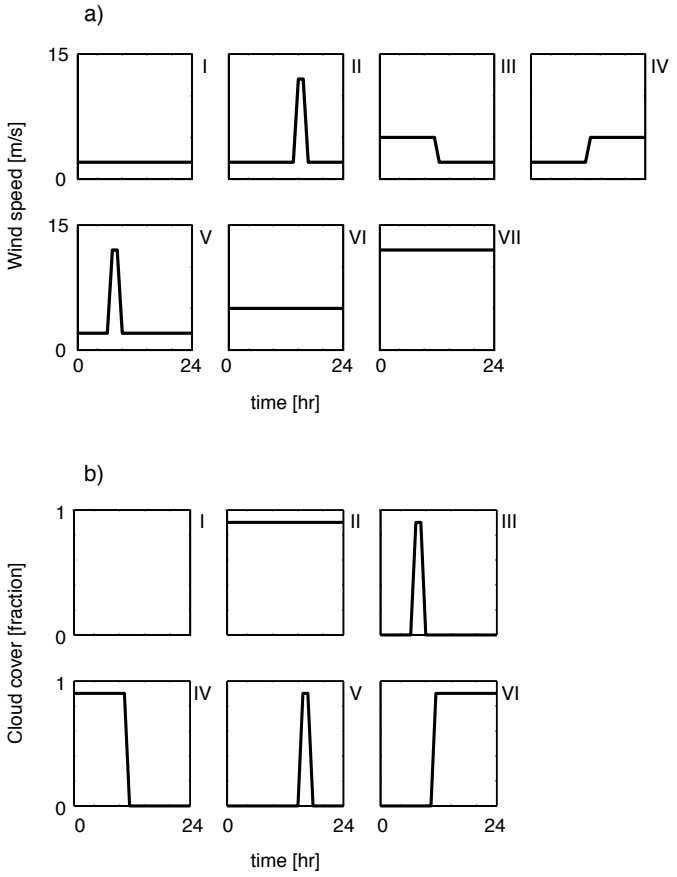

FIGURE 6.6: Schematic showing a) the diurnal wind speed profiles I–VII (m s^{-1}) and b) the diurnal cloud cover profiles I–VI (fraction) used to force the 1-d model as defined in tables 6.3 and 6.4.

forced the model with wind speeds generated from the following periodic function. All other model parameters remain unchanged.

$$\begin{aligned}
&t \leq 4, && u_{10} = u_{min} \\
&4 + nP < t \leq 5 + nP, && u_{10} = \frac{u_{max}}{2} \\
&5 + nP < t \leq 19 + nP, && u_{10} = u_{max} \\
&19 + nP < t \leq 20 + nP, && u_{10} = \frac{u_{max}}{2} \\
&20 + nP < t \leq 24 + nP, && u_{10} = u_{min}
\end{aligned} \tag{6.10}$$

Where t is time in hours ($t = 0$ h corresponds to midnight local time), P is the period and equal to 24 hours and $n = 0, 1, 2, ...6$ is the day number. The wind speed is u_{10}, with a maximum, $u_{max} = 6$ m s^{-1}. The initial wind profile is synchronous with the shortwave radiation (Q_s). Figure 6.8 shows the wind speed over the model run along with the solar heating for phase = 0 h and phase = 12 h. The form of this wind forcing was chosen

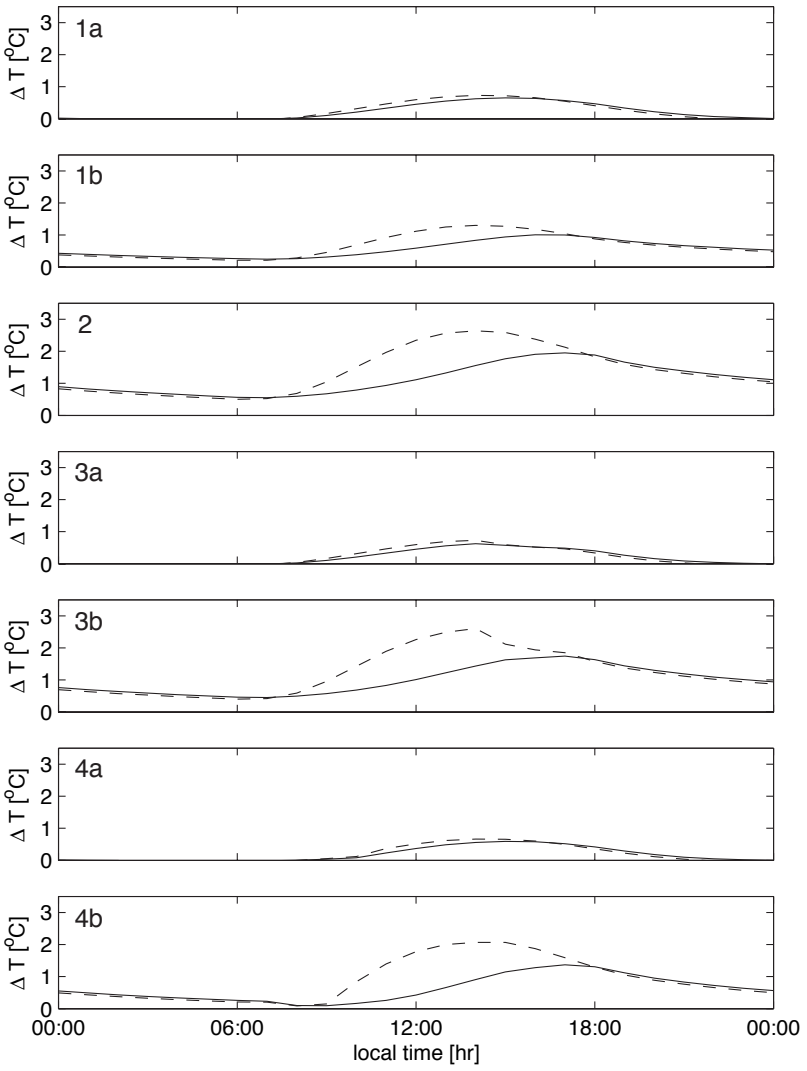

FIGURE 6.7: Modelled examples of diurnal temperature shapes for each diurnal warming classification described in Stuart-Menteth et al. (2005a). 1 m: solid line and subskin: dashed line.

to include a gradual onset and cessation of the wind field in order to minimize inertial effects. A 12 hour phase shift means that the onset of the transition from 2 to 6 m s^{-1} occurs 12 hours later. We choose a minimum wind speed, $u_{min} = 2$ m s^{-1}, as it is unlikely in reality to be completely calm, and wind observing systems are generally unable to resolve wind speeds approaching zero.

The time series of 1 m sea surface temperatures (SST_{1m}) and diurnal mixed layer depths for phase lags of 0, 4, 6, 12 and 18 hours are shown in figure 6.9. The minimum amplitude in the sea surface temperature occurs when the phase lag between the insolation and the wind is 0 hours. The maximum amplitude occurs for a phase lag of 12 hours. These

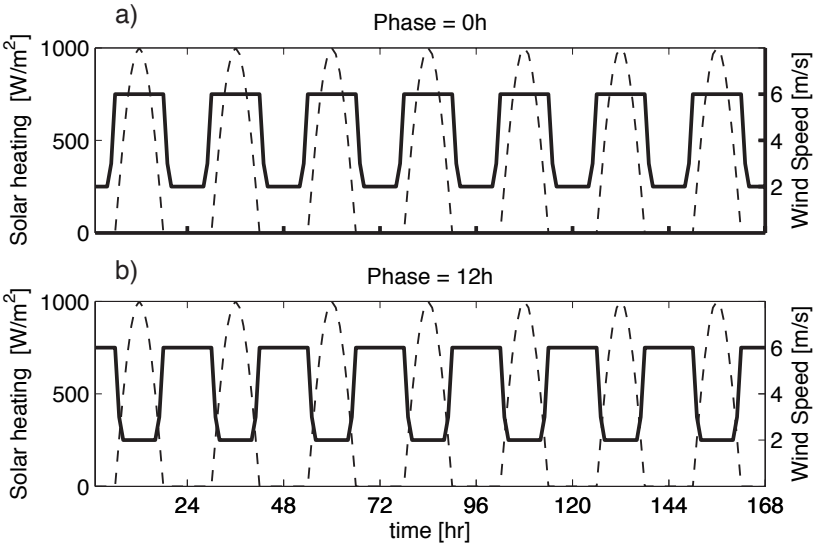

FIGURE 6.8: Dashed line: Solar heating (W m^{-2}) and solid line: Wind forcing (m s^{-1}) used to drive the 1-d model for a) phase = 0 h and b) phase = 12 h.

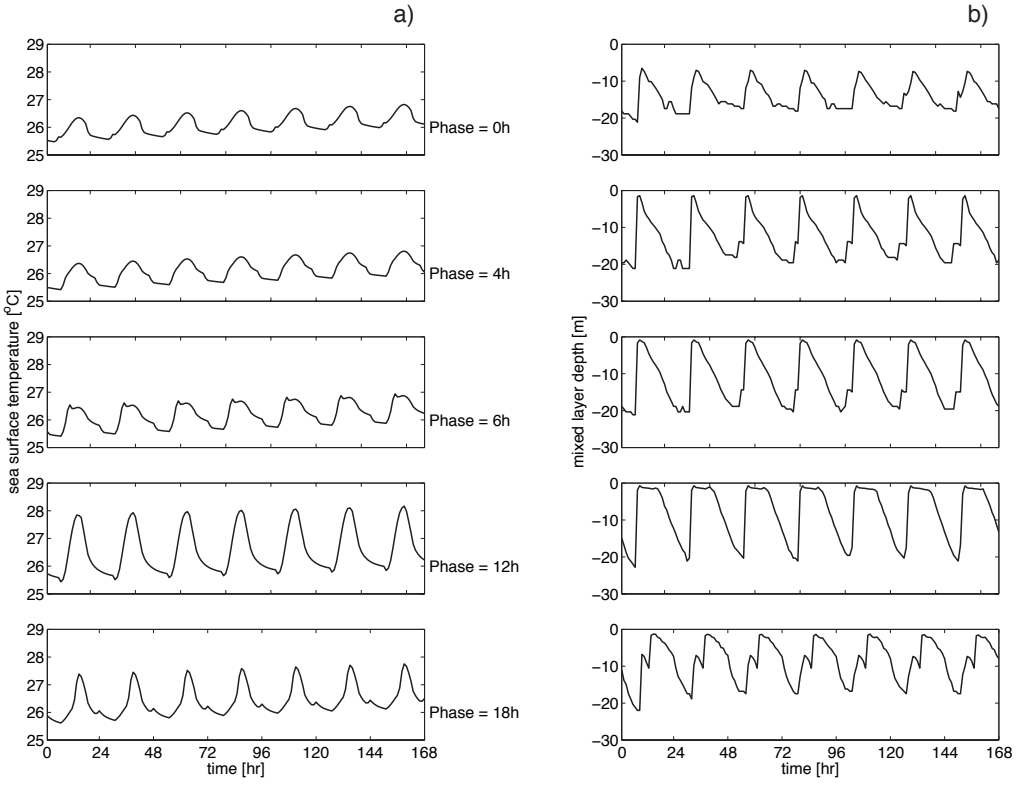

FIGURE 6.9: a) The SST$_{subskin}$ time series. b) The diurnal layer depth time series. Phases of 0, 4, 6, 12 and 18 h between wind and solar heating.

results are in good agreement with those compiled in a similar study by Dickey and Simpson (1983) using a Mellor-Yamada based model. We do not consider the influence of optical water type, but appreciate that its effect is important in determining the depth to which warming will penetrate.

At phase = 0 h, wind mixing prevents the build up of strong stratification near the surface. At night, however, there is little mechanical energy available for mixing and the only source of positive buoyancy production is net long-wave radiative cooling at the surface. This production of turbulent kinetic energy is insufficient to overcome the thermal gradients established during the day. This is reflected in the time series of the mixed layer depths in figure 6.9. For a phase lag of 12 hours, the stratification increases at a greater rate during the day because there is little wind driven turbulent mixing.

If we observe contours of the flux Richardson number (R_i) in figure 6.10, for phase = 0 h and 12 h, we can see the difference in the amount of convectively unstable regions associated with the corresponding temperature structure. The Richardson number is the ratio of negative buoyancy production to shear production. Three distinct regimes of flux Richardson number are defined: (1) stable, $R_i > 0.21$; (2) turbulent and convectively stable, $0 \leq R_i \leq 0.21$; and (3) turbulent and convectively unstable, $R_i < 0$.

For a phase lag of 0 hours, the near surface flux Richardson number alternates between regions which are turbulent and convectively stable during the day, becoming convectively unstable for a short period in the evening and morning. The observed stability during nighttime is a consequence of increasing density with depth combined with a very marginal ratio of buoyancy to shear production, which is sufficient to result in a marginally positive value of R_i. Whilst there is some diurnal variation in phase = 0 h temperatures in figure 6.10a, it is weak compared to the phase = 12 h case. When the wind forcing is 12 hours out of phase with the maximum solar insolation (figure 6.10b), the near surface flux Richardson number alternates between periods that are turbulent and convectively stable during the day, and subsequently during the evening and through the next morning, large regions of convective instability. Following strong diurnal warming, the near surface cools and becomes gravitationally unstable. The warm diurnal surface layer is destroyed through convective turbulence.

The phase dependence of the mean diurnal variability, ΔT_{1m} (°C), mean mixed layer depth (m), the net CO_2 flux (mol m^{-2} yr^{-1}) and mean transfer velocity, k (cm hr^{-1}) are shown in figure 6.11. Table 6.6 shows the effect of the wind phasing on the mean sea surface temperature at 1 m in addition to the above variables for phase lags = 0, 4 6 and 12 h. For each of the variables shown in figure 6.11 there is asymmetry in the 24 hour phase-space. As the diurnal peak of the wind speed moves back through time ΔT increases, at first very slightly. For the first 5 hours the wind peak is sufficiently large to destroy the warm layer. However, after 5 hours the mean ΔT is much greater, as the peak wind speed occurs when heat budget is no longer positive. As the peak approaches

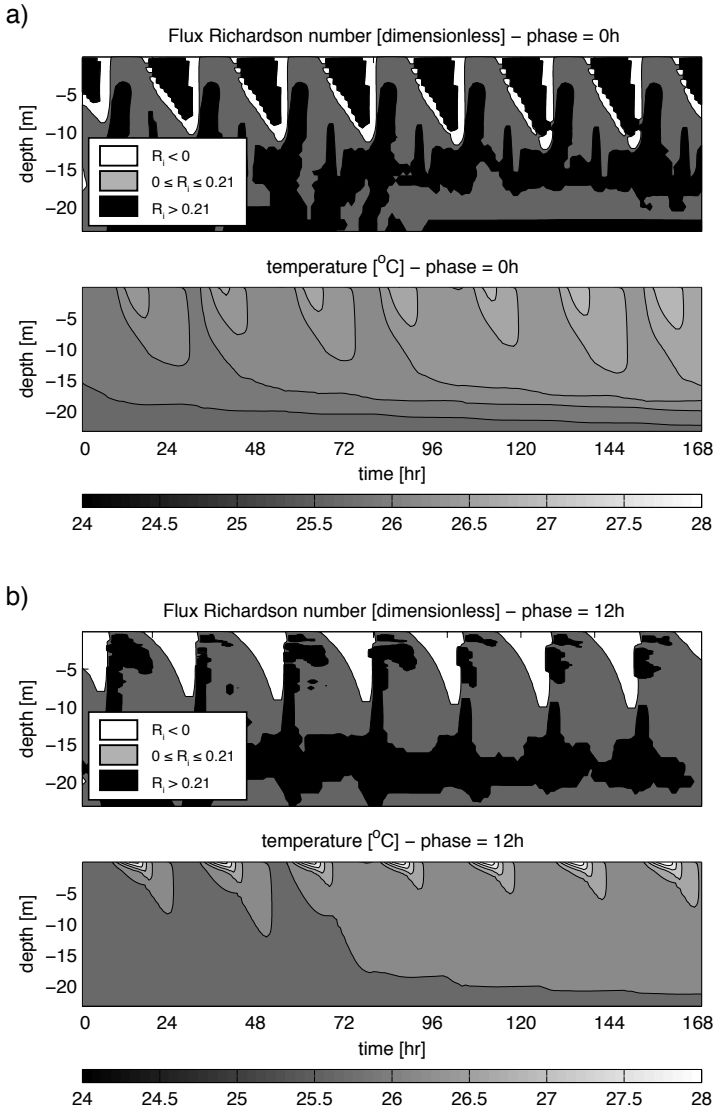

FIGURE 6.10: Isotherms (°C) and contours of flux Richardson number (dimensionless) as functions of depth and time for a) phase = 0 h, b) phase = 12 h. White regions in the upper panels indicate turbulent and convectively unstable conditions at nighttime.

morning, high wind speeds delay the onset of the SST maximum, and the magnitude of ΔT is reduced, leading to the observed asymmetry in the profile. The same is true for the shallowing of the mixed layer. In this particular case, the effect of phasing the wind-speed more than doubles the diurnal temperature difference and halves the diurnal mixed layer depth.

Considering table 6.6, it is clear that wind speed affects predominantly the amount of diurnal warming and the depth of the diurnal mixed layer, and since gas transfer is highly sensitive to temperature changes at low wind speeds, the presence of a large ΔT affects the air-sea CO_2 flux. The increase in ΔT and position of the mixed layer are also important when considering the convective enhancement to the CO_2 flux (Jeffery et al., 2007). With increasing ΔT, and deepening diurnal MLD the flux of CO_2 is further

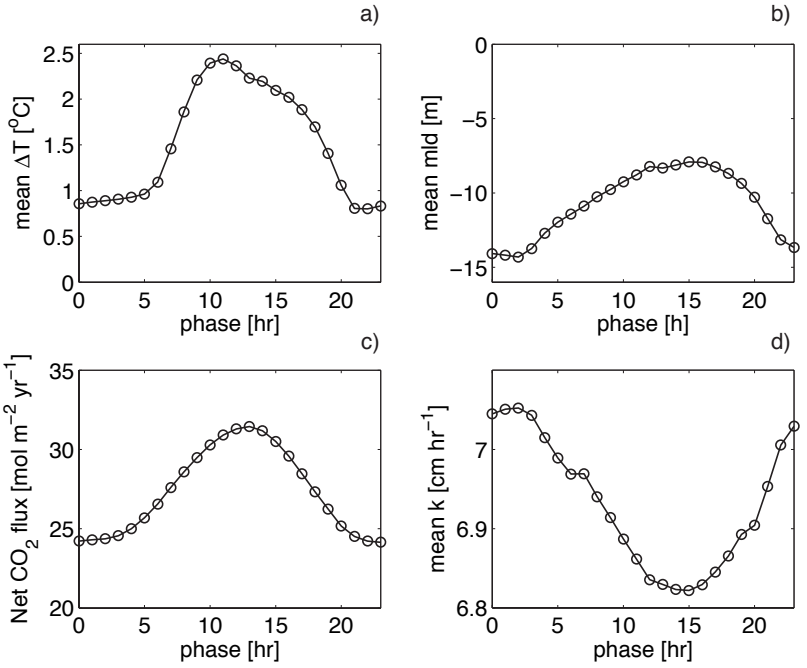

FIGURE 6.11: a) Mean ΔT_{1m} (°C), b) Mean diurnal layer depth (m), c) Net CO_2 flux (mol m^{-2} yr^{-1}), and d) Mean k (cm hr^{-1}) versus wind phase lag.

	Phase lag			
	0 h	4 h	6 h	12 h
Mean SST_{1m} (°C)	26.50	26.48	26.50	26.60
ΔT_{1m} (°C)	0.86	0.93	1.09	2.36
Mean MLD (m)	14.0	12.7	10.9	8.2
Mean k (cm hr^{-1})	7.0	7.0	6.9	6.8
Net CO_2 flux (mol m^{-2} yr^{-1})	24.22	25.01	26.56	31.29

TABLE 6.6: The effect of wind phase on the diurnal temperature structure and air-sea gas exchange over the model period.

enhanced by convective overturning. Whilst the mean diurnally mixed layer depth over the model period is smaller for phase = 12 h, the maximum diurnal MLD reached each night is greater than that achieved by phase = 0 h (see figure 6.9). Thus, the increased turbulence at night following conditions of strong diurnal warming enhances the gas transfer velocity. This is evidenced by the increased turbulent and convectively unstable ($R_i < 0$) regions at phase = 12 h in figure 6.10.

When we consider this phase effect on the gas transfer, we observe only a very small change in k, which can be attributed largely to the convective enhancement; this itself is a strong function of the diurnal variability. Comparatively, a much larger change in CO_2 flux is observed, this is mainly through the dependence of $[CO_{2aq0}]$ on temperature. Increasing SST reduces the surface concentration (in equilibrium with the atmosphere) through its dependence on solubility and results in greater degassing. In our case, this results in an increase in net CO_2 flux from 24.22 to 31.29 mol m^{-2} yr^{-1} a change of

approximately 29% between phase = 0 h and phase = 12 h (see table 6.6). This warm-layer effect is much larger than any temperature related convective effects which are parameterized within the transfer velocity. For comparison, if the warm-layer was not present, the required change in wind speed for an equivalent change in the air-sea CO_2 flux observed in figure 6.11 would be approximately 3–4 m s^{-1}.

Given the low turbulence and high solar insolation conditions for this experiment, the differential heating via incoming radiation over the top 2 to 20 m and the increased stability of the upper ocean layers, led to the formation of a strong warm layer in the phase = 12 h case. Since the mean wind speed over the model periods are the same, it is clear that it is the timing and magnitude of the 'peaks' and 'troughs' in the wind forcing that affect the upper ocean temperature structure, which in turn modifies the flux of CO_2 across the air-sea interface.

6.3.4 Wind and cloud phasing

Each combination of the diurnal wind and cloud scenarios shown in figure 6.6 was also shifted backward in time (phase-lag) through 24 hours in steps of 1 hour to create new profiles, which were then used to force the 1-d model. We opt to show results from 4 of those scenarios (a-d), representing the extremes from all the simulations; these are presented in figure 6.12. The original scenarios a and b correspond to a morning wind and cloud burst respectively, whereas scenarios c and d represent an entire morning of moderate wind speed and high cloud cover respectively. However, in these phase experiments the timing of the events is shifted backward in the day by the stated 'phase'. As with the earlier phase experiments in section 6.3.3, it is the CO_2 flux, ΔT and the depth of the mixed layer that have the largest response to phase dependent wind stress and cloud cover.

The diurnal response to phasing wind events (a and c) is more sensitive than the corresponding cloud events (b and d). As high wind or cloud cover approaches midday, ΔT decreases. Increasing cloudiness results in a reduction in insolation during the daytime. There is also some effect on the net longwave flux over the whole day. In this case of the wind burst (scenario a), the timing of the event ± 5 hours from the local solar maximum had a large effect on both the shape and magnitude of the diurnal response. ΔT was up to 1 °C lower, and the diurnal MLD was more than 4 m deeper where higher wind speed acted to mix sun-warmed water to greater depths.

Whilst the wind burst of scenario a was greater in magnitude, the extended periods of moderate wind speed represented by scenario c led to double the amplitude variation in ΔT. The longer duration, despite lower u_{10} kept the heat distributed through the water column preventing strong diurnal stratification. The depth of the diurnally mixed layer for scenario c varied between 5.5–9 m, and was generally deeper at each time-step than

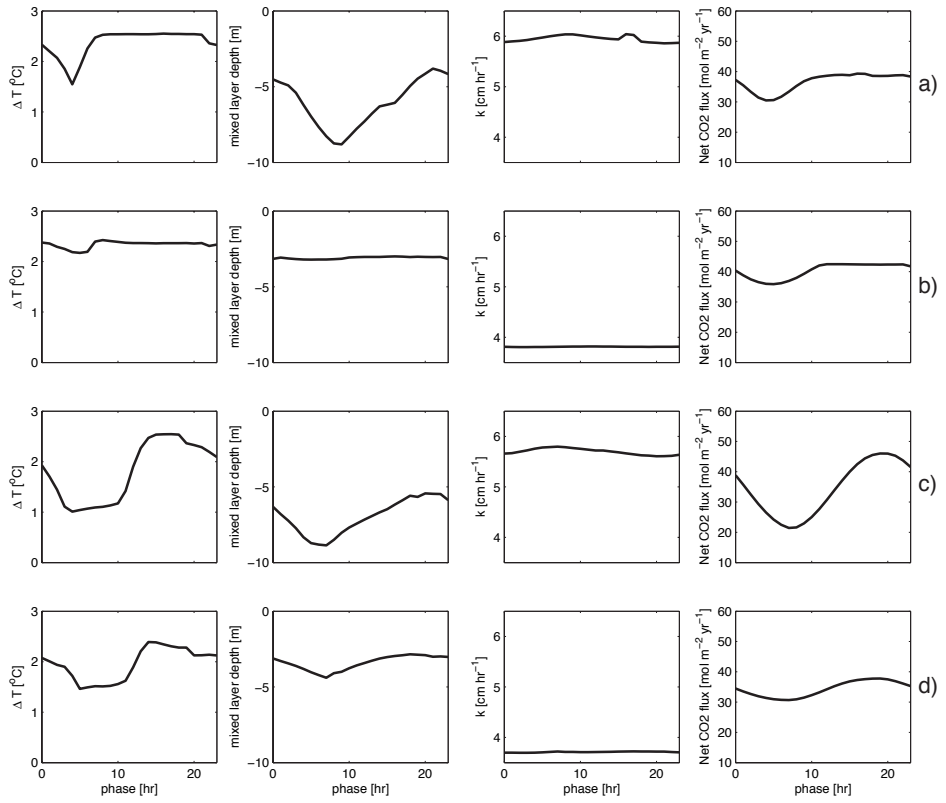

FIGURE 6.12: Modelled results from 4 scenarios (a-d), showing from left to right: ΔT_{1m} (°C); mean diurnal mixed layer depth (m); mean transfer velocity (cm hr^{-1}); net CO_2 flux (mol m^{-2} yr^{-1}) versus phase lag (hr). Scenarios: a) morning wind burst, b) morning cloud burst, c) moderate wind in the morning, and d) cloudy in the morning.

that of scenario a, which varied between 3.5–9 m. Similarly, cloud cover has a greater impact in the longer duration case (scenario d) compared with the short burst of high cloud. The heat gained by the ocean is dramatically reduced when the cloud cover is high during the daytime. The range of ΔT and the depth of the diurnal layer over the phase-space are also larger in scenario d compared to scenario b.

There is little change in the transfer velocity, k, due to phase dependent cloud forcing. k remains at around 3.9 cm hr^{-1} regardless of the phase (scenarios b and d). Given phase dependent wind forcing increases k to around 5.8–6.0 cm hr^{-1}, but does not introduce much variability over the phase-space. The largest increase (0.1–0.2 cm hr^{-1}) is found in scenario a, for a 16 hour phase-lag. This is due to the peak of the wind event occurring at night, following strong diurnal stratification during the preceding day. In comparison, the net CO_2 flux in figure 6.12 is much more sensitive than the transfer velocity.

CO_2 fluxes from scenarios a and b vary primarily around the time of the specific wind or cloud event and its influence. In these scenarios the presence of high wind and cloud reduce ΔT, and thus the flux of CO_2 decreases from 40 mol m^{-2} yr^{-1} to 30 mol m^{-2} yr^{-1} and 36 mol m^{-2} yr^{-1} respectively. In comparison, the scenarios with sustained

high wind or cloud conditions have a much larger response. Scenario c presents the largest variability in net CO_2 transfer, with the flux reduced to a minimum of 20 mol m^{-2} yr^{-1} as the windy period extends over the middle of the day. A similar response it observed for the sustained cloudy period (scenario d), although the magnitude of the flux variability is reduced (from 40 to 30 mol m^{-2} yr^{-1}) since the range of ΔT is smaller.

The phase variation observed in the CO_2 fluxes are a result of changes to both the transfer velocity and the gas solubility. However, it is the change in solubility, brought about by diurnal temperature variation, which is primarily responsible. The is most obvious in scenarios b and d, where there is little change in k versus phase, yet the net flux of CO_2 continues to vary. Since this experiment is conducted in a source region (e.g. $pCO_{2w} > pCO_{2a}$), as ΔT increases the difference between $[CO_{2aqw}]$ and $[CO_{2aq0}]$ becomes greater leading to increased fluxes. A similar situation is observed in scenario d, however the magnitude is reduced as the wind effect is greater than that due to cloud cover.

6.3.5 Comparison of integrated CO_2 fluxes

For each of the model runs conducted in section 6.3.4 we also compared three methods, M, for evaluating the net CO_2 flux:

1. Forced by hourly winds, the 1-d model provides temperature and salinity at various depths for each time step. The CO_2 fluxes are evaluated each hour and the net flux is simply the sum over the model period. This estimate accounts for the 'cool-skin' and 'warm-layer' effects (see equation 6.6).

2. The transfer velocity and CO_2 flux are calculated as above, but in this case we supply the nighttime averages of the wind speed, bulk and skin temperatures and salinity rather than using the 1-d model. The calculation includes the 'cool-skin' correction and temperature correction for the carbonate reaction, but the formation of diurnal warm layers is ignored.

3. The transfer velocity and CO_2 flux are calculated using nighttime average bulk temperature and salinity. In this case, no thermal skin correction or temperature correction for the carbonate reaction is applied (see equation 6.3).

M_1 is the best available for evaluating the air-sea flux of CO_2 as it accounts for more of the temperature-dependent processes occurring on hourly timescales, through the use of the micrometeorological k parameterization and the 1-d model. M_2 and M_3 both replicate 'standard' methods. In most cases the cool-skin in ignored or an afterthought. The fluxes evaluated for each of the diurnal shape classifications (1–5) are presented in table 6.7. The non-temperature corrected CO_2 fluxes as estimated by M_3 are consistently

smaller than those calculated by the 1-d model (M_1) and those including the 'cool skin' correction (M_2). The M_1 and M_2 values are closer, but ignoring the warm-layer, when it is present, underestimates the next flux in those cases.

The differences between methods M_1 and M_2 for diurnal shapes 1b and 2 are 38.2% and 54.2% respectively. These profiles had large ΔT's of up to 2.4 °C, and the lowest transfer velocities as a results of low wind speeds throughout the model run. Case 3b also shows a large discrepancy between methods M_1 and M_2. However, since this example involved a wind burst in the afternoon, the difference here is due to increased wind speed not being represented by the nighttime mean value. Thus it is important to distinguish between the effect of the warm layer and the non-linearity of the wind speed-transfer velocity relationship.

Constant moderate wind forcing generally resulted in a small diurnal response, as in shapes 1a and 4a. Both have a ΔT of 0.63 °C and underestimate the net CO_2 flux by approximately 3.9% and 3.2% if M_2 is used instead of M_1. Shape 3a was also generated with constant moderate winds, however it underestimates the flux by over 17%. In this case, the magnitude of ΔT is much greater; at 1.19 °C.

At low wind speeds, the effect of cloud cover is more readily apparent if we consider longer cloudy periods. This is because the reduction to the solar insolation is greater. Observe the difference between case 1b and 2, which are forced using the same wind field. The persistent high cloud cover in 1b almost halves the ΔT compared to shape 2, and reduces the net CO_2 flux calculated by M_1 from 34.05 to 20.78 mol m^{-2} yr^{-1}.

Whilst the wind speed and cloud cover are at their highest for diurnal shape 5, they are however, constant over the 24 hour period. The flux from the 1-d model (M_1) is slightly smaller than the averaged estimate (M_2) since no warm-layer present ($\Delta T = 0.03$ °C), and there is only a small influence from the thermal skin effect. Using methods M_2 and M_3 fails to account for high frequency temperature variability, and its impact on the net CO_2 flux. This will be further complicated when we consider real wind speed data, as temporal averaging always results in an underestimate of mean transfer velocity due to the non-linear wind speed versus transfer velocity relationship.

We also compare values forced by non-constant profiles that are 12 hours out of phase. Given that these have the same mean wind speed, differences can be attributed to changes in temperature of the diurnal mixed layer. The M_1 and M_2 net CO_2 flux for shape 3b differs from 34.9% to 10.6%, whereas for shape 4a it differs from 3.2% to 1.1%, compared to phase = 0 h. The larger deviations are a result of the timings of the wind and/or cloud events. Where they occur early in the morning or late at night, they have a smaller impact on magnitude of the diurnal warming, compared to the middle of the day. These large changes imply that models attempting to reliably estimate the ΔT and CO_2 fluxes must have wind and temperature information throughout the course of the day, at high enough temporal resolution to resolve the diurnal variability.

	Shape classification							
	1a	1b	2	3a	3b	4a	4b	5*
Phase = 0 h								
(M_1) Net CO_2 flux: GOTM	27.16	20.78	34.05	26.70	24.84	26.56	28.55	91.62
(M_2) Net CO_2 flux: temp. corr.	26.09	12.84	15.61	22.10	16.16	25.70	26.41	95.74
% Difference M_1 to M_2	−3.9%	−38.2%	−54.2%	−17.2%	−34.9%	−3.2%	−7.5%	2.2%
(M_3) Net CO_2 flux: simple	25.10	12.03	13.04	21.79	13.65	24.84	24.75	97.27
% Difference M_1 to M_3	−7.6%	−42.1%	−61.7%	−18.4%	−45.00%	−6.5%	−13.3%	1.7%
Mean k (cm hr^{-1})	7.6	3.6	3.9	7.5	4.1	7.5	7.5	28.4
ΔT_{1m} (°C)	0.63	1.21	2.39	1.19	0.77	0.63	1.33	0.03
Phase = 12 h								
(M_1) Net CO_2 flux: GOTM	–	–	–	27.17	29.48	25.41	28.77	–
(M_2) Net CO_2 flux: temp. corr.	–	–	–	26.40	26.36	25.14	23.07	–
% Difference M_1 to M_2	–	–	–	−2.8%	−10.6%	−1.1%	−19.8%	–
(M_3) Net CO_2 flux: simple	–	–	–	25.00	24.71	25.12	19.44	–
% Difference M_1 to M_3	–	–	–	−8.0%	−16.2%	−1.1%	−32.4%	–
Mean k (cm hr^{-1})	–	–	–	7.5	7.5	7.5	5.9	–
ΔT_{1m} (°C)	–	–	–	1.43	1.43	0.61	1.44	–

TABLE 6.7: Temperature and air-sea gas exchange statistics over the model period for diurnal shape classifications as described in Stuart-Menteth et al. (2005a). Net CO_2 fluxes calculated for 3 methods, $M_{1:3}$, units: mol m^{-2} yr^{-1}. M_1: hourly wind data, temperature from 1-d model; M_2: daily average wind data, with 'cool-skin' correction; M_3: daily average wind data, no temperature corrections. Statistics shown for phase = 0 h and 12 h. *Note that shape 5 is not defined in the original reference and is a control case with no diurnal response.

6.4 Discussion

Our idealized modelled results aim to represent the diurnal variability of SST driven by the 1-d distribution of heat. This is determined by the balance of incoming solar radiation and the wind energy available to mix the water column. We are able to reproduce the variability in the shape of the diurnal warm layer and the large differences that occur between the surface and 1 m. Limitations of this method include the fact that it cannot account for short timescale changes of SST caused by advection of surface currents or pre-existing horizontal gradients of water temperature. In cases where the diurnal evolution of near surface temperatures are coupled to local processes e.g. advection in coastal regions and areas near boundary currents, the model would not be expected to resolve accurately the SST.

The modelled results describe the upper-ocean temperatures for a typical period (February) during summer in the southern Tropical Atlantic. Dickey and Simpson (1983) draw the following conclusions which are equally applicable to the results presented here. The magnitude of the diurnal signal in SST is generally less in winter than in summer. In addition, the magnitude of the diurnal response is significantly more latitude dependent in winter than in the summer, because the latitudinal variation in solar heating is much greater in winter. Diurnal signals in SST can exist during the winter under particular forcing conditions. The upper ocean temperature structure results from the same turbulence mechanisms, only the rate of production and their relative spatial and temporal evolution differ. These differences are caused primarily by seasonal differences in the thermal boundary condition.

As reported by Stuart-Menteth et al. (2005b), the timing of the peak SST can vary from pre-noon to late afternoon and the phase will change with depth; usually with an increasing lag in the time of the maximum SST, depending on the depth of the diurnal warm layer and the amount of wind mixing. We modelled large differences between the surface ($\Delta T_{subskin}$) and 1 m (ΔT_{1m}) during low winds and SST$_{subskin}$ responded instantaneously to changes in wind speed resulting in increased variability in the timing of the SST maximum at the surface than at depth. Furthermore we observed that the shallower the warm layer, the greater its sensitivity to diurnal fluctuations.

Ward (2006) observed that the passage of cloud had an immediate effect on the SST, due to a reduction in solar insolation. The upper few decimeters responded to this drop in downwelling radiation rapidly, and the warming recommenced after the sun emerged from behind the cloud. Similarly, changes in insolation due to cloud cover in our model experiments caused instantaneous changes in SST. The magnitude of the change in SST caused by cloud was much less than that caused by wind. However, extended cloudy periods resulted in a significant reduction of ΔT, as less energy is available to warm the upper layers. Cloud fraction was observed to be more important for the amplitude rather than the phase of the diurnal signal.

McNeil and Merlivat (1996) introduce the concept of regional asymmetry in net CO_2 flux brought about by processes such as the warm surface layer. For example, equatorial and mid-latitudes are generally sources for CO_2 (Takahashi et al., 2002). In addition, areas such as the tropics and northern Indian Ocean are strongly affected by diurnal stratification (Gentemann et al., 2003). Thus in those regions we expect CO_2 evasion from the ocean that is enhanced significantly by the formation of diurnal warm layers. Conversely, high latitude regions, would not be expected to develop a warm layer. In these regions, the effects should be minimal.

Whilst the experiments conducted during this work have all taken place in a weak CO_2 source region ($pCO_{2a} \simeq 350$ and $pCO_{2sw} \simeq 360$), it is also important to consider what happens in sink regions. Assuming that below the mass boundary layer $[CO_{2aqw}]$ does not change appreciably, increasing SST acts to decrease $[CO_{2aq0}]$. Thus, in source regions diurnal warming will increase the difference between the aqueous gas concentrations during the day and result in larger fluxes. However in sink regions, where $pCO_{2a} > pCO_{2w}$, the formation of diurnal warm-layers will act to reduce the difference between the $[CO_{2aqw}]$ and $[CO_{2aq0}]$, and reduce the flux. Regardless of the direction of the flux diurnal warming decreases $[CO_{2aq0}]$, which is controlled by the CO_2 concentration in the atmosphere and the temperature (and salinity) at the top of the boundary layer. This results in either an increase in the source or a decrease in the sink. Given the asymmetry of these effects on the out-gassing and in-gassing regions, only a small change in either direction would be required to alter the global net flux of CO_2.

Accounting for upper ocean convective processes, as described in Jeffery et al. (2007), which are most important during low winds and strong insolation, increases k and thus act to increases CO_2 flux. The thermal skin effect on the net CO_2 flux is generally small, however in cases where there is a very small difference between the gas concentrations either side of the interface (e.g. very weak sources and sinks) the cool-skin effect across the surface diffusive layer becomes more important. However we have shown that these effects are small in comparison to the solubility effect on $[CO_{2aq0}]$. As such models calculating the net CO_2 flux should aim to include diurnal temperature variation, and to calculate the flux using SST_{skin} or risk introducing large errors, especially at low wind speeds.

Recent studies by Ward et al. (2004); McGillis and Wanninkhof (2006); Zhang and Cai (2007) have argued that the excess CO_2 uptake proposed by Robertson and Watson (1992) has been overemphasized. Since the thermal diffusive sub-layer is an order of magnitude deeper than the mass diffusive layer, the cool skin effect is overestimated when calculated with the temperature across the thermal layer instead of the mass diffusive layer. Additionally Zhang and Cai (2007) noted the salty-skin effect which is opposite to the cool-skin effect and is significant. It is correct that the temperature difference across the mass diffusive layer will be quite small, but this is not the most critical issue. Rather

the concentration at the top of the aqueous mass boundary layer, $[CO_{2aq0}]$ must be calculated from atmospheric values using the appropriate solubility (thus temperature and salinity). Strictly this requires values of absolute surface temperature and salinity but a radiometric skin temperature is an adequate and practical substitute where necessary. However if a 'sub-skin' or 'foundation' temperature is used the errors are unacceptably high as originally identified by Robertson and Watson (1992). In this study deviations of surface temperature and salinity from 'foundation' values are included, though a haline skin effect has been neglected. Generally the most important influence on gas flux in this study is through an increase in surface temperature (a reduction in solubility) resulting from diurnal warm layers.

Zhang and Cai (2007) also investigated the effect of introducing a non-zero transfer velocity at low wind speeds. The authors use a simple non-zero adjustment of 10 cm hr^{-1}, which produced a large increase the estimation of out gassing from the equatorial regions (+0.2 Pg C yr^{-1}). The authors suggest that in low wind speed regimes, convective forcing may be a a significant factor in causing the variability of gas transfer velocities. Our work focuses primarily on the enhancement to the transfer velocity (k) at low wind speeds, through the use of a physically based parameterization which includes convective effects (Jeffery et al., 2007), thus we would expect a similar outcome if applied globally.

The use of daily average wind speeds significantly underestimates the air-sea CO_2 flux due to the mathematical artifact of smoothing out short-term wind variability during averaging. Bates and Merlivat (2001) investigate the effect of short-term variability on the CO_2 flux using high sampling frequency wind speed and pCO_2 data collected by the autonomous CARbon Interface OCean Atmosphere (CARIOCA) buoy in the western North Atlantic. They compared CO_2 fluxes evaluated with hourly versus daily averaged wind speed, and found that the air-sea CO_2 flux was up to three times greater if high frequency wind data was used instead of the daily averaged data. In addition, they suggest that it is more important to capture short-term wind speed variability rather than the seawater pCO_2 variability. As our intention was to investigate the diurnal processes and their effect on gas transfer, our idealized diurnal wind profiles do not contain the range of hourly wind variability present in the CARIOCA dataset. In comparison, our idealized model experiments focus primarily on the low wind speed range. The results from Bates and Merlivat (2001) showed that many of the the high % differences occur on days with low wind speed and negligible CO_2 flux, these are consistent with our results in section 6.3.5. We suggest that these discrepancies will be even greater, especially in regions susceptible to strong diurnal warming and convective enhancement, as the fluxes presented in Bates and Merlivat (2001) were evaluated using only wind-speed dependent k parameterizations.

High frequency diurnal variability will obscure the true upper ocean mixed layer temperature which is of interest for many climate studies, this has implications for creating accurate and stable climate SST products from both satellite and in situ observation.

Precise knowledge of the diurnal heating at the time and depth of measurement will allow for datasets to be corrected to obtain the true mixed layer temperature (Donlon, 2004). The diurnal cycle can change dramatically in immediate response to changes in wind speed (Stuart-Menteth et al., 2005a), thus the inclusion of wind bursts and extreme wind events is necessary to evaluate both the diurnal response and to calculate its affect on net CO_2 transfer.

Skin temperature is the most physically appropriate SST for calculating air-sea heat and gas fluxes, as it is effectively located at the top of the diffusive boundary layer (McGillis and Wanninkhof, 2006). Heat flux errors according to Ward (2006) associated with the warm layer will be of the order 10–50 W m^{-2}, whereas errors from the cool skin will approach 1–10 W m^{-2}. A strong diurnal cycle results in increased heat loss to the atmosphere (Cornillon and Stramma, 1985) and a reduced CO_2 transfer into the oceans (McNeil and Merlivat, 1996). We have presented results from only 1 PIRATA location, and in order to describe the global or regional significance a more thorough study will be required. We acknowledge that the idealized results presented here do not represent the true flux of CO_2 nor are they intended to, but provide an order of magnitude estimate of the impact of the diurnal variability and the response to wind history over the diurnal cycle. With an increase ΔT of 1.5 °C resulting in an increased net CO_2 flux of almost 30% in one such case. The results presented, while limited, shed light on questions related to the sampling strategy for measurements of air-sea fluxes. In particular, phase between variables is critical and representation of forcing in models needs to be at the same scale as the anticipated ocean mixing (e.g. order of an hour instead of a day).

We neglect the chemical enhancement of gas transfer which can occur at low winds (Johnson, 1982); whereby chemically reactive gases can bypass the rate-limiting molecular diffusion step by undergoing hydration reactions within the boundary layer with hydroxide ions and water molecules. Although it has been shown to have only a minor impact on air-sea gas transfer during average oceanic turbulent conditions, during period of low winds and high SST, especially areas such as the equatorial CO_2 source regions, its effect is more pronounced, at around 4–8% of the total CO_2 exchanged (Wanninkhof and Knox, 1996).

In this paper we have focused on sub-daily variations in wind and thermal forcing. Further refinement of CO_2 fluxes requires inclusion of chemical enhancement, the haline skin effect, biology, and additional processes that alter transfer velocity such as rain and sea state. Whilst we have only considered a single location in the tropical Atlantic, diurnal warming can become large even in the high latitudes, especially during summer Kawai and Wada (2007). In situ observations that can resolve the diurnal SST cycle are not sufficiently close to the Polar regions, thus further studies focusing on the high latitudes should be conducted. The high latitudes act as sinks for CO_2, due to the presence of colder, nutrient rich water and the associated biological drawdown effect on

pCO_2 (Takahashi et al., 2002). In these regions diurnal warming acts to reduce the sink. Ultimately, this means that the annual net uptake of CO_2 by the oceans may have been overestimated. Future modelling work will aim to address the issue of the regional and global significance.

6.5 Conclusions

Our 1-d model results address similar cases to the observations analyzed by Stuart-Menteth et al. (2005b); those diurnal shapes classified by Stuart-Menteth et al. (2005b) are reproducible by the idealized simulations given appropriate meteorological forcing. The good agreement between the model and the in situ buoy measurements highlights the effectiveness of the model for representing diurnally varying processes. An unexpected but interesting consequence of this study is that a 1-d turbulence closure model, given enough met-ocean information, could predict the magnitude of the ΔT and hence be used to correct for its effect in regions unaffected by local processes such as advection.

The results from our phase-dependent simulations concur with those of the simple model experiments conducted by Dickey and Simpson (1983). Phase dependent wind stress and cloud fraction can, during low wind speed conditions, lead to enhanced diurnal sea surface temperature amplitudes and variation in mixed layer depths. These have important implications for calculating the air-sea exchange of CO_2.

In addition to the influence of short-term wind variability on air-sea CO_2 exchange (Bates and Merlivat, 2001), when the wind speed is low and solar heating is large, strong diurnal warming may exist, which can result in significant ocean degassing. Hence, the calculated flux of CO_2 will not be representative of the true integrated exchange unless those diurnal processes are accounted for. The shape of the diurnal signal and magnitude of ΔT ultimately depend on the wind and cloud cover at earlier time-steps, up to ± 5 hours before local solar noon. Thus the amount of gas exchanged at low wind speeds in the presence of a strong diurnal signal is determined, not only by the mean wind stress over the observational period, but by the timing and duration of specific wind and cloud 'events'.

We attribute differences between the observations and our 1-d model simulations to environmentally dependent factors such as the time of year, water type, latitude and the simplification of our idealized forcing parameters, such as the lack of variability. Since solar insolation, wind speed and ΔpCO_2 vary both spatially and temporally, a further study will seek to evaluate the global significance.

A simple treatment of the CO_2 flux (see table 6.7) largely underestimates the flux during low wind speeds in source regions. We suggest that, in regions such as the tropics, where diurnal variability is prevalent, the use of high sampling frequency wind and skin

temperature data is necessary not only to reduce the smoothing-out of extreme values, but to account for the temperature-related and subsequent convective effects on air-sea CO_2 exchange.

Chapter 7

A global modelling perspective

Whilst the theoretical modelling experiments conducted in the previous chapters have provided insight into the physical processes affecting air-sea gas exchange, they do not explicitly provide information about the significance of such processes (Jeffery et al., 2007, 2008). For this we need to consider the relationship between times and places where convectively driven gas exchange occurs and the patterns of outgassing and ingassing cross the world ocean. Only then can we determine whether the modifications to the gas flux equations introduced in chapter 5 and 6 really matter for the estimation of the global CO_2 budget. Thus in this chapter the focus is shifted away from the tropical Atlantic and from idealized conditions to investigate what happens over the course of a year, and also what happens on a global scale.

7.1 Yearly integration of GOTM

The jump from 1-d modelling to global modelling involves a number of challenges and compromises that must be undertaken in order to reach the goal of identifying the importance of convective CO_2 transfer. One of these compromises is that the forcing data used to drive a global physical model of the ocean will not be of such high resolution as that used during the 1-d experiments. Thus, the question is posed: How affected are estimates of the CO_2 flux and global carbon uptake by the resolution of the input data? By first conducting some experiments using the 1-d model with varying input data resolutions we can examine the effect these have on yearly estimates of the air-sea CO_2 flux. This will provide us with a basis for assessing whether the results of experiments concerning convective effects on integrated CO_2 fluxes using the U.K. Met Office global 3-d model are seriously compromised by the present limitations of that model.

7.1.1 Model set-up

GOTM was run for the period of 15/01/02–25/12/02 at 10°S10°W. The maximum model depth was 200 m, spread over 200 levels with a range of level thicknesses from the surface to 200 m (see figure B.1). This is the same site and model setup that was used in chapters 4 and 5. The particular location is ideal for running the 1-d model as advective processes, which are neglected by the model, are reasonably low (Foltz et al., 2003).

The PIRATA surface meteorology was combined with NCEP pressure data and cloud cover estimates from Meteosat-7 and the ISCCP to produce the model forcing. The model was initialized with temperature and salinity profiles from the PIRATA mooring, and was allowed to free-run for the duration of the experiment. The model time-step was 1 hour.

Model forcing, consisting of wind speed, air temperature, pressure, cloud cover, relative humidity was resampled in order to examine the effect of lower temporal resolutions on the accuracy of the model, and the impact that this has on both the gas transfer velocity and air-sea CO_2 flux. An initial model run was conducted over the experimental period using 1 h resolution for the input data, this baseline uses the same forcing resolution as that of the previous chapters. The subsequent runs used resampled data of the following temporal resolutions; 2, 3, 4, 6, 12 and 24 h.

Air-sea CO_2 transfer was calculated by the 1-d model at every time-step using the modified COARE gas transfer velocity parameterization. Monthly average values for the oceanic pCO_2 and atmospheric pCO_2 values were taken from the Takahashi et al. (2002) climatology (with $pCO_{2w} \simeq 360$ and $pCO_{2a} \simeq 350$). The atmospheric pCO_2 data were modified using the method presented in Kettle and Merchant (2005) to account for temporal averaging of sea-level pressure.

7.1.2 Yearly integration

Figure 7.1 shows the results of the baseline yearly integration of GOTM. Panel a shows the model 1 m SST (black) and the corresponding 1 m SST as recorded by the PIRATA mooring at 10°S10°W. In general, over the duration of the model period, GOTM provides a reasonable representation of the observed 1 m SST. However there are times of the year, where the 1-d model overestimates the SST, namely March-April and October-December. In addition the model also underestimates a warm spike in the observations during July 2002. The 10 m wind speed for the duration of the model run (panel b) varies between 1 m s^{-1} to a maximum of approximately 14 m s^{-1}, with both of these extreme values occurring during July and August respectively. The high frequency, sub-diurnal variability of the wind speed is clear and for the majority of the year lies between 5 and 10 m s^{-1}.

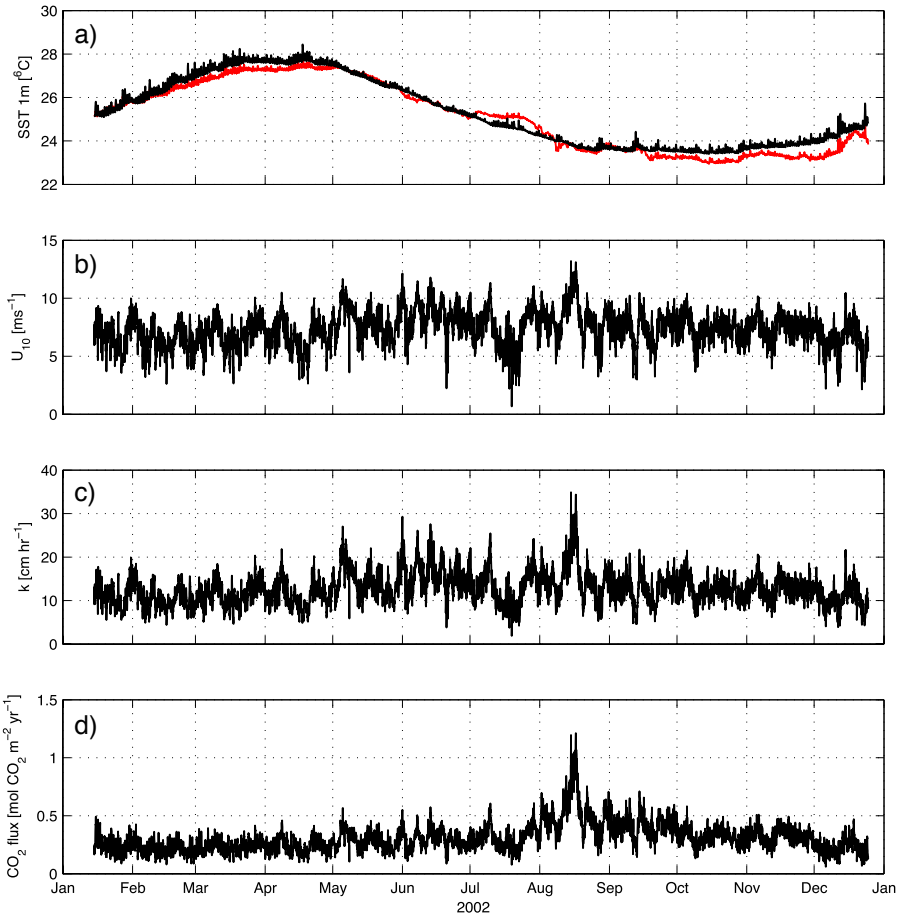

FIGURE 7.1: Results from GOTM model run at 10°S10°W for the period 15/01/02 - 25/12/02. a) 1 m SST (°C) for GOTM (black line) and PIRATA mooring (red line). b) 10 m Wind speed (m s^{-1}). c) Transfer Velocity k (cm hr^{-1}). d) Air-sea CO_2 flux (mol CO_2 m^{-2} yr^{-1}). Model forcing data sampled at 1 h resolution.

The modified COARE gas transfer parameterization presented in chapter 4 was used to calculate the gas transfer velocities (k) at 1 hour resolution (figure 7.1c). In this example the following values for the tuning parameters A=1.85 and B=1.0 were chosen, these values correspond to the sub-layer buoyancy scaling and bubble mediated parameters respectively. Given that detailed model runs using multiple coefficients were included in chapter 5, it was deemed unnecessary to conduct those model runs during this experiment. The use of the modified COARE model allows k to vary with not only wind speed and temperature, but is also enhanced during conditions of buoyancy-driven nocturnal convection. In this regard, the transfer velocity shows the same high frequency sub-diurnal nature as the wind speed, with peaks and troughs corresponding to the those found in the wind data.

The surface pCO_2 at 10°S10°W was slightly larger than the atmospheric pCO_2 for the duration of the model run, thus the air-sea flux remains positive indicating that the region is a weak source for CO_2. For the majority of the year the CO_2 flux (figure 7.1d)

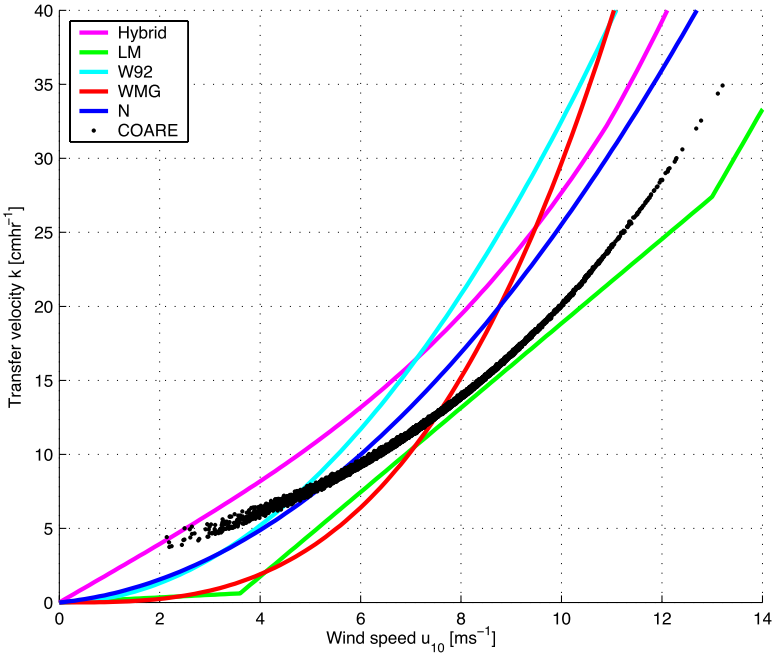

FIGURE 7.2: Wind speed (m s^{-1}) versus transfer velocity (cm hr^{-1}) for the following gas transfer velocity models with $S_c = 660$): W92, WMG, LM, N and Hybrid for CO_2 at 20 °C. Data from the GOTM run between 15/01/02 - 25/12/02 using the modified COARE model is shown.

remains below 0.5 mol CO_2 m^{-2} yr^{-1}, the exception being between August and September where values reach approximately 1.8 mol CO_2 m^{-2} yr^{-1}. Given the non-linearitiy of the transfer velocity versus wind speed relationship, the largest fluxes correspond to the strongest wind speeds.

Figure 7.2 shows all of the transfer velocity data points from the model simulation versus the corresponding average wind speed. In addition 5 simple gas transfer velocity parameterizations are also plotted on the same axis for comparison. The LM: Liss and Merlivat (1986), W92:Wanninkhof (1992), WMG:Wanninkhof and McGillis (1999), N:Nightingale et al. (2000b) and Hybrid:Woolf (1997) models are shown in addition to the modified COARE parameterization. Note that these simple models have been calculated with a fixed value of Sc=660, whereas the Schmidt number in the COARE model varies according to changes in kinematic viscosity and mass diffusivity.

This particular implementation of the COARE model results in slightly lower transfer velocities compared to some of the simple-wind speed based relationships at higher wind speeds. At low wind speeds, less that 4–5 m s^{-1}, the COARE model produces significantly larger transfer velocities and hence CO_2 fluxes. Only the hybrid model produces sufficiently large transfer velocities at low wind speeds, however even this model still tends toward zero for zero wind speed. It is important to note that this is only one possible tuning of the COARE model, and that in previous chapters the result

of varying the empirical coefficients was highlighted. We know that by increasing the weighting to the bubble-mediated coefficient B and sub-layer buoyancy coefficient A we can produce a significant change in the magnitude of the model, in order to 'fit' the parameterization to observations.

As this is a 'hypothetical' study of the impact of the changes made to the parameterization and their subsequent effects on the air-sea flux of CO_2 we choose to apply only one of the predetermined sets of empirical coefficients for the experiment.

7.1.3 The effect of input data resolution

The baseline 1-d experiment was repeated with input data of varying temporal resolution. This was achieved by resampling the raw surface meteorology and ancillary data used to create the necessary input files needed to initialize GOTM. The model time-step was kept constant at 1 hour in order to highlight the effect of the resampling. Table 7.1 shows mean model SST and wind speed, as well as statistics based on the comparison of the 1-d model with the coincident temperature available from the PIRATA mooring located at 10°S10°W.

Looking at the mean yearly SST for each of the different input data resolutions in table 7.1 reveals that as the temporal resolution of the data becomes coarser the average SST increases. However the increase in SST with decreasing temporal resolution is small, with only roughly 0.05 °C difference between the baseline resolution and the resampled 24 h inputs. Noticeably, RMSE and standard error of the mean increase as the resolution becomes coarser. The R^2 coefficient decreases as expected, with decreasing data resolution, as the fit between the model and the observations gets worse.

The gas transfer results are shown in table 7.2. It shows the yearly mean values for the transfer velocity, air-sea CO_2 flux, global carbon transfer and the convective residual

Resolution	SST (°C)				Wind speed (m s^{-1})
	mean	RMSE	Std. error	R^2	mean
1 h	25.316	0.362	0.017	0.962	7.35
2 h	25.321	0.367	0.017	0.962	7.32
3 h	25.325	0.373	0.017	0.961	7.31
4 h	25.333	0.382	0.017	0.959	7.30
6 h	25.334	0.394	0.017	0.956	7.29
12 h	25.360	0.440	0.018	0.947	7.27
24 h	25.364	0.443	0.018	0.947	7.25

TABLE 7.1: Table showing the impact of input data resolution on mean SST and mean wind speed for a yearly integration of GOTM over 2002. The 1-d model was run between 15/1/02–25/12/02, R^2 for SST values were calculated at the 95% confidence level using comparison of model with PIRATA mooring observations for the same time.

Resolution	k (cm hr^{-1})		CO_2 flux (mol m^{-2} yr^{-1})		Carbon transfer	Conv. residual
	mean	range	mean	range	(GT C yr^{-1})	(%)
1 h	12.67	1.90–34.91	0.31	0.06–1.21	3.02e−5	3.68
2 h	12.59	3.80–33.17	0.30	0.07–1.17	2.99e−5	3.72
3 h	12.55	4.37–31.81	0.30	0.08–1.12	2.98e−5	3.75
4 h	12.53	4.40–31.99	0.30	0.09–1.12	2.97e−5	3.79
6 h	12.49	4.61–30.41	0.29	0.09–1.10	2.94e−5	3.91
12 h	12.43	5.45–28.93	0.29	0.11–1.03	2.89e−5	4.16
24 h	12.25	6.09–25.50	0.29	0.12–0.91	2.87e−5	4.22

TABLE 7.2: Table showing the impact of input data resolution on mean transfer velocity, CO_2 flux, carbon transfer and residual convective enhancement for a yearly integration of GOTM over 2002.

as calculated by GOTM using the specified input data resolutions. The yearly mean transfer velocity decreases from 12.67 cm hr^{-1} to 12.25 cm hr^{-1}. Looking at the range of values for k we can see that as resolution is reduced the maximum values are reduced and the minimum values are increased, constraining the range over the model period. The same is true for the CO_2 flux. Since this region is a weak source for CO_2 it results in the amount of degassing over the year being reduced.

However, the enhancement caused by using the modified COARE parameterization instead of the original actually increases as the data resolution decreases. This can be explained by looking at the wind speed in table 7.1 or the transfer velocity in table 7.2, the means of which are reduced with decreasing resolution. More importantly, although the minimum values are increased in the range of k, the maximum values decrease allowing greater enhancement through the convective terms in the gas transfer parameterization. This is a direct result of averaging, which leads to a reduction in peak values. These peak values are important when considering the net CO_2 flux, due to the non-linearity of the wind-speed relationship with the gas transfer velocity.

In each of the cases, changing the temporal resolution of the surface meteorological input data degrades the model output. However, there remains a correlation between the modelled and the observed surface temperatures. Even at 12 and 24 h temporal resolution, the modelled mean transfer velocities and fluxes only differ by around 3.5% to 7% respectively.

The calculated convective residual is slightly larger than the residuals estimated in the baseline experiment. This results from a reduction in the magnitude of the peak transfer velocity at coarser temporal resolutions. These discrepancies would be tolerable in a global simulation given constraints of processing time and computational expense. As noted earlier, a global modelling perspective will require some compromise in terms of the accuracy of the fluxes returned. These simple 1-d experiments highlight the effects of reduced temporal resolution in the forcing data, and show that this particular discrepancy should be reasonably small.

7.2 Ideal scenario

1-d model experiments with GOTM and the improved COARE gas transfer parameterization have shown that convective gas exchange is important in the tropical Atlantic at 10°S10°W. Diurnal temperature variability has important implications for net CO_2 transfer especially during low wind speeds. In order to address the question of its global and regional significance a new approach is necessary as it is impractical to run the 1-d model at every ocean grid point.

In an ideal world a global modelling approach would present the best means of assessing how important the convective CO_2 exchange processes studied in this thesis are to the global CO_2 budget. Features of such a model would include:

1. The ability to model the near surface ocean in sufficient vertical resolution
2. The capacity to describe the diurnal cycle of SST
3. A small enough time step to incorporate high frequency wind events
4. High resolution ocean and atmosphere CO_2 fugacities for the flux calculation

Accurate representation of the near surface ocean in terms of the vertical temperature structure and its temporal evolution throughout the day is necessary to properly incorporate changes in solubility. Furthermore it is necessary for the inclusion of the increased turbulence during nighttime restratification of the upper warm layer.

Previous literature and experimentation has shown that temporal averaging poorly represents the peak wind speeds experienced, and that this is an important factor when considering the integrated air-sea exchange of carbon dioxide over some time period. This is inherently due to the mathematical artifact of smoothing, and the non-linear nature of the gas transfer velocity relationship to the surface roughness.

The 1-d experiments presented previously used monthly climatological means for describing the oceanic and atmospheric pCO_2 concentrations, allowing them only to vary with temperature and sea level pressure respectively. The Takahashi et al. (2002) data is the most comprehensive and widely used climatology of surface water pCO_2 observations, however it is still extremely limited. Thus, given the available data, the choice was made to concentrate on identifying the physical mechanisms responsible for affecting gas transfer, rather than attempting to present a real-world estimate of the CO_2 flux in the tropical atlantic. In order to expand upon these results, incorporation of the biogeochemical processes responsible for the upper ocean pCO_2 concentrations is necessary.

The COARE gas transfer parameterization requires considerably more information than its simplified wind speed-based counterparts. The necessary inputs as detailed in chapter

5, must come either from the forcing information or must be calculated by the global model. This could be achieved by calculating the surface heat budget with the NOAA-COARE v3.0 heat flux model, as this calculates many of the extra variables required by the the gas transfer subroutines.

A coupled ocean-atmosphere model could meet requirements 1–3, providing that the input data are of high enough resolution, and the model time-step is short enough to resolve the important diurnal temperature changes on both global and regional scales.

Unfortunately, because of the paucity of the ocean CO_2 partial pressure data currently available, global coverage of ΔpCO_2 fields does not have a temporal resolution on par with that currently available for the meteorological parameters such as wind speed and SST. Additionally current remote sensing estimates of ocean surface pCO_2 have so far been confined to regional experiments, such as the Caribbean study conducted by Olsen et al. (2004).

An alternative method to interpolating observations of ocean CO_2 concentrations, would be to generate them using a carbon chemistry model that could represent the marine ecosystem. This would provide realistic input parameters for the gas exchange calculation, and as such the fluxes would be spatially and temporally representative of ocean sources and sinks.

One such system that could potentially provide required fields to answer the convective CO_2 exchange question, is that currently used by the U.K. Met Office for ocean forecasting purposes (see section 3.6.1).

7.3 Global integration method

The U.K. Met Office Unified Model consists of a suite of atmospheric and oceanic models which provides the necessary framework for implementing the modified gas transfer parameterization developed using the 1-d GOTM test-bed. Whilst a global model approach is suitable for addressing the significance of convective CO_2 transfer, we must, however, ultimately compromise on some of our ideal requirements (section 7.2). This is not only to limit the computational expense such a set-up would require, but also to reduce the number of changes that would need to be made to the system.

7.3.1 Model setup

This study uses the coarse resolution global configuration of FOAM (see section 3.6.1) with 20 vertical levels and a timestep of 1 h. Model levels are unevenly spaced with the vertical resolution decreasing with depth from 10 m near the surface to 600 m in the deep ocean. The FOAM model is run in delayed mode with Numerical Weather

Model output	Units	Resolution
Sea surface temperature (10 m)	°C	24 hr mean
Wind mixing energy	W m^{-2}	24 hr mean
Mixed layer depth	m	24 hr mean
Air-sea CO_2 flux	mol CO_2 m^{-2} yr^{-1}	24 hr mean

TABLE 7.3: FOAM-HadOCC diagnostic parameters output in addition to regular model results.

Prediction (NWP) surface fluxes and meteorology obtained from a previous run of the atmospheric sub-model used as forcing. The surface forcing data is of 6-hourly resolution and is interpolated onto the model time-step. The initialization files, which included the necessary spin-up information, were taken from a previous FOAM experiment and thus required that the model be run for the period 1^{st} January 2003–31^{st} December 2003. The model output is then averaged into 24 hour bins.

The FOAM model is coupled to the HadOCC (see section 3.6.2) model, enabling the calculation of the air-sea CO_2 fluxes. The individual ecosystem model parameters were not the primary focus of these experiments and were not changed from their default value. These can be found in table 2 of Palmer and Totterdell (2001). Parameters for which no source is given were determined by Palmer and Totterdell (2001) by fitting the biological model to data using a simple 1-d column version of the model. Many of the zooplankton parameters were obtained in this way, because the zooplankton compartment represents both micro- and meso-zooplankton.

The FOAM-HadOCC model is run in 10-day segments, which are automatically assigned by the SCSUI. The model is run on a number of nodes within an NEC SX-6 supercomputer at the U.K. Met Office. Model output are 64-bit Fortan PP files for each 10-day segment, which require conversion to 32-bit floating data and export to netCDF format. In addition to the regular FOAM model output, a number of additional diagnostic quantities were added to the output file (see table 7.3). Unfortunately, several parameters such as the gas transfer velocity or surface and atmospheric pCO_2 were not available to output from the model, without significant code changes.

The gas transfer velocity was calculated using the improved COARE gas transfer parameterization described in chapters 5 and 6. Whilst atmospheric pCO_2 was set to a constant climatological value, the ocean pCO_2 value varies according to changes in the marine carbon cycle as calculated by HadOCC. In comparison, the earlier 1-d experiments used a fixed climatological value for both pCO_{2a} and pCO_{2w}. Thus the global CO_2 flux calculated by FOAM-HadOCC should reflect the biological, in addition to the physical, processes responsible for the flux.

7.3.2 Modifications

In order to introduce the modified COARE parameterization into the FOAM-HadOCC system a number of changes to FOAM's 'Tracer' subroutine were necessary. These changes took the form of proprietary modification sets which were enabled during the compilation of the model executable. Logical switches were added to the subroutine, providing additional functionality to the model. These switches could be activated either by manually providing 'hand-edits' (a text file containing the switch options, read by the model) or by selecting or de-selecting particular modsets via the UMUI tool. Additions made to the model did not overwrite any existing functionality of the model, and were not necessary for compiling a successful executable.

As with the 1-d model, many of the necessary parameters for the COARE gas transfer parameterization are calculated by the NOAA COARE v3.0 air-sea bulk flux model. Thus the choice was made to implement the bulk heat flux model, with the intention of using the variables calculated to help drive the gas transfer parameterization. Table 7.4 shows the input and output variables of the heat flux model.

Input	Output
Date	Sensible heat flux (W m^{-2})
Wind speed (m s^{-1})	Latent heat flux (W m^{-2})
SST (°C)	Skin temperature (°C)
Air temperature (°C)	Surface stress (N m^{-2})
Air specific humidity (g kg^{-1})	Sensible heat flux due to precip. (W m^{-2})
Pressure (Pa)	Cool skin deviation (°C)
Solar irradiance (W m^{-2})	Warming across warm layer (°C)
Downwelling longwave irradiance (W m^{-2})	Warm layer thickness (m)
Rain (mm hr^{-1})	Cool skin thickness (m)
Lat (N =+)	Buoyancy flux (W kg^{-1})
Lon (E =+)	

TABLE 7.4: NOAA COARE v3.0 heat flux model inputs and outputs

A switch to activate an alternative piston velocity, namely the improved COARE gas transfer parameterization was added. This allowed the existing model setup which includes the Wanninkhof (1992) parameterization to be compared with the changes made for this study. The gas flux subroutine itself was also rewritten in order to better take into account changes in temperature and solubility, and to accept the additional parameters provided by the heat flux model. The existing simple equation (see equation 3.5) relies on solubility and the CO_2 concentration differences being called from functions external to the subroutine. Implementing equation 7.1, it was necessary to allow access to the external functions from within the gas transfer subroutine itself.

$$F = k\alpha_s[(pCO_{2w}\frac{\alpha_w}{\alpha_s}(1 + 0.015\delta_T) - pCO_{2a})] \tag{7.1}$$

Using the above equation for calculating the air-sea flux, F, requires that solubility, α, be recalculated based on the appropriate temperature and salinity. Changing the input temperature also requires that the equilibrium constants and subsequently the pCO_2 routines be made available from within the gas transfer subroutine. See chapter 6 for a detailed description of the temperature dependencies of the CO_2 flux.

It was also necessary to modify the position of the mixed layer subroutine with regard to the timing of the call. Since the mixed layer depth variable is a requirement of the alternative piston velocity subroutine, it was necessary to call the mixed layer function prior to the gas exchange calculations, enabling the output to be used by subsequent functions. In practice it was not possible to alter the timing of the call within the code itself. The solution was to copy the function, and call it twice during the execution of the 'Tracer' loop, once before the piston velocity calculation and a second time in its original location.

In addition to the extensive changes made to FOAM's 'Tracer' subroutine, a number of serious compromises were necessary to enable a successful executable to be built. Firstly a number of input parameters for the COARE v3.0 heat flux model had to be substituted (see table 7.5)

Required parameter	Substituted parameter
Downwelling long wave irradiance	non-solar penetrating radiation
air temperature	FOAM SST (10 m)
air pressure	fixed value = 1016 Pa

TABLE 7.5: NOAA COARE v3.0 heat flux model inputs and FOAM substitute parameters

The reason for these substitutions was that the particular development version of the FOAM-HadOCC model available for this study was not coupled to the atmospheric model. Many of the parameters required such as the air temperature and radiation variables exist within the atmospheric model, but were not included in the model forcing files by default, and thus were not available for this particular study. Given the limited access to the Met Office computing facilities, it was deemed too time consuming to recreate the model forcing files from scratch and extract the required parameters. As such, substitution of variables that contained a roughly equivalent range of values to the usual inputs was necessary.

The representation of warm layers in the model is limited to the standard FOAM model grid. Whilst we appreciate that the top FOAM temperatures are not the same as the near surface temperatures necessary for the best evaluation of the air-sea CO_2 flux, compromise was inherently necessary in a global model if the goal of estimating the significance of convective CO_2 exchange was to be achieved. Since the FOAM surface temperature still contains some diurnal variability, it will provide an acceptable order

of magnitude approximation. The modifications made to FOAM were written in such a way that, should the warm layer model be activated, the updated temperatures with an enhanced warm layer would be automatically accepted by the gas transfer sub-routine, leaving the option open for improving future experiments.

As a result of these limitations the transfer velocities generated by the implementation of the improved COARE model within FOAM-HadOCC are likely to provide, at best, an order of magnitude approximation. However, it is important to remember that this is still the best possible estimate of the global transfer coefficient, which incorporates those processes important for evaluating convective air-sea CO_2 exchange.

7.3.3 Experiments

Given the limitations of implementing the changes above, the calculated transfer velocities and fluxes are unlikely to be representative of the real-world counterparts we are trying to estimate. However, this does not de-value any comparisons that are made between different model runs, since they will still be internally consistent. To take advantage of this, three global model integrations over the model period (1/1/03–31/12/03) are considered.

Firstly, a baseline simulation was conducted with all of the new modification sets deactivated. The CO_2 flux from this model run was calculated using the Wanninkhof (1992) parameterization for instantaneous wind speeds. This is the default setup used by the U.K. Met Office, and no changes were made to the model. Secondly, a model run was conducted using the COARE gas transfer parameterization as described in Fairall et al. (2000), with the convective terms set to minimum values. Finally, the third model simulation uses the improved COARE parameterization developed in chapter 5. This model run includes the convective processes highlighted by the previous 1-d experiments (see chapters 5 and 6).

The difference between the model setup for each of the three model runs can be seen in table 7.6. From this point forward the individual FOAM-HadOCC experiments will be referred to as Baseline, COARE A and COARE B.

As with the 1-d yearly integration experiment described in section 7.1.2, only one set of empirical coefficients for the COARE gas transfer parameterization was implemented. This was primarily done to reduce the number of model runs in the experiment. Also, given the results from the yearly integration, we can be reasonably confident that interpolating the 6 hourly NWP surface forcing onto the model time-step of 1 hour should not introduce too large an error in the air-sea CO_2 exchange or the convective residual. However, it is important to recall that a reduction in the temporal resolution of the input will result in the range of transfer velocities and hence CO_2 fluxes being reduced.

Model setup	Baseline	COARE A	COARE B
FOAM-HadOCC	yes	yes	yes
Model grid	1°×1°	1°×1°	1°×1°
Timestep	1 h	1 h	1h
Input forcing and resolution	NWP (6 h)	NWP (6 h)	NWP (6 h)
Improved gas flux equation	no	yes	yes
Gas transfer parameterization	Wanninkhof (1992)	Fairall et al. (2000)	Jeffery et al. (2007)
Convective processes	-	minimum	active
A coefficient	–	1.85	1.85
B coefficient	–	1.0	1.0

TABLE 7.6: Experimental set-up

The residuals of the two COARE model runs compared to the baseline can be examined to identify the global and regional effects of the new parameterization, and ultimately answer the question posed by this work: Is convective air-sea CO_2 exchange significant? It is important to note the main caveat of this methodology which is that the model near surface temperatures are unlikely to experience diurnal warming of the magnitude that was observed during the 1-d model studies. As a result the FOAM-HadOCC fluxes and the convective enhancement will probably be underestimated.

7.4 Results

7.4.1 Comparison to standard climatology

In this section the baseline air-sea CO_2 flux for 2003 is compared with an existing climatology. The baseline results were calculated using the default configuration for the global model in use at the U.K. Met Office (see table 7.6). The comparison data is based on that presented in Fangohr et al. (2008). Daily average SST and wind speed from the Advanced Microwave Scanning Radiometer (AMSR-E), a passive microwave instrument were used to calculate the gas transfer velocity k for 2003. When combined with the Takahashi et al. (2002) ΔpCO_2 dataset, it was possible to determine the air-sea flux. Note that the ΔpCO_2 data is based on a reference year, 1995, and does not include the effects of El Niño.

In both the FOAM-HadOCC and AMSR-E cases the CO_2 flux is calculated using the (Wanninkhof, 1992) parameterization for the gas transfer velocity. In this way the difference between fluxes from the coupled physical-ecosystem model and a standard methodology for creating global satellite-based climatologies may be observed. Whilst the transfer velocities will not be precisely the same, almost all of the differences between the two calculations will result from pCO_2 differences. Furthermore, neither of the calculations incorporate any potential enhancement due to convective gas transfer.

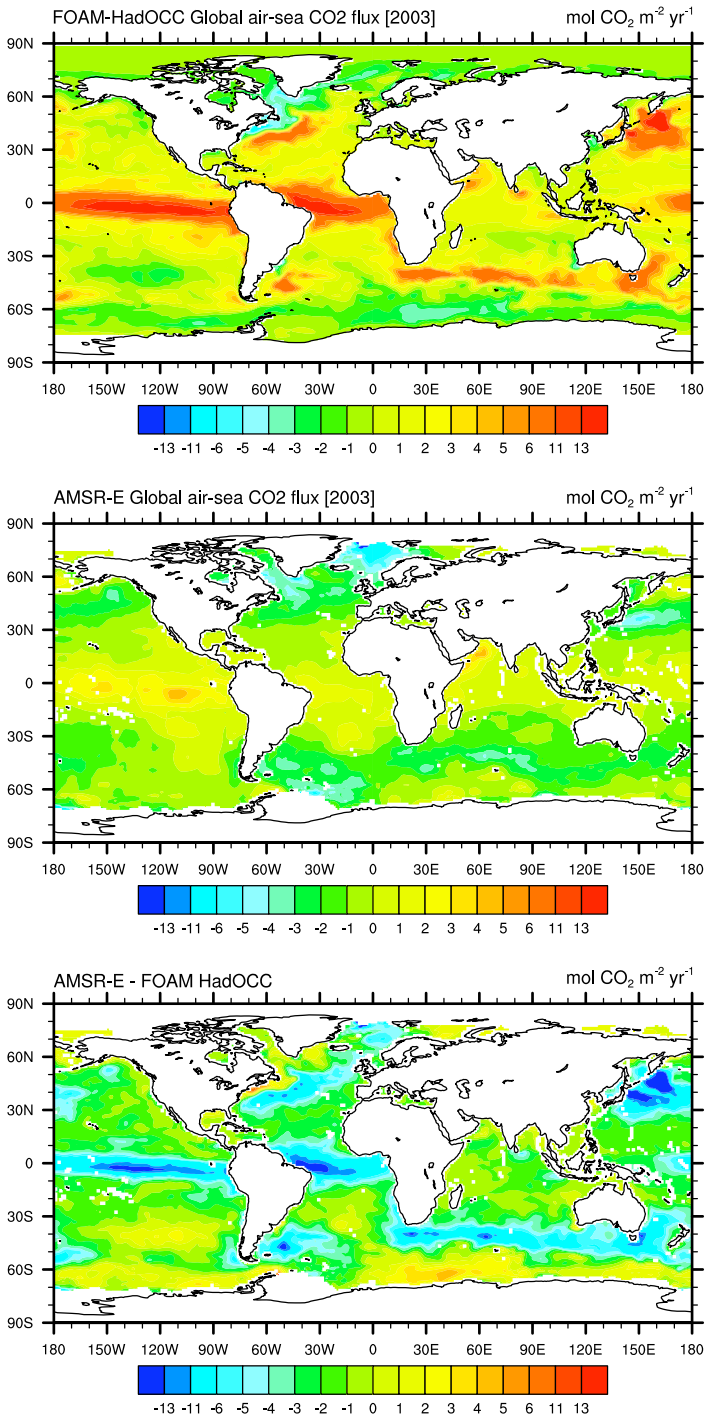

FIGURE 7.3: Comparison of average global air-sea CO_2 fluxes (mol CO_2 m^{-2} yr^{-1}). a) Baseline FOAM-HadOCC CO_2 flux for 2003 b) AMSR-E satellite derived CO_2 flux for 2003 c) AMSR-E−FOAM-HadOCC difference. Both global flux estimates were calculated with the (wind speed)^2 k (Wanninkhof, 1992). AMSR-E flux based on results from Fangohr et al. (2008).

The top panel in figure 7.3 shows the net global air-sea CO_2 flux for the baseline experiment. Although the minimum and maximum values for the CO_2 flux range from $\pm$ 13 mol CO_2 m^{-2} yr^{-1}, the majority of the globe is either slightly positive or slightly negative indicating source and sink regions for CO_2 respectively. However, the source regions cover a greater area than that occupied by the sinks. High latitudes, above 60°N and below 60°S, are sinks for CO_2. Conversely, the equatorial Pacific and Atlantic are strong sources for CO_2, and mid-latitudes and the equatorial Indian Ocean appear as weak sources of CO_2.

The AMSR-E derived net flux for 2003 is shown in the middle panel. Spatially, the source regions for CO_2 are located in similar areas to model estimates. The equatorial Pacific, Atlantic and northern Indian Ocean are source regions, of the order 0–3 mol CO_2 m^{-2} yr^{-1}. The Arabian Sea and the eastern equatorial Pacific contain extreme values of 5–6 mol CO_2 m^{-2} yr^{-1}. The outgassing at the mid and high latitudes is generally in between 2–4 mol CO_2 m^{-2} yr^{-1}. These fluxes are significantly weaker compared to those from FOAM-HadOCC over the same period. Similar to Takahashi et al. (2002) (see figure 2.2), sink regions cover much larger areas of the Pacific and Atlantic Oceans, extending to much lower latitudes. Namely the regions between 40°–60° latitude, which are sources for deep and intermediate water. These sinks are typically between 0–3 mol CO_2 m^{-2} yr^{-1}. Ultimately this results in the oceans being a net sink for CO_2 of approximately 1.6 Gt C yr^{-1} as calculated by Fangohr et al. (2008).

Differences between the satellite and model flux, AMSR-E−FOAM-HadOCC are shown in the lower panel of figure 7.3. Clearly, the FOAM-HadOCC CO_2 flux is not consistent with previous estimates. In addition to the tendency toward outgassing, a number of regions which should be sinks according to the satellite climatology, appear as sources in the model results. The Gulf Stream and Kuroshio region in particular, which are sinks in the middle panel, are sources for the model. Large differences occur along the equatorial Pacific and Atlantic zone, overestimating the magnitude of the release by more than 6 mol CO_2 m^{-2} yr^{-1} in places. Furthermore, the band along 60°S is a strong source in the FOAM-HadOCC estimate, compared to a strong sink in the climatology. Given that the transfer velocities and pCO_{2a} do not differ significantly, the difference in flux is caused by the inadequate representation of the oceanic pCO_2 by the model.

These results highlight a potentially significant flaw in the FOAM-HadOCC model, a large bias toward outgassing. That is, it represents the ocean as degassing at 9 Gt C yr^{-1} instead of absorbing 1.6 GT C yr^{-1} compared to the satellite-based climatology. Whilst we are aware of the inaccuracies in the performance of the model, we point out that this experiment is the first of its kind, and the methodology ultimately provides a first step toward improving calculation of air-sea CO_2 transfer incorporating convective effects. Thus we attempt to estimate the importance of the convective CO_2 transfer by considering the difference between the COARE A and COARE B model output (see table 7.6) in the subsequent sections.

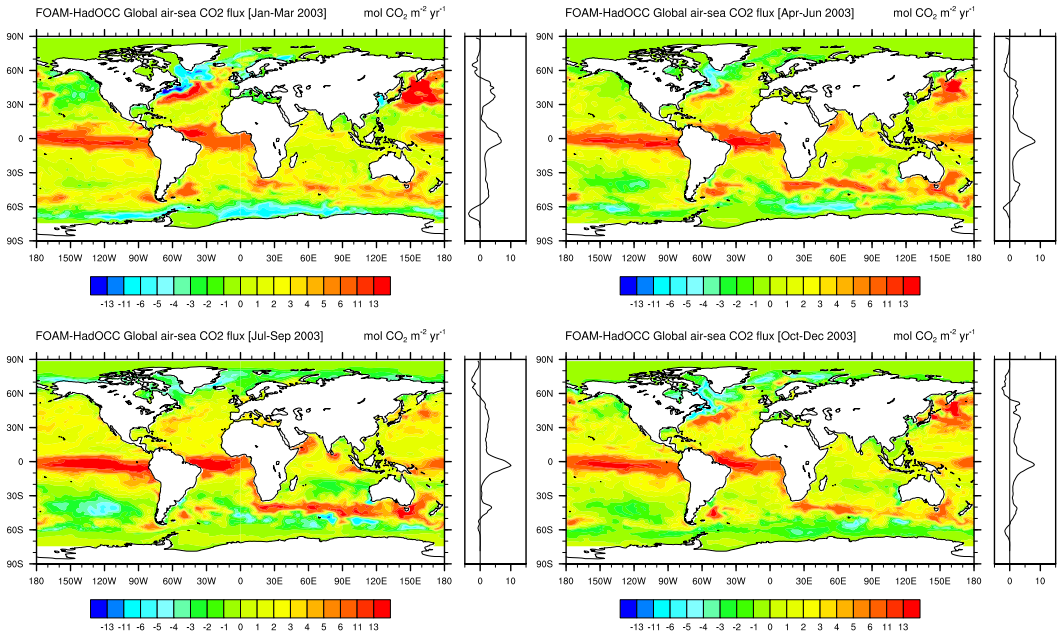

FIGURE 7.4: Quarterly global air-sea CO_2 exchange and zonal averages during 2003 as estimated by FOAM-HadOCC (mol CO_2 m^{-2} yr^{-1}). The modified COARE gas transfer parameterization was used (COARE-A from table 7.6).

7.4.2 Seasonal CO_2 fluxes

The seasonal air-sea CO_2 flux as estimated by FOAM-HadOCC for 2003 can be see in figure 7.4. Quarterly averages of the gas flux are calculated using the modified COARE parameterization. The zonal average is also shown. Spatial distribution of the sources and sinks are consistent with the baseline results in figure 7.3, which are biased toward outgassing.

The period encompassing January to March 2003 contains the lowest magnitude values for the source regions along the equator. However in the northern hemisphere, along the Gulf Stream and in the North Pacific, the Kuroshio area are host to strong source values, between 6 and 13 mol CO_2 m^{-2} yr^{-1}. During this period, the Indian Ocean remains neutral, and the Southern Ocean contains some strong sinks (up to -11 mol CO_2 m^{-2} yr^{-1}) around the Antarctic coastline.

During April to June, the strong sources in the northern hemisphere are significantly reduced. The Indian Ocean begins to show some areas of stronger outgassing near the Persian Gulf. In the Southern hemisphere the magnitude and spatial extent of the Antarctic sink is reduced, and a source region along 60°S appears below Africa, the Indian Ocean and adjacent to Australia.

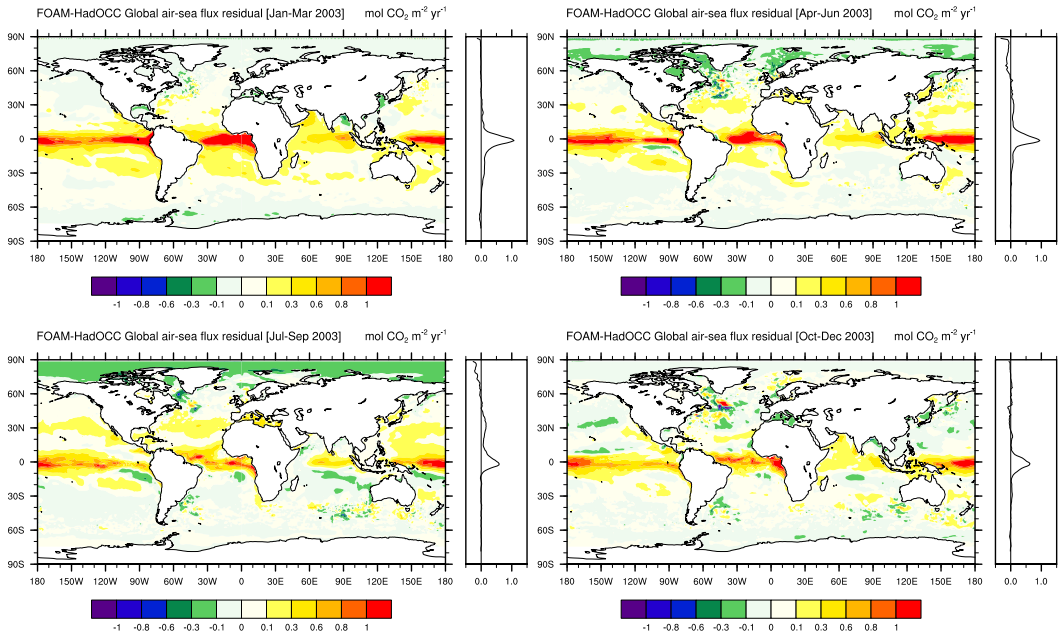

FIGURE 7.5: Quarterly global difference between air-sea CO_2 exchange and zonal averages calculated including and excluding convective effects (mol CO_2 m^{-2} yr^{-1}) (COARE-B−COARE A from table 7.6).

Spatial patterns remain similar during July to September, however the source regions of the equator are at their strongest. The northern Indian Ocean remains a slight source, however the southern part begins to show a small magnitude sink. The Southern Ocean around the Antarctic coastline is reasonably neutral, and in the south Pacific a strong sink is observed centered around 50°S.

Finally in the period October to December, strong source magnitudes return to the north Atlantic and north Pacific upwelling regions. Whilst the strong south Pacific sink has decreased in magnitude, the sink around the Antarctic coastline begins to return to values observed during the 1st quarter of 2003. The Indian Ocean also returns to mainly neutral values.

Overall, whilst there are seasonal fluctuations in the magnitude of both the CO_2 sources and sinks, the equatorial and mid-latitudes remain predominately a strong outgassing area and the high latitudes appear as ingassing areas, or sinks for CO_2. The spatial distribution of the mid-latitude/equatorial outgassing region in the Pacific and Atlantic does not vary much over the course of 2003, Its magnitude also remains in the range of 6–13 mol CO_2 m^{-2} yr^{-1} throughout the year.

The differences between the experimental model runs listed in table 7.6 were calculated from the model output. Figure 7.5 shows the quarterly averages COARE B−COARE A. The differences observed are attributed to the convective processes, which lead to enhanced transfer velocities at night following strong diurnal warming of the upper ocean

during the day. The residuals do not include the full effect of the diurnal temperature changes themselves as the top level of the FOAM model is 10 m.

It is clear from each of the quarterly averages in figure 7.5 that the largest COARE B−COARE A values are concentrated across the equatorial belt, primarily the tropical Pacific and tropical Atlantic between 30°N and 30°S, with the largest differences up to 1 mol CO_2 m^{-2} yr^{-1}. The Indian Ocean also shows some residual difference but is lower, at around 0.3–0.6 mol CO_2 m^{-2} yr^{-1}. These tropical and equatorial residuals are nearly all positive indicating that the flux calculated including the convective processes is greater, in regions that are outgassing. There are also a few regions, in particular those at high latitutes in the northern hemisphere that show negative values (−0.1 to −0.3 mol CO_2 m^{-2} yr^{-1}), these appear to correspond to the sink regions observed in figure 7.4.

Seasonally, the largest positive COARE B−COARE A differences occur during the 1st quarter of 2003. The greatest magnitudes are observed along the equator and cover the largest spatial extent, compared to the other quarters. Regions of 0.3 mol CO_2 m^{-2} yr^{-1} extend to ±30° in both the Pacific and Atlantic basins. The Indian Ocean also shows the greatest area affected compared with the rest of the year. There are very few regions of strongly negative differences, even at the highest latitudes during January to March, those which do show negative values are confined to the Gulf Stream and northern Indian Ocean in the northern hemisphere and the Antarctic coastline in the southern hemisphere. The zonal averages also clearly show that the residuals are heavily biased toward the positive and centered around the equatorial zone.

The spatial distribution of the positive COARE B−COARE A differences remains very similar in the 2nd quarter (April to June) of 2003. However, the magnitude of the positive residuals appears to have decreased slightly. In addition, the spatial extent of the residuals also has reduced in size. The largest differences between this quarter and the first are seen in the northern hemisphere, with a number of slightly negative values now apparent across the Arctic Ocean.

The trend continues during the period July to September, with many of the extreme positive values appearing in patches across the tropical/equatorial zone. The spatial distribution of the positive residuals also appears to be mainly in the northern hemisphere, extending up to 30°N but only down to 10–15°S. The negative residuals extend to cover most of the ocean above 60°N and also appears in patches in the southern hemisphere. However, these negative regions are not as large in magnitude as the positive residuals.

Finally in the fourth quarter of 2003 (October to December) the extent of the negative residuals has been reduced to only a few regions in both the northern and southern hemispheres. The positive residuals remain concentrated across the equator, but show a similar patchiness to that observed in the third quarter of 2003. The main difference

is that the northern extent of the positive residuals has been reduced, it now reaches around 15°N.

The upper panel in figure 7.6 shows a latitude-time Hovmöller plot of the zonal average air-sea CO_2 flux (mol CO_2 m^{-2} yr^{-1}). The spatial patterns previously observed in the seasonal plots are clear, with the equatorial band of outgassing existing throughout the experimental period in the top panel. This signal is greatest between July and September. In the southern hemisphere, seasonal oscillation of the sink regions is observed. Large negative values from January to April move north and decrease in intensity between July and November, then return in December. In the northern hemisphere, between 30°N and 60°N outgassing occurs between January and April but virtually disappears until October, associated with the Gulf Stream. Finally some seasonality is observed in the sink regions above 60°N, which are most negative between July to October.

The air-sea flux anomaly in the lower panel of figure 7.6 also shows extensive seasonality, which is dependent on the distribution of the model's ocean and atmosphere pCO_2 during 2003. The flux anomaly was calculated by subtracting the annual mean CO_2 flux at that latitude, thus positive regions contain CO_2 fluxes greater than the yearly average and vice versa. The region between 30°N and 60°N experiences the largest positive anomaly during January to April, corresponding to the region of high outgassing in the upper panel of the figure. Above 60°N the anomalies are slightly positive for the first half of the year, and become negative between July and November. In the region between ± 30° the largest positive anomalies occur between June and September.

Figure 7.7 contains latitude-time Hovmöller plots of the difference COARE B−COARE A (upper panel) and the COARE B−COARE A anomaly (lower panel) in mol CO_2 m^{-2} yr^{-1}. It is obvious that the largest convective enhancement occurs along the equatorial band, with the difference being greatest in the first half of the year, reaching values of up to 1.5 mol CO_2 m^{-2} yr^{-1}. In comparison, the rest of the ocean has predominately low values ±0.2 mol CO_2 m^{-2} yr^{-1}. The exception is present in the northern hemisphere with a region above 60°N during May to September which contains negative values of around −0.5 mol CO_2 m^{-2} yr^{-1}. Since the convective residuals are effectively the difference between the gas transfer parameterizations, which are always positive, the spatial distribution follows that of the CO_2 flux itself. The negative residuals correspond to sink regions and the positive residuals coincide with regions that are outgassing. This is clearly observed between 30°S and 90°S.

Values for the COARE B−COARE A anomalies (lower panel) rarely exceed 1 mol CO_2 m^{-2} yr^{-1}, and are strongest along the equator, between January and April (0.6 to 1 mol CO_2 m^{-2} yr^{-1}) and above 60°N during May to September (−0.6 to -1 mol CO_2 m^{-2} yr^{-1}). Similar to the upper panel, the southern hemisphere does not contain the range of values present in the northern hemisphere, with the region between 30°S and 60°S

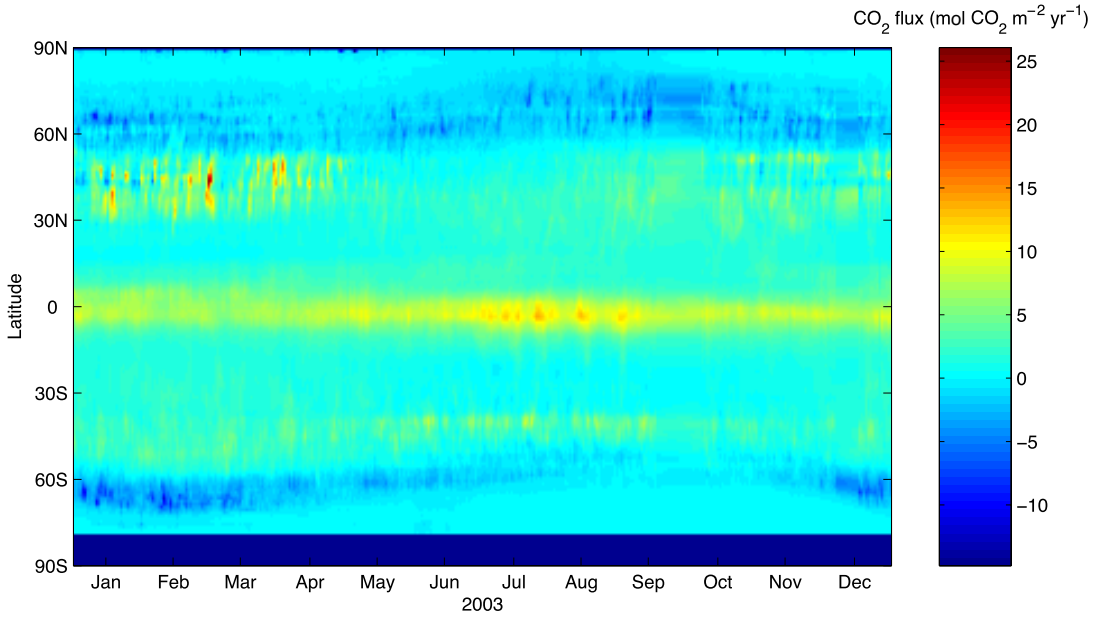

(a) Air-sea CO_2 flux

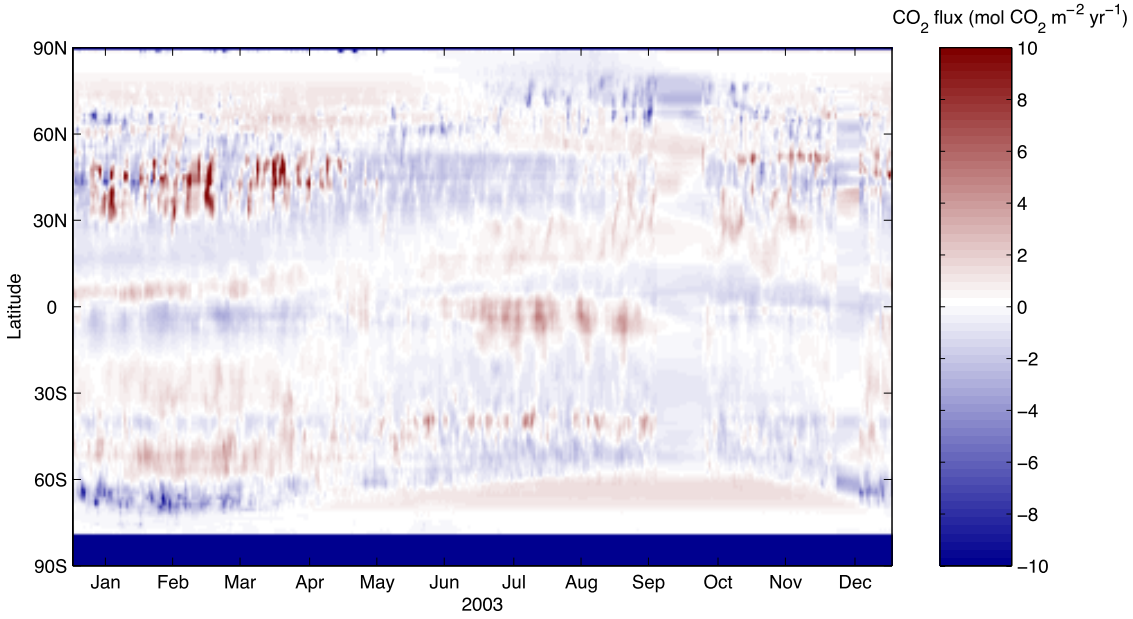

(b) Air-sea CO_2 flux anomaly

FIGURE 7.6: Latitude-time Hovmöller plots showing zonal average; a) air-sea CO_2 flux (mol CO_2 m^{-2} yr^{-1}) for 2003 as calculated by FOAM-HadOCC using the modified COARE gas transfer parameterization. b) The air-sea CO_2 flux anomaly (mol CO_2 m^{-2} yr^{-1}). The anomaly is the flux minus the annual average at that latitude.

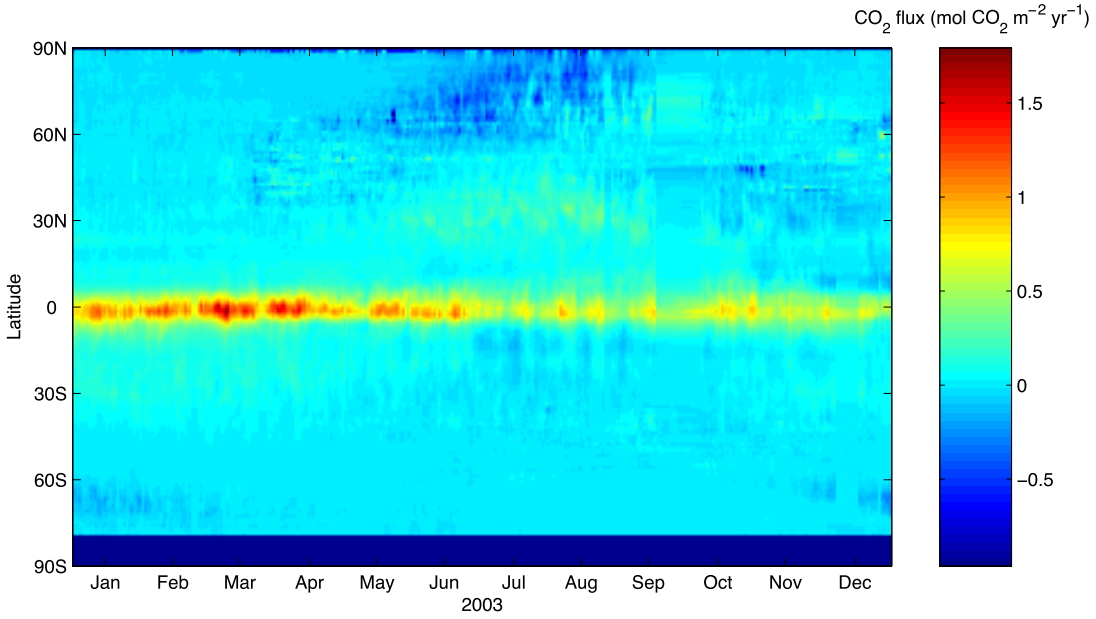

(a) COARE B−COARE A

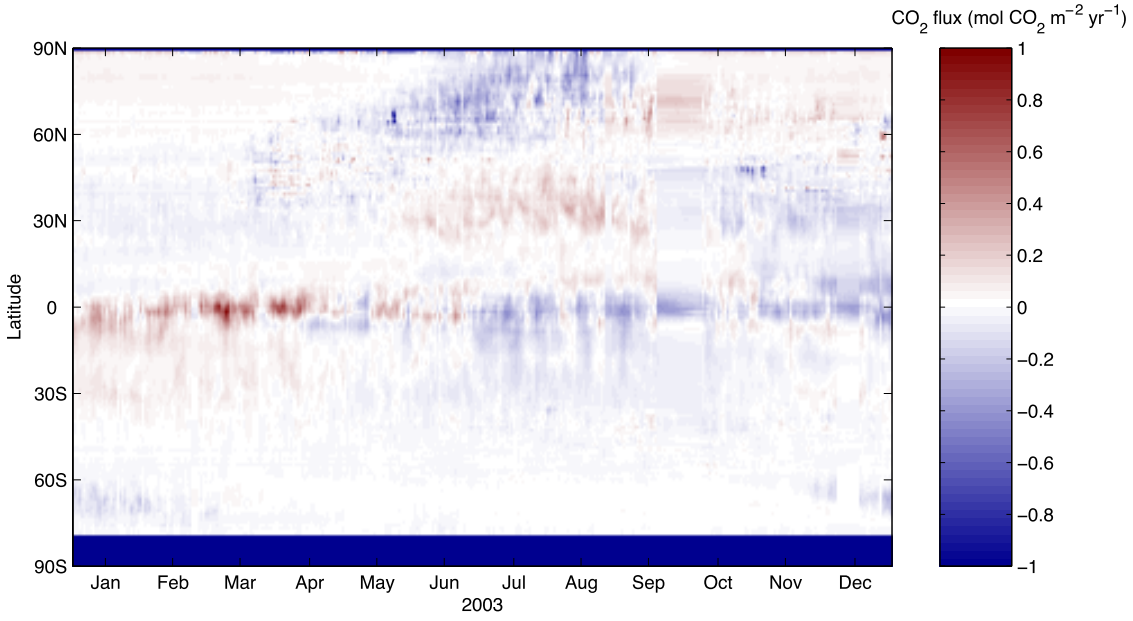

(b) COARE B−COARE A anomaly

FIGURE 7.7: Latitude-time Hovmöller plots showing zonal average; a) COARE B−COARE A (mol CO_2 m^{-2} yr^{-1}) for 2003 as calculated by FOAM-HadOCC using the modified COARE gas transfer parameterization with and without convective effects. b) COARE B−COARE A anomaly (mol CO_2 m^{-2} yr^{-1}) calculated with and without convective effects.

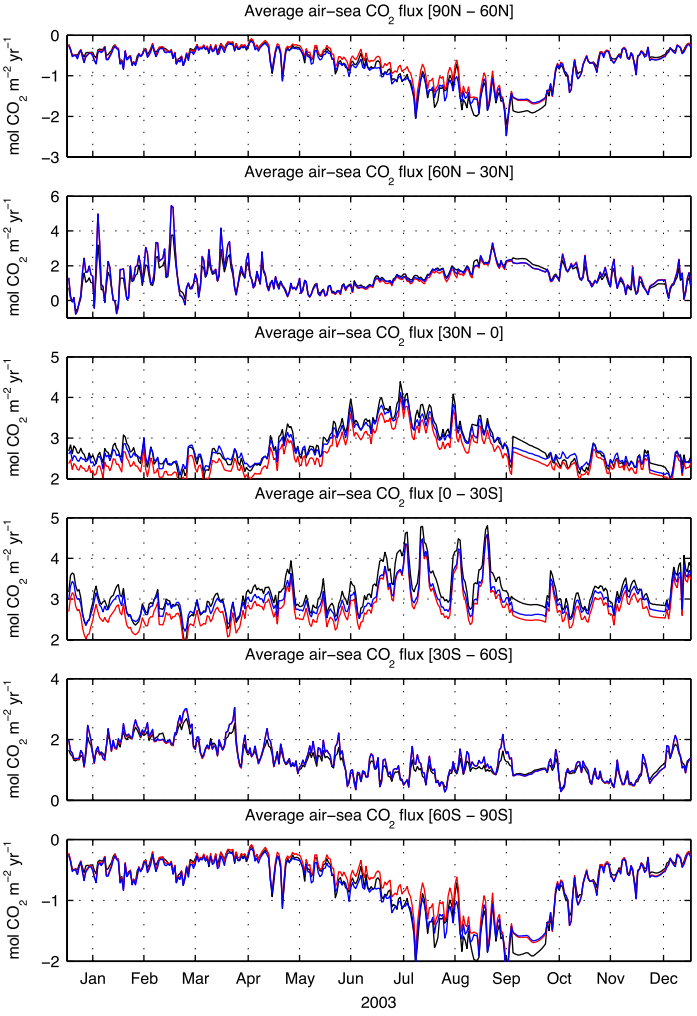

FIGURE 7.8: Average air-sea CO_2 fluxes for six latitude bands as calculated by FOAM-HadOCC. Blue lines: Wanninkhof (1992), red line: COARE gas transfer parameterization without convective effects, black line: Modified COARE parameterization including convective effects.

showing values centered around 0 mol CO_2 m^{-2} yr^{-1}. Contrary to the upper panel however, the convective anomaly along the equator appears slightly negative between July and December. In comparison to figure 7.6 the large values in the northern hemisphere between 60°–30° in the first quarter of the year are not present.

The average air-sea CO_2 fluxes for six latitude bands as calculated by FOAM-HadOCC (mol CO_2 m^{-2} yr^{-1}) are shown in figure 7.8. Each of the parameterizations described in table 7.6 is shown. Note that the difference between the gas transfer parameterizations is considerably smaller than the magnitude of the daily and seasonal fluctuations in the CO_2 flux itself.

The difference between the parameterizations is at its greatest in the 30°N–0 and 0–30°S bands. Where the flux of CO_2 is positive, indicating a region of outgassing, the COARE A parameterization produces the smallest flux, and the COARE B produces the

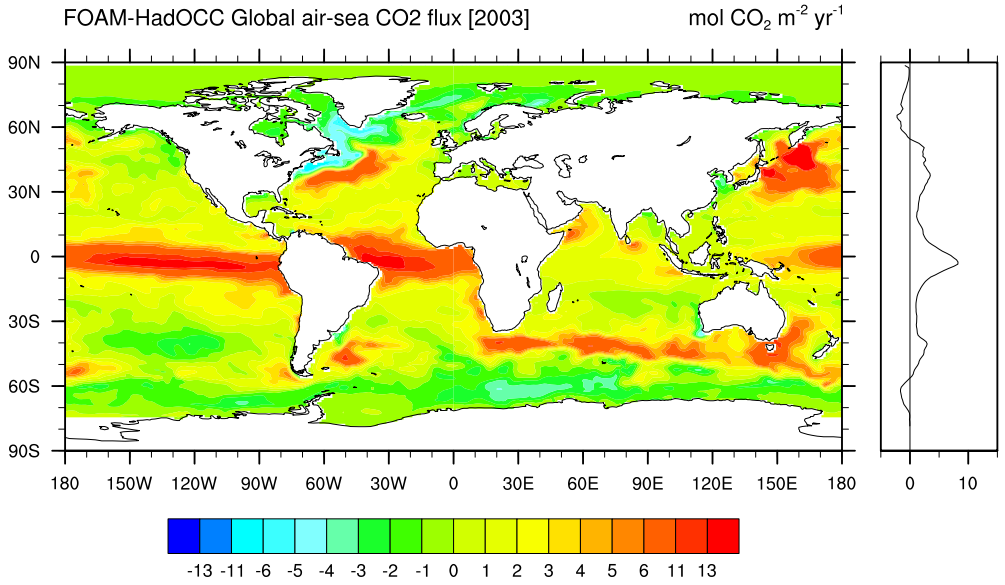

FIGURE 7.9: Net global air-sea CO_2 exchange and zonal averages during 2003 as estimated FOAM-HadOCC (mol CO_2 m^{-2} yr^{-1}). The modified COARE gas transfer parameterization was used.

largest. Fluxes from the baseline experiment lie in between the two. In the mid-latitudes, 30°N–60°N and 60°S–30°S the difference in flux between the experiments is much less, indicating that little convective enhancement is occurring in these areas, consistent with the earlier figures. With the exception of the high latitudes, the average air-sea flux of CO_2 in each of the latitude bands is positive. Looking at the 90°N–60°N and 60°S–90°S bands, the same order is present, with the COARE A experiment providing the lowest fluxes, the baseline in the middle and the COARE B experiment producing the largest negative fluxes as a result of enhanced transfer velocities from convective processes.

7.4.3 Global carbon transfer

Figures 7.9 and 7.10 show the yearly global average flux and convective residual for 2003 respectively, when calculated using the modified COARE gas transfer parameterization from chapter 5. The yearly average flux of CO_2 highlights that the global flux as calculated by FOAM-HadOCC is almost always positive except at the higher latitudes, and that the magnitude of the sea to air fluxes is greater than that of the air to sea fluxes. The main regions which show strong sea to air fluxes in the yearly average are the tropical Atlantic and Pacific, but the northern Pacific and Atlantic also contain regions off the coast of Japan and the U.S. east coast with strong positive fluxes. In the Southern Ocean a band of strong sea to air flux exists between South Africa and Australia at 60°S

The yearly average difference COARE B−COARE A (figure 7.10) shows a clear spatial trend resulting from the convective enhancement present in the COARE B model

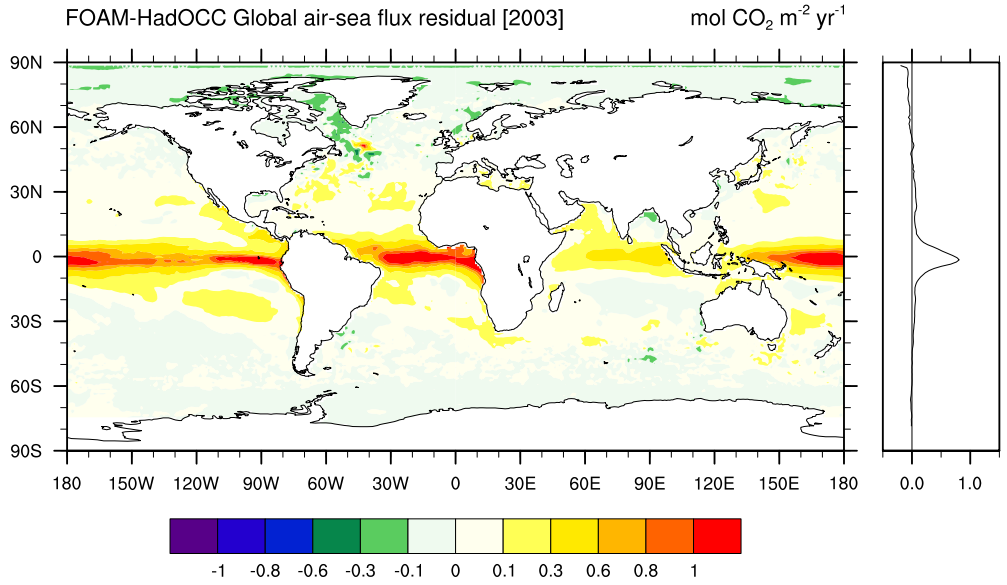

FIGURE 7.10: Net global difference between air-sea CO_2 exchange and zonal averages calculated including and excluding convective effects (mol CO_2 m^{-2} yr^{-1}).

run. The tropical oceans are the regions primarily affected by the enhanced gas transfer velocities. The equatorial zone in the Pacific and Atlantic shows the greatest enhancement, while regions in the north and south Atlantic, south Pacific and tropical Indian Ocean also show enhanced fluxes. In the northern hemisphere there is also some small enhancement to the air to sea flux (negative), but it is not significant globally compared to the sea to air (positive) enhancement.

In order to approximate the effect that convective gas transfer has on net global and regional estimates of carbon exchange, the global carbon transfer for 2003 was estimated using the net air-sea flux calculated during the FOAM-HadOCC experiments. It is estimated by multiplying the air-sea flux with units of mol CO_2 m^{-2} yr^{-1} by the area of the ocean (km^2) and then converting moles to gigatonnes of carbon resulting in units of GT C yr^{-1}. Since the global CO_2 flux is positive (figure 7.9) the direction of the gas transfer is from the ocean to the atmosphere e.g. outgassing, thus the global ocean is a source of carbon in these FOAM-HadOCC experiments. Whilst the magnitude of the flux is affected by the gas transfer coefficient, the direction of the flux is a result of the air-sea pCO_2 difference.

Figure 7.11 shows the net global carbon transfer versus time for 2003 (GT C yr^{-1}) for both the baseline and COARE B experiments (top panel) and the difference COARE B−COARE A (bottom panel). As in figure 7.8, the difference between the gas transfer parameterizations themselves is less than the seasonal variation in the carbon transfer itself. The global release of carbon to the atmosphere is in the range 6–12 GT C yr^{-1}. A simple annual cycle is not readily apparent, although marginally higher values are observed in the period between July and September 2003. The convective residual (lower

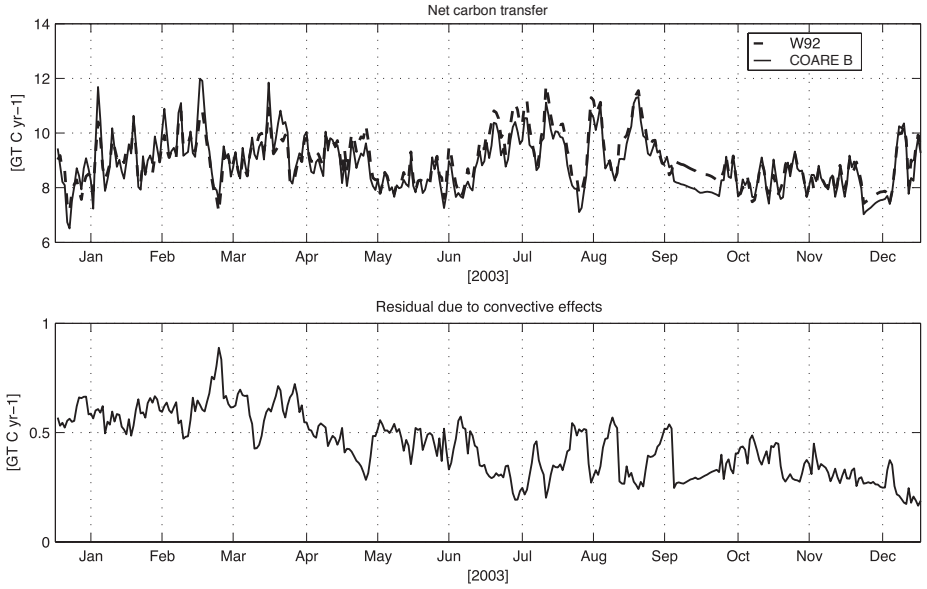

FIGURE 7.11: Upper panel: Net global carbon transfer for 2003 (GT C yr^{-1}). Dashed line: Baseline — Wanninkhof (1992), solid line: COARE B — Modified COARE gas transfer parameterization. Lower panel: Residual due to convective exchange: COARE B−COARE A (GT C yr^{-1}).

panel) is highly dependent on periods of low wind speed. If wind speeds are high, then the convective parameterization will have little effect. Higher values are observed in the first half of the year, with the largest differences occurring in late February, accounting for around 0.8 GT C yr^{-1}.

In addition, table 7.7 contains the yearly net flux, averaged for each of the zonal bands, the convective residual and its associated percentage change. In the north and south equatorial bands the percentage increase resulting from COARE B (as described in chapter 5) is 6.5% and 6.3% respectively. These latitudinal bands also contain the greatest magnitude carbon exchange; around 3 GT C yr^{-1} between 0–30°N and around 4.0 GT C yr^{-1} between 0–30°S. The table also contains the standard deviation and standard error associated with each zonal band. It is important to note that the standard deviation in the zonal net flux is larger than that of the residual difference COARE B−COARE A at the higher latitudes (except for 90°N-60°N). In comparison, the mid and equatorial latitudes have a convective enhancement that is more than twice the standard deviation. The baseline experiment, utilizing the Wanninkhof (1992) parameterization contains the largest standard deviations, with 0.08 GT C yr^{-1} associated with the global carbon transfer for 2003. Generally the standard error is small in comparison to the convective enhancement.

The baseline parameterization produced the largest net transfer in the equatorial zone and the COARE A experiment produces the smallest. At higher latitudes, especially in the northern hemisphere, the net transfer calculated with the COARE B parameterization led to the largest values. The magnitude of the net transfer itself is reduced as

	Carbon transfer (GT C yr^{-1})				
	Baseline	COARE A	COARE B	Residual	Increase (%)
90N - 60N	−0.218	−0.207	−0.219	−0.012	5.400%
-Std. dev.	0.005	0.005	0.005		
-Std. error	0.001	0.001	0.001		
60N - 30N	1.101	1.166	1.179	0.012	1.027%
-Std. dev.	0.030	0.031	0.032		
-Std. error	0.005	0.006	0.006		
30N - 0	2.982	2.703	2.892	0.190	6.552%
-Std. dev.	0.074	0.066	0.074		
-Std. error	0.013	0.012	0.014		
0 - 30S	4.031	3.576	3.814	0.239	6.258%
-Std. dev.	0.111	0.099	0.107		
-Std. error	0.020	0.018	0.020		
30S - 60S	1.405	1.470	1.483	0.013	0.890%
-Std. dev.	0.038	0.040	0.039		
-Std. error	0.007	0.007	0.007		
60S - 90S	−0.299	−0.289	−0.293	−0.003	1.094%
-Std. dev.	0.016	0.016	0.016		
-Std. error	0.003	0.003	0.003		
Global	9.004	8.419	8.875	0.456	5.138%
-Std. dev.	0.080	0.072	0.077		
-Std. error	0.006	0.005	0.006		

TABLE 7.7: Zonally averaged, net carbon transfer for 2003 as calculated by FOAM-HadOCC, using the following gas transfer parameterizaions: Wanninkhof (1992), COARE A (without convective effects) and COARE B (the improved COARE gas transfer parameterization with convective effects). Standard deviation and standard error are calculated for each of the gas transfer parameterizations. Increase (%) is irrespective of outgassing or ingassing.

latitude increases north and south of the equator. In the 60°N–30°N zone net carbon transfer is only 1.2 GT C yr^{-1} (for COARE B) and the convective residual has been reduced to around 1%. Similarly in the southern hemisphere, the transfer between 30°S–60°S is 1.5 GT C yr^{-1} and the residual difference is 0.9%. Only at the highest zonal bands north and south does the modelled ocean release carbon, and whilst the residual in the northern hemisphere is large (5%) the magnitude of the exchange is small; around -0.2 to -0.3 GT C yr^{-1} compared to that which is being transferred to the atmosphere at the mid-latitudes.

Globally, the net carbon transfer for 2003 as calculated by FOAM-HadOCC is positive indicating release from the ocean. The magnitude of the exchange is between 8.4–9 GT C yr^{-1} depending on which FOAM-HadOCC run is considered. The globally integrated difference COARE B−COARE A is 5.2%, with the majority of the residual originating from the mid and equatorial latitudes. When integrated over the world's oceans the difference between the three gas transfer parameterizations is approximately the same order of magnitude as the convective enhancement in the equatorial bands.

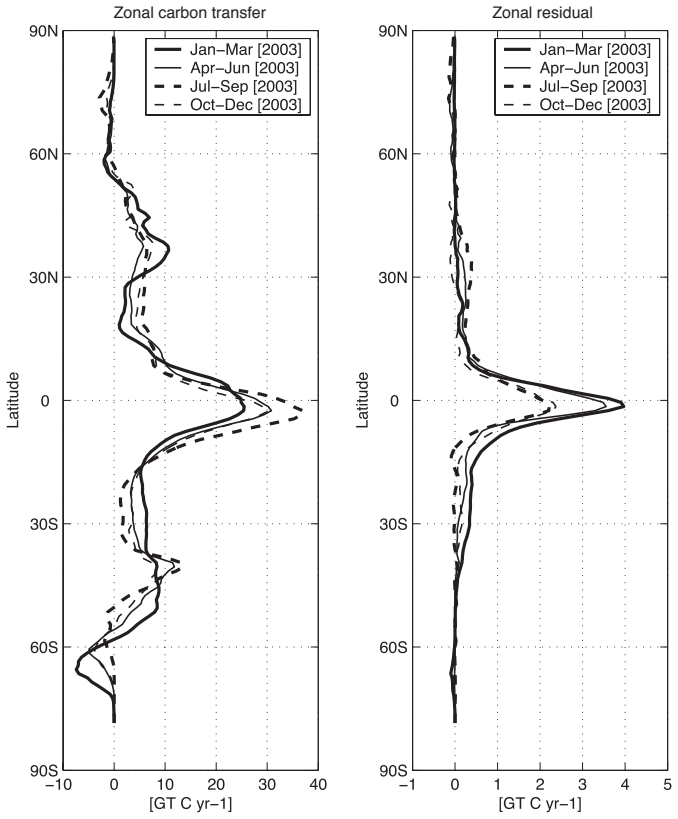

FIGURE 7.12: Left panel: Quarterly zonal carbon uptake (GT C yr^{-1} per degree of latitude). Right panel: Quarterly zonal residual due to convective exchange (GT C yr^{-1} per degree of latitude).

The seasonal changes in the carbon exchange and the convective residual per degree of latitude can be seen in figure 7.12. The zonal average of both the transfer and residual is calculated for 4 three-monthly periods; Jan-Mar; Apr-Jun; Jul-Sep; and Oct-Dec. Seasonal variability in the carbon exchange (uptake and release of CO_2) is apparent at almost all latitudes and the magnitude of the seasonal variation is approximately 3–4 GT C yr^{-1} per degree of latitude. Conversely, the variation in the difference between the COARE A and COARE B model experiments is mainly confined to the mid and equatorial latitudes. The seasonal variation in the residuals is less than the exchange itself, at about 1–2 GT C yr^{-1} per degree of latitude.

Whilst the greatest value for the carbon transfer in figure 7.12 occurs between 15°N–15°S in the period covering July to September (almost 40 GT C yr^{-1} per degree of latitude), this period also contains the smallest residual value (just over 2 GT C yr^{-1} per degree of latitude). It is the period January to March which contains the greatest difference COARE B−COARE A at almost 4 GT C yr^{-1} per degree of latitude. The same three monthly period also has the smallest net transfer (approximately 20 GT C yr^{-1} per degree of latitude) in the equatorial zone. This is probably because the wind speeds in those regions were lower during the first quarter than the third quarter of 2003. The largest negative values, indicating uptake of carbon by the the ocean, are

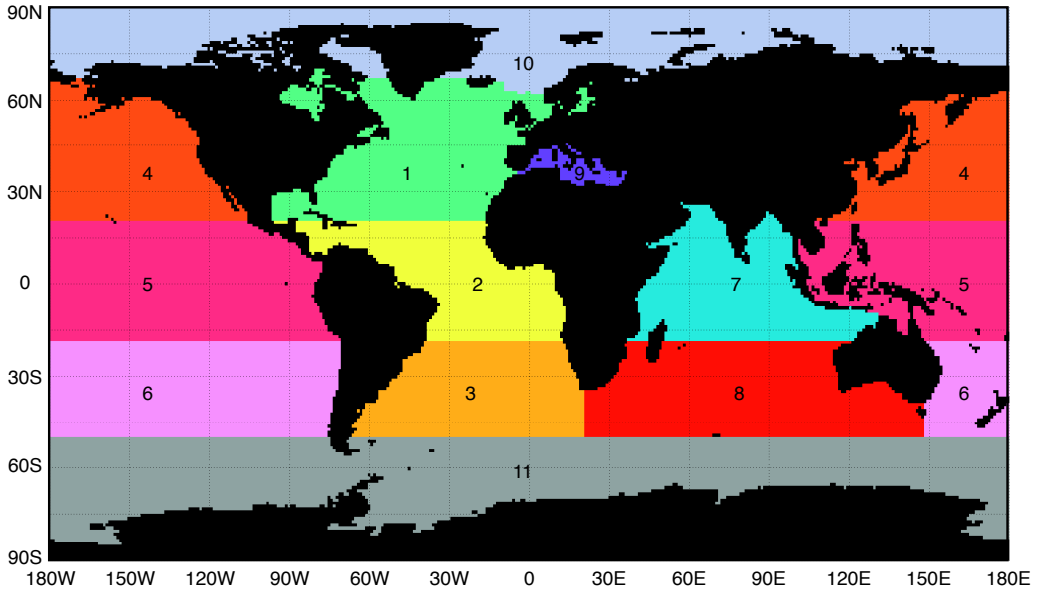

FIGURE 7.13: World map showing 11 colour-coded ocean regions; 1: North Atlantic, 2: Tropical Atlantic, 3: South Atlantic, 4: North Pacific, 5: Tropical Pacific, 6: South Pacific, 7: Tropical Indian, 8: South Indian, 9: Mediterranean, 10: Arctic and 11: Southern. The WOA05 mask was used to determine the ocean basin boundaries (Collier and Durack, 2006).

present around 60°S, and are at their largest, approximately -8 GT C yr^{-1} per degree of latitude, during January to March 2003. In the northern hemisphere slightly negative values also persist above 60°N, but these are much smaller in magnitude.

7.4.4 Regional carbon exchange

The CSIRO netCDF version of the NODC World Ocean Atlas 2005 (WOA05) ocean basin mask (Collier and Durack, 2006) was used to select 11 ocean regions in which to calculate the carbon transfer and assess the significance of the COARE convective parameterization. The chosen colour-coded regions are shown in figure 7.13. Calculating the regional exchange was possible by applying each of the masks, which are of the same resolution, to the global 1°×1° data prior to calculating the carbon uptake.

Since a different land mask has been applied to the data, the total global carbon uptake obtained from summing the ocean regions in figure 7.13 is slightly lower than that obtained from using the unmasked FOAM-HadOCC data. This is because the total ocean area after applying the WOA05 mask is less than that from the FOAM output. This does not however change any of the regional analysis, as we do not directly compare the two totals, we are more interested in the scale of the residual difference between the model simulations.

		Ocean area		Carbon transfer (GT C yr^{-1})			Residual	Area
	Region	(10^8 km^2)	%	W92	COARE A	COARE B	%	%
1.	North Atlantic	0.27	7.8	0.276	0.273	0.279	2.22	3.94
2.	Tropical Atlantic	0.26	7.3	1.267	1.130	1.216	7.06	17.20
3.	South Atlantic	0.22	6.4	0.323	0.322	0.330	2.52	4.67
4.	North Pacific	0.40	11.5	0.504	0.497	0.506	1.64	7.15
5.	Tropical Pacific	0.73	20.9	3.525	3.154	3.382	6.75	47.84
6.	South Pacific	0.42	12.1	0.870	0.890	0.905	1.58	12.80
7.	Tropical Indian	0.28	7.9	0.456	0.420	0.453	7.35	6.41
8.	South Indian	0.31	8.9	0.062	0.058	0.061	3.96	0.86
9.	Mediterranean	0.02	0.6	0.061	0.061	0.062	2.08	0.88
10.	Arctic	0.12	3.5	−0.322	−0.031	−0.031	1.29	0.44
11.	Southern	0.46	13.1	−0.091	−0.088	−0.093	5.15	1.32

TABLE 7.8: Table showing: Ocean regions defined in figure 7.13; The area for each region ($\times 10^8$ km^2); Net carbon transfer (GT C yr^{-1}) during 2003 calculated using three gas transfer parameterizations. W92: Wanninkhof (1992); COARE A: Without convective effects; COARE B: including convective effects; the residual difference (%) due to convective effects; and the proportion of the total transfer for each of the regions.

Table 7.8 shows the net carbon transfer for each of the colour-coded regions in figure 7.13 as calculated in each of the 3 experimental FOAM-HadOCC model simulations for 2003. The ocean area (km^2), convective residual (%) and carbon transfer as a fraction of the global ocean area (%) are also shown. The largest region in figure 7.13 is that of the tropical Pacific. It accounts for 20.9% of the world's ocean area, and has the largest carbon exchange out of the eleven regions selected, approximately 3.4 GT C yr^{-1}. The difference between the COARE model-runs amounts to a 6.75% enhancement. The tropical Pacific is by far the most significant region for carbon exchange in the FOAM-HadOCC experiments, accounting for almost 48% of the global carbon transfer.

In comparison, the next most significant region is that of the tropical Atlantic, which accounts for around 17% of the global carbon exchange. The tropical Atlantic region selected covers 7.3% of the ocean area, and has a magnitude of approximately 1.2 GT C yr^{-1}. The convective residual for this region is slightly larger at 7%. The tropical Indian Ocean has the largest residual difference between the COARE experiments 7.35%, however the carbon export is only about 0.4 GT C yr^{-1}, and the region accounts for only 6.4% of the global carbon exchange, whilst its ocean area is 7.9%.

In the northern hemisphere, the north Atlantic and Pacific account for 7.8% and 11.5% of the global ocean surface area. The carbon exchange is small compared to the tropics at 0.3 and 0.5 GT C yr^{-1} respectively and the convective residual is only around 2%. These regions also only account for 3.9% and 7.2% of the total carbon exchange across the global ocean. The Mediterranean region is relatively insignificant, covering only 0.6% of the global ocean surface area, and accounting for less than 1% of the total carbon exchange.

The South Atlantic, Pacific and Indian Oceans have larger surface areas than the corresponding northern regions; 6.4%, 12.1% and 8.9% respectively. The carbon exchange in the Atlantic and Pacific regions are around 0.3 and 0.9 GT C yr^{-1} and they account for 4.7% and 12.8% of the global carbon exchange. The residual difference between the COARE A and B model runs is low, as in the northern hemisphere, at only 2.5% and 1.6% respectively. The Southern Indian exchange is similar in magnitude to that of the Mediterranean region, with a value of approximately 0.06 GT C yr^{-1}. Even though the surface area is far greater, the exchange as a percentage of the oceans globally is less than 1%.

The Arctic and Southern Ocean regions both contain negative values as the ocean acts as a sink for carbon in these regions. The Southern Ocean has the second largest global ocean area (13.1%), and whilst the convective residual is large (5%), the absolute change is small compared to tropical regions. In the Arctic the residual is approximately 1.3%. The magnitude of the carbon uptake is small at only -0.1 GT C yr^{-1} for the Southern Ocean and -0.03 GT C yr^{-1} for the Arctic Ocean. Even though the percentage surface area for the Southern Ocean is large, the carbon exchange is only 1.3% of that which occurs globally. Comparatively, the Arctic accounts for even less; only 0.4% of the global exchange.

In summary, convective exchange results in approximately 7% enhancement to the CO_2 flux. This occurs over 36.1% of the oceans (the tropics), which in truth are the main source regions for CO_2. We assume that the change in transfer velocities will be similar. The other regions show around a 2% enhancement, which in truth correspond to mostly sink regions.

7.5 Discussion

The results presented in this chapter aim to assess the significance of convective CO_2 transfer both on regional and global scales. We have previously shown the importance of gas transfer under such conditions (chapter 5), and have highlighted the variability introduced by the diurnal cycle of SST (chapter 6), however those results were based on 1-d model experiments using GOTM, and were confined to 10°S10°W in the tropical Atlantic. To answer the question posed at the beginning of this chapter, a new global modelling approach was necessary. Thus we use a modified, development version of the U.K. Met Office FOAM-HadOCC model; a coupled physical ocean model and simple ocean carbon cycle model. This setup was used to estimate the air-sea CO_2 flux using the improved COARE gas transfer parameterization developed in the earlier chapters.

The yearly integration results from GOTM using coarse resolution, sub-sampled input data showed that over 2002 the 1-d turbulence closure model produced results of acceptable accuracy, when compared to the hourly resolution experiments conducted

previously. Coarser resolution input data led to an increase in the uncertainty, and a small increase in the convective enhancement. The magnitude of the CO_2 flux was also marginally overestimated. With this in mind, it was assumed that the results from the global FOAM-HadOCC experiments would be similarly affected, given that the input forcing for the global model is of 6 hourly resolution, and the model time-step is 1 hour.

Restricted computational resources make it difficult to refine the temporal and vertical resolution of an Ocean General Circulation Model (OGCM) such as FOAM, to accurately reproduce the diurnal thermocline. Existing models with coarse vertical resolutions of 10–15 m in the upper ocean have been shown to recreate diurnal variability to a certain extent (Schiller and Godfrey, 2003; Danabasoglu et al., 2006). However more realistic simulations require much finer vertical resolution, such as that employed during the 1-d experiments with GOTM. The temporal resolution of the forcing fluxes and vertical resolution required to accurately reproduce the diurnal temperature cycle by a numerical model was discussed by Bernie et al. (2005). The authors indicate that a temporal resolution of less than 3 h and a vertical resolution of less than 1 m is required to reproduce more than 90% of the amplitude of the diurnal SST variation.

The limitations, described in section 7.3.2 were significant, but were necessary in order to produce useable output. Thus, the fluxes calculated by the FOAM-HadOCC model for 2003 are unlikely to represent their real world equivalents. Instead we choose to focus on the difference between the model runs themselves, which still contain important information. These residual differences highlight the spatial and temporal discrepancy between the original and improved COARE parameterizations and a simple wind-speed dependent model (Wanninkhof, 1992) currently in use at the U.K. Met Office.

For the global calculations, an ocean carbon cycle model was used in order to incorporate the variability in the ocean pCO_2 as a result of biological processes, as well as temperature changes. In comparison, the 1-d experiments used monthly climatological pCO_2, which varied only according to temperature. However, the NPZD model incorporated within the HadOCC model is a very simple representation of the ocean ecosystem. This simplicity is due to computer memory storage and run-time constraints, but is consistent with the desire to develop a model of the marine carbon cycle which is capable of being understood in detail (Palmer and Totterdell, 2001). Thus it is important to consider whether the model's ability to represent the marine carbon cycle has been significantly compromised by its simplicity.

The comparisons to existing climatologies, highlighted that global air-sea CO_2 fluxes from FOAM-HadOCC are substantially biased toward outgassing. Fangohr et al. (2008) give an estimate of 1.6 GT C yr^{-1} for the global uptake flux obtained using the Wanninkhof (1992) (wind speed)^2 dependence. In contrast, the results from FOAM-HadOCC indicate that the ocean is, on average, a source for CO_2 with an annual flux of 9 GT C yr^{-1}, which was obtained using the same parameterization. Thus the default setup

of FOAM-HadOCC does not agree with other estimates of the mean global uptake of about 2 GT C yr^{-1} (e.g. Sarmiento et al. (1992); Siegenthaler and Sarmiento (1993); Joos and Bruno (1998); Takahashi et al. (2002); Sweeney et al. (2007)).

Whilst there are strong similarities to the spatial distribution of the sources and sinks in the Takahashi et al. (2002) climatology, there a number of differences in the FOAM-HadOCC 2003 fluxes. Anomalous outgassing regions are present in the southern hemisphere, between south Africa and Australia at 50°–60°S. In addition, there is a lack of strong sink regions in the transition zone between the subtropical gyres and the sub-polar waters i.e. 40°–60°. The sink regions that are present, are much smaller in magnitude compared to those of the climatology.

The increased outgassing is most likely caused by the air-sea pCO_2 difference being overestimated at mid and equatorial latitudes and underestimated at high-latitudes. Given that the gas transfer velocity k is always positive and the atmospheric pCO_2 concentration does not vary significantly, the lack of sink regions in the model must be a result of inaccurate oceanic pCO_2 calculated by FOAM-HadOCC. Unfortunately this cannot be confirmed as the gas transfer velocity and pCO_2 fields were not output by the model. Subsequent investigations should aim to rectify this important omission.

One possible reason for this is that the physical model brings too much deep carbon-rich water to the surface in the equatorial Pacific. This widespread issue of deep DIC surfacing leads to the observed bias in the flux. Palmer and Totterdell (2001) show that global export by the HadOCC model is within the range of observations from sediment traps, however the geographical distribution is incorrect, with the model incorrectly predicting some export fluxes. In addition they observe that the amount of CO_2 returned to solution in the surface waters is also in error, as there are additional processes that affect surface DIC that are not easy to predict.

In theory the FOAM-HadOCC model incorporates many of the important physical and biological processes that determine the air-sea flux of carbon dioxide. In practice the model does not fully represent the amount of carbon taken up during phytoplankton growth. Palmer and Totterdell (2001) compared global fields of primary production estimated from satellite ocean colour data. The main differences occurred in the sub-tropics (20°–40° north and south) in the Pacific and from 0°–30°N in the Atlantic. The present ecosystem model is unable to capture all of the variability in the sub-tropics. Additionally, the feature in the Atlantic at 0°-30°N is a result of a coastal region of high primary production. As the model physics operates at a coarse resolution, it is unable to represent these coastal features well.

Another important caveat is that the global experiment does not fully address the implications of the diurnal temperature variation. This is because the top most level in FOAM is at 10 m depth, as such the magnitude of ΔT, the average warming experienced during the course of the day, would be considerably smaller than that witnessed

during the 1-d experiments in chapters 5 and 6. As we know from our previous chapters, utilizing the correct near surface temperatures and accounting for diurnal warming has a large effect on the net CO_2 flux, through changes in solubility and pCO_2.

A benefit of using the NOAA COARE v3.0 heat flux model is that it contains optional warm-layer and cool-skin models (Fairall et al., 2003). In the previous 1-d experiments only the cool-skin model was active since GOTM was already modelling the near surface ocean, and the diurnal temperature structure. However, it was not possible to utilize the optional warm-layer code in FOAM-HadOCC, because it requires at least 12 hours of input data for the iteration loop to calculate the necessary heat and momentum integrals. As the COARE model is called at every time-step in the 'Tracer' subroutine this was not possible, without significant code changes. In this study the warm layer model remains deactivated, and as such our results reflect only the convective effects parameterized within the transfer velocity expression.

Future studies could store the required input variables in an auxiliary file during the model spin-up period, and update the file at every time-step. Since the 'Tracer' subroutine loops over each $1^\circ \times 1^\circ$ grid box, the entire global dataset, for each variable, would have to be stored in the auxiliary file for at least 12 hours. This file could then be used to force the warm layer model within the tracer array. Thus, a new pseudo-surface temperature variable could be created and used in the calculation of the gas transfer. It should also be noted that whilst many studies focus on the tropics and subtropics, Kawai and Wada (2007) note that diurnal warming exists even at higher latitudes. As such, in situ observations that can resolve the diurnal SST cycle sufficiently close to polar regions and modelling studies focused on higher latitudes should be considered. The lack of strong diurnal warming in FOAM-HadOCC means that the solubility changes discussed in chapter 6 are almost certainly underestimated.

The relative CO_2 flux increase resulting from the warm layer effect can correspond to a large absolute increase in outgassing. Ward et al. (2004) described the warm layer deviation in the eastern tropical Pacific where the absolute value of the CO_2 flux is large. They also indicated that the estimated difference of fCO_2 across the warm layer of a few meters thickness can reach 20 μatm or more. On longer timescales, in the eastern equatorial Pacific, the diurnal SST amplitude becomes larger during La Niñas and lower during El Niños. Thus, the impact of the warm layer on the surface CO_2 flux will vary with the ENSO cycle (Cronin and Kessler, 2002).

Even though the net air-sea CO_2 flux predicted by FOAM-HadOCC is flawed, intercomparisons of the gas transfer velocity models are still useful. The difference between the Wanninkhof (1992) and Fairall et al. (2000) models does not account for the outgassing bias. The modified COARE model produces stronger fluxes in the equatorial and tropical oceans as a result of increased transfer velocities. Low wind speeds and high solar insolation, which occur more frequently in the equatorial and tropical oceans, result

in increased amounts of exchange via convective processes. Use of the improved COARE parameterization to calculate the gas transfer velocity in FOAM-HadOCC results in a large residual, around 7% in the tropical oceans, and around 5% globally.

The FOAM-HadOCC results show that convective enhancement is primarily occurring in regions that are typically sources for CO_2, thus the increased fluxes all act in the same direction. It is important to remember that should some of those areas become sinks for CO_2, whilst the transfer velocities would still be enhanced, the flux in those regions would be in the opposite direction. Finally, given the results presented in chapter 6 based on the idealized diurnal wind speed profiles, we can speculate that including the full range of diurnal temperature variability near the surface would lead to further enhancement. Thus a proper treatment of the air-sea gas transfer should aim to include these important effects, both at a regional and global scales.

7.6 Conclusions

The global and regional significance of convective CO_2 transfer is assessed by analyzing output from the U.K. Met Office's FOAM-HadOCC model. The NOAA-COARE v3.0 air-sea flux parameterization was implemented within the FOAM system, along with a modified version of the COARE gas transfer parameterization, including additional upper-ocean convective terms.

The use of a physical ocean model, combined with an ecosystem model allows the marine carbon cycle to vary in response to carbonate chemistry, biological production and export as well as the physical mechanisms. Calculation of the fugacity of CO_2 in the surface waters by HadOCC allows the air-sea flux of CO_2 to be estimated. In addition, the original configuration of the model, incorporating the Wanninkhof (1992) relationship for gas transfer velocity, was compared with the version incorporating the COARE parameterization. The model was run for the period 1^{st} of January 2003 to 31^{st} December 2003.

Global model results using the original configuration showed that the calculated air-sea CO_2 fluxes were not in agreement with existing climatologies based on observations e.g. Takahashi et al. (2002); Fangohr et al. (2008). This disagreement was found to be a result of the coupled model, which fails to adequately reproduce the surface distribution of fCO_2. Results show a consistent bias toward outgassing fluxes due to high concentrations of CO_2 in the surface waters, possibly as a result of deep DIC surfacing. Ultimately, further work is needed to improve the model performance, so that the carbon cycle can be better resolved.

Whilst the absolute net CO_2 flux estimated by FOAM-HadOCC is not representative, useful information was still obtained from the inter-comparison of model runs. The

residual difference between the improved COARE parameterization (chapter 5; Jeffery et al. (2007)) and the original Fairall et al. (2000) model with minimal convective effects, showed that convective CO_2 transfer was largely confined to the tropics and sub-tropics. These are typically regions where the oceanic CO_2 concentration is greater than the atmospheric CO_2 concentration.

Integrating the results over the year, and over different ocean basins showed that both the regional and global carbon transfer would be affected by the introduction of the new parameterization. The primary areas affected were the tropical oceans, which were enhanced by approximately 7%. It is important to be cautious about such results given the flaws in FOAM-HadOCC. Whilst the proportion of the global carbon exchange of those regions (around 65%) is highly model dependent, the enhancement over the tropics is more robust, as those areas are in truth source regions for CO_2. Even a small increase to the transfer velocity over these areas can result in a change that is significant worldwide.

This modelling study was a new type of experiment, it unfortunately uncovered some significant faults in the FOAM-HadOCC model that limited the success; but it was an important learning experience. This study is a first step toward highlighting the regional and global significance of gas transfer that occurs at low wind speeds. The limitations of the global model and of the implementation itself meant that only the additional convective terms in the transfer velocity were properly accounted for. Further studies are ultimately required to fully characterize the combined effect of diurnal temperature variability and the convective enhancement.

Future work should aim to identify the effect and extent of diurnal temperature variability at higher latitudes. In situ studies are necessary for tuning and validation of the gas transfer parameterization. In addition, improvements to the ecosystem and ocean models are necessary to refine the absolute CO_2 flux estimates. Ultimately, finer vertical resolutions, shorter time-steps and model forcing on the same scale as the ocean mixing are required to adequately resolve the near surface ocean and air-sea CO_2 exchange which are important for accurately estimating the marine carbon cycle and the potential anthropogenic impact upon it.

Whilst limited, this study gives perspective to the earlier 1-d experiments. The results reveal that convective CO_2 exchange is important globally, and corresponds to approximately a 5% increasing in outgassing regions. Given that this does not fully include effects of diurnal temperature variability, we suggest that our estimate presented here is conservative.

Chapter 8

Conclusions

The final chapter of this thesis synthesizes the main findings from the previous experimental chapters. A research summary is presented, along with general conclusions and suggestions for future work.

8.1 Summary of research

8.1.1 1-d model development

In order to investigate the heat and gas transfer relevant to the study of convective CO_2 exchange it was decided to develop a one-dimesional model framework. In this way the fine details of the important surface process could be incorporated into the calculations. The General Ocean Turbulence Model (GOTM) was evaluated for use in the tropical Atlantic. The model was set up with the aim of accurately representing near surface temperature so that this variability could be properly included in the calculation of air-sea gas transfer. The 1-dimensional k_e-ϵ turbulence closure model was forced with surface meteorological data from a PIRATA mooring located at 10°S10°W during 2002. When combined with satellite cloud data from Meteosat-7 and climatological pressures from NCEP reanalysis, the required model forcing was available to initialize and run the model. Evaluating the data available in the tropical Atlantic, it was found that the in situ PIRATA data is highly variable in terms of its availability and consistency.

The air-sea interaction routines within the 1-d model were modified to output individual latent, sensible, longwave and shortwave heat fluxes. The surface fluxes estimated by the model were similar to those found in the literature and surface ocean temperatures agreed well with the in situ mooring data for the same period. These results illustrate

that GOTM is an appropriate framework for modelling near surface temperature over the diurnal cycle under both convective and non-convective conditions.

This GOTM configuration was used to produce estimates of skin and bulk temperature over the course of a day, with the aim of modelling the diurnal warming (ΔT). Accounting for the temperature variability is important for gas exchange due to its effect on solubility. Accurately recreating the diurnal cycle in the model was the foundation for the rest of this research. A simple calculation using the Wanninkhof (1992) (wind speed)^2 dependence of the gas transfer velocity, and a flux equation that accounted for skin and bulk temperatures was compared with a traditional approach which did not take into account ΔT. This revealed a difference of 2.5% in CO_2 flux integrated over a day during convective conditions. Subsequent refinement to GOTM enabled the surface fluxes to be calculated using the NOAA-COARE v3.0 bulk flux parameterization, and input solar radiation to be used as model forcing.

In addition, GOTM was also compared to the Kraus-Turner bulk model, the KPP scheme of Large et al. (1994) at OWS Papa, and against data from an Argo float (see appendix A; Acreman and Jeffery (2007)). The bulk model and GOTM were found to mix too deeply at OWS Papa but to give a good representation of mixed layer depth in the Argo float case study. The mixed layer depth was defined according to the density criteria of Kara et al. (2000). Conversely the KPP model of Large et al. (1994) was found to give a good representation of the mixed layer depth at OWS Papa, provided the vertical resolution was sufficiently high, although when the KPP model was validated using the Argo float the mixed layer depth was found to be too shallow. This comparison experiment further validated the model setup with regards to describing the important upper ocean processes.

8.1.2 1-d modelling in the tropical Atlantic

Refining the earlier model setup, a combination of in situ and satellite derived radiometric measurements and a modified version of GOTM, which included the COARE air-sea gas transfer parameterization, was used to investigate heat and carbon dioxide exchange over the diurnal cycle in the Tropical Atlantic. A new term was developed to better represent the transfer taking place during upper ocean convective conditions. This was based on a water-side convective velocity scale (w_{*w}) analogous to the 'gustiness' parameter implemented on the atmospheric side. Since the greatest enhancement from w_{*w} to the CO_2 flux occurs when diurnal warming is large, air-sea fluxes of CO_2 calculated using traditional parameterizations underestimate the contribution from convective processes. Results showed that diurnal changes in seawater temperature affect the amount of air-sea gas exchange taking place through changes in solubility and buoyancy-driven nocturnal convection, which enhances the gas transfer velocity.

Meteorological data from the PIRATA mooring located at 10°S10°W in the Tropical Atlantic were again used, in conjunction with cloud cover estimates from Meteosat-7, to calculate fluxes of longwave, latent and sensible heat along with a heat budget and temperature profiles during February 2002. Twin model experiments, representing idealistic and realistic conditions, revealed that over daily time scales the additional contribution to gas exchange from convective overturning was important. Increases in transfer velocity of up to 20% were observed during times of strong insolation and low wind speeds (< 6 ms^{-1}).

This study serves to highlight the importance of convective processes for estimates of gas transfer, in particular air-sea CO_2 fluxes. Tropical regions, susceptible to the greatest effect, tend to have a net sea to air flux of CO_2, thus failing to consider convective processes may underestimate the globally integrated air to sea flux. Neglecting this additional low wind speed contribution will cause errors that are significant when evaluating local/regional space-time variability of CO_2 fluxes. These results support the need for parameterizations of gas transfer that are based on more than wind speed alone and include information about the heat budget.

8.1.3 Phase dependent forcing and diurnal warming

With the model adequately configured from the previous experiments, it was forced hourly with a variety of idealized diurnal wind and cloud profiles to investigate the sensitivity of the diurnal response and its effect on air-sea CO_2 transfer, at low to moderate wind speeds. In many cases a diurnal warm layer is formed and this affects gas fluxes. Our 1-d model results address similar cases to the observations analyzed by Stuart-Menteth et al. (2005b); those diurnal shapes classified by Stuart-Menteth et al. (2005b) were reproducible by the idealized simulations given the appropriate meteorological forcing. The good agreement between the model and the in situ buoy measurements highlighted the effectiveness of the model for representing diurnally varying processes.

The results showed that phase-dependent wind speed and cloud fraction with respect to solar insolation are important for determining the magnitude and shape of the diurnal variability and the depth of the diurnal mixed layer. These results concur with those of the simple model experiments conducted by Dickey and Simpson (1983). Phasing the wind forcing could double the diurnal temperature difference (e.g. for solar insolation 12 hours out of phase with maximum wind stress), and in the same case the net CO_2 flux was increased by approximately 30%.

Low wind speed conditions coupled with strong solar insolation can result in significant ocean degassing. Calculated air-sea fluxes of CO_2 must account for low wind speed processes if the integrated fluxes over a diurnal cycle are to be accurate. The shape of the diurnal signal and magnitude of ΔT ultimately depend on the wind, which provides

mechanical turbulence to mix heat down, and cloud cover which can affect the amount of heat available to warm the mixed layer. Idealized experiments showed these factors to be important up to ± 5 hours before local solar noon. The air-sea gas transfer at low wind speeds, in the presence of a strong diurnal signal, is determined by the magnitude, timing and duration of specific wind and cloud 'events'.

Exact calculations of air-sea CO_2 flux were compared to simplified calculations based on night-time temperatures, with or without a 'cool-skin' correction and average wind speed. These simplified calculations underestimated the net CO_2 flux in a weak source region. When ΔT was at it largest the net daily air-sea CO_2 flux was reduced by up to 61.7% if daily average values for wind speed and SST were used, compared to the flux obtained from the 1-d model.

It is important to note that short-term wind speed variability leads to large discrepancies as a result of the non-linear relationship between wind speed and CO_2 transfer (Bates and Merlivat, 2001), which is even further enhanced by diurnal processes and subsequent convective enhancement. Irrespective of varying winds or clouds, the formation of a diurnal warm layer has a significant effect on air-sea CO_2 transfer resulting in increased ocean degassing.

8.1.4 A global modelling perspective

The previous 1-d experiments highlighted the importance of correctly accounting for both diurnal temperature variation and the subsequent nocturnal convective effects. However, limited insight about the regional and global significance was gained from those studies. A global modelling study was deemed necessary. With this in mind, the NOAA-COARE v3.0 air-sea flux parameterization was implemented within the U.K. Met Office FOAM-HadOCC system, along with the improved COARE gas transfer parameterization. The use of a model of ocean physics, combined with an ecosystem model allowed the marine carbon cycle to vary in response to carbonate chemistry, biological production and export as well as the physical mechanisms. This is different to the previous 1-d experiments where climatological data had been used for ΔfCO_2. Calculation of the fugacity of CO_2 in the surface waters by HadOCC allows the air-sea flux of CO_2 to be estimated.

The model was run for the period 1^{st} of January 2003 to 31^{st} December 2003 using the original configuration in use at the U.K. Met Office, which incorporates the Wanninkhof (1992) relationship for the gas transfer velocity. These results showed that the calculated fluxes did not agree with existing climatologies based on observations e.g. Takahashi et al. (2002); Fangohr et al. (2008). This disagreement was found to be a result of the coupled ecosystem model (FOAM-HadOCC). The model does not adequately reproduce the surface distribution of fCO_2, possibly as a result of too much deep DIC surfacing.

The experiment was further limited by the fact that the near surface temperatures in the model are not well represented. The top level of FOAM is at 10 m and, while the model resolution is 1 hour, the surface forcing data are interpolated from 6-hourly data. Thus the effect of diurnal warming is not fully considered in this global experiment.

Useful results however were still obtained from the inter-comparison of model runs using different gas transfer parameterizations. The residual difference between the improved COARE parameterization (chapter 5; Jeffery et al. (2007)) and the original Fairall et al. (2000) model with minimal convective effects, showed that convective CO_2 transfer was mainly confined to the tropics and sub-tropics. The equatorial and sub-tropical latitudes are typically source regions for CO_2. Regional integrations over various ocean basins showed that global carbon uptake would be significantly affected by convective CO_2 transfer. The primary areas affected were the tropical Pacific and tropical Atlantic Oceans, which were enhanced by approximately 7%. This is important as these regions cover a large proportion of the world's ocean, more than 30% and are typically sources for CO_2. Convective enhancement of the transfer velocity in these areas can result in a significant change in net global flux.

Whilst the original aim of quantifying the contribution to gas transfer from low wind speed processes was not fully achieved, the global modelling study is a key first step toward highlighting the importance of gas transfer under low wind speeds. Such an experiment has not previously been attempted, and revealed significant faults in the FOAM-HadOCC model that limited its success. Regardless, this study provides a global perspective to the earlier 1-d experiments. The results reveal that convective CO_2 exchange appears to be significant globally. We tentatively estimate a 5% increase to the global sea to air flux of CO_2 based on the model results.

8.2 Main findings

The primary development of this thesis has been an improved gas transfer velocity parameterization based on the NOAA-COARE gas transfer model originally proposed by Fairall et al. (2000). A modified model incorporates new terms based on a water-side convective velocity scale for better describing the air-sea transfer of gas under upper ocean convective conditions.

Model based experiments, incorporating the new parameterization, in the tropical Atlantic were carried out using a 1-d turbulence closure model (GOTM) to accurately describe the physical, temperature related processes affecting gas transfer at low wind speeds. In order to estimate the regional and global significance of convective air-sea CO_2 transfer the U.K. Met Office FOAM-HadOCC model was used.

The main findings of this thesis are listed below;

1. Convective gas transfer was found to enhance the gas transfer velocity by up to 20%, and increase the magnitude of the daily net CO_2 flux by up to 3% at a typical site in the tropical Atlantic.

    - The water-side convective velocity scale leads to increased transfer velocities, this has the effect of increasing the flux regardless of whether the region is a source or sink for CO_2.

2. Failure to account for the near surface temperature structure and diurnal variability when estimating air-sea CO_2 exchange can lead to large discrepancies in the integrated flux over longer timescales, almost 60% in certain cases e.g. a decrease from 34.05 to 13.04 mol m^{-2} yr^{-1} if average nighttime temperatures are used (for $\Delta T_{1m} = 2.4$ °C).

    - The effect of increasing SST is to decrease the $[CO_{2aq0}]$, this results either in an increase in source or to a decrease in sink for CO_2.

3. The most important regions for convective CO_2 transfer are the tropical Atlantic and Pacific, based on the results from FOAM-HadOCC.

    - These regions are typically sources of CO_2, thus convective transfer increases outgassing.

4. The global impact of using the improved COARE gas transfer model as calculated with the FOAM-HadOCC system is estimated at around a 5% increase in outgassing of source regions.

    - The HadOCC ecosystem model does not produce realistic surface fCO_2, with global air-sea CO_2 significantly biased toward outgassing. Future versions should aim to resolve these issues.

The objectives, presented in section 1.4, were generally met. The 1-d model provided an ideal framework for developing the improved transfer velocity model, which was key to accurately estimating CO_2 fluxes in the tropical Atlantic. However, limitations of the physical-biogeochemical model meant that the estimates of global carbon uptake were not particularly representative. Instead, the global model was used to compare parameterizations of the gas transfer velocity with and without the convective terms present.

Inclusion of the processes investigated during the course of this thesis in future studies of net air-sea gas exchange are likely to result in a decrease of the global ocean uptake for CO_2. This has important implications for both the marine carbon cycle and climate change studies, such as those highlighted in chapter 1, section 1.3.

8.3 Future work

While this work has attempted to fulfill the aims as laid out in chapter 1, a number of questions have been left unanswered. The following section outlines possible future work that could be developed from the findings made during the completion of this research.

8.3.1 In situ observations

Because of the combination of small concentrations and/or small fluxes, the determination of air-sea gas fluxes presents difficulties. Direct measurements (i.e., eddy correlation) of the fluxes are rarely attempted. An important step in future improvements to gas transfer parameterizations will be to increase the number of in situ observations, not only for moderate to high winds, but also for low wind conditions. Previous air-sea gas exchange cruises such as GasEx-98 and GasEx-2001 enabled significant progress toward understanding air-sea gas transfer and toward the development of realistic parameterizations, such as the COARE gas transfer parameterization (Fairall et al., 2000).

The study presented in this thesis has highlighted the importance of low wind speed exchange, which is influenced by diurnal temperature variability and subsequent processes. Measurements from in situ radiometers and profiling floats have been shown to resolve the diurnal warm layer and cool skin. Coincident measurements of air-sea gas transfer would go a long way to expand on the current data available. These measurements could then be used to validate and tune the gas transfer models. The gas transfer velocities can be validated by dividing measured fluxes by the interfacial concentration difference.

The conditions which can lead to noticeably significant modifications to the gas transfer velocity and air-sea flux of CO_2 are quite diverse, both spatially and temporally. Kawai and Wada (2007) point out that whilst most research on diurnal warming has focused on the tropics and sub-tropics, diurnal warming is still observed at higher latitudes. Further studies incorporating in situ observations that can resolve the diurnal cycle of SST sufficiently close to the polar regions are required.

8.3.2 Improvements to global modelling

Air-sea flux estimates from FOAM-HadOCC revealed that the oceanic surface concentration of CO_2 appears to be overestimated, either as a result of the physical upwelling of carbon rich water, or due to the simplicity of the ecosystem model not fully representing changes in the marine carbon cycle. Improvements to the coupled FOAM-HadOCC ecosystem model are necessary to refine estimates of fCO_2 and hence the air-sea CO_2 flux. The use of satellite ocean colour data assimilation may help to improve the model fit to observations.

To properly characterize the gas flux in the model, the near surface ocean must also be well represented. The FOAM model's current uppermost vertical level is at 10 m, which results in a reduced thermal variability over the diurnal cycle. The results presented in this thesis have highlighted the need for finer vertical resolutions, shorter time-steps and model forcing on the same scale as the ocean mixing, which are required to adequately resolve the near surface structure. Additional datasets or forcing parameters such as rain may play an important role. Furthermore future experiments should have access to model output of both the transfer velocity, k and the air and ocean CO_2 fugacities.

Given that this research only presents a global estimate of the convective enhancement to the gas transfer, further studies are required to fully characterize the combined effect of diurnal temperature variability and the buoyancy-driven enhancement. Future work should also consider the non-linearity of wind speed relationship to the gas transfer velocity, as the numerical artifact of averaging always reduces the gas transfer velocity. Improved global model estimates of the air-sea CO_2 fluxes are important for accurately estimating the global carbon uptake and the potential anthropogenic impact upon it.

8.3.3 Remote sensing of CO_2 fluxes

In regions such as the tropics, where diurnal variability is prevalent, the use of high sampling frequency wind and skin temperature data is necessary not only to reduce the smoothing-out of extreme values, but to account for the temperature-related and subsequent convective effects on air-sea CO_2 exchange.

A combination of microwave and infra-red satellite based radiometers could provide sufficient information about the near surface ocean temperature to improve calculation of gas fluxes. These instruments measure the sea surface temperature at different depth, IR corresponds to SST_{skin} and MW to $\mathrm{SST}_{subskin}$. Furthermore sensors on geostationary satellites over the equatorial regions such as SEVIRI can provide observations up to every 15 minutes, enough to resolve the diurnal cycle.

Ultimately global measurements of ocean-atmosphere CO_2 flux and oceanic CO_2 uptake will require remote sensing techniques, as only these can provide a synoptic view of the world's oceans. The problem of computing the flux can be broken down into determining the gas transfer velocity and the air-sea concentration difference. The required parameters for both components all need to be derived from remote sensing observations.

A satellite-based version of the COARE 3.0 model for air-sea heat flux estimates has been implemented at NOAA ESRL as part of work funded by NASA and the methods could be extended to the gas transfer parameterization. In addition, efforts to remotely obtain the oceanic CO_2 concentration have been based primarily on observed correlations to the sea surface temperature and related quantities. Relationships between SST and seawater fCO_2 have been found to exist in the subtropical and equatorial Pacific and

Caribbean Sea. Additional relationships between the oceanic fCO_2, SST and chlorophyll content have been observed in the Southern Ocean. These expressions however exhibit significant variations between regions and seasons. So far, no such algorithm is robust on a global scale.

Atmospheric CO_2 concentrations have been obtained solely from direct measurements but the variability of the atmospheric concentration is much smaller both spatially and temporally and this has not been a major factor limiting the accuracy of the flux estimates. To advance global estimates of gas transfer, improved satellite based estimates of the gas transfer velocity, the corresponding input parameters, such as wind speed, temperature, air temperature and specific humidity, as well as the oceanic concentrations are necessary.

8.3.4 Other gases

Since the COARE gas transfer parameterization is a physically-based model, derived from surface renewal and turbulent molecular diffusion theory near the air sea interface, it can be applied to any trace gas provided the solubility and the Schmidt number (S_c) for the gas are known.

In addition to the flux of CO_2, Dimethylsulphide (DMS) is another important trace gas that is the continuing subject of interest due to its link with global climate. DMS is the principal precursor for atmospheric sulphate aerosol and cloud condensation nuclei in remote marine regions covering large areas of the globe.

Direct flux measurements have shown that simple exchange velocity formulations are not flexible enough to describe the behavior of both DMS and CO_2. Models based on a quadratic fit to tracer or radiocarbon data overestimate the DMS flux at higher wind speeds and underestimate the flux as wind speed approaches zero (Blomquist et al., 2006). Parameterizations such as Wanninkhof (1992) which have a quadratic dependence on wind speed, with adjustment to the Sc to account for the molecular diffusivity of the trace gas, are unable to explain the observed wind speed dependence of k_{DMS}. The adjustments to the Sc tend to move the k vs. u curve up or down.

The best power-law fit to observed k_{DMS} is $u^{1.3}$, a much flatter curve than the quadratic dependence of most simple transfer velocity models. This appears to result from DMS having a greater solubility than CO_2, reducing the impact of bubbles on the transfer velocity. The impact of bubbles depends strongly on solubility of each specific trace gas thus more accurate gas exchange predictions will result from models that account for this effect. Given that the modified COARE model developed during this thesis properly accounts for changes in solubility, there is scope for future experimentation involving other gases.

8.4 Final remarks

The results presented within this work help to address a gap in the current understanding of the air-sea exchange of gases such as CO_2, and are important to the ongoing monitoring of CO_2 changes in the ocean-atmosphere system. Traditional estimates of gas transfer that are based on simple wind-speed dependent relationships have a tendency to underestimate the gas transfer velocity, during low wind conditions, and hence affect the net amount of gas exchanged. Whilst other methods, such as N_2/O_2 ratio, can be used to determine the global net flux of CO_2, accurate transfer velocities are required for constraining regional fluxes.

At low wind speeds, the air-sea gas transfer is more sensitive to factors such as temperature. Diurnal variability in seawater temperature can affect the amount of air-sea gas exchange taking place through changes in solubility and buoyancy-driven nocturnal convection. These are in effect tied to two separate processes; the kinetics of gas transfer at the air-water interface and the solubility pump. The effects on these processes are not well represented in existing models of gas transfer. This thesis explored these effects via the use of one-dimesional and three-dimensional ocean models combined with an improved gas transfer velocity parameterization. The result has been to confirm that such low wind speed processes are important for CO_2 transfer both regionally and globally.

The wider implications of these findings relate to the study of our planet's changing climate as discussed in section 1.3. Current estimates give the global oceans as a net sink for carbon of around 2.2 ($+22\%$ or -19%) GT C yr^{-1} (Takahashi et al., 2002) using the (wind speed)^2 dependence of the CO_2 gas transfer velocity of Wanninkhof (1992). Due to the nature of the large regional sources and sinks in the atmosphere and ocean, only a small percentage change is required in either direction to significantly alter the net uptake of CO_2 by the oceans. Reducing the errors in calculations of the global ocean uptake of CO_2 provides constraints on one of the major sinks in the global carbon cycle. Its accurate estimation will ultimately improve climate model predictions.

Appendix A

Mixed layer modelling

This appendix chapter is a research article that has been published in Ocean Modelling, Volume 19, Issues 1–2, Pages 53–69, doi:10.1016/j.ocemod.2007.06.005. The manuscript was submitted on the 4^{th} January 2007, accepted 18^{th} June 2007 and was available online on the 30^{nd} June 2007.

The text has been re-edited and is based upon Acreman and Jeffery (2007). Model results from GOTM were prepared by the author of this thesis and the Kraus-Turner Modelling was conducted by Dr. David Acreman at the U.K. Met Office. Section A.1.2 was written by the author of this thesis, the remainder of the manuscript was written by Dr. Acreman. The results serve to compare multiple 1-d models and illustrate that GOTM adequately describes the upper ocean boundary layer.

The representation of the upper ocean boundary layer is an important component of ocean forecasting and climate models. Upper ocean boundary layer parameterizations must reproduce observed behavior and careful setting of the tunable parameters is an important part of achieving this aim. Tuning and validation studies are often performed using 1-d models, which are computationally cheap to run but neglect advection. The meteorological and oceanographic observations taken at Ocean Weather Station Papa (OWS Papa) have been used to test model performance over an annual cycle in many previous studies (e.g. Martin (1985); Gaspar et al. (1990); Large et al. (1994); Kantha and Clayson (1994)) as the effects of advection are thought to be small at this location.

More recently data from the Argo project have become available. Argo floats are autonomous profiling floats which measure temperature and salinity profiles with a typical period of ten days and have a working life of several years. These data allow validation of mixed layer models over an annual cycle with unprecedented spatial coverage.

This paper presents results from model validation and tuning using both the OWS Papa data and newer Argo data. Section A.1 describes the three models used in this study and the solar radiation parameterisation common to all the models. Comparisons of the models to OWS Papa data and Argo data are presented in Section A.2. Section A.3 presents results from tuning the Kraus-Turner model, using OWS Papa data and data from a sample of Argo floats. The performance and sensitivities of the tuned model are investigated in Section A.4. Conclusions are presented in Section A.5.

A.1 Model descriptions

Three different upper ocean boundary layer models will be used in the subsequent studies. The first is based on the bulk model of Kraus and Turner (1967), the second is the two equation k_e-epsilon turbulence closure model from GOTM and the third is the K-profile parameterization (KPP) model of Large et al. (1994). All three models assume horizontal homogeneity hence the effects of advection are not considered. The models are forced with prescribed fluxes and there is no relaxation to or assimilation of observed temperature and salinity profiles unless otherwise stated. Descriptions of the three model implementations and the solar radiation parameterization, common to all three models, are presented below.

A.1.1 Kraus-Turner model

The Kraus-Turner model uses an integrated form of the turbulent kinetic energy (TKE) equation to balance the generation of turbulence by wind mixing and convection with the work done in overturning stable stratification. In reality current shear also produces TKE but the Kraus-Turner model used here does not explicitly include a shear production term, unlike some bulk models.

From dimensional arguments the wind mixing energy w can be represented by

$$w = \lambda \rho_w u_*^3 \tag{A.1}$$

where ρ_w is the density of sea water, u_* is the friction velocity and λ is a non-dimensional, tunable parameter of order unity. The wind mixing energy is the rate at which the wind inputs turbulent kinetic energy into the ocean and has units of W m^{-2}. If the water column is unstable potential energy is released by convective overturning and a fraction of 0.15 of the potential energy is converted to TKE. The TKE is assumed to decay exponentially with depth with an e-folding length δ. The partial mixing scheme of (Thompson, 1976) is used to balance wind mixing against work done in cases where an entire model level cannot be entrained into the mixed layer.

In contrast, momentum is not observed to be well mixed throughout the layer of uniform density near the surface so applying the Kraus-Turner model to momentum would not give realistic vertical profiles. Instead momentum is mixed using a simplified version of the KPP scheme which assumes neutral stability in the mixed layer (Gordon et al., 2000). A damping term is included in the velocity calculation, to prevent artificial velocity build up (Mellor, 2001) with a damping coefficient of (4 days)$^{-1}$ (Pollard and Millard, 1970).

The overall scheme for the vertical mixing of momentum and tracers is very similar to that used in the HadCM3 climate model (Gordon et al., 2000), but includes modifications used in the later HadGEM1 climate model (Johns et al., 2006).

A.1.2 GOTM configuration

The General Ocean Turbulence Model (GOTM) is an open source, one-dimensional water column model for computing the solutions to the 1-d versions of the transport equations of momentum, heat and salt. It incorporates a number of different parameterizations for vertical turbulent mixing; for this study, we have chosen to use a two-equation $k_e - \epsilon$ turbulence closure scheme (Rodi, 1987), with dynamic dissipation rate equations for the length-scales.

Two-equation turbulence models use one transport equation for turbulent kinetic energy and another for a length scale-related quantity. These have proven to be a good compromise between complexity and simplification (Mellor and Yamada, 1974; Rodi, 1987; Canuto et al., 2001; Stips et al., 2002).

The equations for turbulent kinetic energy k_e and its rate of dissipation ϵ are required for calculating the vertical eddy viscosity and diffusivity. The equations for k_e and ϵ result from carrying out Reynolds decomposition, on the Navier-Stokes equations, into a mean flow and a fluctuating component. Since these equations are no longer closed, closure assumptions are required.

As described by Burchard et al. (1999) the transport equation for k_e can be written as;

$$\frac{dk_e}{dt} - \frac{d}{dz}\left(\frac{vt}{\sigma k_e}\frac{dk_e}{dz}\right) = P + G - \epsilon \tag{A.2}$$

where P is the production of k_e by mean shear, G is the production of k_e by buoyancy and ϵ is the rate of dissipation of k_e.

$$P = v_t\left[\left(\frac{du^2}{dz} + \frac{dv^2}{dz}\right)\right] \tag{A.3}$$

where v_t is the turbulent friction coefficient, u and v are the components of velocity and N_v is the Brunt-Vaisala frequency.

For horizontally homogeneous flows, the sum of the viscous and turbulent transport terms $\mathcal{D}$ can be expressed by a simple gradient formulation

$$\mathcal{D}_\epsilon = \frac{d}{dz}\left(\frac{v_t}{\sigma_\epsilon}\frac{d\epsilon}{dz}\right) \tag{A.4}$$

where σ_ϵ is the constant Schmidt number for ϵ. The rate of dissipation ϵ is balanced according to

$$\frac{d\epsilon}{dt} = \mathcal{D}_\epsilon + \frac{\epsilon}{k_e}(c_{\epsilon 1}P + c_{\epsilon 3}G + c_{\epsilon 2}\epsilon) \tag{A.5}$$

The dissipation rate can either be obtained directly from its parameterized transport equation or from any other model yielding an appropriate dissipative length scale, l. Then ϵ becomes

$$\epsilon = (c_\mu^0)^3 \frac{k_e^{3/2}}{l} \tag{A.6}$$

This turbulence closure model is fitted to the logarithmic law of the wall. However, this law is not valid directly below the surface when wave breaking is present. The wave-enhanced layer is represented within GOTM by the wave breaking parameterisation suggested by Burchard (2001), using the empirical constant $c_w = 100$ suggested by Craig and Banner (1994). We use the stability method as laid out by Kantha and Clayson (1994), and internal waves are incorporated within the model following Large et al. (1994).

The empirical constants used in the turbulence model are summarized in table 1; we use the default GOTM v3.2 empirical coefficients for the $k_e - \epsilon$ model. The turbulent Schmidt number for k_e, σ_k, is a rough estimate (Rodi, 1987), the turbulent Schmidt number for the dissipation rate, σ_ϵ, results from the law of the wall; $c_{\epsilon 1}$ and $c_{\epsilon 2}$ result from laboratory experiments with homogeneous shear flow and grid turbulence, respectively. For stable stratification ($N_v > 0$) $c_{\epsilon 3}$ results from fitting the steady state Richardson number to idealized experiments (see Burchard and Baumert (1995); Burchard (2001)), for unstable stratification ($N_v < 0$) $c_{\epsilon 3}$ needs to be positive to retain a source of dissipation for free convection. The model time-step was set to 5 s with a uniform vertical model resolution of 10, 5, 2 or 0.5 m as specified.

c_μ^0	σ_k	σ_ϵ	$c_{\epsilon 1}$	$c_{\epsilon 2}$	$c_{\epsilon 3}$	$N^2 > 0$ $c_{\epsilon 3}$ $N^2 < 0$
0.5577	1.0	1.3	1.44	1.92	0.0	1.0

TABLE A.1: GOTM constants for the $k_e - \epsilon$ turbulence closure model according to Rodi (1987).

A.1.3 The K-profile parameterization scheme

The KPP scheme of Large et al. (1994) represents the turbulent mixing of a property X using a diffusion equation which includes non-local transport effects

$$\frac{dX}{dt} = \frac{d}{dz}\left(K(z)\frac{dX}{dz} - \gamma\right) \tag{A.7}$$

where $K(z)$ is a depth dependent diffusion coefficient and γ is a counter-gradient term which accounts for non-local effects. In the KPP scheme the diffusion coefficient in the boundary layer is parameterised by

$$K(z) = h_{bl} w(\sigma) G(\sigma) \tag{A.8}$$

where h_{bl} is the depth of the boundary layer, $\sigma = d/h_{bl}$ (where d is the positive depth), $w(\sigma)$ is the turbulent velocity scale and $G(\sigma)$ is a shape function.

The shape function is assumed to be a polynomial of the form

$$G(\sigma) = a_0 + a_1\sigma + a_2\sigma^2 + a_3\sigma^3 \tag{A.9}$$

where a_0, a_1, a_2, a_3 are determined by applying the boundary conditions that $K(z) = 0$ at $\sigma = 0$ (i.e. no turbulent flux at the surface) and that $K(z)$ and the vertical gradient of $K(z)$ match the background values at the base of the boundary layer. In this study the background mixing is determined using the method of Gordon et al. (2000).

The turbulent velocity scale $w(\sigma)$ is given by

$$w(\sigma) = \frac{\kappa u_*}{\omega(d/L)} \tag{A.10}$$

where κ is the Von-Karman parameter, u_* is the friction velocity and $\omega(d/L)$ is a depth dependent, empirically determined stability function of depth d and the Obukhov length L. the function $\omega(d/L)$ is equal to unity under neutral forcing, hence $w(\sigma) = \kappa u_*$. The

effect of $\omega(d/L)$ is to increase $w(\sigma)$ if the forcing unstable and decrease $w(\sigma)$ if the forcing is stable. For more details of the stability function see Large et al. (1994). The boundary layer depth is the depth where the bulk Richardson number exceeds the threshold $Ri_c = 0.3$. The bulk Richardson number Ri_b is given by

$$Ri_b = \frac{(B_r - B(d))d}{\mid \vee_r - \vee(d) \mid^2 + V_t^2(d)} \tag{A.11}$$

where B_r is the buoyancy in the surface layer (averaged over 0.1h), $B(d)$ is the buoyancy at depth d, $\vee(d)$ is the vector difference of the velocity at depth d and the average velocity in the surface layer, and V_t is a term which accounts for shear due to turbulent velocity. The V_t term is given by

$$V_t(d) = \frac{1.33}{Ri_c} N_v(d) w d \tag{A.12}$$

where $N_v(d)$ is the buoyancy frequency at depth d. The factor of 1.33 has been determined using the best fit parameters of Large et al. (1994). Some additional constraints are applied to the boundary layer depth. If the forcing is stable the boundary layer depth must be less than the Obukhov depth; the boundary layer depth is not allowed to exceed 80 m; and the boundary layer depth must not exceed the Ekman depth h_E where

$$h_E = \frac{0.7 u_*}{f} \tag{A.13}$$

and f is the Coriolis parameter.

The counter-gradient term is non-zero only for tracers and only in the case of unstable forcing. The term is given by

$$\gamma = \frac{7.5 \overline{wx_0}}{w(\sigma) h_{bl}} \tag{A.14}$$

where $\overline{wx_0}$ is the flux of quantity X at the surface, $w(\sigma)$ is the turbulent velocity scale and h_{bl} is the boundary layer depth.

A.1.4 Solar radiation

The absorption of solar radiation is treated identically in all models, using the double exponential representation of Paulson and Simpson (1977). The flux at depth z is given by

$$I(z) = I(0)[Rexp(z/\eta_1) + (1-R)exp(z/\eta_2)] \tag{A.15}$$

where $I(z)$ is the flux at depth z and z is measured negative downwards from zero at the ocean surface. The model partitions the solar flux into two components in the ratio R:(1-R). The first component decays exponentially with depth with a length scale η_1 and the second component decays exponentially with depth with a length scale η_2. The parameters η_1 , η_2 and R depend on the optical clarity of the water. Paulson and Simpson (1977) give values of η_1 , η_2 and R for different Jerlov water types (Jerlov, 1968). The following experiments use either Jerlov water type IB ($\eta_1 = 1$ m, $\eta_2 = 17$ m and $R = 0.67$) or Jerlov water type II ($\eta_1 = 1.5$ m, $\eta_2 = 14$ m and $R = 0.77$). Unless otherwise stated the water type is assumed to be Jerlov IB (the same water type used in the U.K. Met Office ocean models) which is broadly representative of open ocean areas (Simonot and Treut, 1986).

A.2 Model comparisons

A.2.1 Model comparisons at OWS Papa

The Kraus-Turner model, KPP model and GOTM were run for 1 year starting on 1 March 1961, the same period used by Large et al. (1994). Model temperature and salinity profiles were initialised from observations and forcing was calculated from observed meteorological variables using bulk formulae. Wind stress, sensible heat flux and latent heat flux were calculated using version 3.0 of the COARE algorithm (Fairall et al., 2003). The down-welling longwave radiation was calculated using the formula of Josey et al. (2003) and the shortwave flux was calculated using the okta model of Dobson and Smith (1988) with albedo from Payne (1972). A freshwater flux was calculated using evaporation from the bulk formulae and precipitation taken from the SOC climatology (Josey et al., 1998) interpolated to the model time. The daily averages of the forcing fluxes are plotted in figure A.1.

The net heat input from the fluxes described above is 42 W m^{-2} for the 1 year period starting on 1 March 1961. This is not a closed cycle but previous studies have also found a net annual heat input at OWS Papa; a summary of heat fluxes at OWS Papa is given in Table 1 of Large (1996). A climatological average of 25 $\pm$ 15 W m^{-2} was found by Large (1996) for the period 1960–1981 and an average of 32 $\pm$ 19 W m^{-2} was found by Smith and Dobson (1984) for the period 1959–1975. The value of 42 W m^{-2} found here is close to the upper error bound of these climatological averages but referring to Fig. 1b of Large (1996) shows that the period under consideration here was a time of higher than average net heat input. Comparing the net heat input of 42 W m^{-2} found here with time series in Figure. 1b of Large (1996) shows good agreement.

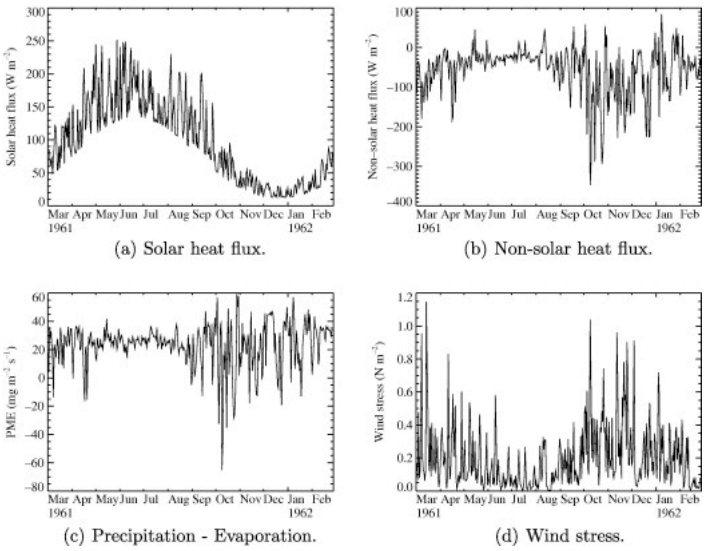

FIGURE A.1: Daily average forcing fluxes in the OWS Papa experiment: (a) solar heat flux, (b) non-solar heat flux, (c) precipiation-evaporation and (d) wind stress.

Model vertical resolutions of 10 m, 5 m, 2 m and 0.5 m were used with sufficient vertical levels to give a total depth of 200 m. Plots of sea surface temperature (SST) and mixed layer depth for the four different resolutions used are shown in figures A.2 and A.3, respectively. Thin solid lines are from the Kraus-Turner model, dashed lines are from GOTM, dotted lines are from the KPP model and thick solid lines are from observations. The Kraus-Turner model uses parameter settings of $\lambda = 0.7$, $\sigma = 100$ m which are the values currently used in the UK Met Office FOAM system (Bell et al., 2004) and the HadCM3 climate model (Gordon et al., 2000). The SST observations have been smoothed using a top-hat filter of width two days to average over tidal and inertial periods (similar to the treatment in Large et al. (1994) Section 5). The mixed layer depth is defined according to the 'optimal mixed layer depth' of Kara et al. (2000), i.e. the depth at which the potential density has increased by an amount corresponding to temperature difference of 0.8 °C at the surface.

The Kraus-Turner model produces mixed layers which are too deep, except for the summer months when the model performs well. The model mixed layer depth is not strongly dependent on vertical resolution and it is apparent that, at all resolutions, the Kraus-Turner model needs to be re-tuned if it is to perform acceptably at OWS Papa. The Kraus-Turner SSTs are somewhat colder than the observed SSTs, consistent with too much vertical mixing. The model summer-time SST shows a resolution dependence; higher resolution runs have more realistic SSTs and more realistic SST variability than the lower resolution runs. As vertical resolution increases, the thermal inertia of the top model level is reduced which allows a more rapid response to changes in the heat input. This effect is most noticeable in summer when the mixed layer is shallow and the heat input is not mixed downwards away from the surface layers. The observed SST is seen to depart significantly from all models in the latter part of the year. Large (1996)

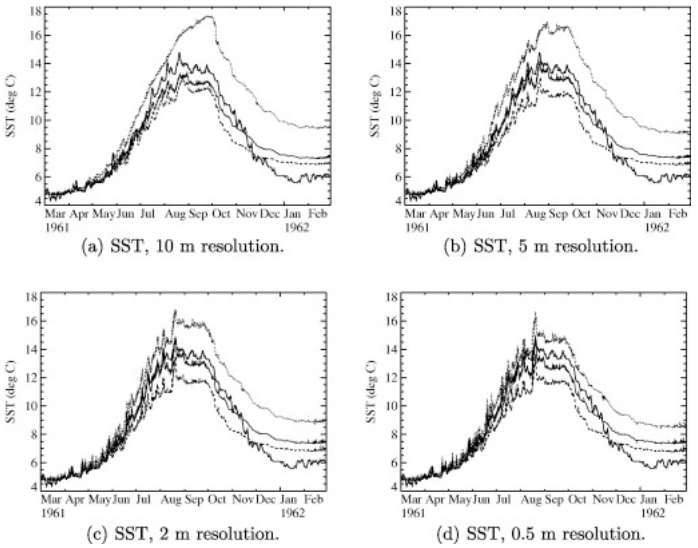

FIGURE A.2: One year evolution of sea surface temperature at OWS Papa for model runs with 10 m, 5 m, 2 m and 0.5 m resolution. Thin solid lines are from the Kraus-Turner model, dashed lines are from GOTM, dotted lines are from the KPP model and thick solid lines are from observations: (a) SST, 10 m resolution; (b) SST, 5 m resolution; (c) SST, 2 m resolution and (d) SST, 0.5 m resolution.

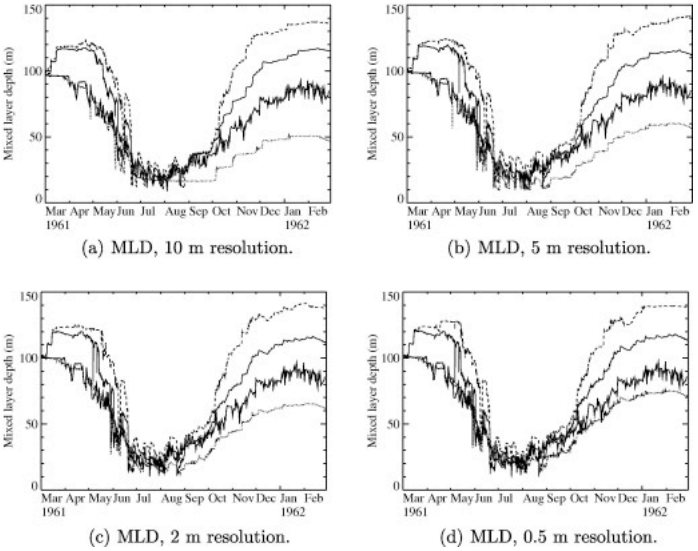

FIGURE A.3: One year evolution of mixed layer depth at OWS Papa for model runs with 10 m, 5 m, 2 m and 0.5 m resolution. Thin solid lines are from the Kraus-Turner model, dashed lines are from GOTM, dotted lines are from the KPP model and thick solid lines are from observations: (a) MLD, 10 m resolution; (b) MLD, 5 m resolution; (c) MLD, 2 m resolution and (d) MLD, 0.5 m resolution.

compares surface heat fluxes at OWS Papa, calculated using bulk formulae, with the heat flux inferred from changes in heat content and concludes that heat fluxes and storage are balanced for much of the year (until August) but that there are significant differences between August and December. Referring to Fig. 3 of Large (1996) shows that the discrepancy is particularly large in November and December, the same months in which the model SST departs most rapidly from the observed SST in Fig. A.2 Consequently the large difference between model and observed SST after October may be attributed to a departure from 1 dimensional heat balance during November and December.

The mixed layer depth from GOTM is very similar to that from the Kraus-Turner model during the first half of the run and shows a similar over deepening at later times. Some differences are seen in GOTM runs at different resolutions but the mixed layer depths from all four runs are similar, even at the lowest vertical resolution. As the mixed layer depth from GOTM was observed to be too deep the Craig-Banner wave breaking term was switched off in these runs resulting in slightly shallower mixed layer depths.

The KPP scheme gives a good mixed layer depth representation during the first half of the year, even with a coarse vertical resolution. However the deepening phase is poorly represented at low resolution, particularly at the lowest vertical resolution of 10 m. The 10 m vertical resolution run exhibits step-like increases in the mixed layer depth between October and December. These step-like increases are also seen in the boundary layer depth diagnosed by the KPP scheme. The increases in the KPP boundary layer depth occur slightly before the increases in diagnosed mixed layer depth indicating that the former drives the latter. The mixing coefficients are proportional to the boundary layer depth so this is expected. At higher vertical resolutions the KPP model performance improves and at 0.5 m resolution the KPP model represents mixed layer depth significantly better than the other models. The resolution dependence of the KPP model was noted by Large et al. (1994) in sensitivity studies under idealised forcing (see Appendix C of Large et al. (1994)). The SST from the KPP model also shows a lack of variability at low resolution and at the highest resolution the variability in all the model SSTs is similar.

A.2.2 Model comparisons using Argo float Q4900131

A case study was performed using data from Argo float Q4900131 over the period November 2002-October 2003, when the float was located close to the OWS Papa site. The Kraus-Turner model, KPP model and GOTM were run at 0.5 m vertical resolution with 500 vertical levels. Initial temperature and salinity profiles were obtained by interpolating observed profiles, from the Argo float, onto the model vertical levels. Forcing fluxes of heat, momentum and moisture were taken from the U.K. Met Office NWP system. The fluxes are generated 6 h and were interpolated to hourly values, plots of the daily averaged fluxes are shown in Fig. A.4. The fluxes are generally similar to the fluxes

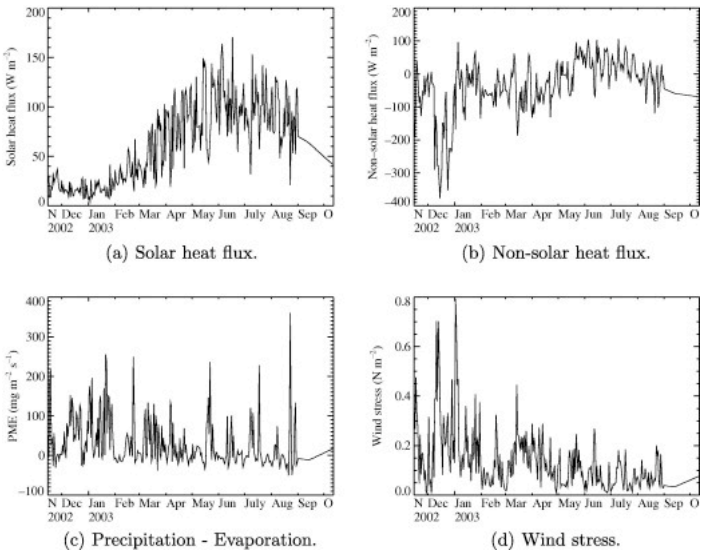

FIGURE A.4: Daily average forcing fluxes used with Argo float Q4900131: (a) Solar heat flux, (b) Non-solar heat flux, (c) Precipitation-evaporation and (d) Wind stress.

used in the OWS Papa experiment (see Fig. A.1) apart from the freshwater flux. The difference may be attributed to the greater variability in precipitation from the NWP model compared to using a precipitation climatology. Although the temporal variability of the freshwater flux is different in the two experiments the average freshwater input over the year is similar; for OWS Papa the average freshwater input is 23 mg m^{-2} s^{-1} and for this experiment is it 25 mg m^{-2} s^{-1}. There is a net heat input from these fluxes of 25 W m^{-2} which is smaller than the 42 W m^{-2} heat input from the OWS Papa fluxes but in good agreement with the observations. As the solar flux from the U.K. Met Office NWP system is in a different band to that used by Paulson and Simpson (1977) it was necessary to change the value of the R parameter, described in Section 2.4, from 0.67 to 0.38 for Jerlov type IB water.

Mixed layer depths from the Kraus-Turner model, KPP model and GOTM (with the Craig-Banner term included) are shown in Fig. A.5a, with the observed mixed layer depths from the Argo float plotted as points. The Kraus-Turner model uses parameter settings of $\lambda = 0.7$, $\sigma = 100$ m as in the previous section. The mixed layer depth from the Kraus-Turner model (solid line) is initially good but becomes too shallow after January. The KPP scheme (dotted line) gives mixed layers which are too shallow compared to the observations and lack variability in summer. The GOTM mixed layer depth (dashed line) is the most realistic of all the models and best captures the deepening phase at the start of the run. The Kraus-Turner model and GOTM, which were too deep when validated at OWS Papa, perform well in this case.

In order to assess the impact of the freshwater flux, the Kraus-Turner model was run with zero freshwater flux. Results with the freshwater flux included (solid line) and with no freshwater flux (dashed line) are shown in Fig. A.5b. With no freshwater flux the modelled mixed layer depth is significantly deeper from the beginning of January to the

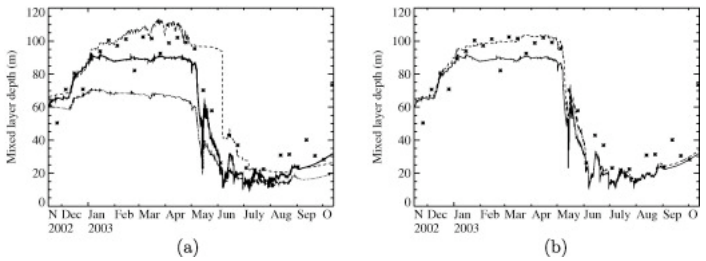

FIGURE A.5: (a) Mixed layer depth from the Kraus-Turner model (solid line), KPP model (dotted line) and GOTM (dashed line) models run at the location of float Q4900131. Mixed layer depths from the Argo float are plotted as points. The Kraus-Turner model uses $\lambda = 0.7$, $\sigma = 100$ m. (b) The Kraus-Turner model with freshwater flux (solid line) and without freshwater flux (dashed line).

end of April. A net input of freshwater provides a positive buoyancy flux which tends to inhibit mixing, so when the freshwater input is removed the mixed layer tends to deepen more. The effect of freshwater flux on vertical mixing has also been studied by McCulloch et al. (2004). They found that freshwater flux affected mixed layer depth at a location in the North East Atlantic near 40°N in December. The Argo float used in this case study is at a similar latitude also in the Eastern part of the ocean basin (albeit in the Pacific) and also shows a significant influence of freshwater flux in winter.

A.3 Kraus-Turner model tuning

A.3.1 Kraus-Turner model tuning at OWS Papa

The Kraus-Turner model did not compare well with observations at OWS Papa, other than in summer when the mixed layer was shallow. In contrast the KPP model performed well at OWS Papa, provided the vertical resolution was sufficiently high, indicating that the forcing fluxes are not significantly in error. The performance of the Kraus-Turner model might be improved by tuning the parameters λ (generation of TKE) and σ (decay of TKE with depth) described in section A.1. The values of $\lambda = 0.7$ and $\sigma = 100$ m used in HadCM3 (Gordon et al., 2000) were chosen to give the same dissipation as the MILE experiment (Davis et al., 1981). In contrast the KPP model was tuned at OWS Papa by (Large et al., 1994) so is expected to perform well at this location, although some differences are expected between the results presented here and those of Large et al. (1994) due to different treatments of forcing fluxes and absorption of solar radiation.

The Kraus-Turner model was run using different values of the λ and σ parameters. The λ parameter was varied from 0 to 1.5 in steps of 0.025 and σ was varied from 0 m to 150 m in steps of 10 m. For each model run the mean and RMS difference between the model and observed mixed layer depth was calculated each time an observation was available. These mean and RMS errors were then averaged to obtain average mean and RMS mixed layer depth errors over the annual cycle. The tuning experiment was run three times

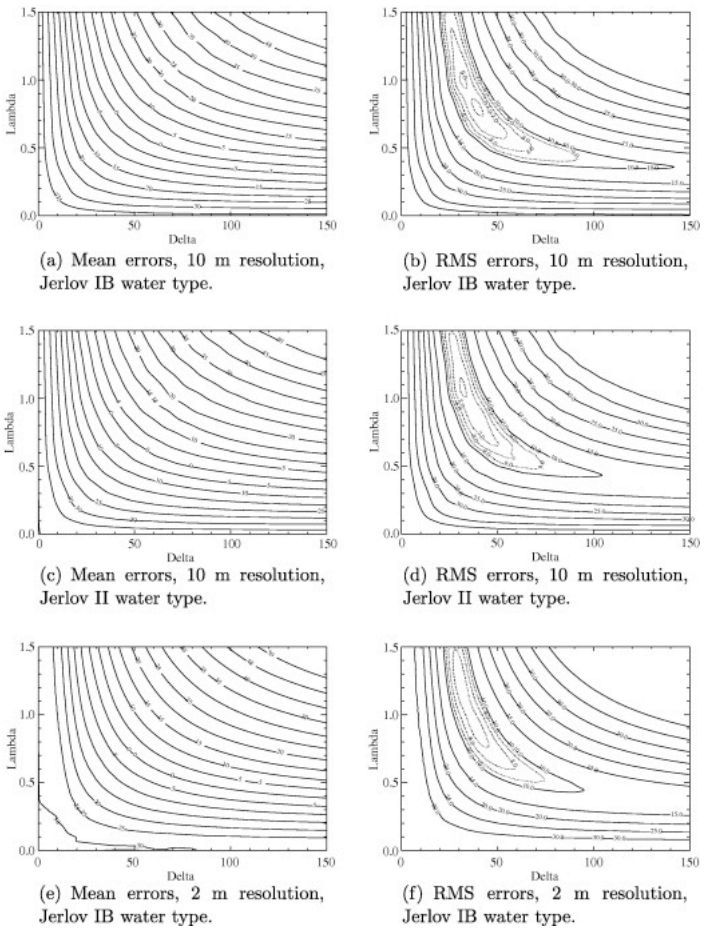

FIGURE A.6: Mean and RMS errors as a function of σ and λ parameters from the OWS Papa tuning experiment. The tuning experiment was performed three times. Firstly at 10 m resolution with type IB water, secondly at 10 m resolution with type II water and thirdly at 2 m resolution with type IB water. Solid contours are at intervals of 5 m, dashed contours are at intervals of 1 m. (a) Mean errors, 10 m resolution, Jerlov IB water type, (b) RMS errors, 10 m resolution, Jerlov IB water type, (c) mean errors, 10 m resolution, Jerlov II water type, (d) RMS errors, 10 m resolution, Jerlov II water type, (e) mean errors, 2 m resolution, Jerlov IB water type and (f) RMS errors, 2 m resolution, Jerlov IB water type.

with different vertical resolutions and Jerlov water types. The first run used a vertical resolution of 10 m and a Jerlov type IB water; this is typical of a U.K. Met Office ocean model used for either operational ocean forecasting or climate purposes. The second run used a vertical resolution of 10 m and a Jerlov type II water. Gaspar (1988) used Jerlov type II water in a 1-d mixed layer model at OWS Papa and Large et al. (1994) perform runs with type IA, type II and a time varying water type. The third run used a higher vertical resolution of 2 m and a Jerlov type IB water. Plots showing how the mean and RMS errors vary with different values of the λ and σ parameters are shown in Fig. A.6. A negative mean error indicates that the model is too deep compared to the observations.

At 10 m resolution, with Jerlov type IB water, the minimum RMS errors are with $\lambda = 0.775$, $\sigma = 40$ m which also gives mean errors close to zero. If σ is fixed at 100

m the best value of λ is approximately 0.4, much lower than the value of 0.7 used in the previous section when σ was 100 m. When Jerlov type II water is assumed the minimum RMS errors are with $\lambda = 1.125$, $\sigma = 30$ m. Although the optimum parameters are different, the overall distribution of RMS errors is very similar to the previous case. At 2 m resolution, with Jerlov water type IB, the smallest errors are with $\lambda = 1.275$, $\sigma = 30$ m. The tuning experiment was also performed with Jerlov type IB water at 0.5 m resolution, giving optimum parameters of $\lambda = 1.225$, $\sigma = 30$ m. The experiment was additionally performed using the uppermost 14 levels from the U.K. Met Office FOAM system (Bell et al., 2004). This comprises 14 vertical levels with level bases at 10.0 m, 20.0 m, 30.0 m, 40.2 m, 55.5 m, 78.5 m, 113.0 m, 164.8 m, 242.6 m, 359.4 m, 534.7 m, 797.9 m, 1193.2 m, 1808.5 m. Optimum parameters at the FOAM vertical resolution are $\lambda = 0.925$, $\sigma = 40$ m. Changes in vertical resolution and Jerlov water type have an effect on the choice of optimum parameter settings however the overall distribution of errors does not vary greatly under these changes. The region bounded by the 10 m RMS error contour is similar in all cases and choosing parameters within this contour (e.g. $\lambda = 1.0$, $\sigma = 30$ m) will give small RMS errors for all resolutions and both water types considered here.

There is a significant interaction between the λ and σ parameters such that small RMS errors can also be obtained with larger λ and smaller σ (greater generation of TKE but more rapid dissipation with depth) or smaller λ and larger σ (less generation of TKE but less rapid dissipation with depth). These results show the importance of considering interactions between parameters when tuning this model. In order to gain a better understanding of the relationship between the λ and σ parameters, the tuning experiment was repeated for shorter time periods. The first time period was 1 March–31 May, a time when the mixed layer is shoaling; the second period is 1 June to 30 September, when there is a shallow mixed layer; the third period is from 1 October to 31 December when the mixed layer deepens. Plots from tuning runs using 2 m vertical resolution are shown in Fig. A.7. If the mixing energy at the surface is $\lambda\rho_w u_*^3$ and the available energy decays exponentially with depth then the mixing energy reaching the base of a well-mixed layer of depth h is given by

$$\lambda\rho_w u_*^3 exp(-h/\delta) \tag{A.16}$$

If we require that some fixed amount of mixing energy $f\rho_w u_*^3$ is available at the base of the well mixed layer, in order to produce a given deepening of the mixed layer, then λ and σ must satisfy the relation

$$\lambda exp(-h/\delta) = f \tag{A.17}$$

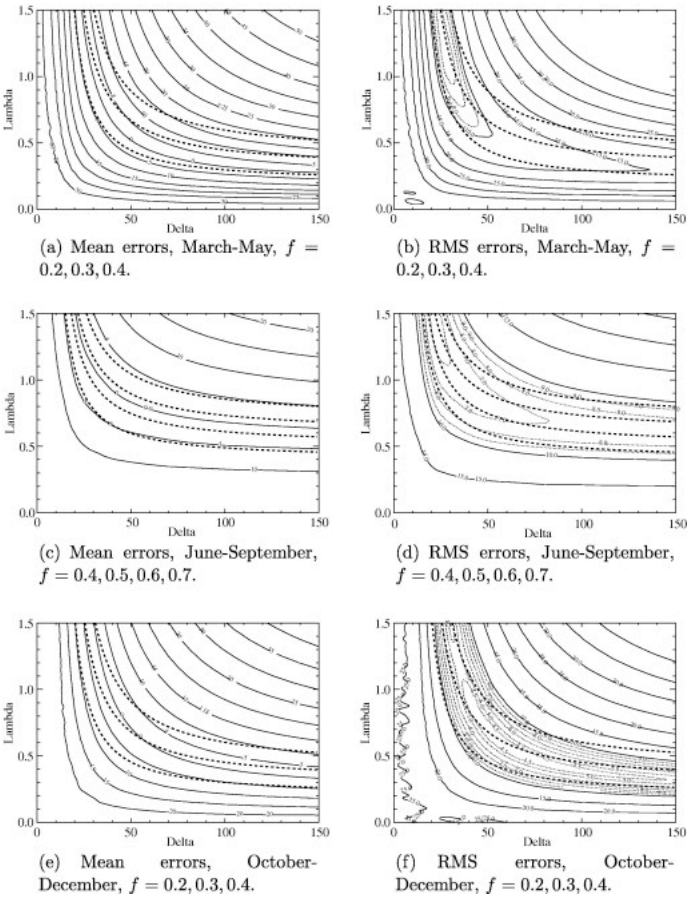

FIGURE A.7: Mean and RMS errors as a function of σ and λ parameters from the OWS Papa tuning experiment. Tuning has been carried out during March–May, June–September and October–December. The heavy dashed line is the relationship between λ and σ if the mixing energy at the base of the mixing layer is required to be constant. (a) Mean errors, March–May, f = 0.2, 0.3, 0.4, (b) RMS errors, March–May, f = 0.2, 0.3, 0.4, (c) mean errors, June-September, f = 0.4, 0.5, 0.6, 0.7, (d) RMS errors, June–September, f = 0.4, 0.5, 0.6, 0.7, (e) mean errors, October–December, f = 0.2, 0.3, 0.4 and (f) RMS errors, October-December, f = 0.2, 0.3, 0.4.

This relation is plotted in Fig. A.7 (heavy dashed line) for different values of f. The well mixed layer depth h is calculated as the average mixed layer depth from observations, using a temperature difference of 0.1 °C, over the time period in question. The depth calculated with this small temperature difference should be representative of the depth of active mixing. The average well mixed layer depths are 40 m (March–May), 20 m (June–September) and 41 m (October–December). The general shape of the contours, for all three time periods, is broadly consistent with the results from the year-long run, but some differences are apparent. In March–May there is a preference for a small value of σ and a large value of λ; the small value of σ prevents mixing energy from penetrating too deeply. In the October–December period there is not the same requirement for a small σ and a large λ, and small RMS errors can be obtained provided the relationship between λ and σ is observed. In the October–December period the important factor is

the mixing energy available at the base of the well mixed layer whereas in the March–May period there is a requirement that the mixing energy is not allowed to penetrate too deeply. In March–May and October–December the relationship between λ and σ is well represented by $f = 0.2$–0.4, i.e. the mixing energy available at the depth of active mixing is (0.2–0.4) $\rho_w u_*^3$. In June-September, when the mixed layer is shallower, the mixing energy available at the depth of active mixing is greater ((0.4–0.7) $\rho_w u_*^3$).

A.3.2 Model tuning using Argo data

Operational forecasting systems will often require a lower vertical resolution than those used in the previous section, in order to strike a balance between model performance and the computational expense of running the model. This section investigates tuning of the Kraus-Turner model at a coarser vertical resolution, but using the wide geographical coverage offered by Argo data. The vertical levels were the uppermost 14 levels from the U.K. Met Office FOAM system, as described in Section A.3.

Initial profiles of temperature and salinity were obtained by interpolating Levitus climatology onto the model levels. The models were then run for one year, starting in November 2002, using fluxes from the Met Office NWP system as described in Section A.2.

When a float report was available a comparison was made between the model mixed layer depth and the observed mixed layer depth (calculated from the Argo temperature and salinity profiles) and mean and RMS difference was calculated. After the comparison was made the temperature and salinity profiles were assimilated into the model over a 10 day window using a linear weighting.

A sample of Argo floats was selected by choosing floats with at least 30 reports, at approximately 10 day intervals, over the period November 2002–October 2003. This gave a sample of 218 floats whose locations are plotted in Fig. A.8. The models were run for each of the floats in the sample with different values of the λ and σ parameters. Mean and RMS differences between model and observed mixed layer depths were calculated for each float report and averaged over all reports for all floats in the sample. The effects of horizontal advection were quantified by comparing the observed change in mixed layer heat content with the heat input from the forcing fluxes. If the observed change in mixed layer heat content differed by more than 50 W m^{-2} from the heat input from the forcing fluxes the report was excluded from the calculation of average errors. 50 W m^{-2} was estimated to be the combined error in heat flux and heat storage based on Fig. 3 of Large (1996). Plots of the mean and RMS errors, averaged over all floats, for different values of λ and σ, are plotted in Fig. A.9a and b, respectively. The minimum RMS errors are with $\lambda = 1.5$, $\sigma = 40$ m with a corresponding mean error of -0.7 m (a negative mean error indicates the model is too deep on average). These results are

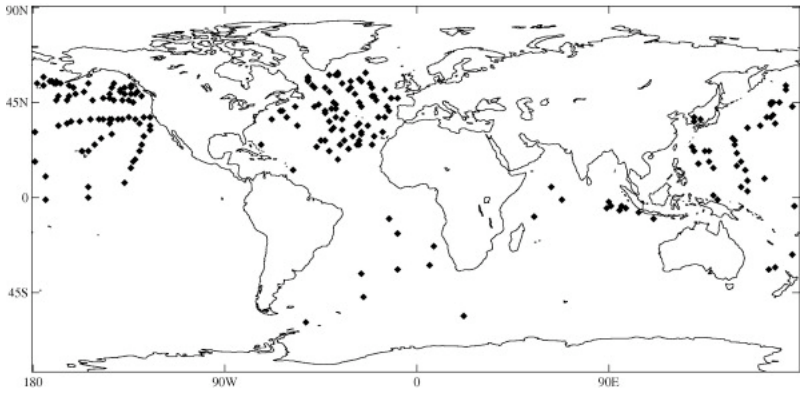

FIGURE A.8: Locations of the 218 Argo floats used in the tuning experiment.

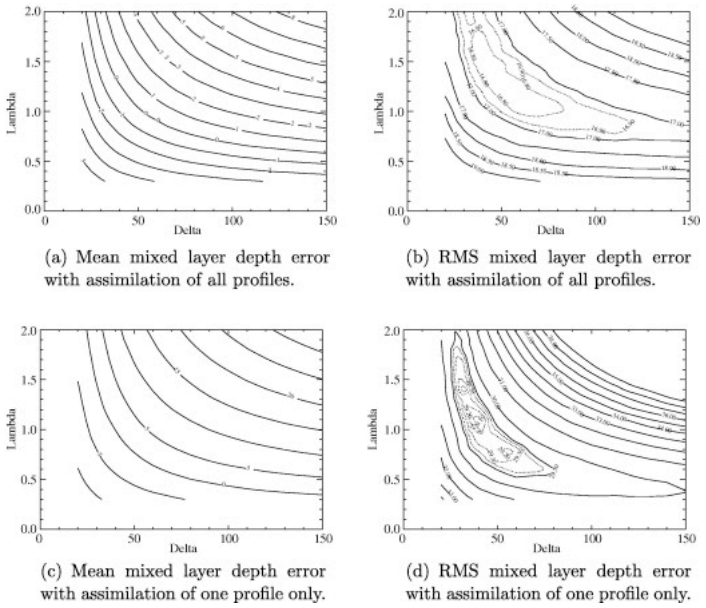

FIGURE A.9: Mean and RMS errors as a function of λ and σ parameters from the Argo tuning experiment. The experiment was run twice; once with assimilation of all profiles (top) and secondly with assimilation of the first set of profiles only (bottom). (a) Mean mixed layer depth error with assimilation of all profiles, (b) RMS mixed layer depth error with assimilation of all profiles, (c) mean mixed layer depth error with assimilation of one profile only and (d) RMS mixed layer depth error with assimilation of one profile only.

similar to the results from tuning the Kraus-Turner model to OWS Papa in that there is a requirement for a larger λ and smaller σ than the values of $\lambda = 0.7$, $\sigma = 10$ m used in HadCM3 and FOAM, however the best values of λ and σ are larger than those from the OWS Papa experiment indicating greater generation of TKE and less rapid decay with depth. The inclusion of assimilation was found to increase the model temperature gradients so when assimilation is included it is expected that larger values of λ and σ are required to reproduce the observed mixed layer deepening, due to the need to mixing against greater stratification.

In order to assess the impact of data assimilation on the choice of λ and σ parameters

the tuning experiment was repeated but only temperature and salinity profiles from the first float report were assimilated. The assimilation of profiles from only the first report ensures that the initial model profiles are realistic but prevents the assimilation from increasing the thermocline gradient during the course of the simulation. This is also a better comparison with the OWS Papa results, which did not include data assimilation. Mean and RMS errors are plotted in Fig. A.9c and d, respectively. The distribution of RMS errors is now more similar to the results from tuning at OWS Papa than the previous case. The smallest RMS errors are with $\lambda = 1.1$, $\sigma = 40$ m compared to values of $\lambda = 0.925$, $\sigma = 40$ m for OWS Papa at the same vertical resolution. These results suggest that different parameter choices are required in models with data assimilation (e.g. forecast models) than in models with no data assimilation (e.g. climate models).

A.4 Model sensitivities and performance of tuned Kraus-Turner scheme

A.4.1 OWS Papa

This section examines the performance of the tuned Kraus-Turner model and the sensitivity of the Kraus-Turner and KPP models to differences in water type and the assumed freshwater flux. The Kraus-Turner and KPP models were run at 2 m resolution with a Jerlov type IB water; the Kraus-Turner model used parameters of $\lambda = 1.275$, $\sigma = 30$ m derived from the tuning in Section A.3. Mixed layer depths and SSTs are plotted in Fig. A.10a and b. The tuned Kraus-Turner model gives a good representation of mixed layer depth and the representation of SST is good until November, when it is thought that advective effects become important, as discussed in Section A.2. At this resolution the KPP model tends to produce mixed layers which are too shallow and SSTs which are too warm, although it should be emphasised that the KPP model has not been tuned using the flux and water type parameterizations in use here. Large et al. (1994) use a more sophisticated time varying water type parameterization than used here so a direct comparison between the KPP and Kraus-Turner will tend to favour the Kraus-Turner model.

The buoyancy input from a positive freshwater flux can cause significant changes to the mixed layer depth (McCulloch et al., 2004). In order to assess the significance of the freshwater flux the models were re-run with the freshwater flux set to zero. SST is plotted in Fig. A.10c and mixed layer depth is plotted in Fig. A.10d. The mixed layer depths from both models have been slightly altered with a slight improvement in the KPP mixed layer depth, however the summer-time SSTs from the Kraus-Turner model have become too cold. The freshwater flux does have some effect on the simulated annual cycles of mixed layer depth and SST but it does not appear to be a dominant process in this case.

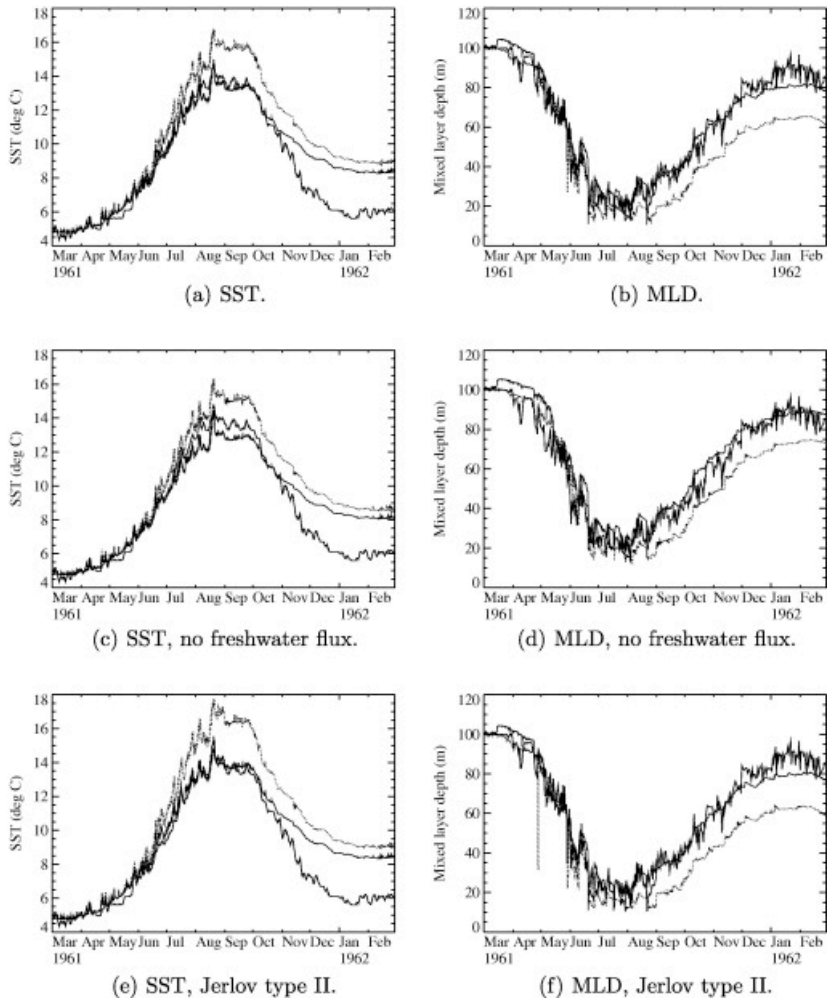

FIGURE A.10: One year evolution of sea surface temperature (left) and mixed layer depth (right). Thin solid lines are from the Kraus-Turner model, dotted lines are from the KPP model and thick solid lines are from observations: (a) SST; (b) MLD; (c) SST, no freshwater flux; (d) MLD, no freshwater flux; (e) SST, Jerlov type II and (f) MLD, Jerlov type II.

Another set of model runs was performed with the freshwater flux reinstated but with the water type changed to Jerlov type II from Jerlov type IB. The Kraus-Turner model parameters were kept as $\lambda = 1.275$, $\sigma = 30$ m. SST is plotted in Fig. A.10e and mixed layer depth is plotted in Fig. A.10f. The change of water type does not have a significant impact on the mixed layer depths but does have an impact on the SST. SSTs with the type II water are warmer than with the type IB water, as expected if the water is more turbid and absorption of solar radiation is occurring closer to the surface. The Kraus-Turner model SSTs are warmer than before and agree slightly better with the observations. These results indicate that care should be taken when using SST to validate mixed layer models as the water type used by the model can affect the results. The KPP model exhibits a rapid shoaling of the mixed layer at the end of April. This is caused by a period of heating, which results in the brief formation of a shallow mixed layer, before the water column is then mixed by an input of wind mixing energy. When

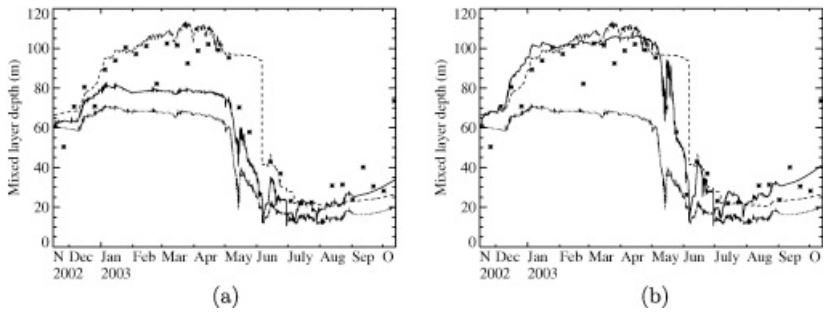

FIGURE A.11: Mixed layer depth from the Kraus-Turner model (solid line), KPP model (dotted line) and GOTM (dashed line) models run at the location of float Q4900131. Mixed layer depths from the Argo float are plotted as points. The Kraus-Turner model uses $\lambda = 1.1$, $\sigma = 40$ m (left) and $\lambda = 1.1$, $\sigma = 100$ m (right).

the more turbid type II water is used the solar radiation is absorbed nearer the surface, making the formation of shallow mixed layers more effective. The Kraus-Turner model does not exhibit the rapid shoaling of the mixed layer at the end of April as it performs more near surface mixing than the KPP model at this time.

A.4.2 Argo float Q4900131

The mixed layer depth from the Kraus-Turner model, with $\lambda = 1.1$, $\sigma = 40$ m, is plotted in Fig. A.11a with the mixed layer depths from GOTM and the KPP model. The performance of the Kraus-Turner scheme with these parameters is similar to the performance of the untuned model although $\lambda = 1.1$, $\sigma = 40$ m performs worse when the mixed layer is deep and better when the mixed layer is shallow, in particular the variability after May is improved.

If the Kraus-Turner parameters are changed to $\lambda = 1.1$, $\sigma = 100$ m (shown in Fig. 11b) the annual cycle is well represented. Compared to the parameters of $\lambda = 1.1$, $\sigma = 40$ m derived in Section A.3 this particular case requires much less dissipation of TKE with depth (larger value of σ) for the same TKE generation (same value of λ). This may indicate less rapid dissipation of TKE but care must be taken not to over interpret this result due to the degeneracy of the λ and σ parameters.

A.5 Conclusions

The Kraus-Turner bulk model, the KPP scheme of Large et al. (1994), and the GOTM turbulence closure model were compared at OWS Papa and against data from an Argo float. The bulk model and GOTM were found to mix too deeply at OWS Papa but to give a good representation of mixed layer depth in the Argo float case study. Conversely the KPP model of Large et al. (1994) was found to give a good representation of the mixed layer depth at OWS Papa, provided the vertical resolution was sufficiently high,

however when the KPP model was validated using the Argo float the mixed layer depth was found to be too shallow. In both the OWS Papa experiment and the Argo float case study the effect of the net freshwater input from the forcing fluxes was found to have an impact on the modelled mixed layer depth although the effect was not dominant over the annual cycle.

The Kraus-Turner model was tuned using both Argo data and OWS Papa data and the results were found to be consistent, in the absence of data assimilation. In models with no ongoing data assimilation parameter values of $\lambda = 1.0$–1.1 and $\sigma = 30$–40 m are near-optimum in both cases. Results from tuning using Argo data show that if data assimilation is included in the model a larger value of $\lambda = 1.5$ is required but the preferred value of σ is not altered. Assimilation was found to increase the temperature gradient in the model thermocline such that a larger input of TKE is required to reproduce observed mixed layer deepening. The λ parameter, describing the generation of mixing energy, and the σ parameter, describing the decay of mixing energy, were related by requiring that a fixed amount of mixing energy reach the base of the typical well mixed layer. The resulting simple relation gave a good representation of the interaction between the λ and σ parameters.

Appendix B

Additional plots

B.1 GOTM levels

Schematic B.1 shows the exponential model grid, with increased resolution near the surface, used in chapters 5, 6 and 7. There are 200 levels, with the uppermost level located at 2.7×10^{-3} m, approximately the $\mathrm{SST}_{subskin}$ depth.

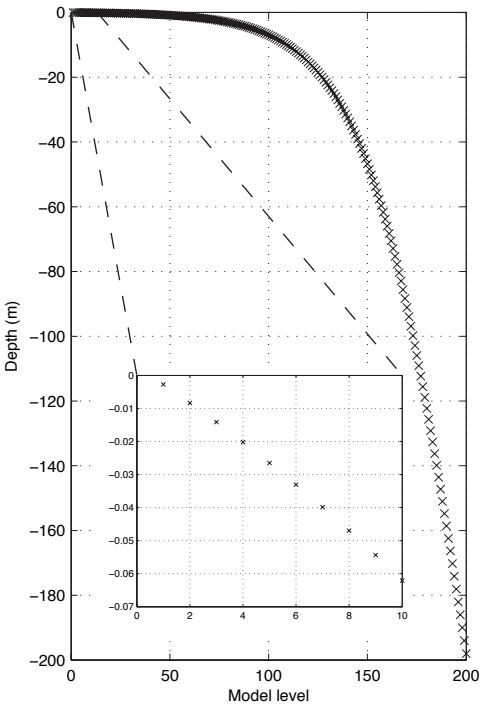

Figure B.1: Schematic showing GOTM model levels versus depth (m)

References

Acreman, D. M., Jeffery, C. D., 2007. The use of Argo for validation and tuning of mixed layer models. Ocean Modelling 19 (doi:10.1016/j.ocemod.2007.06.005), 53–69.

Anderson, S. P., Weller, R. A., Lukas, R. B., 1996. Surface buoyancy forcing and the mixed layer of the western Pacific warm pool: Observations and 1-d model results. Journal of Climate 9 (12), 3056–3085.

Anis, A., Moum, J. N., 1992. The superadiabatic surface layer of the ocean during convection. Journal of Physical Oceanography 22, 1221–1227.

Anis, A., Moum, J. N., 1994. Prescriptions for heat flux and entrainment rates in the upper ocean during convection. Journal of Physical Oceanography 24, 2142–2155.

Arnault, S., Kestenare, E., 2004. Tropical Atlantic surface current variability from 10 years of TOPEX/Poseidon altimetry. Geophysical Research Letters 31, doi:10.1029/2003GL019210.

Arrhenius, S., 1896. On the influence of carbonic acid in the air upon the temperature of the ground. Philosophical Magazine and Journal of Science 41 (5), 237–276.

Bartholomew, J. C., 1973. The Advanced Atlas of Modern Geography. Clarke, Irwin & Company, Toronto, Vancouver.

Bates, N., Merlivat, L., 2001. The influence of short-term wind variability on air-sea CO_2 exchange. Geophysical Research Letters 28 (17), 3281–3284.

Bell, M., Acreman, D., Barciela, R., Hines, A., Martin, M., Sellar, A., Stark, J., Storkey, D., 2004. The forecasting ocean assimilation model (FOAM) system. In: 35th COSPAR Scientific Assembly. p. 1730.

Bell, M., Forbes, R., Hines, A., 2000. Assesment of the FOAM global data assimilation system for real-time operational ocean forecasting. Journal of Marine Systems 25, 1–22.

Bernie, D. J., Woolnough, S. J., Slingo, J. M., Guilyardi, E., 2005. Modelling of diurnal and intraseasonal variability of the ocean mixed layer. Journal of Climate 18, 1190–1202.

Blomquist, B. W., Fairall, C. W., Huebert, B. J., Kieber, D. J., Westby, G. R., 2006. DMS sea-air transfer velocity: Direct measurements by eddy covariance and parameterization based on the NOAA/COARE gas transfer model. Geophysical Research Letters 33 (L07601), doi:10.1029/2006GL025735.

Bock, E. J., Hara, T., Frew, N. M., McGillis, W. R., 1999. Relationship between air-sea gas transfer and short wind waves. Journal of Geophysical Research 104 (25), 25821–25831.

Bock, E. J., McCready, M. J., 1988. Effects of small-wavelength waves on gas-transfer across the ocean surface. Journal of Geophysical Research 93, 5143–5152.

Boutin, J., Etcheto, J., Dandonneau, Y., Bakker, D. C. E., Feely, R. A., Inoue, H. Y., Ishii, M., Ling, R. D., Nightingale, P. D., Metzl, N., Wanninkhof, R., 1999. Satellite sea surface temperature: A powerful tool for interpreting in situ pCO_2 measurements in the equatorial Pacific Ocean. Tellus 51B, 490–508.

Boutin, J., Etcheto, J., Merlivat, L., Rangama, Y., 2002. Influence of gas exchange coefficient parameterization on seasonal and regional variability of CO_2 air-sea fluxes. Geophysical Research Letters 29 (8), doi:10.1029/2001GL013872.

Brainerd, K. E., Gregg, M. C., 1993a. Diurnal restratification and turbulence in the oceanic surface mixed layer 1. Observations. Journal of Geophysical Research 98 (C12), 22645–22656.

Brainerd, K. E., Gregg, M. C., 1993b. Diurnal restratification and turbulence in the oceanic surface mixed layer 2. Modelling. Journal of Geophysical Research 98 (C12), 22657–22664.

Broecker, H. C., Peterman, J., Siems, W., 1978. The influence of wind on CO_2 exchange in a wind wave tunnel, including the effects of monolayers. Journal of Marine Research 36, 595–610.

Broecker, H. C., Siems, W., 1984. The role of bubbles for gas transfer from water to air at higher wind speeds. Experiments in the wind-wave facility in Hamburg. In: Brusaert, W., Jirka, G. H. (Eds.), Gas Transfer at Water Surfaces. D. Reidel Publishing Company, pp. 229–236.

Broecker, W., Peng, T. H., Ostlund, G., Stuiver, M., 1985. The distribution of bomb radiocarbon in the ocean. Journal of Geophysical Research 90, 6953–6970.

Broecker, W., Sutherland, S. C., Smethie, W. M., Peng, T. H., Ostlund, G., 1995. Oceanic radiocarbon: Separation of the natural and bomb components. Global Biogeochemical Cycles 9 (263-288).

Bryan, K., 1969. A numerical method for the study of the World Ocean. Journal of Computational Physics 4, 347–376.

Bryan, K., 1975. A global ocean-atmosphere climate model II: The oceanic circulation. Journal of Physical Oceanography 5, 30–46.

Buesseler, K. O., Boyd, P. W., 2003. Will ocean fertilization work? Science 300 (67-68).

Burchard, H., 2001. Simulating the wave-enhanced layer under breaking surface waves with two-equation turbulence models. Journal of Physical Oceanography 31, 3133–3145.

Burchard, H., Baumert, H., 1995. On the performance of a mixed layer model based on the k-turbulence closure. Journal of Geophysical Research 100, 8523–8540.

Burchard, H., Bolding, K., 2001. Compartive analysis of four second-moment turbulence closure models for the oceanic mixed layer. Journal of Physical Oceanography 31, 1943–1968.

Burchard, H., Bolding, K., Villarreal, M., 1999. GOTM — A general ocean turbulence model. Theory, applications and test cases. Tech. Rep. EUR 18745 EN, European Commission.

Canuto, V, M., Howard, A., Cheng, Y., Dubovikov, M. S., 2001. Ocean turbulence I: One-point closure model. Momentum and heat vertical diffusivities with and without rotation. Journal of Physical Oceanography 31, 1413–1426.

Carton, J. A., Zhou, Z. X., 1997. Annual cycle of sea surface temperature in the tropical Atlantic Ocean. Journal of Geophysical Research 102, 27813–27824.

Chiapello, I., Bergametti, G., Gomes, L., Chatenet, B., Dulac, F., Pimenta, J., Suaros, E. S., 1995. An addtional low layer transport of Sahelian and Saharan dust over the North-Eastern Tropical Atlantic. Geophysical Research Letters 22 (23), 3191–3194.

Clark, J. F., Wanninkhof, R., Schlosser, P., Simpson, H. J., 1994. Gas exchange rates in the tidal Hudson River using a dual tracer technique. Tellus 43B, 274–285.

Clark, N. E., Eber, L., Laurs, R. M., Renner, J. A., Saur, J. F. T., 1974. Heat exchange between the ocean and atmosphere in the eastern North Pacific for 1961. NOAA Tech. Rep. 108 (NMFS SSRF-682).

Clayson, C. A., Weitlich, D., 2006. Variability of tropical diurnal sea surface temperature. Journal of Climate 20 (doi: 10.1175/JCLI3999.1), 334–352.

Climate Lab section of the Environmental Change Research Group, 2000. Global climate animations, department of Geography, University of Oregon.
URL `http://geography.uoregon.edu/envchange/clim_animations/index.html`

Collier, M. A., Durack, P. J., 2006. CSIRO netCDF version of the NODC World Ocean Atlas 2005. Tech. Rep. Marine and Atmospheric Research Paper 015, Commonwealth Scientific and Industrial Research Organisation.

Colling, A., 2001. Ocean Ciculation 2nd Edition. Butterworth Heinemann, Ch. Other Major Current Systems, pp. 143–189.

Cornillon, P., Stramma, L., 1985. Distribution of diurnal sea surface warming events in the western Sargasso Sea. Journal of Geophysical Research 90, 11811–11815.

Cox, M., 1984. A primative equation 3-dimensional model of the ocean. Tech. Rep. GFDL Ocean Group Tech. Rep. No. 1, Geophysical Fluid Dynamics Laboratory.

Cox, P. M., Betts, R. A., Jones, C. D., Spall, S. A., Totterdell, I. J., 2000. Acceleration of global warming due to carbon cycle feedbacks in a coupled climate model. Nature 408, 184–187.

Craig, P. D., Banner, M. L., 1994. Modelling wave-enhanced turbulence in the ocean surface layer. Journal of Physical Oceanography 24, 2546–2559.

Cronin, M., McPhaden, M. J., 1997. The upper ocean heat balance in the western equatorial Pacfic warm pool during September–December 1992. Journal of Geophysical Research 102 (C4), 8533–8553.

Cronin, M. F., Kessler, W. S., 2002. Seasonal and interannual modulation of mixed layer variability at 0°, 110°W. Deep-Sea Research I 49, 1–17.

Csanady, G. T., 1997. The 'Slip Law' of the free surface. Journal of Oceanography 53, 67–80.

Da Cunha, L. C., Quéré, L., Buitenhuis, E. T., 2005. Riverine influence on the biogeochemistry of the tropical Atlantic Ocean, ASLO Summer Meeting 2005, Santiago de Compostela, Spain.

Danabasoglu, G., Large, W. G., Tribbia, J. J., Gent, P. R., Briegleb, P. B., McWilliams, J. C., 2006. Diurnal coupling in the tropical oceans of CCSM3. Journal of Climate 19, 2347–2365.

Danckwerts, P. V., 1951. Significance of liquid-film coefficients in gas absorption. Industrial Engineering Chemistry Fundamentals 43, 1460.

Davis, R., deSzoeke, R., Niiler, P., 1981. Variability in the upper ocean during MILE. Part II modeling the mixed layer response. Deep-Sea Research 28A (12), 1453–1475.

Deacon, E. L., 1977. Gas transfer to and across an air-water inferface. Tellus 29, 363–374.

Dickey, D., Simpson, J., 1983. The influence of optical water type on the diurnal response of the upper ocean. Tellus 35B, 142–154.

Dixon, A., 1981. An exact definition of total alkalinity and a procedure for the estimation of alkalinity and total inorganic carbon from titration data. Deep-Sea Research 28A, 609–623.

Dobson, F., Smith, S., 1988. Bulk models of solar radiation at sea. Quaterly Journal of the Royal Meterological Society 114, 165–192.

DOE, 1994. Handbook of methods for the analysis of the various parameters of the carbon dioxide system in sea water; version 2. ORNL/CDIAC-74.

Donelan, M., Wanninkhof, R., 2002. Gas transfer at water surfaces — concepts and issues. In: Gas Transfer at Water Surfaces. Vol. 127 of Geophysical Monograph. American Geophysical Union, pp. 1–10.

Doney, S. C., 1994. Irreversible thermodynamic coupling between heat and matter fluxes across the air-water interface. Journal of the Chemical Society Faraday Transactions 90, 1865–1874.

Donlon, C. J., 2004. The GODAE High Resolution Sea Surface Temperature Pilot Project - Development & Intergration Plan. In: Proceedings of the International Symposium En route to GODAE. Biarritz, France, 13-15th June, pp. 55–60.

Donlon, C. J., 2007. The GODAE High Resolution Sea Surface Temperature Pilot Project - Development & Intergration Plan. Tech. Rep. v0.6, GHRSST-PP Project Office.

Donlon, C. J., Minnett, P. J., Gentemann, C. L., Nightingale, T., Barton, I., Ward, B., Murray, J., 2002. Towards improved validation of satellite sea surface skin temperature measurements for climate research. Journal of Climate 15, 353–369.

Donlon, C. J., Nightingale, T. J., Sheasby, T., J., T., Robinson, I., Emery, W. J., 1999. Implications of the oceanic thermal skin temperature deviation at high wind speed. Geophysical Research Letters 26 (16), 2505–2508.

Donlon, C. J., Robinson, I. S., 1997. Observations of the oceanic thermal skin in the Atlantic Ocean. Journal of Geophysical Research 102 (C8), 18585–18606.

Donlon, C. J., Robinson, I. S., Casey, K. S., Vazquez-Cuervo, J., Armstrong, E., Arino, O., Gentemann, C., May, D., LeBorgne, P., Piollé, J., Barton, I., Beggs, H., Poulter, D. J. S., Merchant, C. J., Bingham, A., Heinz, S., Harris, A., Wick, G., Emery, B., Minnett, P., Evans, R., Llewellyn-Jones, D., Mutlow, C., Reynolds, R. W., Kawamura, H., N., R., 2007. The Global Ocean Data Assimilation Experiment High-resolution Sea Surface Temperature Pilot Project. Bulletin of the American Meteorological Society 88 (8), 1197–1213.

Dorrestein, R., 1979. On the vertical buoyancy flux below the sea surface as induced by atmospheric factors. Journal of Physical Oceanography 9 (229-231).

du Penhoat, Y., Treguier, A. M., 1985. The seasonal linear response of the Tropical Atlantic Ocean. Journal of Physical Oceanography 15, 316–329.

Duce, R. A., Liss, P. S., Merrill, J. T., Atlas, E. L., 1991. The atmospheric input of trace species to the world ocean. Global Biogeochemical Cycles 5, 193–259.

Dufresne, J.-L., Fairhead, L., Le Treut, H., Berthelot, M., Bopp, L., Ciais, P., Friedlingstein, P., Monfray, P., 2002. On the magnitude of positive feedback between future climate change and the carbon cycle. Geophysical Research Letters 29 (10), doi:10.1029/2001GL013777.

Etcheto, J., Boutin, J., Merlivat, L., 1991. Seasonal variation of the CO_2 exchange coefficient over global ocean using satellite wind speed measurement. Tellus 43B, 247–255.

Eugster, W., Kling, G., Jonas, T., McFadden, J. P., Wuest, A., MacIntyre, S., Chapin III, F. S., 2003. CO_2 exchange between air and water in an Arctic Alaskan and midlatitude Swiss lake: Importance of convective mixing. Journal of Geophysical Research 108 (D12), doi:10.1029/2002JD002653.

EUMETSAT, 1998. Cloud analysis format guide no. 8. Tech. Rep. EUMETSAT EUM FG 8, The Meteosat Archive.

Fairall, C. W., Bradley, E., Rogers, D., Edson, J. B., Young, G., 1996a. Bulk parameterization of air-sea fluxes for Tropical Ocean-Global Atmosphere Coupled-Ocean Atmosphere Response Experiment. Journal of Geophysical Research 101 (C2), 3747–3764.

Fairall, C. W., Bradley, E. F., Godfrey, J. S., Wick, G. A., Edson, J. B., Young, G. S., 1996b. Cool-skin and warm-layer effects on sea surface temperature. Journal of Geophysical Research 101 (C1), 1295–1308.

Fairall, C. W., Bradley, E. F., Hare, J. E., Grachev, A. A., Edson, J. B., 2003. Bulk parameterization of air-sea fluxes: Updates and verification for the COARE algorithm. Journal of Climate 16, 571–591.

Fairall, C. W., Hare, J. E., Edson, J. B., McGillis, W. R., 2000. Parameterization and micrometerological measurement of air-sea gas transfer. Boundary-Layer Meteorology 96, 63–105.

Falkowski, P. G., Barber, R. T., Smetacek, V., 1998. Biogeochemical controls and feedbacks on ocean primary production. Science 281, 200–206.

Fangohr, S., Woolf, D. K., Jeffery, C. D., Robinson, I. S., 2008. Calculating long-term global air-sea flux of carbon dioxide using scatterometer, passive microwave, and model re-analysis wind data. Journal of Geophysical Research In press (doi:10.1029/2005JC003376).

Feely, R. A., Wanninkhof, R., McGillis, W. R., Carr, M.-E., Cosca, C. E., 2004. Effects of wind speed and gas exchange parameterizations on the air-sea CO_2 fluxes in the equatorial Pacific Ocean. Journal of Geophysical Research 109, doi:10.1029/2003JC001896.

Fischer, H., Wahlen, M., Smith, J., Mastroianni, D., Deck, B., 1999. Ice core records of atmospheric CO_2 around the last three glacial terminations. Science 283, 1712–1714.

Flament, P., Firing, J., Sawyer, M., Trefois, C., 1994. Amplitude and horizontal structure of a large sea surface warming event during the Coastal Ocean Dynamics Experiment. Journal of Physical Oceanography 24, 124–139.

Foltz, G. R., Grodsky, S. A., Carton, J. A., 2003. Seasonal mixed layer heat budget of the tropical Atlantic Ocean. Journal of Geophysical Research 108 (C5), doi:10.1029/2002JC001584.

Frew, N. M., 1997. The role of organic films in air-sea gas exchange. In: Liss, P. S., Duce, R. A. (Eds.), The Sea Surface and Global Change. Cambridge University Press, pp. 121–172.

Frew, N. M., Bock, E. J., Schimpf, U., Hara, T., Haußecker, H., Edson, J. B., McGillis, W. R., Nelson, R. K., McKenna, S. P., Mete Uz, B., Jähne, B., 2004. Air-sea gas transfer: Its dependence on wind stress, small-scale roughness and surface films. Journal of Geophysical Research 109 (C08S17), doi:10.1029/2003JC002131,.

Frew, N. M., Glover, D. M., Bock, E. J., McCue, S. J., 2007. A new approach to estimation of global air-sea gas transfer velocity fields using dual-frequency altimeter backscatter. Journal of Geophysical Research 112 (C11003,), doi:10.1029/2006JC003819,.

Frew, N. M., Goldman, J. C., Dennett, M. R., Johnson, A. S., 1990. Impact of phytoplankton-generated surfactants on air-sea gas exchange. Journal of Geophysical Research 95, 3337–3352.

Friedlingstein, P., Bopp, L., Ciais, P., Dufresne, J.-L., Fairhead, L., LeTreut, H., Monfray, P. Orr, J., 2001. Positive feedback between future climate change and the carbon cycle. Geophysical Research Letters 28 (8), 1543–1546.

Friedlingstein, P., Dufresne, J.-L., Cox, P. M., Rayner, P. J., 2003. How positive is the feedback between climate change and the carbon cycle? Tellus 55B, 692–700.

Gaspar, P., 1988. Modeling the seasonal cycle of the upper ocean. Journal of Physical Oceanography 18, 161–180.

Gaspar, P., Gregoris, Y., Lefevre, J.-M., 1990. A simple eddy kinetic energy model for simulations of the oceanic vertical mixing: Test at station Papa and long-term upper ocean study site. Journal of Geophysical Research 95, 16179–16193.

Gentemann, C. L., Donlon, C. J., Stuart-Menteth, A. C., Wentz, F. J., 2003. Diurnal signals in satellite sea surface temperature measurements. Geophysical Research Letters 30 (3), 1140, doi:10.1029/2002GL016291.

Gerdes, R., Koberle, C., Willebrand, J., 1991. The influence of numerical advection schemes on the results of ocean general circulation models. Climate Dynamics 5, 211–226.

Godfrey, J. S., Beljaars, A. C. M., 1991. On the turbulent fluxes of buoyancy, heat and moisture at the air-sea interface at low wind speeds. Journal of Geophysical Research 96 (C12), 22043–22048.

Goldman, J. C., Dennett, M. R., Frew, N. M., 1988. Surfactant effects on air-sea gas exchange under turbulent conditions. Deep-Sea Research 35, 1953–1970.

Gordon, C., Cooper, C., Senior, C., Banks, H., Gregory, J., Johns, T., Mitchell, J., Wood, R., 2000. The simulation of SST, sea ice extents and ocean heat transports in a version of the Hadley Centre coupled model without flux adjustments. Climate Dynamics 16, 147–168.

Haney, R., 1971. Surface thermal boundary conditions for ocean circulation models. Journal of Physical Oceanography 1, 241–248.

Hare, J. E., Fairall, C. W., McGillis, W. R., Edson, J. B., Ward, B., Wanninkhof, R., 2004. Evaluation of the National Oceanic and Atmospheric Administration/Coupled-Ocean Atmosphere Response Experiment (NOAA/COARE) air-sea gas transfer parameterization using GasEx data. Journal of Geophysical Research 109 (C08S11), doi:10.1029/2003JC001831.

Hasse, L., 1963. On the cooling of the sea surface by evaportation and heat exchange. Tellus 4 (363-366).

Hasse, L., 1971. The sea surface temperature deviation and the heat flux at the sea-air interface. Boundary-Layer Meteorology 1 (368-370).

Hastenrath, S., 1977. Hemispheric asymmetry of oceanic heat budget in the equatorial and eastern Pacific. Tellus 29, 523–529.

Hellerman, S., Rosenstein, M., 1983. Normal monthly wind stress over the world ocean with error estimates. Journal of Physical Oceanography 13, 1093–1104.

Hesshaimer, V., Heimann, M., Levin, I., 1994. Radiocarbon evidence for a smaller oceanic carbon dioxide sink than previously believed. Nature 370, 201–203.

Hibler, W., 1979. A dynamic-thermodynamic sea ice model. Journal of Physical Oceanography 9, 815–846.

Ho, D. T., Ledwell, J. R., Smethie Jr, W. M., 2008. Use of SF_5CF_3 for ocean tracer release experiments. Geophysical Research Letters 35, doi:10.1029/2007GL032799.

Horrocks, L. A., Harris, A. R., Saunders, R. W., 2003. Modelling the diurnal thermocline for daytime bulk SST from AATSR. Tech. Rep. FR 418, Met Office.

Houghton, R. W., 1989. Influence of local and remote wind forcing in the Gulf of Guinea. Journal of Geophysical Research 94 (C4), 4816–4828.

IPCC, 2007. Summary for Policymakers. In: Solomon, S., Qin, D., Manning, M., Chen, Z., Marquis, M., Averyt, K. B., Tignor, M., Miller, H. L. (Eds.), Climate Change 2007: The Physical Science Basis. Contribution of Working Group I to the Fourth Assessment Report of the Intergovernmental Panel on Climate Change. Cambridge University Press, United Kingdom and New York, NY, USA.

Ivanov, A., 1977. Ocean absorption of solar energy. Oxford: Pergamon Press, Ch. 5 Modelling and prediction of upper layer of the ocean, p. 325.

Ivanov, L. I., Polonskiy, A. B., 1992. Seasonal variation in the temperature and salinity in the northwest Tropical Atlantic. Oceanology 32 (4), 445–449.

Jähne, B., Haußecker, H., 1998. Air-water gas exchange. Annual Review of Fluid Mechanics 30, 443–468.

Janowick, J. E., Arkin, P. A., Morrissey, 1994. An estimation of the diurnal cycle in oceanic tropical rainfall using satellite and in situ data. Monthly Weather Review 122, 2296–2311.

Jeffery, C. D., Robinson, I. S., Woolf, D. K., Donlon, C. J., 2008. The response to phase-dependent wind stress and cloud fraction of the diurnal cycle of SST and air-sea CO_2 exchange. Ocean Modelling 23 (10.1016/j.ocemod.2008.03.003), 33–48.

Jeffery, C. D., Woolf, D. K., Robinson, I. S., Donlon, C. J., 2007. 1-d modelling of convective CO_2 exchange in the Tropical Altantic. Ocean Modelling 19 (doi:10.1016/j.ocemod.2007.07.003), 161–182.

Jerlov, N., 1968. Optical Oceanography. Elsevier, New York.

Johns, T., Carnel, R., Crossley, J., Gegory, J., Mitchell, J., Senior, C., Tett, S., Wood, R., 1997. The second Hadley Centre coupled ocean-atmosphere GCM: Model description, spinup and validation. Climate Dynamics 13, 103–134.

Johns, T., Durman, C., Banks, H., Roberts, M., McLaren, A., Ridley, J., Senior, C., Williams, K., Jones, A., Rickard, G., Cusack, S., Ingram, W., Crucifix, M., Sexton, D., Joshi, M., Dong, B.-W., Spencer, H., Hill, R., Gregory, J., Keen, A., Pardaens, A., Lowe, J., Bodas-Salcedo, A., Stark, S., Searl, Y., 2006. The new Hadley Centre climate model HadGEM1: Evaluation of coupled simulations. Journal of Climate 19, 1327–1353.

Johnson, K. S., 1982. Carbon dioxide hydration and dehydration kinetics in seawater. Limnological Oceanography 27, 849–855.

Joos, F., Bruno, M., 1998. Long-term variability of the terrestrial and oceanic carbon sinks and the budgets of the carbon isotopes ^{13}C and ^{14}C. Global Biogeochemical Cycles 12, 277–295.

Joos, F., Gian-Kasper, P., Stocker, T. F., Marchal, O., Schmittner, A., 1999. Global warming and marine carbon cycle feedbacks on future atmospheric CO_2. Science 284, 464–467.

Josey, S., Kent, E., Taylor, P., 1998. The Southampton Oceanography Centre (SOC) ocean-atmosphere heat, momentum and freshwater flux atlas. Tech. Rep. 6.

Josey, S. A., Pascal, R. W., Taylor, P. K., Yelland, M., 2003. A new formula for determining the atmospheric longwave flux at the ocean surface at mid-high latitudes. Journal of Geophysical Research 108 (C4), doi:10.1029/2002JC001418.

Kantha, L. H., Clayson, C. A., 1994. An improved mixed layer model for geophysical applications. Journal of Geophysical Research 99 (C12), 25235–25226.

Kara, A. B., Rochford, P. A., Hurlburt, H. E., 2000. An optimal definition for ocean mixed layer depth. Journal of Geophysical Research 105 (C7), 16803–16821.

Katsaros, K. B., Liu, W. T., Businger, J. A., Tillman, J. E., 1977. Heat transport and thermal structure in the interfacial boundary layer measured in an open tank of water in turbulent free convection. Journal of Fluid Mechanics 83 (2), 311–335.

Kawai, Y., Wada, A., 2007. Diurnal sea surface temperature variation and its impact on the atmosphere and ocean: A review. Journal of Oceanography 63, 721–744.

Kettle, H., Merchant, C. J., 2005. Systematic errors in global air-sea CO_2 flux caused by temporal averaging of sea-level pressure. Atmospheric Chemistry and Physics 5, 1459–1466.

Khundzhua, G. G., Gusev, A. M., Andreyev, Y. G., Gurov, V. V., Skorokhvatov, N. A., 1977. Structure of the cold surface film of the ocean and heat transfer between the ocean and the atmosphere. Izv Atmosphere and Ocean Physics (Engl. Transl.) 12, 506–509.

Kondo, J., 1975. Air-sea bulk transfer coefficients in diabatic conditions. Boundary-Layer Meterology 9 (1), 91.

Kortzinger, A., 2003. A significant CO_2 sink in the Tropical Atlantic Ocean associated with the Amazon River plume. Geophysical Research Letters 30 (24), doi:10.1029/2003GL018841.

Kraus, E., Turner, J., 1967. A one-dimensional model of the seasonal thermocline II: The general theory and its consequences. Tellus 19 (1), 98–105.

Lapshin, V. B., Ovinova, N. V., Postnov, A. A., 1998. Variability of carbon dioxide partial pressure in the tropical Atlantic. Russian Meterology and Hydrology 12, 51–59.

Lapshin, V. B., Ovinova, N. V., Postnov, A. A., 1999. Long-term trends of carbon dioxide partial pressure in surface waters of the tropical Atlantic. Russian Meterology and Hydrology 4, 57–61.

Large, W., 1996. An observational and numerical investigation of the climatological heat and salt balances at OWS Papa. Journal of Climate 9, 1856–1876.

Large, W. G., McWilliams, J. C., Doney, S. C., 1994. Ocean vertical mixing: A review and a model with a nonlocal boundary layer parameterization. Reviews of Geophysics 32 (4), 363–403.

Lefevre, N., Moore, G., Aiken, J., Watson, A. J., Cooper, D. J., Ling, R., 1998. Variability of pCO_2 in the Tropical Atlantic in 1995. Journal of Geophysical Research 103 (C3), 5623–5634.

Levitus, S., 1994. World Ocean Atlas CD-ROM Data Set Doc., Volume 3: Salinity and Volume 4: Temperature. Tech. rep., National Oceanic and Atmospheric Administration, Washington D.C.

Liss, P. S., 1983. Gas transfer: Experiements and geochemical implications. In: Liss, P. S., Slinn, W. G. N. (Eds.), Air-Sea Exchange of Gases and Particles. Dordrecht, Holland: Kluwer Academic Publishers, pp. 241–298.

Liss, P. S., Merlivat, L., 1986. Air-sea gas exchange rates: Introduction and synthesis. In: Buat-Menard, P. (Ed.), The Role of Air-Sea Exchange in Geochemical Cycling. Dordrecht, Holland: Kluwer Academic Publishers, pp. 113–127.

Liu, W. T., Businger, J. A., 1975. Temperature profile in the molecular sublayer near the interface of a fluid in turbulent motion. Geophysical Research Letters 2 (9), 403–404.

Lombardo, C. P., Gregg, M. C., 1989. Similarity scaling of viscous and thermal dissipation in a convecting surface boundary layer. Journal of Geophysical Research 94 (C5), 6273–6284.

Lorenc, A., Bell, R., MacPherson, B., 1991. The Meterological Office analysis correction data assimilation scheme. Quaterly Journal of the Royal Meterological Society 117, 59–89.

MacIntyre, S., Eugster, W., Kling, G., 2002. The critical importance of buoyancy flux for gas flux across the air-water interface. In: Gas Transfer at Water Surfaces. Vol. 127 of Geophysical Monograph. American Geophysical Union, Washington DC, pp. 135–140.

Manabe, S., Stouffer, R. J., 1994. Multiple-century response of a coupled ocean-atmosphere model to an increase of atmospheric carbon-dioxide. Journal of Climate 7, 5–23.

Martin, J. H., 1990. Glacial-interglacial CO_2 change: The iron hypothesis. Paleoceanography 5, 1–13.

Martin, P., 1985. Simulation of the mixed layer at OWS November and Papa with several models. Journal of Geophysical Research 90 (9), 903–916.

McCulloch, M., Alves, J., Bell, M., 2004. Modelling shallow mixed layers in the north-east Atlantic. Journal of Marine Systems 52, 107–119.

McGillis, W. R., Edson, J. B., Zappa, C. J., Ware, J. W., McKenna, S. P., Terray, E. A., E., H. J., Fairall, C. W., Drennan, W., Donelan, M., DeGrandpre, M. D., Wanninkhof, R., Feely, R. A., 2004. Air-sea CO_2 exchange in the Equatorial Pacific. Journal of Geophysical Research 109 (C08S02), doi:10.1029/2003JC002256.

McGillis, W. R., Wanninkhof, R., 2006. Aqueous CO_2 gradients for air-sea flux estimates. Marine Chemistry 98, 100–108.

McNeil, C. L., Farmer, D. M., 1995. Observations of the influence of diurnal convection on upper ocean dissolved gas measurements. Journal of Marine Research 53, 151–169.

McNeil, C. L., Merlivat, L., 1996. The warm oceanic surface layer: Implications for CO_2 fluxes and surface gas measurements. Geophysical Reseach Letters 23 (24), 3575–3578.

Mellor, G. L., 2001. One-dimensional, ocean surface layer modelling: A problem and a solution. Journal of Physical Oceanography 31, 790.

Mellor, G. L., Yamada, T., 1974. A hierarchy of turbulence closure models for planetary boundary layers. Journal of Atmospheric Sciences 31, 1791–1806.

Mellor, G. L., Yamada, T., 1982. Development of a turbulence closure model for geophysical fluid problems. Reviews of Geophysics 20, 851–875.

Memery, L., Merlivat, L., 1985. Influence of gas transfer on the CO_2 uptake by the ocean. Journal of Geophysical Research 90 (C4), 7361–7366.

Merle, J., 1980. Seasonal heat budget in the equatorial Atlantic Ocean. Journal of Physical Oceanography 10, 464–469.

Millero, F. J., 2007. The marine inorganic carbon cycle. Chemistry Review 107, 308–341.

Minnett, P. J., 2003. Radiometric measurements of the sea-surface skin temperature - the competing roles of the diurnal thermocline and the cool skin. International Journal of Remote Sensing 24, 5033–5047.

Mohr, T. (Ed.), 1999. CGMS Directory of Meteorological Satellite Applications. Ch. 10: Satellite Instruments.
URL `http://www.wmo.ch/pages/prog/sat/CGMS/Directoryofapplications/en/cover.htm`

Molinari, R. L., Festa, J. F., Marmolejo, E., 1985. Evolution of the sea surface temperature in the tropical Atlantic Ocean during FGGE. Journal of Marine Research 43, 67–81.

Monahan, E. C., Spillane, M. C., 1984. The role of oceanic whitecaps in air-sea gas exchange. In: Brusaert, W., Jirka, G. H. (Eds.), Gas Transfer at Water Surfaces. D. Reidel Pub. Co., pp. 495–503.

Nesbitt, S. W., Zisper, E. J., 2003. The diurnal cycle of rainfall and convective intensity according to three years of trmm measurments. Journal of Climate 16, 1456–1475.

Nightingale, P. D., Liss, P. S., Schlosser, P., 2000a. Measurements of air-sea gas transfer during an open ocean algal bloom. Geophysical Research Letters 27 (14), 2117–2120.

Nightingale, P. D., Marlin, G., Law, C. S., Watson, A. J., Liss, P. S., Liddicoat, M. I., Boutin, J., Upstill-Goddard, R. C., 2000b. In situ evaluation of air-sea gas exchange parameterizations using novel conservative and volatile tracers. Global Biogeochemical Cycles 14 (1), 373–387.

Niiler, P. P., Kraus, E. B., 1975. Modelling and Prediction of the Upper Layers of the Oceans. Pergamon Press, Ch. One-dimensional models of the upper ocean, pp. 143–172.

Nobre, P., Shukla, J., 1996. Variations of sea surface temperature, wind stress and rainfall over the Tropical Atlantic and South America. Journal of Climate 9, 2464–2479.

Ohlmann, J. C., Sigel, D. A., 2000. Ocean radiant heating. Part II: Parameterizing solar radiation transmission through the upper ocean. Journal of Physical Oceanography 30, 1849–1865.

Olsen, A., Trinanes, J. A., Wanninkhof, R., 2004. Sea-air flux of CO_2 in the Caribbean Sea estimated using in situ and remote sensing data. Remote sensing of Environment 89, 309–325.

Olsen, A., Wanninkhof, R., Trinanes, J. A., Johannessen, T., 2005. The effect of wind speed products and wind speed-gas exchange relationships on interannual variability of the air-sea CO_2 gas transfer velocity. Tellus 57B (95-106).

Pacanowski, R., Philander, S., 1981. Parameterization of vertical mixing in numerical models of tropical oceans. Journal of Physical Oceanography 11, 1443–1451.

Palmer, J., Totterdell, I. J., 2001. Production and export in a global ecosystem model. Deep-Sea Research I 48, 1168–1198.

Paulson, C. A., Simpson, J. J., 1977. Irradiance measurements in the upper ocean. Journal of Physical Oceanography 7, 952–956.

Paulson, C. A., Simpson, J. J., 1981. The temperature difference across the cool skin of the ocean. Journal of Geophysical Research 86 (C11), 11044–11054.

Payne, R. E., 1972. Albedo of the sea surface. Journal of Atmospheric Sciences 9, 959–970.

Peacock, S., 2004. Debate over the ocean bomb radiocarbon sink: Closing the gap. Global Biogeochemcial Cycles 18, doi:10.1029/2003GB002211.

Philander, S. G. H., Chao, Y., 1991. On the contrast between the seasonal cycle of the equatorial Atlantic and Pacific Oceans. Journal of Physical Oceanography 21, 1399–1406.

Philander, S. G. H., Gu, D., Halpern, D., Lambert, G., Lau, N. C., Li, T., Pacanowski, R. C., 1996. Why is the ITCZ mostly north of the equator? Journal of Climate 9, 2958–2972.

Phillips, L. F., 1991. CO_2 transport at the air-water interface: Effects of coupling of heat and matter fluxes. Geophysical Research Letters 18, 1221–1224.

Pollard, R., Millard, R., 1970. Comparison between observed and simulated wind-generated inertial oscillations. Deep-Sea Research 17, 813–821.

Price, J. F., Weller, R. A., Boewers, C. M., Briscoe, M. G., 1987. Diurnal response of SST observed at the long term upper ocean study (34°N, 70°W) in the Sargasso Sea. Journal of Geophysical Research 92, 14480–14490.

Price, J. F., Weller, R. A., Pinkel, R., 1986. Diurnal cycling: Observations and models of the upper ocean response to diurnal heating, cooling and wind mixing. Journal of Geophysical Research 91 (C7), 8411–8427.

Rangama, Y., Boutin, J., Etcheto, J., Merlivat, L., Takahashi, T., Delille, B., Frankignoulle, M., Bakker, D. C. E., 2005. Variability of the net air-sea CO_2 flux inferred from shipboard and satellite measurements in the Southern Ocean south of Tasmania and New Zealand. Journal of Geophysical Reseach 110 (c09005), doi:10.1029/2004JC002619.

Redi, M., 1982. Oceanic isopycnal mixing by coordinate transformation. Journal of Physical Oceanography 12, 1154–1158.

Reed, R. J., Jaffe, K. D., 1981. Diurnal variation of summer convection over West Africa and the tropical eastern Atlantic during 1974 and 1978. Monthly Weather Review 109, 2527–2534.

Reynolds, R. W., Smith, T. M., 1994. Improved global sea surface temperature analyses using optimum interpolation. Journal of Climate 7, 929–948.

Richardson, P. L., Reverdin, G., 1987. Seasonal cycle of velocity in the Atlantic North Equatorial Countercurrent as measured by surface drifters, current meters and ships. Journal of Geophysical Research 92, 3691–3708.

Robertson, J. E., Watson, A. J., 1992. Thermal skin effect of the surface ocean and its Implications for CO_2 uptake. Nature 358, 738–740.

Rodi, W., 1987. Examples for calculation methods for flow and mixing in stratified fluids. Journal of Geophysical Research 92 (C5), 5305–5328.

Rosati, A., Miyakoda, K., 1988. A general circulation model for upper ocean simulation. Journal of Physical Oceanography 18, 1601–1626.

Sarmiento, J. L., Orr, J. C., Siegenthaler, U., 1992. A perturbation simulation of CO_2 uptake in an ocean general circulation model. Journal of Geophysical Research 97, 3621–3645.

Saunders, P. M., 1967. The temperature at the ocean-air interface. Journal of the Atmospheric Sciences 24, 269–273.

Schiller, A., Godfrey, J. S., 2003. Indian Ocean intraseasonal varaibility in an Ocean General Circulation Model. Journal of Climate 16, 21–39.

Schlüssel, P., Emery, W. J., Grassl, H., Mammen, T., 1990. On the bulk-skin temperature difference and its impact on satellite remote sensing of the sea surface temperature. Journal of Geophysical Research 95 (C8), 13341–13356.

Schlüssel, P., Soloviev, A. V., Emery, W. J., 1997. Cool and freshwater skin of the ocean during rainfall. Boundary-Layer Meterology 82, 437–472.

Schmitz, W. J., Richardson, P. L., 1991. On the sources of the Florida Current. Deep-Sea Research 38, 379–409.

Schuster, U., Watson, A. J., 2007. A variabile and decreasing sink for atmospheric CO_2 in the North Atlantic. Journal of Geophysical Research 112 (C11006), doi:10.1029/2006JC003941.

Semtner, A., 1976. A model for the thermodynamic growth of sea ice in numerical investigations of climate. Journal of Physical Oceanography 6, 369–389.

Serra, Y. L., McPhaden, M. J., 2004. In situ observations of diurnal variability in rainfall over the Tropical Pacific and Atlantic Oceans. Journal of Climate 17, 3496–3509.

Shankaranarayanan, K., Donelan, M. A., 2001. A probabilistic approach to scatterometer model function verification. Journal of Geophysical Research 106 (C9), 19969–19990.

Shay, T. J., Gregg, M. C., 1984. Turbulence in an oceanic convective mixed layer. Nature 310, 282–285.

Shay, T. J., Gregg, M. C., 1986. Convectively driven turbulent mixing in the upper ocean. Journal of Physical Oceanography 16, 1777–1798.

Shiffer, R. A., Rossow, W. B., 1983. The International Satellite Cloud Climatology Project (ISCCP): The first project of the World Climate Research Programme. Bulletin of the American Meterological Society 64, 779–784.

Shinoda, T., 2005. Impact of the diurnal cycle of solar radiation on intraseasonal SST variability in the western equatorial Pacific. Journal of Climate 18, 2628–2636.

Shinoda, T., Hendon, H. H., 1988. Mixed layer modelling of intraseasonal variability in the tropical western Pacific and Indian Oceans. Journal of Climate 11, 2668–2685.

Siegenthaler, U., Sarmiento, J. L., 1993. Atmospheric carbon dioxide and the ocean. Nature 365, 119–125.

Sigenthaler, U., 1983. Uptake of excess CO_2 by outcrop diffusion model of the ocean. Journal of Geophysical Research 88, 3599–3608.

Simonot, J.-Y., Treut, H. L., 1986. A climatological field of mean optical properties of the world ocean. Journal of Geophysical Research 91 (C5), 6642–6646.

Simpson, J. J., Paulson, C. A., 1999. Mid-ocean observations of atmospheric radiation. Quaterly Journal of the Royal Meterological Society 105, 487–502.

Smethie, W. M., Takahashi, T., Chipman, D. W., 1985. Gas exchange and CO_2 flux in the Tropical Atlantic Ocean derrived from 222Rn and pCO_2 measurements. Journal of Geophysical Research 90 (C4), 7005–7022.

Smith, S., Dobson, F., 1984. The heat budget at Ocean Weather Station Bravo. Atmosphere-Ocean 22, 1–22.

Soloviev, A. V., Schlüssel, P., 1994. Parameterization of the cool skin of the ocean and of the air-ocean gas transfer on the basis of modeling surface renewal. Journal of Physical Oceanography 24, 1339–1346.

Soloviev, A. V., Schlüssel, P., 2002. A model of air-sea gas exchange incorporating the physics of the turbulent boundary layer and the properties of the sea surface. In: Gas Transfer at Water Surfaces. Vol. 127 of Geophysical Monograph. American Geophysical Union, Washington DC, pp. 141–146.

Stephens, M. P., Samuels, G., Olson, R. A., Fine, R. A., Takahashi, T., 1995. Sea-air flux of CO_2 in the North Pacific using shipboard and satellite data. Journal of Geophysical Reseach 100 (13571-13583).

Stips, A., Burchard, H., Bolding, K., Eifler, W., 2002. Modelling of convective turbulence with a two-equation k-ϵ closure scheme. Ocean Dynamics 52, 153–168.

Stommel, H., 1969. Observations of the diurnal thermocline. Deep-Sea Research 16, 269–284.

Stramma, L., Cornillon, P., Weller, R. A., Price, J. F., Briscoe, M. G., 1986. Large diurnal sea surface temperature variability: Satellite and in situ measurements. Journal of Physical Oceanography 56, 345–358.

Stramma, L., Rhein, M., Brandt, P., Dengler, M., Boning, C., Walter, M., 2005. Upper ocean circulation in the Western Tropical Atlantic in boreal fall 2000. Deep-Sea Research 52, 221–240.

Stuart-Menteth, A. C., Robinson, I. S., Challenor, P. G., 2003. A global study of diurnal warming using satellite-derived sea surface temperature. Journal of Geophysical Research 108 (C5), doi:10.1029/2002JC001534.

Stuart-Menteth, A. C., Robinson, I. S., Donlon, C. J., 2005a. Sensitivity of the diurnal warm layer to meteorological fluctuation. Part 2: A new parameterization for diurnal warming. Journal of Atmospheric and Ocean Science 10 (3), 209–234.

Stuart-Menteth, A. C., Robinson, I. S., Weller, R. A., Donlon, C. J., 2005b. Sensitivity of the diurnal warm layer to meteorological fluctuations. Part 1: Observations. Journal of Atmospheric and Ocean Science 10 (3), 193–208.

Stull, R. B., 1994. A convective transport theory for surface fluxes. Journal of the Atmospheric Sciences 51 (1), 3–22.

Sverdrup, H. U., Johnson, M. W., Fleming, R. H., 1942. The Oceans, Their Physics, Chemistry and General Biology. New York: Prentice-Hall.

Sweeney, C., Gloor, E., Jacobson, A. R., Key, R. M., McKinley, G., Sarmiento, J. L., Wanninkhof, R., 2007. Constraining global air-sea gas exchange for CO_2 with recent bomb ^{14}C measurements. Global Biogeochemcial Cycles 21, doi:10.1029/2006GB002784.

Szeri, A. J., 1997. Capillary waves and air-sea gas transfer. Journal of Fluid Mechanics 332, 341–358.

Takahashi, T., Olafsson, J., Goddard, J. G., W., C. D., Sutherland, S. C., 1993. Seasonal variation of CO_2 and nutrients in the high-latitude surface oceans: A comparative study. Global Biogeochemical Cycles 7 (4), 843–878.

Takahashi, T., Sutherland, S. C., Sweeny, C., Poisson, A., Metzl, N., Tilbrook, B., Bates, N., Wanninkhof, R., Feely, R. A., Sabine, C., Olafsson, J., Nojiri, Y., 2002. Global sea-air CO_2 flux based on climatological surface ocean pCO_2 and seasonal biological and temperature effects. Deep-Sea Research II 49, 1601–1622.

Takahashi, T., Sutherland, S. C., Wanninkhof, R., Sweeney, C., Feely, R. A., Chipman, D. W., Hales, B., Friederich, G., Chavez, F., Sabine, C., Watson, A., Bakker, D. C. E., Schuster, U., Metzl, N., Inoue, H. Y., Ishii, M., Midorikawa, T., Nojiri, Y., Koertzinger, A., Steinhoff, T., Hoppema, M., Olafsson, J., Arnarson, T. S., Tilbrook, B., Johannessen, T., Olsen, A., Bellerby, R., Wong, C. S., Delille, B., Bates, N. R., de Baar, H. J. W., 2008. Climatological mean and decadal change in surface ocean pCO_2 and net sea-air CO_2 flux over the global oceans. Deep-Sea Research II, accepted.

Tans, P. P., Fung, I. Y., Takahashi, T., 1990. Observational constraints on the global atmospheric co2 budget. Science 247, 1431–1438.

TAO Project Office, 2008. Pilot Research Moored Array in the Atlantic (PIRATA). TAO Project Website.
URL `http://www.pmel.noaa.gov/pirata/`

Thompson, R., 1976. Climatological numerical models of the surface mixed layer of the ocean. Journal of Physical Oceanography 6, 496–503.

Tovar-Sanchez, A., Sañudo Wilhelmy, S., Kustka, A. B., Agusti, S., Dachs, J., Hutchins, D. A., Capone, D. G., Duarte, C. M., 2006. Effects of dust deposition and river discharges on trace metal composition of *Trichodesmium* spp. in the tropical and subtropical North Atlantic Ocean. Limnological Oceanography 51 (4), 1755–1761.

Umlauf, L., Burchard, H., 2003. A generic length-scale equation for geophysical turbulence models. Journal of Marine Research 61, 235–265.

Umlauf, L., Burchard, H., 2005. Second-order turbulence closure models for geophysical boundary layers. A review of recent work. Continental Shelf Research 25, 795–827.

Umlauf, L., Burchard, H., Bolding, K., 2006. GOTM: Sourcecode and test case documentation - Version 3.2. Tech. rep., Baltic Sea Research Institute in Warnemünde.

U.S. Naval Oceanographic Office and the U.S. Naval Ocean Research and Development Activity, 1983. DBDB5 (Digital Bathymetric Data Base - 5 minute grid). Tech. rep., U.S.N.O.O., Bay St. Louis.

Van Scoy, K. A., Morris, K. P., Robertson, J. E., Watson, A. J., 1995. Thermal skin effect and air-sea flux of carbon dioxide: A seasonal high-resolution estimate. Global Biogeochemical Cycles 9 (2), 253–262.

Wang, C. Z., Enfield, D. B., 2001. The tropical western hemisphere warm pool. Geophysical Research Letters 28, 1635–1638.

Wanninkhof, R., 1992. Relationship between wind speed and gas exchange over the ocean. Journal of Geophysical Research 97 (C5), 7373–7382.

Wanninkhof, R., Doney, S. C., Takahashi, T., McGillis, W. R., 2002. The effect of using time-averaged winds on regional air-sea CO_2 fluxes. In: Gas Transfer at Water Surfaces. Vol. 127 of Geophysical Monograph. American Geophysical Union, pp. 351–356.

Wanninkhof, R., Knox, M., 1996. Chemical enhancement of CO_2 exchange in natural waters. Limnological Oceanography 41 (4), 689–697.

Wanninkhof, R., Ledwell, J. R., Broecker, W. S., 1985. Gas exchange wind speed relation measured with sulphur hexafluoride on a lake. Science 227, 1889–1892.

Wanninkhof, R., McGillis, W. R., 1999. A cubic relationship between air-sea CO_2 exchange and wind speed. Geophysical Research Letters 26 (13), 1889–1892.

Ward, B., 2006. Near-surface ocean temperature. Journal of Geophysical Research 111 (C02004), doi:10.1029/2004JC002689.

Ward, B., 2007. Air-water interfacial laboratory measurements. In: Garbe, C. S., Handler, R. A., Jähne, B. (Eds.), Transport at the Air Sea Interface - Measurements, Models and Parameterizations. Springer Verlag, pp. 193–203.

Ward, B., Donelan, M. A., 2006. Thermometric measurements of the molecular sublayer at the air-water interface. Geophysical Research Letters 33 (L07605), doi:10.1029/2005GL024769.

Ward, B., Gentemann, C., Wanninkhof, R., 2006. The diurnal warm layer and its implication for the air-sea flux of carbon dioxide. EOS Transactions AGU 87, (36), Ocean Science Meeting Supplement, Abstract OS35G-16.

Ward, B., Wanninkhof, R., McGillis, W. R., Jessup, A. T., DeGrandpre, M. D., Hare, J. E., Edson, J. B., 2004. Biases in the air-sea flux of CO_2 resulting from ocean surface temperature gradients. Journal of Geophysical Research 109 (C08S08), doi:10.1029/2003JC001800.

Webster, P. J., Clayson, C. A., Curry, J. A., 1996. Clouds, radiation and the diurnal cycle of SST in the tropical western Pacific. Journal of Climate 9, 1712–1730.

Weingartner, T. J., Weisberg, R. H., 1991. A description of the annual cycle in sea surface temperature and upper ocean heat in the equatorial atlantic. Journal of Physical Oceanography 21, 83–96.

Weisberg, R. H., Tang, T. Y., 1987. Further studies on the response of the equatorial thermocline in the Atlantic Ocean to the seasonally varying trade winds. Journal of Geophysical Research 92 (C4), 3709–3727.

Weisberg, R. H., Tang, T. Y., 1990. A linear analysis of equatorial Atlantic ocean thermocline variability. Journal of Physical Oceanography 20 (12), 1813–1825.

Weiss, R. F., 1974. Carbon dioxide in water and seawater: The solubility of a non-ideal gas. Marine Chemistry 2, 203–215.

Weller, R. A., Anderson, S. P., 1996. Surface meteorology and air-sea fluxes in the western equatorial Pacific warm pool during the TOGA Coupled Ocean-Atmosphere Response Experiment. Journal of Climate 9 (8), 1959–1990.

Wentz, F. J., Peteherych, S., Thomas, L. A., 1984. A model function for ocean radar cross sections at 14.6 GHz. Journal of Geophysical Research 89, 3689–3704.

Woods, J. D., Barkman, W., 1986. The response to the upper ocean to solar heating. I: The mixed layer. Quaterly Journal of the Royal Meterological Society 112, 1–27.

Woods, J. D., Barkman, W., Horch, A., 1984. Solar heat of the ocean-diurnal seasonal and meridional variation. Quaterly Journal of the Royal Meterological Society 110, 977–997.

Woolf, D. K., 1993. Bubbles and air-sea transfer velocity of gases. Atmosphere-Ocean 31, 517–540.

Woolf, D. K., 1997. Bubbles and their role in gas exchange. In: Liss, P. S., Duce, R. A. (Eds.), The Sea Surface and Global Change. Cambridge University Press, Cambridge, UK, pp. 173–206.

Woolf, D. K., 2005. Parameterization of gas transfer velocities and sea-state-dependent wave breaking. Tellus 57B, 87–94.

Yang, G.-Y., Slingo, J., 2001. The diurnal cycle in the tropics. Monthly Weather Review 129, 784–801.

Yokoyama, R., Tanba, S., Souma, T., 1995. Sea surface effects on the SST estimation by remote sensing. International Journal of Remote Sensing 16, 227–238.

Zappa, C. J., Asher, W. E., Jessup, A. T., 2001. Microscale wave breaking and air-water gas transfer. Journal of Geophysical Research 106 (C5), 8385–9391.

Zhang, X., Cai, W., 2007. On some biases of estimating the global distribution of air-sea CO_2 flux by bulk parameterization. Geophysical Research Letters 34 (L01608), doi:10.1029/2006GL027337.

Zülicke, C., 2005. Air-sea fluxes including the effect of the molecular skin layer. Deep-Sea Research II 52, 1220–1245.